UNIVERSITÉ DE STRASBOURG

ÉCOLE DOCTORALE DES SCIENCES CHIMIQUES

Institut Pluridisciplinaire Hubert Curien

THÈSE présentée par :

Chen XIE

soutenue le : **19 juillet 2021**

pour obtenir le grade de : **Docteur de l'université de Strasbourg**

Discipline/ Spécialité : Chimie

Complexes à base de lanthanides en tant que systèmes intégrés multifonctionnels en théranostique photodynamique

---

THÈSE dirigée par :
  Dr. CHARBONNIERE Loïc   Directeur de thèse, université de Strasbourg
  Pr. WONG Ka-Leung   Directeur de thèse, Hong Kong Baptist University

RAPPORTEURS :
  Dr. MAURY Olivier   Rapporteur Externe, École normale supérieure de Lyon
  Pr. LAM Hon Wah   Rapporteur Externe, City Univerisity of Hong Kong

---

AUTRES MEMBRES DU JURY :
  Dr. NONAT Aline   Examinateur, université de Strasbourg

Chen XIE

Complexes à base de lanthanides en tant que systèmes intégrés multifonctionnels en théranostique photodynamique

Résumé

Cette thèse présente mes travaux de conception, de préparation et de caractérisation de plusieurs types de nouveaux complexes de lanthanides pour des applications dans le domaine de la théranostique photodynamique. Tous les produits rapportés fonctionnent comme des systèmes intégrés sur lesquels diverses fonctions peuvent être réalisées simultanément. Bien que les termes "complexes de lanthanides" et "théranostique photodynamique" soient des domaines de recherche relativement larges. Les intérêts spécifiques se concentrent sur l'utilisation des lanthanides et de leurs ligands dans d'éventuelles imageries cliniques et thérapies photodynamiques (PDT). Les lanthanides dont il sera question ici sont principalement Eu(III), Gd(III) et Yb(III), en raison de leurs propriétés spectroscopiques uniques. Les méthodes de diagnostic à utiliser sont l'imagerie moléculaire par lumière visible/proche infrarouge et l'imagerie par résonance magnétique. Les effets médicaux possibles sont justifiés par la génération d'oxygène singulet, une espèce active dans la TPD.

Le premier chapitre fournit des descriptions de plusieurs sujets liés aux concepts fondamentaux ou aux techniques appliquées dans mes projets. Bien que certaines sections ne couvrent pas l'évolution de toutes les théories ou le fonctionnement de chaque instrument, tous les éléments clés associés à la discussion qui suit sont élucidés. Pour être plus précis, l'origine des propriétés spéciales des lanthanides et de leurs ligands (porphyrines) est présentée ; le développement de la préparation/caractérisation des complexes de lanthanides est rapporté ; et les principes de la théranostique photodynamique moderne sont expliqués.

Le deuxième chapitre présente mon premier projet dans lequel une série de complexes à double étage lanthanide-porphyrine ont été préparés et caractérisés à l'aide de techniques avancées (par exemple, la microscopie à effet tunnel, la spectroscopie d'absorption transitoire et la spectroscopie d'émission NIR à basse température). Grâce à la conception moléculaire stratégique, les complexes rapportés ont montré des performances

théranostiques avantageuses par rapport aux analogues précédemment rapportés et à certains composés disponibles dans le commerce.

Dans le chapitre III, un objectif toujours présent est d'explorer les agents théranostiques multimodaux avec la meilleure combinaison de techniques d'imagerie et de traitement médical. Mon effort consiste à présenter plusieurs complexes bimétalliques porphyrine-cyclène. Le ligand présentant la capacité de TPD est capable de chélater un ou deux métaux et révèle des effets synergiques. Pour les complexes gallium-gadolinium, une capacité d'imagerie couplée TEP/IRM pourrait être obtenue avec la génération simultanée d'oxygène singulet.

Le dernier chapitre vise à combler le vide de la chimie bioorthogonale, un domaine en plein essor qui étudie les réactions chimiques qui se produisent dans des conditions douces et avec une grande spécificité. Cependant, il n'existe que quelques rapports concernant le suivi instantané des réactions bioorthogonales par émission luminescente. Par conséquent, un complexe à base d'Eu(III) a été préparé qui peut traiter une réaction bioorthogonale typique, et l'expansion résultante des ligands a garanti une sensibilisation efficace du chromophore au centre du lanthanide, puis une forte émission visible.

En résumé, mes trois projets ont été proposés et terminés dans le but d'étudier le potentiel des complexes de lanthanides comme agents théranostiques photodynamiques. Différentes stratégies moléculaires ont été appliquées pour explorer les ligands optimaux améliorant à la fois les performances spectroscopiques des lanthanides et les effets PDT des porphyrines.

Mots clés : Lanthanide ; Porphyrine ; Photodynamique ; Théranostique ; Chimie bioorthogonale

Résumé en anglais

This thesis presents my works in designing, preparing, and characterizing several types of novel lanthanide complexes for application in the fields of photodynamic theranostics. All the reported products are working as integrated systems on which various functions can be achieved simultaneously. Although the terms "lanthanide complexes" and "photodynamic theranostics" are relatively broad research fields. The specific interests are focused on utilizing lanthanides and their ligands in possible clinical imaging and photodynamic therapies (PDT). Lanthanides to be discussed here mainly are Eu(III), Gd(III), and Yb(III) based on their unique spectroscopic properties. The diagnostic methods to be used are molecular imaging by visible/near-infrared light and

magnetic resonance imaging. The possible medical effects are justified by the generation of singlet oxygen, an active species in PDT.

The first chapter provides descriptions of several topics related to the fundamental concepts or techniques applied in my projects. Although some sections do not cover the evolution of all theories or the operation of every instrument, all key elements associated with the ensuing discussion are elucidated. To be specific, the origin of special properties of lanthanides and their ligands (porphyrins) are introduced; the development of preparing/characterizing lanthanide complexes are reported; and the principles of modern photodynamic theranostics are explained.

The second chapter is my first project in which a series of lanthanide-porphyrin double-decker complexes were prepared and characterized with advanced techniques (for example, scanning tunneling microscopy, transient absorption spectroscopy, and low-temperature NIR emission spectroscopy). With the strategic molecular design, the reported complexes showed advantageous theranostic performance over the previously reported analogs and some commercially available compounds.

In chapter III, one ever-present goal is to explore multimodal theranostic agents with the best combination of imaging techniques and medical treatment. My effort is to introduce several porphyrin-cyclen bimetallic complexes. The ligand featuring PDT ability is capable of chelating one or two metals and reveals synergistic effects. For the gallium-gadolinium complexes, a possible PET/MRI coupled imaging ability could be achieved with singlet oxygen generation simultaneously.

The last chapter is to fill the gap of bioorthogonal chemistry, a rising field investigating chemistry reactions that undergo on mild conditions and with high specificity. However, there are only a few reports concerning the instant monitor of bioorthogonal reactions by luminescent emission. Therefore, a Eu(III)-based complex was prepared which can process a typical bioorthogonal reaction, and the resulting expansion in the ligands guaranteed efficient sensitization from the chromophore to the lanthanide center, and then strong visible emission.

In summary, all my three projects were proposed and finished for the purpose of investigating the potential of lanthanide complexes as photodynamic theranostic agents. Different molecular strategies have been applied to explore the optimal ligands improving both the spectroscopic performance of lanthanides and the PDT effects of porphyrins.

Lanthanide-based Complexes as Multifunctional Integrated Systems in Photodynamic Theranostics

XIE Chen

A thesis submitted in partial fulfilment of the requirements

for the degree of

Doctor of Philosophy

Principal Supervisors:

Prof. WONG Ka-Leung (Hong Kong Baptist University)

Dr. CHARBONNIÈRE Loïc (University of Strasbourg)

August 2021

ABSTRACT

This thesis presents my works in designing, preparing, and characterizing several types of novel lanthanide complexes for application in the fields of photodynamic theranostics. All the reported products are working as integrated systems on which various functions can be achieved simultaneously. Although the terms "lanthanide complexes" and "photodynamic theranostics" are relatively broad research fields. The specific interests are focused on utilizing lanthanides and their ligands in possible clinical imaging and photodynamic therapies (PDT). Lanthanides to be discussed here mainly are Eu(III), Gd(III), and Yb(III) based on their unique spectroscopic properties. The diagnostic methods to be used are molecular imaging by visible/near-infrared light and magnetic resonance imaging. The possible medical effects are justified by the generation of singlet oxygen, an active species in PDT.

The first chapter provides descriptions of several topics related to the fundamental concepts or techniques applied in my projects. Although some sections do not cover the evolution of all theories or the operation of every instrument, all key elements associated with the ensuing discussion are elucidated. To be specific, the origin of special properties of lanthanides and their ligands (porphyrins) are introduced; the development of preparing/characterizing lanthanide complexes are reported; and the principles of modern photodynamic theranostics are explained.

The second chapter is my first project in which a series of lanthanide-porphyrin double-decker complexes were prepared and characterized with advanced techniques (for example, scanning tunneling microscopy, transient absorption spectroscopy, and low-temperature NIR emission spectroscopy). With the strategic molecular design, the reported complexes showed advantageous theranostic performance over the previously reported analogs and some commercially available compounds.

In chapter III, one ever-present goal is to explore multimodal theranostic agents with the best combination of imaging techniques and medical treatment. My effort is to introduce several porphyrin-cyclen bimetallic complexes. The ligand featuring PDT ability is capable of chelating one or two metals and reveals synergistic effects. For the gallium-gadolinium complexes, a possible PET/MRI coupled imaging ability could be achieved with singlet oxygen generation simultaneously.

The last chapter is to fill the gap of bioorthogonal chemistry, a rising field investigating chemistry reactions that undergo on mild conditions and with high specificity. However, there are only a few reports concerning the instant monitor of bioorthogonal reactions by luminescent emission. Therefore, a Eu(III)-based complex was prepared which can process a typical bioorthogonal reaction, and the resulting expansion in the ligands guaranteed efficient sensitization from the chromophore to the lanthanide center, and then strong visible emission.

In summary, all my three projects were proposed and finished for the purpose of investigating the potential of lanthanide complexes as photodynamic theranostic agents. Different molecular strategies have been applied to explore the optimal ligands improving both the spectroscopic performance of lanthanides and the PDT effects of porphyrins.

ACKNOWLEDGEMENTS

It is never easy to pursue an academic career from the first day when I entered the university to the last day on which I finished this thesis. There will be more difficulties and challenges on the future road. It is even never easy to live a fruitful life; I might fall, and we might feel lonely, but that is why I should be grateful for anyone who ever helped me, and that is why I am writing this Acknowledgements.

To pursue a Ph.D. degree is a process of learning, not only from books or papers but also from people around me. I have been trying my best to turn to be a qualified researcher by continuously learning from other people. If they were not so generous with their knowledge, I might have taken roundabout routes, or even never gained some outcomes. Beyond scientific knowledge or operation techniques, most people I know are always kind to me and teach me some life principles, perhaps unintentionally. Every people I met and everything I encountered, no matter good or bad, are a part of my life, and the materials I can gain experience from.

I say thank you to my father and mother here. They always respect my choices and exhaust their abilities to help me. It is fortunate to live in my family, and I will make them proud of me.

I want to express my gratitude to my supervisors. Professor WONG, Gary Ka-Leung,

and Doctor CHARBONNIÈRE Loïc. Prof. Wong has known me many years ago, and I have been learning from him when I was an undergraduate student in 2013. His expertise in chemistry and insightful perspective in research benefit me dramatically. He has strict research requirements on me but also kindly cares about my problems in university life. I appreciate what he has helped me with and believe we can achieve more in the future relationship. Dr. Charbonnière is my supervisor at the University of Strasbourg, France. I usually call him Loïc because we are also like friends. He is an intelligent researcher in the field of lanthanide luminescence and more, and he inspired me a lot with his ideas and designs. Besides, he was never reluctant to solve my problems either in the lab or in my French living period.

Besides my supervisors, many professors have ever guided or taught me in my research work. They are all the top researchers and provided me great help in person. They are Prof. JEAN-CLAUDE G. Bünzli, Prof. TANNER Peter, Prof. ASFARI Zouhair, Dr. NONAT Aline, Dr. CHRISTINE Câline, and Dr. CHEIGNON Clémence.

I also want to thank all the lab members both from the Hong Kong Baptist University (HKBU) research team and the University of Strasbourg (UNISTRA) research team. They ever taught me the experimental procedures and the operation of instruments works. Some of us had great collaborations on some projects. What is more important

is that we are in good relationships and that is one reason I could enjoy my Ph.D. life. From HKBU, they are Dr. JIANG Lijun, Dr. ZHANG Jing-Xiang, Dr. LIU Zhenyu, Dr. CHAN Wai-Lun, Dr. ZHANG Yonghong, Dr. WANG Lei, Dr. PAN Fengjuan, Dr. TONG Sheng, Dr. LI Liyi, Dr. FUNG Yanho, Dr. ZHA Shuai, Dr. LUO Yuxia, Dr. ZHONG Yifang, Dr. CHAU Hofai, Ms. FOK Wanyiu, Mr. LI Xiong, Mr. WU Yue, Mr. THOR Waygen, Ms. MA Xia, Ms. LIAO Yun, Ms. HUANG Anjun, Ms. ZHOU Wanqi, Ms. MATUSZEWSKA Celina, and Mr. PAŃCZUK Tomasz. From UNISTRA, they are Dr. KNIGHTON Richard, Dr. BANERJEE Mainak, Dr. CHARPENTIER Cyrille, Mr. LECOINTRE Alexandre, Dr. SY Mohamadou, Dr. GOETZ Joan, Dr. ZABIEROWSKI Piotr, Ms. GODEC Léna, Ms. JOURDAIN Elsa, Mr. KASSIR Ali, Ms. LAVILLEY Gemma, Mr. SORO Lohona Kevin, and Ms. SY Maryame.

I appreciate all the assistance provided by the scientific and administrative officers from both universities and other collaborative institutes. Perhaps they considered what they have done as routine works, but I would never finish my study without their efforts.

At last, all friends I have off-campus are also a large part of my Ph.D. career, and I want to give my sincere thanks to them. Although most of them do not understand the research fields I am working with, or even some of them never meet me in daily life, they are always willing to share their happiness with me and listen to my difficulties. Those people are the ones to whom I express my gratitude in my whole life.

Table of Contents

List of Tables

List of Schemes

Scheme 1. The general scheme of the organic synthesis procedure for the double-decker porphyrinate lanthanide complexes, LnDD.

Scheme 2. The general scheme of the organic synthesis procedure for PZnLGd

Scheme 3. The general scheme of the organic synthesis procedure for PfLGd

Scheme 4. The general scheme of the organic synthesis procedure for LnBT (Ln = La, Eu).

Scheme 5. The general scheme of the organic synthesis procedure for DBCO-mannosamine conjugate.

relatively low attenuation coefficient. (*right*) The relative penetration depth of light *in vivo* at different wavelengths (550 nm, 630 nm, 700 nm, and 800 nm).

Figure 1.10. Simplified Jablonski energy diagram of energy transitions for singlet oxygen generation with the presence of photosensitizers.

Figure 1.11. Surface array of H_2-T(C_{22}OP)P at the 1-phenyloctane/highly ordered pyrolytic graphite (HOPG) interface. (a) STM image. (b) Molecular models.

Figure 2.1. Molecular structures of LnDD in this work and LnN as referencing samples for comparison.

Figure 2.2. The room-temperature ^{1}HNMR spectra of (a) the ligand Por(2DEG) in $CDCl_3$ and (b) LaDD in $CDCl_3$: DMSO-d6 1:1 mixed with 1% hydrazine hydrate.

Figure 2.3. Structure characterization. The first trial of STM imaging for YbDD drop-cast onto HOPG: (*left*) 5 μL toluene with 1 mmol YbDD sample, 140 × 140 nm^2, -1.5 V sample bias, 50 pA, (inset) blue box: a high magnification image, cyan and green lines: denoting height line profiles. (*right top*) Line profile from the left figure along the row of features; (*right bottom*) line profile across the HOPG step edge, the height of the feature ~1 nm (bottom terrace) is indicated.

Figure 2.4. Structure characterization. The second trial of STM imaging for YbDD drop-cast onto HOPG: (*left*) 25 μL chloroform with 1 mmol YbDD sample, 270 × 270 nm^2 image, + 2 V sample bias, 100 pA, (*right*) 75 × 75 nm^2, image +2 V sample bias, 100 pA, (*inset*) blue height profile across rows.

Figure 2.5. UV/vis absorption spectra of a aqueous solution of 10μM LnDD (Ln= Yb, Er, La and Gd).

Figure 2.6. (*Left column*) NIR emission spectra (λ_{ex} = 425nm) of DCM or H$_2$O solution of YbDD; (*right column*) the plot of integrated emission peak area *vs* absorbance, compared with YbTPP(Tp)).

Figure 2.7. NIR emission spectra (λ_{ex} = 425 nm) of YbDD, YbN, and YbTPP(Tp) in DCM (*top left*), H$_2$O (*top right*), toluene (*bottom left*), and MeOH (*bottom right*).

Figure 2.8. Comparison of emission bands of YbN (*black*) and YbDD (*red*) at 298 K in aqueous solution (λ_{ex} = 425 nm).

Figure 2.9. Decay curve of Yb^{3+} emission in the form of complex YbDD (*top*) or YbN (*bottom*) and with monoexponential function fitting.

Figure 2.10. The near-infrared ^{1}O$_2$ phosphorescence spectrum sensitized by GdDD, GdN, and the standard tetraphenylporphyrin H$_2$TPP (in CHCl$_3$. Abs. = 0.05 at the excitation wavelength of 425 nm).

Figure 2.11. Absorption spectra of ABDA mixed with different probes: (a) no probe; (b) Rose Bengal; (c) GdDD; (d) GdN in phosphate-buffered saline (PBS) buffer. The excitation power density was 6 mW cm^{-2}.

Figure 2.12. Plots of the changes in absorbance of ABDA at 402 nm (mixed with10 µM GdDD, GdN, and standard RB) *versus* the irradiation time. The excitation power density was 6 mW cm^{-2}.

Figure 2.13. The 77 K phosphorescence spectrum of GdDD and GdN in MeOH (Conc.: 10 µM, λ_{ex} = 425 nm).

Figure 2.14. (*Top*) fs-TA spectra at different time delays at low pump fluence (15 µJ cm^{-2}), (*bottom*) ground state bleach recovery dynamics at 424 nm, and excited-state

List of Symbols

η_{sens} energy transfer efficiency

Φ_{int} intrinsic quantum yield

K_{ML} Thermodynamic stability constant

K'_{ML} conditional stability constant

Φ_{Δ} quantum yield

λ_{ex} excitation wavelength

ΔA change in absorbance

ε molar absorption coefficient

List of Abbreviations

ABDA   9,10-anthracenediyl-bis(methylene)dimalonic acid

acac   acetylacetonate

a.u.   arbitrary unit

CAN   acetonitrile

CDCl$_3$ deuterated chloroform

DBCO   dibenzocyclooctyne

DBU   1,8-diazabicyclo[5.4.0]undec-7-ene

DCM   dichloromethane

DEG   diethylene glycol

DI water   deionized water

DIBAC   aza-dibenzocyclooctyne

DIPEA   N,N-diisopropylethylamine

DMEM   Dulbecco's modified eagle medium

DMF   N,N-dimethylformamide

DMSO   dimethyl sulfoxide

DOTA   tetraazacyclododecane-1,4,7,10-tetraacetic acid

DTPA   diethylenetriaminepentaacetic acid

ED   electronic dipole

EDTA   ethylenediaminetetraacetic acid

ESI-HRMS   electrospray ionization high resolution mass spectroscopy

FRET	Förster resonance energy transfer
fs	femtosecond
GBCA	Gd(III)-based contrast agents
Gd-DOTA	gadoterate meglumine
HATU	1-[bis(dimethylamino)methylene]-1H-1,2,3-triazolo[4,5-b]pyridinium 3-oxide hexafluorophosphate
HeLa	cervical cancer cells
HOPG	highly ordered pyrolytic graphite
Hp	hematoporphyrin
H_2TPP	tetraphenylporphyrin
IC	internal conversion
ISC	intersystem crossing
IUPAC	International Union of Pure and Applied Chemistry
Ln^{III} or Ln(III)	trivalent lanthanide ion
MALDI – TOF	Matrix-assisted laser desorption/ionization – time of flight
MEM	minimum essential medium
MeOH	methanol
MRC5	normal lung cells
MRI	magnetic resonance imaging
MS	mass spectra
MSCl	methanesulfonyl chloride
MTT	3-(4,5-dimethylthiazol-2-yl)-2,5-diphenyltetrazolium bromide

NIR	near-infrared
NMR	nuclear magnetic resonance
PBS	phosphate-buffered saline
PDD	photodynamic disinfection
PDT	photodynamic therapy
PET	positron emission tomography
PIT	photoimmunotherapy
PMT	photomultiplier tube
PTI	photodynamic therapeutic index
RB	rose bengal
ROS	reactive oxygen spices
SAP	square antiprismatic
SPAAC	strain-promoted azide–alkyne cycloadditions
SPE	solid-phase extraction
SPECT	single-photon emission computed tomography
STM	scanning tunneling microscopy
TAS	transient absorption spectroscopy
TBAF	tetra-n-butylammonium fluoride
*t*Bu-DO3A	tri-*tert*-butyl 2,2',2''-(1,4,7,10-tetraazacyclododecane-1,4,7-triyl)triacetate
TCB	1,2,4-trichlorobenzene
TCSPC	time-correlated single photon counting

TFA   trifluoroacetic acid

TLC   thin-layer chromatography

TSAP   twisted square antiprismatic

UV   ultra-violet

VT-NMR   variable-temperature nuclear magnetic resonance

Chapter I Introduction

1.1 Overview of this chapter

This chapter serves to briefly introduce the important principles or techniques involved in my projects. As presented in my thesis title are two major factors – lanthanides and photodynamic theranostics. Both of them have been studied by a huge number of researchers for decades. Even though my works are just a drop in the ocean, there are still various aspects of topics covered here. Some concepts and results I am going to elucidate are seldom considered as common knowledge even to most workers in this area.

To facilitate all readers' understanding of this thesis, general descriptions of related topics are included as the first chapter of this work. The fundamental theories and technical working principles are discussed while detailed results will be shown in the following chapters.

1.2 History of lanthanides

Lanthanides are 15 elements from No. 57 lanthanum (La) to No. 71 lutetium (Lu) in the periodic table. No.21 scandium (Sc) and No. 39 yttrium (Y) are considered collectively as rare earth elements (REE) because of their similar chemical properties,

Nowadays, most REE mineral is consumed in industrial production. In the United

States in 2019, 75% end-use was estimated as a catalyst, following by metallurgical applications and alloys, 5%; ceramics and glass, 5%; polishing, 5%.[1] Besides, lanthanide metals are also used in life science because of their advantageous spectroscopic properties. For example, Gadolinium(III) is widely used in magnetic resonance imaging (MRI) in the form of Gd-DOTA as an MRI contrast agent.

Occurrences of rare earth elements are not rare in the Earth's crust, but those elements are in great geochemical divide, and difficult to mine and extract from ore. Major reserving countries include China, the US, India, Brazil, and Australia, but China (having approximately 30% of the world's total reserves) serves for more than 95% world's production.[2] Although there are relatively few REE occurrences in France, the most significant enrichment can be found in Brittany. In the Le Grand-Fougeray placer, monazite (a phosphate mineral) mined from there was found to be rich in europium (0.2 to 1% Eu_2O_3) and neodymium (13% Nd_2O_3).[3]

In the following sections, the originality of their unique spectroscopic properties of trivalent lanthanide ions will be elucidated and related examples are also discussed.

1.3 Atomic Orbitals and Electronic Configuration

General research focuses were attracted on lanthanides because of their special or even unique performance in spectroscopic, chemical, pharmaceutical fields.[4] One key reason for lanthanide elements having a series of characteristic properties is their unusual

electronic configurations. As for one trivalent lanthanide ion (Ln^{III}), the atomic orbital consists of one xenon core (consisting of 54 electrons), and the other electrons are located on the 4f orbitals, in which the orbital composition[5] can be written as 4f^n. Figure 1.1[6] shows a theoretical illustration providing a direct visualization in which the valence 4f orbitals. Those electrons on 4f orbitals are located far from their nuclear and have few chances to interact with other electrons.
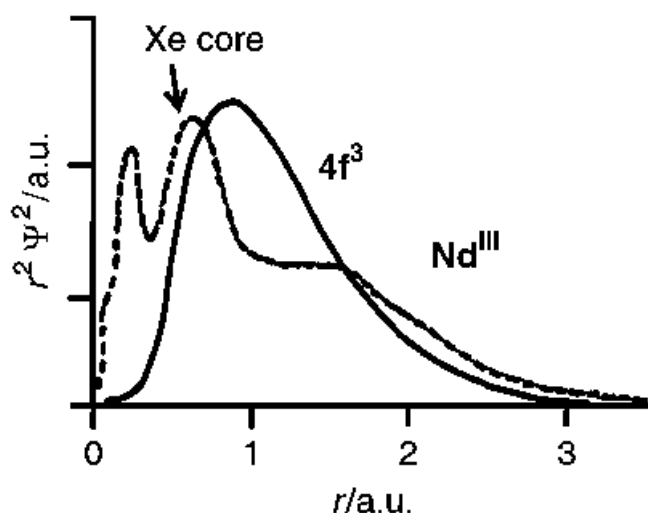
Figure 1.1. Radial wavefunction illustrations: electrons on Nd(III) 4f orbital (*solid line*) and xenon core (*broken line*). a. u. means atomic units here.

1.4 Energy levels and energy transitions

Lanthanide ions can serve as light emitters. Before introducing their unique photophysical properties, the energy transfer pathways will be generally described here, and more importantly, locations of lanthanide-energy-states are provided. Similar to most chromophores, lanthanide ions can absorb excitation energy (commonly in photons), and their 4f electrons get promoted to the excited states with higher energy,

while all energy transitions, no matter excitation or emission, can only happen between two different energy levels. Those energy levels are intrinsic and all lanthanides have no similar energy level patterns.

The gap between energy levels is the key to the efficient sharp intraconfigurational 4f-4f transitions. The diagram indicating all lanthanide trivalent ions is provided as below (Figure. 1.2). It is worth noting that this diagram is not complete because the upper limit for lanthanide energy levels might extend to 193000 cm^{-1} for the $^1S(1)_0$ level of terbium.[7] The calculated energy level diagram has been established from 39000 to 75000 cm^{-1} for the lowest $4f^n - 4f^{n-1}5d$ transitions.[8] Although there are other types of electronic transitions concerning lanthanides, for example, 4f-5d transitions, metal-to-ligand charge transfer, and ligand-to-metal charge transfer, this thesis mainly focuses on the transitions among 4f orbitals and their properties. One of the most direct indications of energy transitions among lanthanides' f orbitals is the receive and release of light (electronic wave energy).
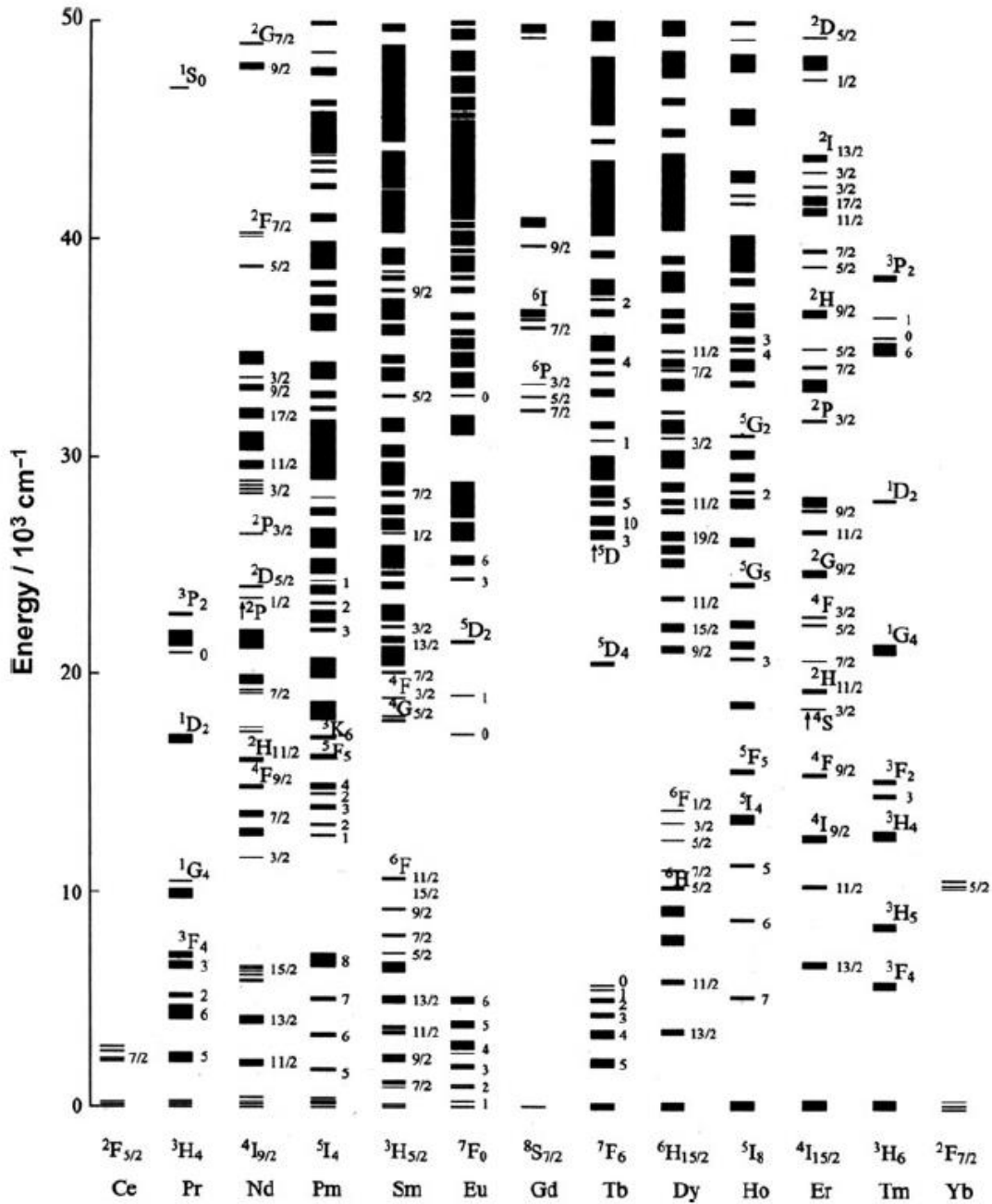
Figure 1.2. A partial energy diagram for Ln(III); determined by doped in LaF$_3$ crystal.[6]

1.5 Absorption and emission spectra

As mentioned in the previous sections, lanthanide ions can get excited by absorbing

photons and get relaxed by emitting light. These phenomena are dominated by

electronic dipole (ED) transitions. ED transitions describe types of energy transitions

happening between energy levels, and its releasing energy is always in the form of electromagnetic waves (normally light or heat). By following the definition of ED transitions, lanthanides' f-f transitions also have to follow the forbidden rule, also called the Laporte rule. The Laporte rule claims that there should be a selection rule where energy transitions can only happen between states which are different in parity (g→u, or u→g, g means gerade, and u means ungerade.) Therefore, since f-f transitions conserve the parity, they should have been forbidden by the ED mechanism. However, there are exceptions where those transitions are partially allowed. When the lanthanide ion is doped in a ligand, it will experience the ligand-field effect which is mostly a non-centrosymmetric interaction and can alter energy states' parity. As a result, some transitions will be allowed, and they are called induced (or forced) electric dipole transitions. Some transitions are quite sensitive to small changes in the lanthanide surrounding environment. They are called hyper-sensitive transitions and are normally considered as important signs for the investigations on crystal fields' effects, wven though they are not always the most intensive ones. In Table 1.1, Görller-Walrand *et al.* have determined all hypersensitive transition bands for lanthanides in 1998.[9] Besides, the derivation of Laporte rule is based on several hypotheses which make it not fulfill the reality at all the time. It will be more accurate to think about "forbidden transitions" as ones could happen a low probability.[6]

Table 1.1. Hypersensitive transitions for trivalent lanthanide ions observed in optical spectra.

Ln	Transition	$\tilde{v}/\text{cm}^{-1}$	λ/nm
Pr	$^3F_2 \leftarrow {}^3H_4$	5,200	1,920
Nd	$^4G_{5/2} \leftarrow {}^4I_{9/2}{}^a$	17,300	578
	$^2H_{9/2}, {}^4F_{5/2} \leftarrow {}^4I_{9/2}$	12,400	806
	$^4G_{7/2}, {}^3K_{13/2} \leftarrow {}^4I_{9/2}$	19,200	521
Sm	$^4F_{1/2}, {}^4F_{3/2} \leftarrow {}^6H_{5/2}$	6,400	1,560
Eu	$^5D_2 \leftarrow {}^7F_0$	21,500	465
	$^5D_1 \leftarrow {}^7F_1$	18,700	535
	$^5D_0 \rightarrow {}^7F_2$	16,300	613
Gd	$^6P_{5/2}, {}^6P_{7/2} \leftarrow {}^8S_{7/2}$	32,500	308
Tb	$-^b$	–	–
Dy	$^6F_{11/2} \leftarrow {}^6H_{15/2}$	7,700	1,300
	$^4G_{11/2}, {}^4I_{15/2} \leftarrow {}^6H_{15/2}$	23,400	427
Ho	$^3H_6 \leftarrow {}^5I_8$	27,700	361
	$^5G_6 \leftarrow {}^5I_8$	22,100	452
Er	$^4G_{11/2} \leftarrow {}^4I_{15/2}$	26,400	379
	$^2H_{11/2} \leftarrow {}^4I_{15/2}$	19,200	521
Tm	$^1G_4 \leftarrow {}^3H_6$	21,300	469
	$^3H_4 \leftarrow {}^3H_6$	12,700	787
	$^3F_4 \leftarrow {}^3H_6$	5,900	1,695

Most trivalent lanthanide ions can produce light emission except for La(III) and Lu(III) because they have either empty or full 4f orbitals where energy transitions cannot happen there. As for the emission from lanthanides, also called luminescence, it covers a wide spectrum with ultra-violet (UV) light from Gd(III), visible light from Pr(III), Sm(III), Eu(III), Tb(III), Dy(III), Tm(III), and near-infrared (NIR)from Pr(III), Nd(III), Ho(III), Er(III), Yb(III).[9]

There are several special characters on lanthanide luminescence: firstly, all f-f emission bands are quite narrow and characteristic, because comparing with organic chromophores having a large number of energy states and various pathways for energy transitions, the f orbital transition patterns are limited which limit the number energy

gaps and their resulting emission light wavelengths (see Figure 1.2). Secondly, lanthanide luminescence has small Stokes shifts. Stokes shifts describe the energy difference between the most intensive absorption peak and the most intensive emission peak. It is worth noting that one shift between two transitions belong to the transitions happening between the same energy states but many people have mistakenly compared two highest peaks from the spectra. The reason for small Stokes shifts of lanthanides is because electrons on 4f orbitals usually do not participate in the bonding between Ln(III) and the ligands and also the internuclear distances remain similar in the excited state. The illustration in Figure 1.3 shows that the difference in lengths of broken lines indicates the band width and the horizontal intervals between two broken lines represent Stokes shifts. It should be emphasized that a large number of publications have claimed that lanthanide-based materials have "large Stokes shifts". This statement is the mis-use of the term: those works mistakenly refers the large difference between the excitation and emission energies as a Stokes shift. However, the absorption process happens on chromophores while emission on the lanthanides, so they must belong to different energy transitions. For this case, the term "Antenna-generated Shift" was suggested to be used here.[10] Thirdly, forbidden by the selection rules, f-f transitions bands have although long decay time but the very weak intensity and it becomes one major challenge when applying lanthanide luminescence.
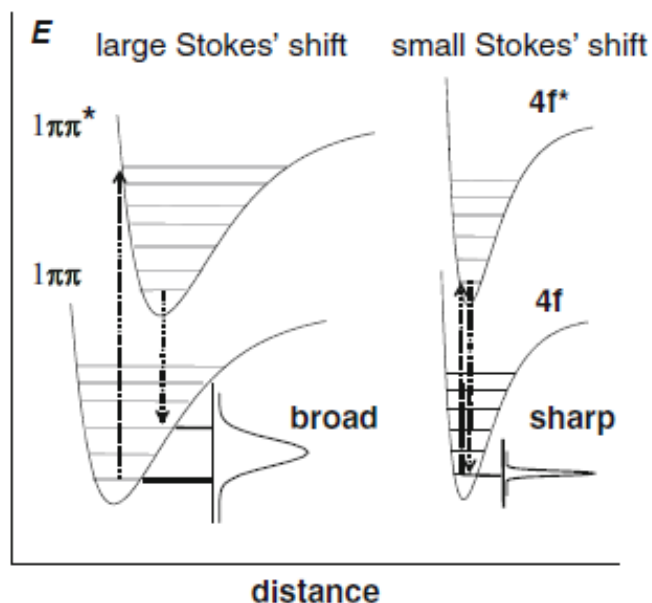
Figure 1.3. Franck–Condon principle energy diagrams for emission from an organic chromophore (*left*) and a lanthanide ion (*right*).[6]

1.6 Sensitization of Lanthanide Luminescence

Because the f-f transitions have been forbidden by the Laporte rule, we might apply very strong direct excitation energy on ground-state 4f orbitals to receive the resulting emission at a moderate intensity. Even if the intrinsic quantum yield does not worsen the energy transfer efficiency, lanthanide ions usually show poor ability to absorb excitation energy. To better utilize lanthanide-based materials, researchers have come across different solutions. A common one is to coordinate lanthanide ions into other organic chromophores and achieve luminescence sensitization, also called the antenna effect. Those organic ligands serve as great light harvesters because they have large unsaturated structures to achieve efficient aromatic transitions (n→π* or π→π*). Instead of Laporte-forbidden f-f transitions, all energy transfers involved in the antenna

9

effect are allowed. Starting from ligand-centered absorptions, electrons on ligands'
(antenna) ground states are excited to the singlet excited states. Excluding release of
the heat or light (the wave line and the broken line between S_1 and S_0), the excitation
energy is transferred to the long-lived ligand triplet state ($S_1 \rightarrow T_1$) and then to the metal-
centered excited states ($T_1 \rightarrow (Ln^{3+})^*$). The whole process is illustrated in Figure 1.4.
where ^5D_J and ^7F_J represent the excited and ground states for Eu(III) and Tb(III).
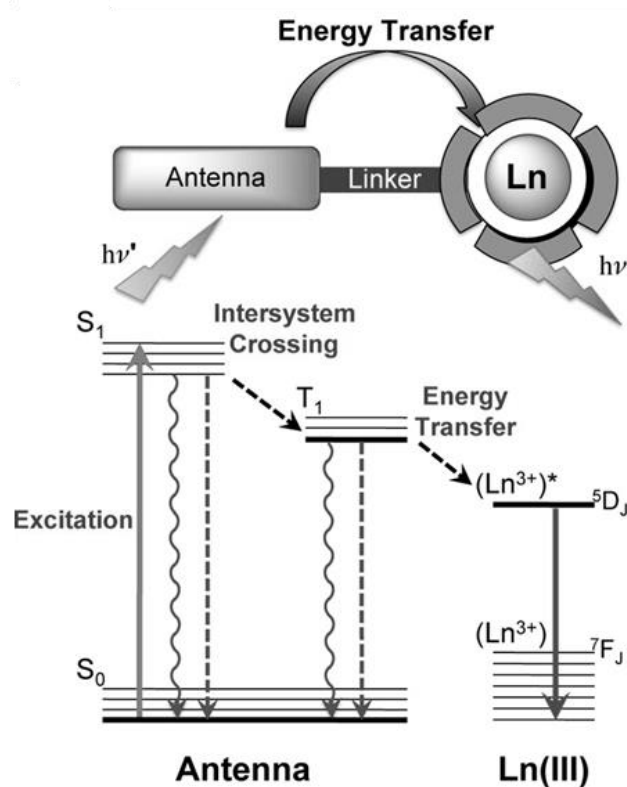
Figure 1.4. (*Top*) The general architecture of a emissive Ln(III) ion chelated and linked
with an antenna for absorbing excitation; (*bottom*) a simplified Jablonsky diagram
illustrating antenna effect.

1.7 Quantum Yields

Quantum yield is one of the most important properties for judging the performance of luminescent materials. According to the definition in the International Union of Pure and Applied Chemistry (IUPAC) Gold Book,[11] quantum yield is:

$$\Phi(\lambda) = \frac{number\ of\ events}{number\ of\ photons\ absorbed} \qquad (1)$$

The symbol λ refers to the excitation wavelength. However, this is usually omitted in many publications, where the authors report quantum yields simply as Φ and mention the excitation wavelengths in the experimental section but do not put λ next to the quantum yields. It is also noticeable that not only monochromatic light can be used in the determination of quantum yields. UV lamps and solar simulator light sources are also used for more practical applications, such as photostability and photodynamic therapy.[12] In these cases, it is not applicable to determine quantum yields specifically at one excitation wavelength but should follow light source specifications. One difficulty which researchers could come across with is from the practice of quantum yield measurement. A direct method in determining the quantity of light absorbed is by direct measurement of the scattered excitation light before and after inserting samples. The difference in the integrated areas of excitation light spectra are treated as the light absorbed.[13] However, by the IUPAC definition, quantum yields are supposed to be measured with monochromatic excitation light, which theoretically has no area under curve. Furthermore, there is only a few advanced light sources or monochromators can produce single-wavelength excitation light.

The number of events in *equation (1)* could be used to represent any substances related

to photochemical process or photophysical process. In a photochemical process, it refers to the amount of reactant consumed or product formed inside. For example, singlet oxygen quantum yield is a value showing the ability of a photosensitizer when it is exciting. Here the number of events will become the amount of singlet oxygen generated.

Considering luminescent lanthanide-based materials, quantum yields mainly refer to the ratios of the number of photons emitted and those absorbed, which are usually used for intersystem crossing, fluorescence, phosphorescence, and luminescence. There are mostly more than one photophysical processes involved in a lanthanide-doped complex/matrix, so the overall quantum yield can be written as the product of energy transfer efficiency (η_{sens}) times intrinsic quantum yield (Φ_{int}).

Commonly, those materials work as substances converting excitation light into emission light with lower energy, and the quantum yield is theoretically not lower than 100% with one photon absorbed and one photon released. In general, for a downshifting process, internal conversion of excitation energy will lead to <100% quantum yield; in an upconversion energy transfer, normally two photons with lower energy are absorbed and one higher-energy photon is emitted, so the quantum yield is not higher than 50%; while down-conversion materials are producing more photons than they absorb, the quantum yield is larger than 100%.

1.8 Brightness

Brightness is a useful concept similar to quantum yield in judging the performance of emissive materials, especially for bioprobes and bionanomaterials, because brightness does not only involve the efficiency of converting excitation light but the ability to absorb it. In the IUPAC gold book, brightness is defined as the product of molar absorption coefficient and quantum yield at a certain excitation wavelength.[14]

The expression for the definition of brightness could be easy to understand.[13]

$$B = \Phi \times \varepsilon(\lambda) = \frac{number\ of\ photons\ emitted}{number\ of\ photons\ absorbed} \times \frac{number\ of\ photons\ absorbed}{number\ of\ incident\ photons} \qquad (2)$$

It can be seen that the brightness for an emitter can still be high if it has a massive molar absorption coefficient but low quantum yield. The term brightness sometimes is a more practical measurement for bioprobes.[15]

1.9 Effects of distances on energy transfer

The efficiency of the sensitization effect highly depends on the distance between the donor and the acceptor (antenna chromophore and the lanthanide ion here). There are two mechanisms proposed for the simple pathway from the first singlet state ($^1S_1$) to triplet state ($^3T^*$) and to lanthanide excited state (4f*). As sketched in Figure 1.5,[16] they are Dexter and Forster mechanisms. Dexter mechanism involves a two-electron exchange pathway where one excited electron is transferred from the donor to the acceptor while the other one back. Therefore, the Dexter mechanism requires the overlapping wavefunction of two parts which limits the operable distance smaller than

10 Angstrom.[17] However, the Förster mechanism can work in a much longer distance up to 100 Angstrom.[18] The latter mechanism is the phenomenon where energy is transferred to the acceptor through a non-radiative process but not transferring electrons. Although some people claimed that the Dexter mechanism dominates here because they believe the poor energy-accepting ability of lanthanide f orbitals will lead to their preference of accepting electrons.[19] Researchers agree more that both mechanisms could happen on lanthanide-based complexes depending on the nature of the ligands.[20] Ytterbium trivalent ions, Yb(III), should be considered as a special case because it has the only low-energy excited state ($^2F_{5/2}$) locating at around 10000 cm^{-1}. There is seldomly found overlapping between the ligand emission spectra and Yb(III) f-f transition bands, but sensitization effects could still happen. One explanation is that the excited chromophore might transfer one electron to Yb(III) and form Yb(II). After the charge combination, oxidation states recover and the released energy promotes Yb(III) electrons to the excited 4f orbitals.
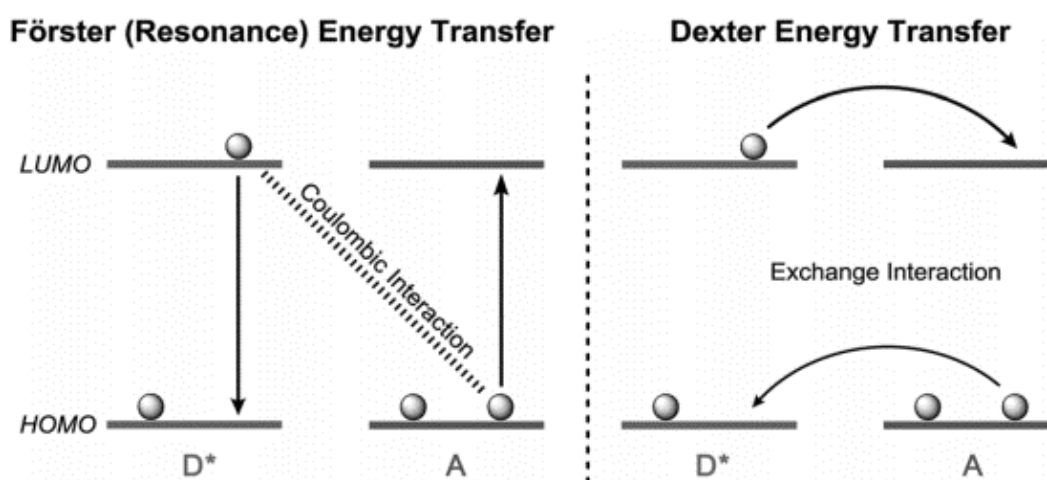
Figure 1.5. Schematic depiction of Förster and Dexter energy transfer processes.

Not only Dexter mechanism highly relies on short internuclear (acceptor and donor) distances for efficient electron transfer, the efficiency of Förster resonance energy transfer (FRET) is also inversely proportional to the sixth power of internuclear distances.[21] It should be pointed out that the longer distances between the light-harvesting ligand and the lanthanide ions only result in the decrease of luminescence intensity, but might facilitate the generation of fluorescence or phosphorescence, as well as other energy transfers starting from the singlet and triplet states of organic chromophores (ligands).

1.10 Principles for designing efficient lanthanide luminescence complexes

To design a practicable lanthanide-based complex with great photophysical properties, one of the foremost tasks is to design a good ligand chelating with central metals. There are many criteria for optimum and robust ligands used in lanthanide probes, concerning sensitization efficiency, stability, and coordination chemistry.

More specific requirements for the lanthanides' ligands include:

1. Efficient sensitization of lanthanide ions. The ligand triplet state energy should be adjusted by introducing different functional groups so that energy transfer from the triplet state to the excited 4f orbitals is efficient. However, nearby energy levels might have back energy transfer. The optimized energy difference is commonly accepted to be around $2500 - 3000$ cm^{-1}.[6]

2. The chelation with metal ions should be rigid and complete because any cavity that remained after coordination could become the space for solvent molecules, and those solvent molecules possibly quench the excited states non-radioactively.

3. Good water solubility of the ligand or the complex is the key to a wide application in biological environments.

4.Both high thermostability and kinetic inertness to uninterested molecules are important to lanthanide complexes for their consistent properties.

5. It is recommended for the ligand to have an intense absorption wavelength longer than 330 nm because firstly, it is the short limit for the detectable light by human eyes; and secondly, UV radiation is highly harmful to human bodies and is one major cause of different skin cancers.[22]

6. The bioactivity and biotoxicity of the ligands and the complexes should be carefully studied. It is worth noting that some complexes reveal different toxicity with/without light irradiation.

Porphyrins are common synthetic dyes characterized by their specific molecular structure. Based on their conjugated parts, porphyrins have specificities and advantages in spectral and photoelectric properties. For example, they are usually applied as anticancer therapeutic agents because of their ability to generate singlet oxygen as photosensitizers, by which their big conjugating systems can produce free radicals upon light excitation. From the view of chemical structures, although not only porphyrins consist of four pyrroles, they are the only group of compounds having all pyrrole rings

linked by alpha carbons as bridges. By contrast, phthalocyanines contain four indole units and typical corroles have the lack of one methane carbon for bridging, even though they also showed some bio-application potential.

Although most porphyrins can exist stably as free bases, porphyrin-based metallo complexes have also been classical for investigation, since stable products can be obtained by simply introducing metals into the center of pyrrole rings. Besides these, wide applications are achieved by modifying side-chains of porphyrins or metal capping.

1.11 Porphyrin and the Preparation of metalloporphyrin

Porphyrins are stable organic molecules that consist of exceeding delocalized π systems. Similar to other tetrapyrrole derivatives, porphyrins have a wide range of intriguing optical, electrical, and magnetic properties which provide them high application potentials in catalysis, biology, and medicine. A combination of lanthanides' unique optical properties with porphyrins could yield more advanced performance, including applications as light-emitters, bioprobes, and photosensitizers.

One of the most general methods in the preparation of lanthanide-porphyrin complexes is to reflux two equivalents of tris(2,4-pentanedionate)lanthanide(III) salts in 1,2,4-trichlorobenzene (TCB) for 4 hours. The crude is then purified by column chromatography to yield the target complex (Figure 1.6).[23] When a lanthanide ion

(originated from lanthanide salts) reacts with a porphyrin macrocycle to form a monoporphyrinate complex, there will be a strong tendency to form a double or triple-decker but not a mono one. This is because the coordination number of lanthanides is eight or nine, but when the lanthanide cation binds to the tetraaza core of the porphyrin ring for nitrogen, it will require additional molecules to fulfill the empty coordination positions. If only solvent molecules, simple anions, or ancillary ligands participate in the additional binding, the lanthanide-porphyrin complex will be unstable and easy to decompose in solution. Otherwise, it will prefer to bind to an extra porphyrin for full coordination. One common way to stabilize monoporphyrinate lanthanide complexes is to add strong coordinating ligands such as acetylacetonate (acac) or capping tripodal ligands (for example, Kläui ligand [24, 25]) as depicted in Figure 1.6.

It is a major concern to improve the solubility of porphyrin and metalloporphyrin for better applications and there have been many successful examples: Wong's group synthesized lanthanide porphyrin with pyridyl-substituents;[26] Zhang et al. reported ytterbium complexes with carboxylate and cationic phosphonium groups.[27] There is no significant changes in reaction conditions for the complexation process, but the changes in starting materials for the preparation of different porphyrin.

There is increasing interest in the preparation of bimetallic complexes with porphyrins linking with another chelating agent such as ethylenediaminetetraacetic acid (EDTA), diethylenetriaminepentaacetic acid (DTPA), or tetraazacyclododecane-1,4,7,10-

tetraacetic acid (DOTA). Dianhydrides of those chelators were directly mixed with equimolar quantities of porphyrin in anhydrous solvents and heated with the presence of a base, such as triethylamine.[28-30]
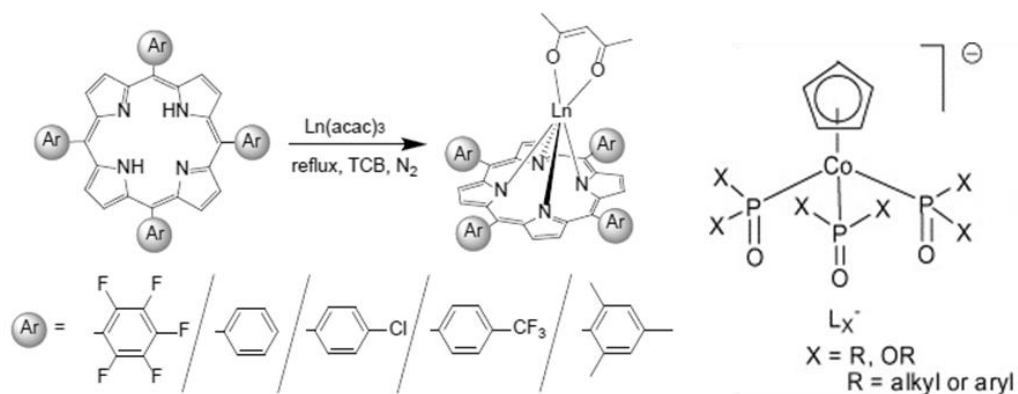
Figure 1.6. General preparation methods for monoporphyrinate lanthanide complexes with acac (*left*). The general structure of Kläui ligand (*right*).

As mentioned previously that lanthanide-based metalloporphyrins are possible to form stacked arrangements as multiple deckers, these phenomena have drawn great attention for their improved magnetic/optical properties and the possible applications. Researchers are putting efforts into the controlled and efficient synthesis of them.

The first series of examples for lanthanide-based multiple decker complexes without other bridging ligands but porphyrin was reported in the 1980s by Weiss et al.[31] These complexes, Ce^{IV} bis(octaethylporphyrinate) $[Ce(OEP)_2]$ and dicerium(III) tris(octaethylporphyrinate) $[Ce_2(OEP)_3]$ were directly prepared by refluxing $Ce(acac)_3 \cdot 3H_2O$ with $H_2(OEP)$ in TCB for 20 hours. The improved reaction efficiency

was reported by Jiang et al. in 1992[32] by using n-butyllithium porphyrins to improve the reagent solubility and the resulting reactivity. However, those examples were based on the divalent of quadrivalent metal ions. Chabach's group was pioneering in the application of trivalent central lanthanide ions in multiple decker systems. Lanthanides including La, Pr, Nd, Eu, Gd, Er, Lu, and Y were coordinated as porphyrin-phthalocyanine sandwich-type complexes.[33, 34] There is one noticeable difference between smaller lanthanide ions (Er, Lu) and larger lanthanide ions (La-Gd) in the complexation process. The smaller ones in the form of acetylacetonate salts prefer to react with phthalocyanines, so the preparation of heteroleptic complexes starts from the reaction between smaller lanthanide salts and dilithium phthalocyanine in boiling TCB and then with tetraporphyrin. By contrast, those larger ones should react with tetraphenylporphyrin (H_2TPP) in TCB firstly and then with Li_2Pc for better coordination. The choice of base in the synthesis of lanthanide-porphyrin double-decker complexes is usually 1,8-diazabicyclo[5,4,0]undec-7-ene (DBU) since it was firstly reported in 2000.[35] It avoided the formation of LnPor(acac) as the intermediates.

The same as many researchers working on the porphyrin-related compounds, it is our target to achieve the efficient preparations of lanthanide-based porphyrinate complexes. Additional stability and water solubility are the keys to biocompatibility which confer them with wide applicability in biological studies or treatment. Porphyrin derivatives have typical absorption spectra consisting of a Soret band and Q bands originated from different energy states. Detailed discussion and assignment of peaks will be provided

in the following section concerning the real-case absorption and emission spectra.
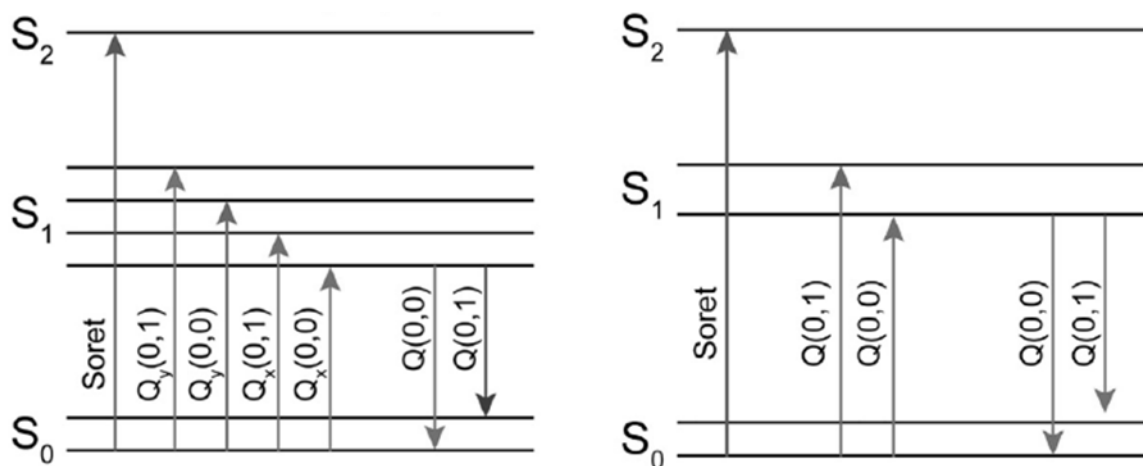
Figure 1.7. Typical energy level diagram of free-base porphyrins (*left*) and metalloporphyrins (*right*).

1.12 Magnetic resonance imaging and contrast agents

Magnetic resonance imaging is a powerful diagnostic technique that can be used to provide direct visualization of tissues and organs under skin covering. The working principle of MRI is by applying a strong and uniform magnetic field, hydrogen atoms originated from water or fat in the human body can be mapped

The administration of MRI contrast agents is necessary for specific imaging because contrast agents can enhance the longitudinal or transverse (T_1 or T_2) relaxation rates for water molecules. Therefore, they help to improve the contrast of different tissues in MRI images (Figure 1.8). Gadolinium(III)-based complex is an ideal candidate for contrast agents (Gd(III)-based contrast agents, GBCA) because Gd(III) has a half-filled

4f orbitals with seven unpaired electrons, which provide it strong paramagnetism, and it, therefore, can relax water molecules efficiently.
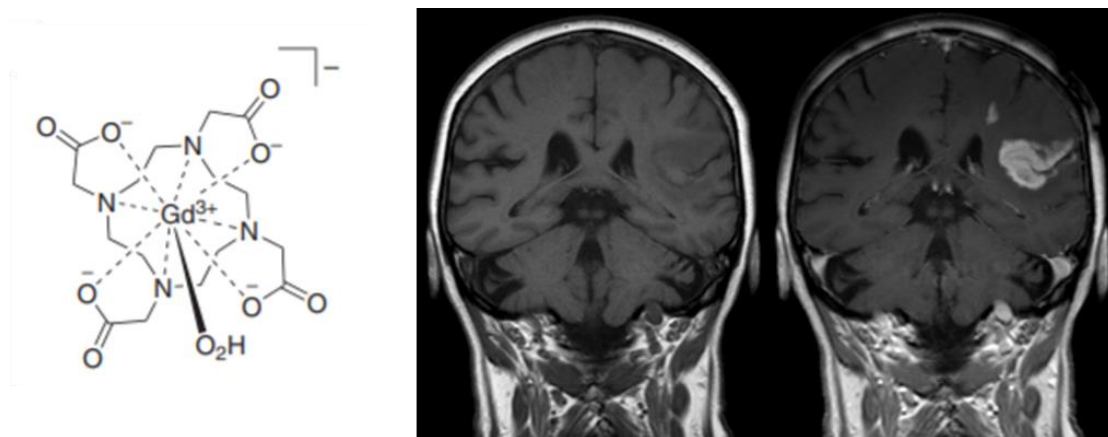
Figure 1.8. Molecular structure of gadoterate meglumine (or Gd-DOTA, or Dotarem®), a classical GBCA (*left*); the comparison of human brain MRI images without (middle) or with (*right*) the used of GBCA.

1.13 Complex stability

Lanthanide complexes' stability is always one of the most important concerns. Taking Gd(III)-based MRI contrast agents as an example, MRI imaging sometimes requires a high dosage of contrast agents for clear and complete results. However, it might cause severe adverse effects on patients if free Gd(III) ions were released from Gd(III)-based contrast agents, because Gd(III) ion has a similar ionic radius to Ca(II) ions and it can interfere some calcium0mediated signaling pathways. It has been reported the median lethal dose of free Gd(III) ions is 0.2 mmol/kg for mice.[36, 37] For the bio-safety of lanthanide complexes, specific strategies should be applied in molecular designs and stability tests should be performed if possible.

Thermodynamic stability constant K_{ML} (or Kt_{herm}, K_{st}) is used to judge the applicability and safety of complexes, including lanthanide complexes. KML is defined with the equation:

$$K_{ML} = \frac{[ML]}{[M][L]} \qquad (3)$$

It can be calculated by the concentrations of the complex, the free metal ions, and the free ligands in solution. One method is to perform a spectrophotometric titration experiment where equimolar solutions of the metal and respective ligand were titrated over the pH range 3-9. Thermodynamic constants were given by software with the provided conditions and parameters.[38]

One parameter with a more specific condition and application potential was introduced as a conditional stability constant K'_{ML} (or K_{cond}, K_{eff}). It is more suitable for physiological applications because, for most ligands, thermodynamic stability depends on both the binding affinity to metal ions and the basicity. Sometimes bias could be found for some complexes in stability when a more basic condition induces a larger difference in stability constants of two complexes, even though both of them will only be used at physiological pH.[39] Conditional stability constants only concern the values measured at pH=7.4 by using 1 to 1 ligand-to-metal ratio solution.

There is one common term called pM value for the measure of complex stability. It is also written as pGd or pLn for gadolinium/lanthanide-based complexes. The definition

of pM is pM = -log[M]free at pH 7.4 with a ligand-to-metal concentration ratio of 10:1.[6,40] One determination method for pM is to direct determine the concentrations of other species by their photophysical properties and then calculate free metal concentrations on the fixed conditions. While the other determination method, although more popular, is partially problematic. The determination is done by a comparison of stability constants between a well-documented reference ligand L_2 and the target one L_1. Varying the concentration ratios of two ligands, a plot of $log([L_2]/[L_1])$ vs. $log([ML_2]/[ML_1])$ can be extrapolated. It is claimed that at the x-intercept ($log([ML_2]/[ML_1]) = 0$), metal ions can coordinate equally between two ligands. If the x-intercept is z, pM_1 equals the sum of pM_2 and z.

$$pM_1 = pM_2 + z \tag{4}$$

One reported example [**2003doble**] is given by using DTPA as a reference and a equation was given:

$$pGd_{GdL} = pGd_{GdDTPA} + z \tag{5}$$

However, little discussion on the reason why we can calculate in that way was not given in the literature. To perform a formula derivation, I start with dissociation constants K of complexes:

$$K \ (or \ K_d) = \frac{[M][L]}{[ML]} \quad \rightarrow \quad [ML] = [M][L]/K \tag{6}$$

In a competing solution (containing one to-be-determined ligand L_1 and the other reference ligand L_2, as the one used in the previous case), we can have the equation at the x-intercept (y = 0):

$$log([ML_2]/[ML_1])=0$$

which means

$$[ML_1] = [ML_2] \neq 0 \tag{7}$$

by applying *equation (6) into (7):*

$$[M_1][L_1]/K_1 = [M_2][L_2]/K_2$$

When presenting in the same solution, $[M_1] = [M_2]$, the free metal ion concentration ($[M]$ or pM) is omitted and has no meaning in the following formula derivation.

$$K_1/K_2 \;=\; [L_1]/[L_2] \tag{8}$$

Also, at the x-intercept ($x = z$):

$$z = log([L_2]/[L_1])$$

$$z = log\,(K_2/K_1)$$

$$z \;=\; log\ K_2 \;-\; log\ K_1 \;=\!-pK_2 \;+\; pK_1 \tag{9}$$

Therefore,

$$pK_1 = pK_2 + z \tag{10}$$

E*quation (10)* is consistent with *equation (5)*, but it is proven that the dissociation constants should be used in this equation, not but free metal concentration. In a solution with the mixture of two complexes, they will have the same free metal ion concentrations, so pM_1 must equal pM_2 (1 and 2 denote two different complexes) and they cannot be used to represent complex stability.

With the increasing complex stability, two parameters, $[M_{free}]$ (pM) and dissociation constants K (pK) both decrease. Besides, conditional dissociation constant pK always gives the same value as pM. Many papers confused the definition of complex stability

constants and incorrectly used pM referring to dissociation constants, although the values of results were correct.

1.14 Photodynamic therapy – singlet oxygen

Photomedicine is one of the most popular clinical applications in the past decades. Beyond traditional medicine or clinical practice, photomedicine is still pioneering new methods or agents, but not only focusing on the optimization of existing fruits. There are three major areas in this field, including photodynamic disinfection (PDD), photodynamic therapy (PDT), and photoimmunotherapy (PIT).

PDT is mostly related to my projects. In a PDT application, one effective photosensitizer is used to generate reactive oxygen species (ROS) under light excitation. The excitation energy which has been tuned to the best wavelength light is absorbed by the photosensitizer and then the energy is transferred to molecular oxygen. The molecular oxygen gets excited and turned to be ROS which is responsible for the inhibition of cancer cells. There are many difficulties for the practical uses of PDT, including the choice/accessibility of light source, the photostability of photosensitizers, the safety and the normal cell toxicity of treatment, and medicine targeting. Doctors and researchers spare no effort on making the best use of ROS oxidizing power while keeping ROS with the lowest adverse effects. A good PDT practice must follow two requirements: the first is that the ROS is only generated on the target position to avoid any unwanted harm; secondly, the photosensitizer is stable enough on the way of

administration and nontoxic before irradiation.

There are three major components in PDT: light source, molecular oxygen, and photosensitizers. Clinical laser is usually used as light source in PDT. Comparing with normal lamps, lasers can provide coherent and monochromatic light which is optimal photosensitizers, so side effects could be minimized. Light from lasers is also focused without the assistance of additional accessories. With the light focused on the specific treatment area, excitation power can be efficiently used and the nearby biological tissues remain intact. The advantages of lasers are fitting the first requirement for PDT largely. Nowadays, it is common to used NIR lasers in PDT, because NIR provides overwhelmed penetration ability comparing with visible light. NIR refers to light radiation in the region from 780 nm to 2500 nm. Two typical regions of NIR have been categorized based on their wavelength: 700-950 nm (NIR-I window) and 1000-1700 nm (NIR-II window). With the excitation light or emission light in NIR-I and II windows for biomedical purposes, the interference from photon absorption, scattering, and tissue autofluorescence could be remarkably reduced, and deep-tissue imaging can be achieved.[41, 42]
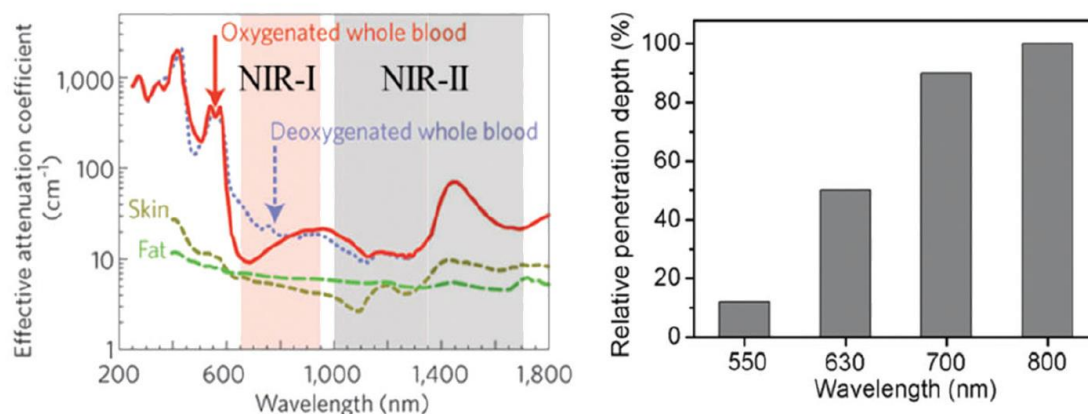
Figure 1.9. NIR photons get less absorption by blood and the optimal penetration depth in living organisms. (*left*) Plots of effective attenuation coefficients of oxygenated blood deoxygenated blood, skin, and fat at wavelengths from 250 nm to 1800 nm. The first (NIR-I, 700–950 nm) and the second (NIR-II, 1000–1700 nm) windows show a relatively low attenuation coefficient. (*right*) The relative penetration depth of light *in vivo* at different wavelengths (550 nm, 630 nm, 700 nm, and 800 nm).

The energy transitions happening in photosensitizers and from photosensitizers to molecular oxygen have been illustrated in Figure 1.10, S_n stands for a certain singlet state (for example, S_0 is the ground state of a photosensitizer); T_n means one certain triplet state with different electronic configurations with singlet states; P (such as $^1P^*$) denotes photosensitizers and O_2 is the molecular oxygen; besides, IC and ISC are two energy transfer pathways, internal conversion, and intersystem crossing. Photosensitizers serve similarly as organic chromophores sensitizing lanthanide ions. They harvest excitation energy and transfer it finally to the stable triplet states of molecular oxygen, and then cause the production of singlet oxygen. The lowest excited energy state for the (diatomic) molecular oxygen is a singlet state where two valence

28

electrons are spin-paired at the antibonding π orbital.[43, 44]
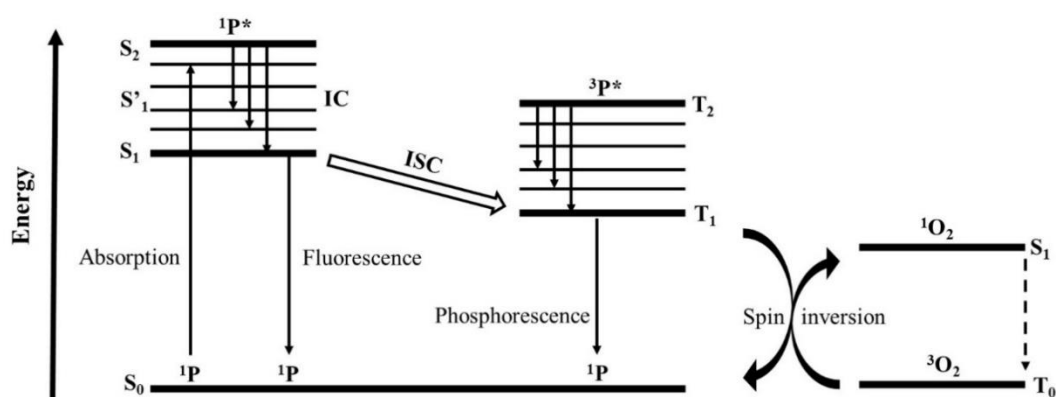
Figure 1.10. Simplified Jablonski energy diagram of energy transitions for singlet oxygen generation with the presence of photosensitizers.

There are two types of singlet oxygen differentiated based on their formation mechanism. As for the type I mechanism, the reactive oxygen species is produced by the transfer of electrons from photosensitizers. The photosensitizers are excited and produced radical anions as intermediates. Those intermediates successively react with molecular oxygen and transfer electrons and form superoxide anions which will subsequently form hydroxyl radicals and hydrogen peroxide. While the type II mechanism involves little charge transfer, but there is mainly a photochemical process. The excitation energy is transferred from the photosensitizer molecule to molecular oxygen and results in the sensitized formation of $^1O_2$. Reactive oxygen species generated from type I and II are both quite harmful to biological tissues and can be applied in PDT. However, our projects and the related compounds are mostly contributing to the formation of single oxygen in type I mechanism.[42]

A photosensitizer is an inevitable part of PDT since it bridges the excitation light and single oxygen. It has been nearly one hundred years since the first photosensitizer, hematoporphyrin (Hp), was reported.[45] Hp is a derivative of porphyrin and the porphyrin moiety is one good singlet oxygen producer which has been being studied till now. The recent modification of Hp was reported as HpD photofrin and HpD has been widely applied to clinical cancer treatment.[46] The first generation photosensitizer has plenty of drawbacks including long clearance time and needs for harmful short-wavelength excitation light. The second-generation photosensitizer has been well developed in the past decade.[43]

The efficient generation of singlet oxygen needs the delicate design of photosensitizers, and several strategies have been introduced:

1. By increasing the proximity of photosensitizers, the production of free radicals and the resulting interaction with oxygen triplet states will be inhibited. Therefore, the generation pathway for singlet oxygen will be secured. The modification of photosensitizers can be done by introducing heavy atoms such as halogens.

2. Aggregation of photosensitizers might lead to the severe quenching of their triplet states, so the excitation energy could not be transferred to molecular oxygen largely. The molecular structures of photosensitizers should be considered from the view of possible aggregation because of some functional groups.

3.Expanding the unsaturated structure of the light harvesters can tune the optimal

absorption wavelengths, and it has been known that longer wavelength light provides better tissue penetration and less harm to the body. More chromophore structures also help the better absorption of light.

4. The balance of molecular water solubility and lipophilicity should be carefully considered because good water solubility guarantees the administration of the PDT agents, but good lipophilicity helps cellular uptake and localization. This can be adjusted by introducing different functional groups.

1.15 Scanning tunneling microscopy

Scanning tunneling microscopy (STM) is one advanced technique to directly visualize and investigate the surface of substances at the molecular level. When the tip of the equipment approaching the substance surface, the electric current between two ends will change as a function of spatial position. After collecting the electric signals while scanning, the thickness and topology can be revealed clearly. A bunch of reviews has been published on the topic of STM studying porphyrins because of their suitable 2D assemblies.[47]
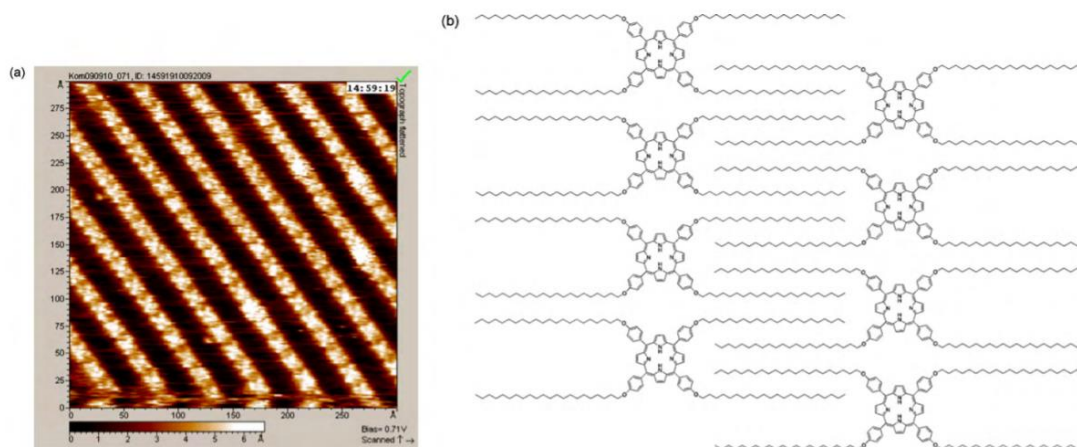
Figure 1.11. Surface array of H_2-T(C_{22}OP)P at the 1-phenyloctane/highly ordered pyrolytic graphite (HOPG) interface. (a) STM image. (b) Molecular models.

1.16 Transient absorption spectroscopy

Conventional photophysical measurements are focusing on mostly the results averaging on a period due to the limitations of measurements and a continuous light source is applied for most cases. Therefore, it is difficult to reveal the energy transfer process instantly and analyze the separated pathways. Transient absorption spectroscopy (TAS), also called ultrafast transient absorption spectroscopy, is introduced as one of the advanced techniques to investigate instant steps of photochemical reactions and intermediates formed there. Moreover, TAS can be directly applied to measure one single compound to show its intra/intersystem energy transfer pathways. Comparing with common light absorption measurements, TAS is using an ultrafast laser pulse to excite samples, and the difference between exciting samples and ground-state samples will be measured, and then the dynamic process in the sample systems can be studied.

Chapter II Impressive Near-Infrared Brightness and Singlet Oxygen Generation from Strategic Lanthanide–Porphyrin Double-Decker Complexes in Aqueous Solution

2.1 Introduction

Near-infrared (NIR) luminescent lanthanide materials have been widely utilized and increasingly researched in biomedical science by virtue of their extraordinary photophysical properties as introduced in the previous section. Ytterbium(III) as one of the lanthanides showing characteristic emission peaks in the NIR region, has potentials in different applications. To circumvent the weak-intensity issue of common NIR emitting compounds, π-conjugated hetero-macrocycles, such as porphyrins, possessing (i) high absorption cross-sections, (ii) triplet states resonating well with lanthanide absorption bands, and (iii) four "hard" nitrogen donor atoms matching "hard" lanthanides, have become promising antenna in use for optimal energy sensitization and protective coordination.[48, 49] Sandwich-type lanthanide–porphyrin complexes can afford more preferable or even surprising emission results, given that double-decker lanthanide complexes have recently spanned many fields although few bio-related counterparts. Despite their well-characterized long-lived NIR emission and $^1O_2$ generation, most lanthanide-macrocycle complexes suffer from inferior water solubility that considerably hampers their further development in biomedical fields.[50] The porphyrin structure is rigid and its exciting energy can be non-radiatively transferred to an acceptor. Herein, there are introduced four water-soluble porphyrin-based lanthanide

double-decker complexes (LnDD, where Ln = La, Er, Gd, and Yb), and some are of remarkable NIR photophysical properties in an aqueous solution. Upon the strategic installation of two optimally short hydrophilic methylated diethylene glycol (DEG) chains on the tailor porphyrin Por(2DEG) for sandwich lanthanide complexation, YbDD exhibited the improved NIR luminescence quantum yield and lifetime in water which outstrips those of previously reported YbN.[51] The singlet oxygen generation efficiency in terms of quantum yield (Φ_{1O2}) of GdDD was measured to be slightly higher than that of GdN.[51] Our findings substantiate the hypotheses that the double-decker complexation between porphyrins can (i) facilitate better lanthanide sensitization in the presence of two antenna chromophores rather than one; and (ii) minimize the inner-sphere quenching effect by lowering the number of bound water molecules under the macrocyclic sandwich fashion. This work provides unique results for the photophysical data of LnDD in aqueous media and more importantly, a new dimension for the future design and development of molecular theranostics-based water-soluble double-decker lanthanide bisporphyrinates. A structural elucidation in this study was conducted by various techniques, as now described. This work has been published as "*Impressive near-infrared brightness and singlet oxygen generation from strategiclanthanide–porphyrin double-decker complexes in aqueous solution*" on the journal Light: Science & Application (*Light Sci. Appl.* 8, 46 (2019). https://doi.org/10.1038/ s41377-019-0155-9) with credits to Jing-Xiang Zhang (co-first author), Wai-Lun Chan (co-first author), Chen Xie (co-first author), Yan Zhou, Ho-Fai Chau, Partha Maity, George T. Harrison, Aram Amassian, Omar F. Mohammed, Peter

A. Tanner, Wai-Kwok Wong & Ka-Leung Wong. The works I have been contributed in

are discussed in this chapter.

Figure 2.1. Molecular structures of LnDD in this work and LnN as referencing samples

for comparison.[51]

2.2 Results and Discussion

2.2.1 Structural characterization by nuclear magnetic resonance

The synthesis and characterization of the double-decker porphyrinate lanthanide

complexes with Ln = La, Gd, Yb trivalent ions are shown in the Appendix for Chapter II. and the Experimental section in this chapter. Due to the paramagnetic properties resulted from electrons on f orbitals of the Gd(III), and Yb(III) complexes, LaDD was synthesized as the analog for ^{1}H nuclear magnetic resonance (NMR) analysis. Upon the addition of hydrazine hydrate, a well-resolved NMR spectrum of LaDD could be obtained (Figure 2.2), because hydrazine hydrate served as a reducing agent and assisting the formation of monoanionic diamagnetic complexes. The protons of the single ligand Por(2DEG) can be categorized into peripheral and internal. The peripheral aromatic protons are typically located around 6.5-10.0 ppm, whilst the DEG sidechain aliphatic protons normally lie within the range of 1.5-4.0 ppm. The peak of hydrazine hydrate mixed with DMSO-d6 (DMSO: dimethyl sulfoxide) is observed at 2.6 ppm. The ring current effect strongly shifts the two internal protons on the porphyrin upfield to -3.2 ppm. The disappearance of internal N-H peaks and the proton shifting can then serve as an indication of metallization with the lanthanide ion. No signal is observed in the negative range (equated to internal N-H protons) in the spectrum of LaDD, while all peaks are subjected to down-field shifting due to the anisotropy of the f-metal ion as well as the impact of lanthanide-induced shifts. For a single sandwich, four benzene rings on the sidechains could possibly have π–π stacking effects. In fact, there is no evidence found from the NMR spectra or STM images for the π–π stacking, it could because those benzene rings freely rotate and the distance between two porphyrin rings are too far to achieve any interactions. It is noted that the theoretically most possible supramolecular trimers or even multiple aggregate structures can also give rise to

similar NMR spectra, but the high-resolution MS and STM images corroborate the double-decker structure of LaDD (and thus the LnDD series) unambiguously.
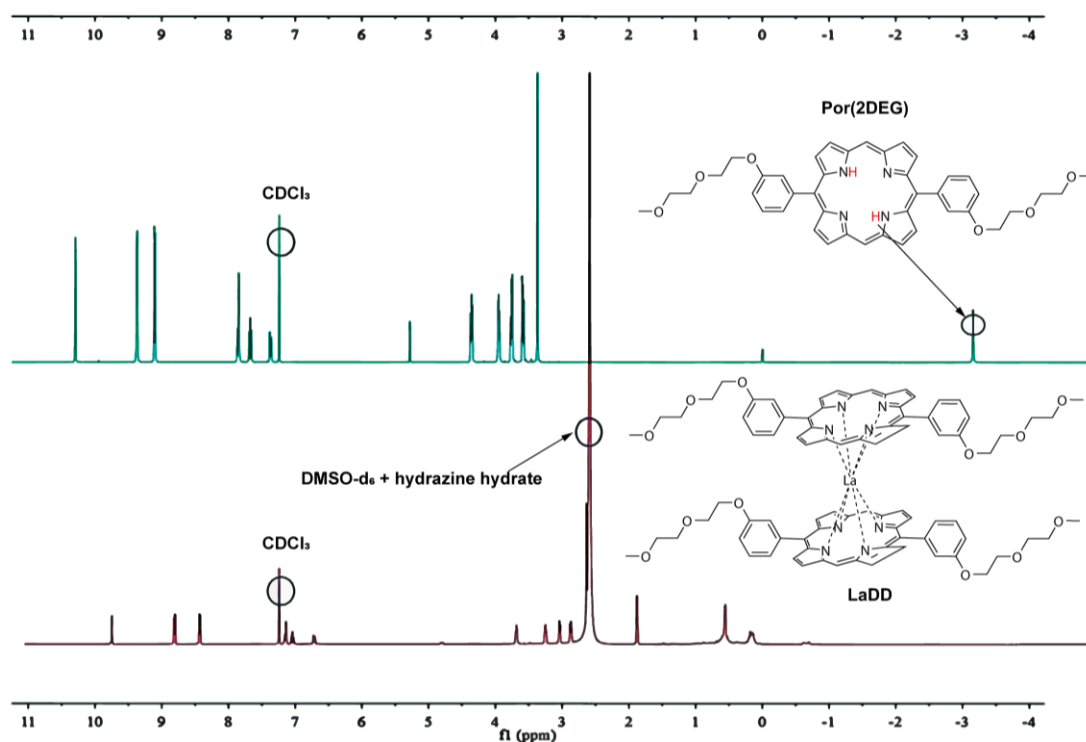
Figure 2.2. The room-temperature ^{1}HNMR spectra of (a) the ligand Por(2DEG) in CDCl$_3$ and (b) LaDD in CDCl$_3$: DMSO-d6 1:1 mixed with 1% hydrazine hydrate.

2.2.2 Structural characterization by scanning tunneling microscopy

Scanning Tunnelling Microscopy is an advanced technique that can be used for probing molecular assemblies on an individual molecule basis as mentioned in the introduction section. The study of porphyrins assembly and structure at the vacuum and liquid interface on surfaces is relatively advanced. In particular, several studies have been undertaken on the double-decker structured molecule.[52] YbDD was deposited on a clean HOPG (0001) surface by placing a drop of dilute solution and evaporating at room

temperature. The molecules formed self-assembled motifs without further treatment, through surface adsorption and diffusion. STM topographic image Figure 2.3 shows a high-magnification image of a region of a drop-cast surface with additional features decorating the step edges. As shown in the zoom-inset, these form a periodic row of separation ~4 nm, and apparent height ~ 1 nm (line profile Figure 2.3) is present. This height recorded at a -1.5 V filled state is strongly influenced by the electronic effects of both the tip apex and molecular-surface junctions.
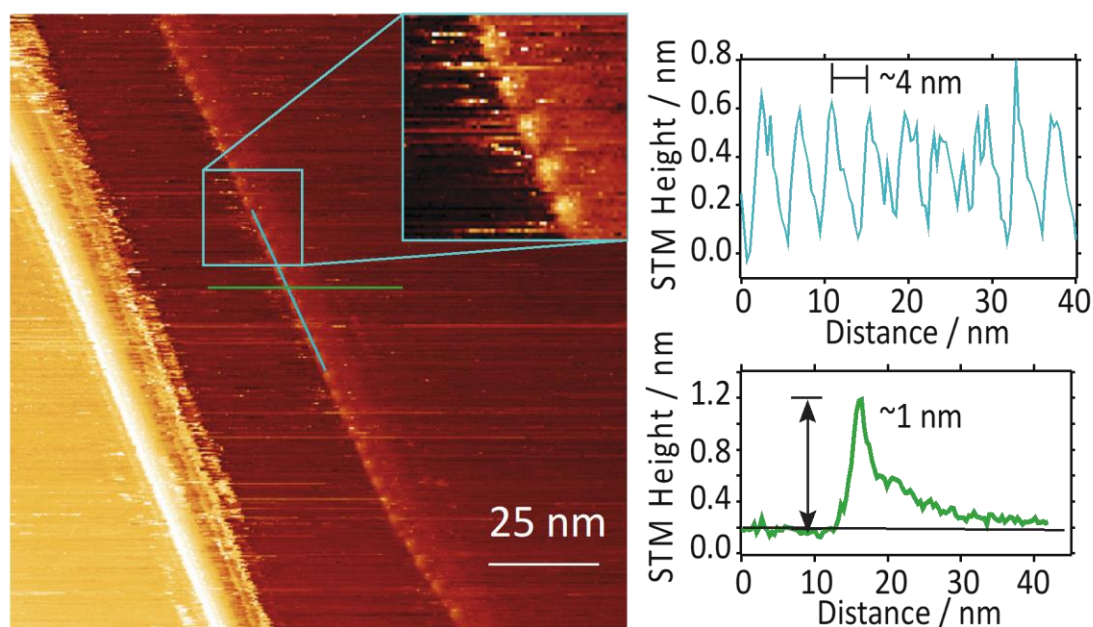
Figure 2.3. Structure characterization. The first trial of STM imaging for YbDD drop-cast onto HOPG: (*left*) 5 µL toluene with 1 mmol YbDD sample, 140×140 nm^2, -1.5 V sample bias, 50 pA, (inset) blue box: a high magnification image, cyan and green lines: denoting height line profiles. (*right top*) Line profile from the left figure along the row of features; (*right bottom*) line profile across the HOPG step edge, the height of the feature ~1 nm (bottom terrace) is indicated.

In a different trial with YbDD, a close-packed arrangement was observed and shown in Figure 2.4. This ordered arrangement is long-ranged ~100 nm and aligned parallel to the HOPG step edge direction. The features also display a separation of ~4 nm in the direction perpendicular to the step direction (parallel unresolved) as indicated by the height line profile in Figure 2.4 inset. Therefore, a templating effect originating at the step is suggested. The overall behaviour of the drop-cast double-decker YbDD on HOPG is in line with previous studies of double-decker motifs and the porphyrin ligands, with a favourable interaction and ability to spontaneously form a periodic assembly. The large ~4 nm spacing between resolvable features is consistent with literature accounts of similarly structured molecules with the spacing correlated to alkyl chain length with individual molecules packing face-on with the oxy-alkyl chain R groups having a favourable arrangement on the HOPG surface, leading to the observed spacing. The observed features, rows, and protrusions are attributed to single molecules, with further work underway to resolve the exact inner-molecular structure.
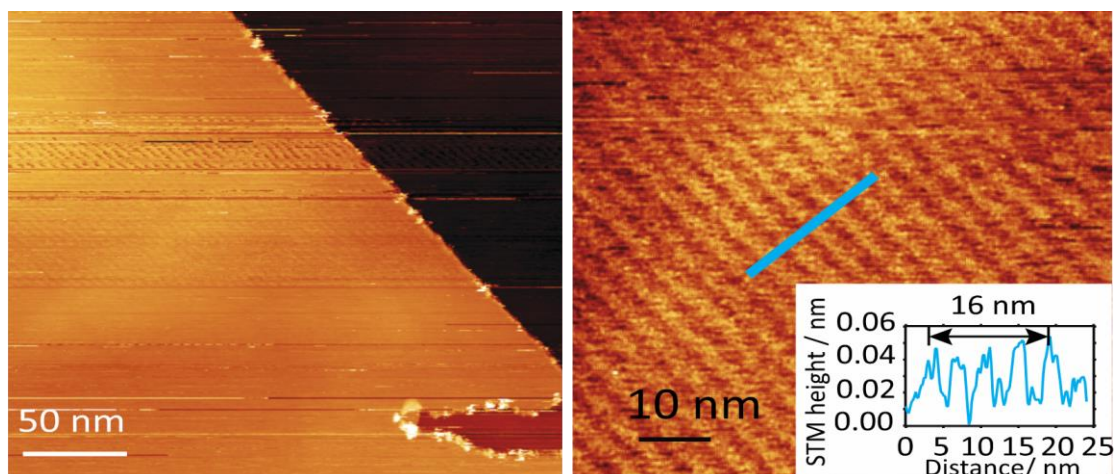
Figure 2.4. Structure characterization. The second trial of STM imaging for YbDD drop-cast onto HOPG: (*left*) 25 μL chloroform with 1 mmol YbDD sample, 270 × 270 nm^2 image, + 2 V sample bias, 100 pA, (*right*) 75 × 75 nm^2, image +2 V sample bias, 100 pA, (*inset*) blue height profile across rows.

2.2.3 Steady-State electronic absorption spectra

Absorption spectra of LnDD complexes were recorded in aqueous solutions at room temperature. Those for GdDD, YbDD, and ErDD show alike spectroscopic properties as their spectra overlap largely, while the one for LaDD is slightly different. Similar to most simple metalloporphyrins, each of all four lanthanide-double-decker complexes feature one strong Soret band (or called B band) corresponding to an $S_2 \leftarrow S_0$ transition with the maximum locating at 400-450 nm. These most intense peaks have large molar absorption coefficients ε around $10^5 \sim 10^6$. Therefore, excitation light wavelengths are always selected in this range for the ligands' best energy harvesting. There are two more absorption peaks found in the range 500-600 nm in each absorption spectra corresponding to the $S_1 \leftarrow S_0$ transition with lower intensities (log ε = 3.5-4.5). Those peaks are called Q bands, labeled as Q (0,0) and Q (1,0) respectively. Noted that if no metal coordinated to the porphyrin ring and the NH protons presenting, two Q bands would be split into four individual bands. The successful complexation was proven by only two Q bands observed from the absorption spectra. Detailed information for all absorption peaks can be found in Table 2.3.
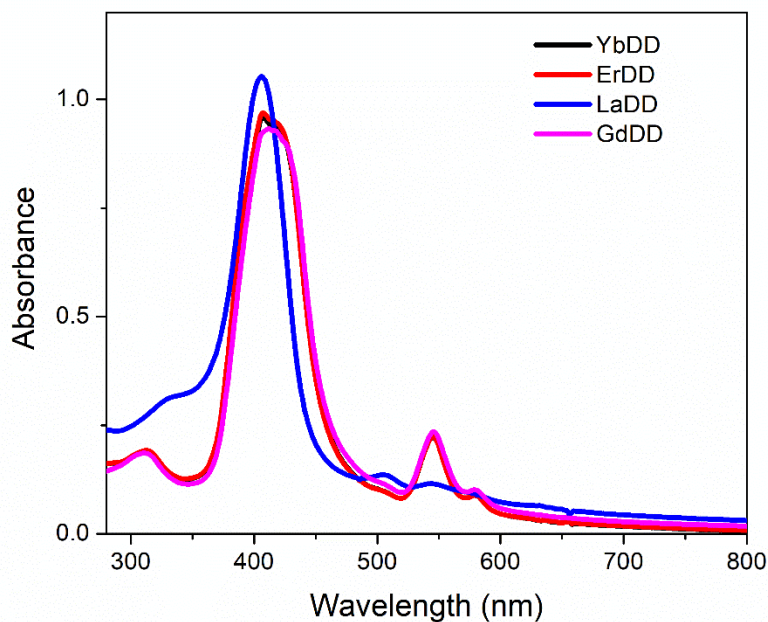
Figure 2.5. UV/vis absorption spectra of a aqueous solution of 10μM LnDD (Ln= Yb, Er, La and Gd).

2.2.4 Quantum yields measurements

The quantum yields measurement were performed under 425 nm excitation, and the NIR range was of interest for YbDD in various solvents (DCM, H_2O, toluene, and MeOH). YbTPP(Tp) was used as a standard in DCM with literature reported quantum yield of 3.2% with 425 nm excitation. YbDD showcases superior photophysical performance than the monoporphyrinato counterpart/analog YbN (serving as the control) under various solvent systems. The NIR quantum yields of YbDD were measured by comparison with the standard YbTPP(Tp), which was reported as 3.2% in dichloromethane with the same excitation wavelength of 425 nm.[51] The NIR emission quantum yields of YbDD in toluene (water) were recorded as 3.5% (2.8%), while those

of YbN in these solvents were 2.8% (2.7%), shown in Table 2.1.

Table 2.**1.** The NIR emission quantum yields of YbDD and YbN in various solvents.

	Quantum yield (Φ)			
Solvent	DCM	H$_2$O	Toluene	MeOH
YbDD	3.9%	2.8%	3.5%	2.6%
YbN	2.8%	2.7%	2.8%	2.5%
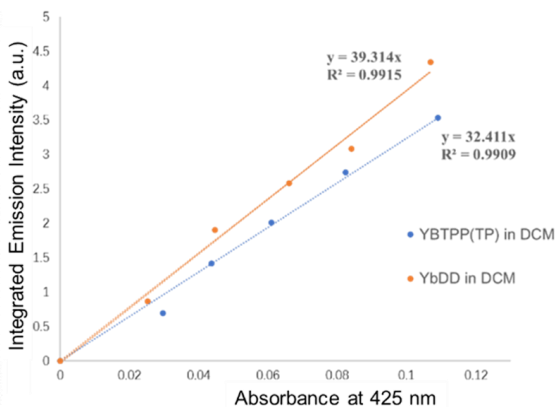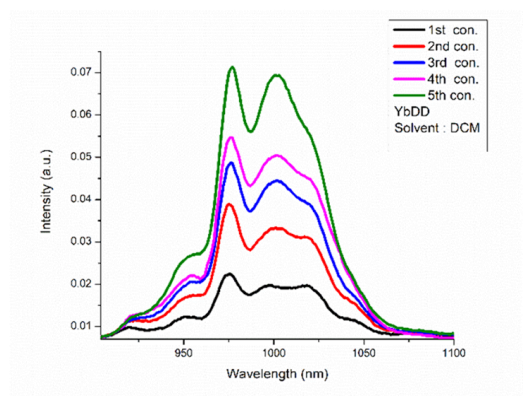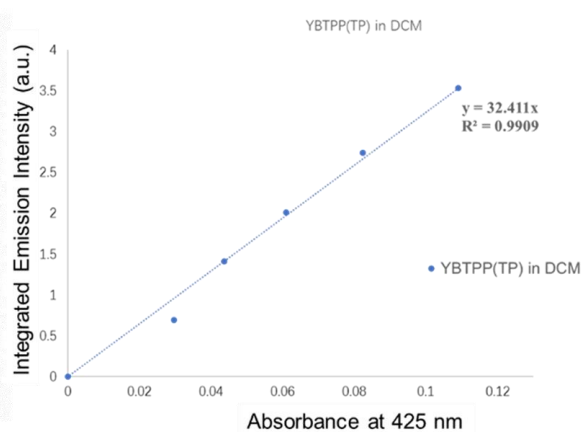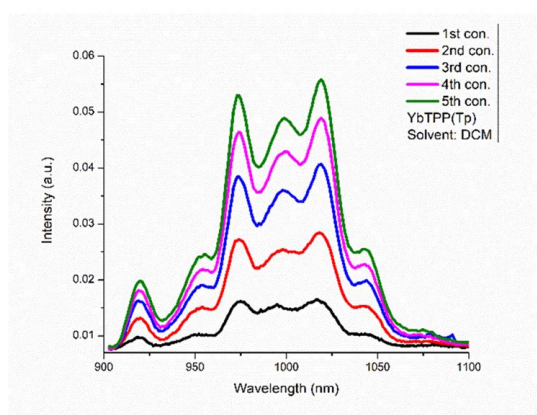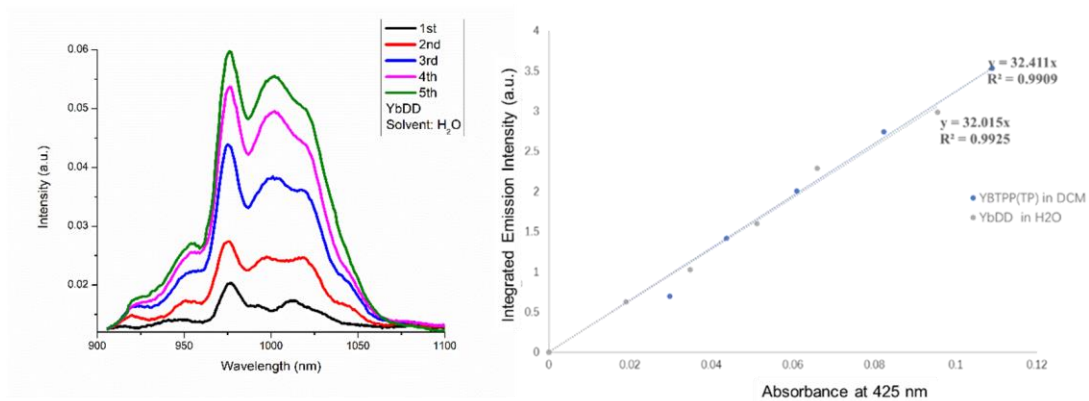
Figure 2.6. (*Left column*) NIR emission spectra (λ_{ex}= 425nm) of DCM or H$_2$O solution of YbDD; (*right column*) the plot of integrated emission peak area *vs* absorbance, compared with YbTPP(Tp)).
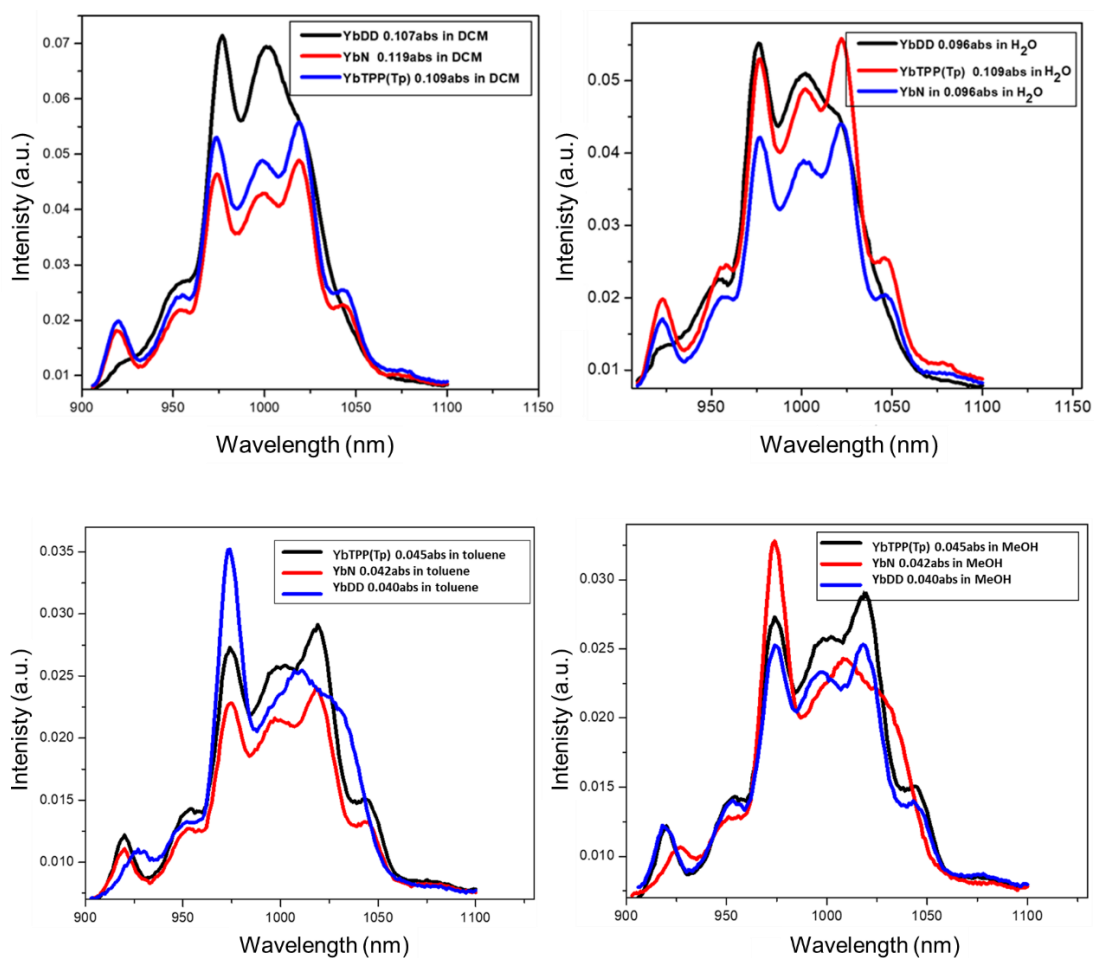
Figure 2.7. NIR emission spectra (λ_{ex} = 425 nm) of YbDD, YbN, and YbTPP(Tp) in DCM (*top left*), H_2O (*top right*), toluene (*bottom left*), and MeOH (*bottom right*).

2.2.5 Emission spectra

As shown in Figure 2.8, the emission spectrum of YbDD comprises several parts: the porphyrin ligand visible-NIR emission and the Yb^{3+} ($^2F_{5/2} \rightarrow {}^2F_{7/2}$) NIR emission, displayed with equal peak height in this figure. The peaks at 647 nm and 699 nm represent the porphyrin fluorescence from the Q-band singlet nominally labeled S1. The S_2 singlet (B-band) emission is also observed at a much weaker intensity and shorter wavelengths (not shown). The hot emission bands 1,2 and band 3 in Figure 2.8 may correspond to the transitions from the three excited states of $^2F_{5/2}$. The energy transfer from the porphyrin ligands to the Yb^{3+} ion is observed to be efficient since the metal ion is not excited by 425 nm radiation in the absence of an antenna. However, the presence of both ligand fluorescence and lanthanide emission at room temperature suggests that the energy transfer rate from the porphyrin to Yb^{3+} is similar to the nanosecond regime. The lower emission quantum yield of YbDD in water than in toluene is attributable to the quenching by high-frequency O-H vibrations. The trivalent lanthanide ions belong to the hard Lewis acid category with the coordination number of up to 8-12 so that under-saturation of the lanthanides' inner coordination sphere by ligands offers vacancies for solvent molecule coordination. The YbN system was confirmed to have unsaturated seven-coordinated Yb^{3+}: four N from the porphyrin ring and three O from the Kläui $[(\eta^5\text{-}C_5H_5)\,Co\{(MeO)_2P{=}O\}_3]^-$ anion capped oxygen atoms.

To shield the Yb^{3+} ion in an aqueous environment and suppress luminescence quenching, the double-decker complexation strategy in YbDD fulfills the eight-coordination number requirement.
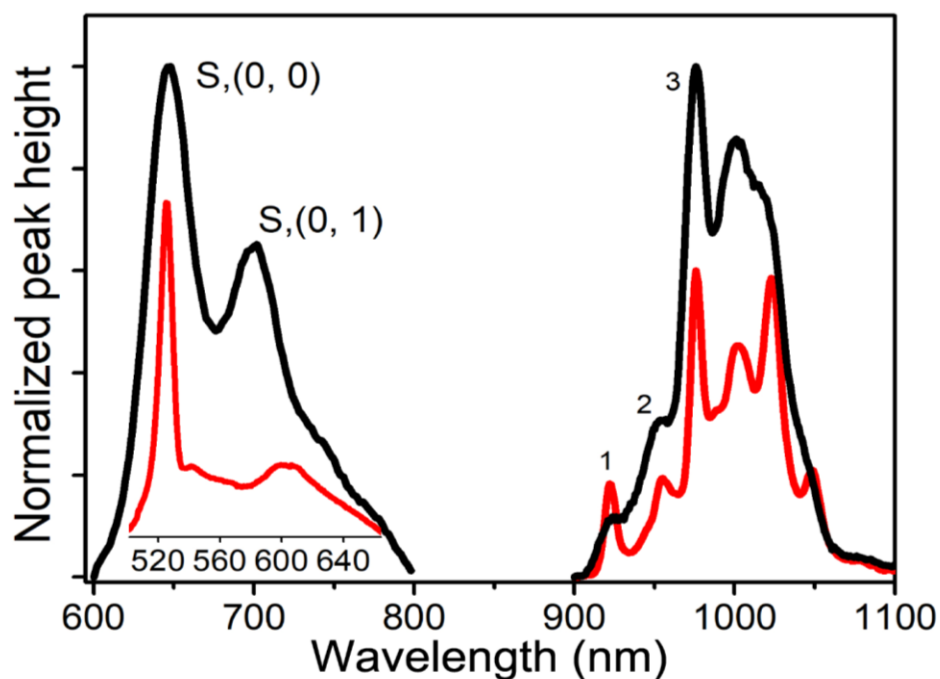
Figure 2.8. Comparison of emission bands of YbN (*black*) and YbDD (*red*) at 298 K in aqueous solution ($\lambda_{ex} = 425$ nm).

2.2.6 Brightness and lifetime

Brightness is the product of quantum yield and molar attenuation coefficient,[53] and it demonstrates the radiant energy emitted per frequency interval unit area per solid angle. For bioimaging purposes where the low dosage is preferred because of adverse effects, it is a superior indicator of applicability than quantum yield, since with higher brightness the low-abundance fluorescent compounds are detected more easily. The brightness of YbDD exceeds that of YbN by the factor of 1.37 (Table 2.2). To explain

this result: YbDD holding two antenna ligand groups should transcend YbN having only one. The emission lifetimes for the transitions $^2F_{5/2} \rightarrow {}^2F_{7/2}$ emission lifetimes were determined in both water and toluene for YbDD and toluene for YbN. The YbDD lifetime is 23.6 μs in water (Figure 2.9) and 28.2 μs in toluene, which are both higher than the value for YbN (Table 2.2). YbDD shows a longer $^2F_{5/2} \rightarrow {}^2F_{7/2}$ lifetime which mainly results from its higher symmetry than YbN. With a higher symmetrical structure, there are fewer possible f-f transitions, and the lifetime for a specific transition will be longer.[54] This trend is consistent with the measured NIR emission quantum yields in water and toluene. It is worth noting that most porphyrin-based NIR dyes for biological applications have little emission in NIR-II biological window because of no metal coordination, meanwhile, their maximal absorption peaks are usually located only from 650 to 800 nm, both reasons limit their application prospect. One commercially available NIR-II dye (NIR-II dye #900883, Sigma-Aldrich), has a similar emission peak located at 1050 nm as that of YbDD, but its NIR emission quantum yield is ~2% which is lower than that of YbDD. The impressive NIR emission quantum yields and long NIR emission lifetime of YbDD in an aqueous solution, together with its hydrophilic property, hold tremendous promise as a (NIR) bioimaging probe.

Table 2.2. Luminescence lifetime (τ), quantum yield (Φ), and brightness (BR) of YbDD and YbN in toluene or water.

	τ (μs)[a]		Φ (%)[b]		BR[c]
Solvent	Toluene	H_2O	Toluene	H_2O	H_2O
YbDD	28.19	23.62	3.5	2.8	2540
YbN	23.02	12.03	2.8	2.7	1850

[a]Determined from the emission decay curve monitored at λ_{em} = 978 nm ($^2F_{5/2} \rightarrow {}^2F_{7/2}$) with λ_{ex} = 425 nm (Conc.: 1 μM). [b]The relative quantum yields of the Yb^{3+} emission (λ_{ex} = 425 nm) from the two Yb^{3+} complexes in toluene and H_2O were obtained by comparison with the standard YbTPP(Tp). [c]Calculated from BR = Molar attenuation coefficient × Quantum yield (unit: M^{-1} cm^{-1}); Molar attenuation coefficients were obtained from the absorption spectra in water at 425 nm by applying the Beer-Lambert Law.
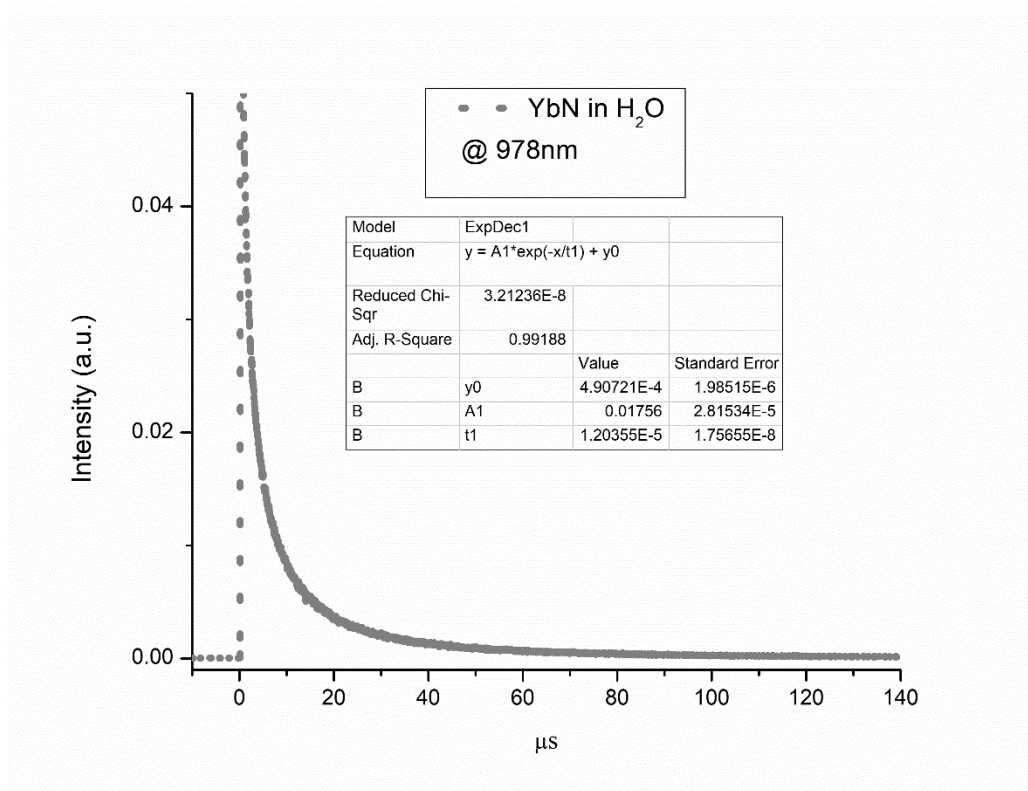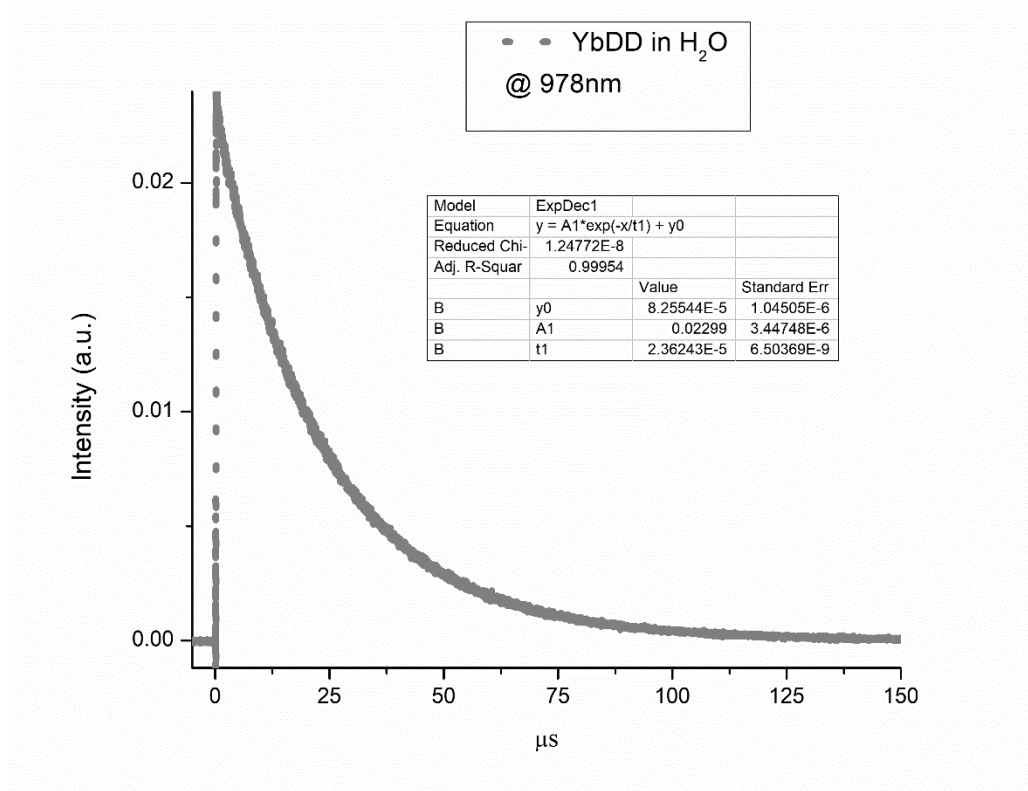
Model	ExpDec1		
Equation	y = A1*exp(-x/t1) + y0		
Reduced Chi-	1.24772E-8		
Adj. R-Squar	0.99954		
		Value	Standard Err
B	y0	8.25544E-5	1.04505E-6
B	A1	0.02299	3.44748E-6
B	t1	2.36243E-5	6.50369E-9

Model	ExpDec1		
Equation	y = A1*exp(-x/t1) + y0		
Reduced Chi-Sqr	3.21236E-8		
Adj. R-Square	0.99188		
		Value	Standard Error
B	y0	4.90721E-4	1.98515E-6
B	A1	0.01756	2.81534E-5
B	t1	1.20355E-5	1.75655E-8

Figure 2.9. Decay curve of Yb^{3+} emission in the form of complex YbDD (*top*) or YbN (*bottom*) and with monoexponential function fitting.

2.2.7 Singlet oxygen generation

As a cross-system validation, the singlet oxygen quantum yield of GdDD was also examined in chloroform by comparison with the spectrum of the reference compound H_2TPP (Φ_Δ = 55% in $CHCl_3$). A new-generation anticancer agent GdN, comprising only one porphyrin ring, with high singlet oxygen quantum yield was chosen to serve as a comparison.[55] The near-infrared $^1O_2$ phosphorescence spectra of GdDD, GdN, and the reference are shown in Figure 2.10. From these spectra, the singlet oxygen quantum yields of GdDD and GdN were measured at 66% and 51%, respectively. Hence GdDD displayed superior singlet oxygen generation in both organic and aqueous media. By comparing with two U.S. Food & Drug Administration approved PDT agents, Porfimer sodium (Photofrin®) and 5-Aminolevulinic acid (Levulan®), although GdDD shows lower singlet oxygen quantum yield (46% in aqueous solution, Photofrin®: 89%; Levulan®: 56%), it has much higher maximal absorptivity (GdDD: 223,872 $M^{-1}cm^{-1}$ @412 nm, and 52480 $M^{-1}cm^{-1}$ @580 nm) than these two commercial photosensitizers (Photofrin®: 3,000 $M^{-1}cm^{-1}$ @632 nm; Levulan®: 5,000 $M^{-1}cm^{-1}$ @632 nm). With double-decker porphyrinato structure and the resulting high molar extinction coefficient values, GdDD shows great applicability in photodynamic effects, which is also consistent with the high brightness of YbDD as mentioned.
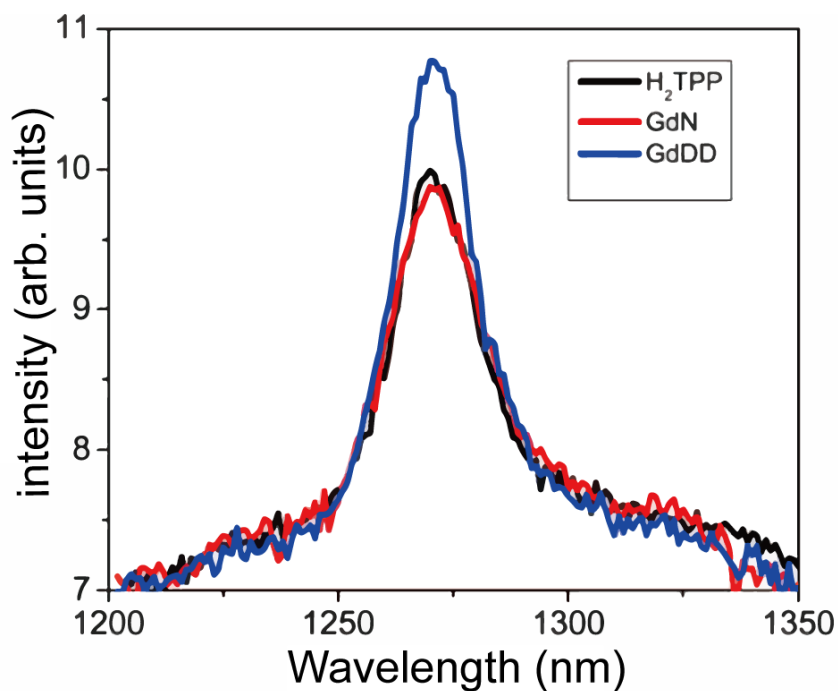
Figure 2.10. The near-infrared $^1O_2$ phosphorescence spectrum sensitized by GdDD, GdN, and the standard tetraphenylporphyrin H$_2$TPP (in CHCl$_3$. Abs. = 0.05 at the excitation wavelength of 425 nm).

Another method of the determination of singlet oxygen generation quantum yields was also conducted to measure them in aqueous solutions. A series of singlet oxygen indicators is introduced to determine the target contents indirectly. There is one challenge for the previous method where singlet oxygen phosphorescence was detected directly: the phosphorescence of singlet oxygen in water is much weaker than it is in organic solvents of deuterium water (D$_2$O), especially compared with the fluorescence of photosensitizers. It has been reported that most organic solvents and deuterium solvents can assist the formation of photosensitizers' triplet states, which results in improved singlet oxygen quantum yields.[56]

In a mixing solution of an indicator and a photosensitizer with light irradiation, the generated singlet oxygen will quickly react with the indicator by oxidizing its unsaturated structure. In our case, 9,10-anthracenediyl-bis(methylene)dimalonic acid (ABDA) was used as a common indicator.[57, 58] It was oxidized by singlet oxygen and its absorbance decreased linearly. Therefore, we can obtain the singlet oxygen generation rates associating with the absorbance decreasing rates, and the exact singlet oxygen quantum yields can be calculated by comparing them with the value from a reported standard photosensitizer on the same experimental conditions. Rose Bengal (RB) was chosen as a reference with the literature value as 75% in water. In Figure 2.11, although no change in absorbance for ABDA solely under irradiation, there was obvious photobleaching found in RB, GdN, and GdDD groups. The singlet oxygen quantum yield for GdDD was 46% in water and it was slightly higher than GdN (Figure 2.12). The lower values found in aqueous solutions were also consistent with the previous reports where H2O is not a good medium for singlet oxygen generation.[56]
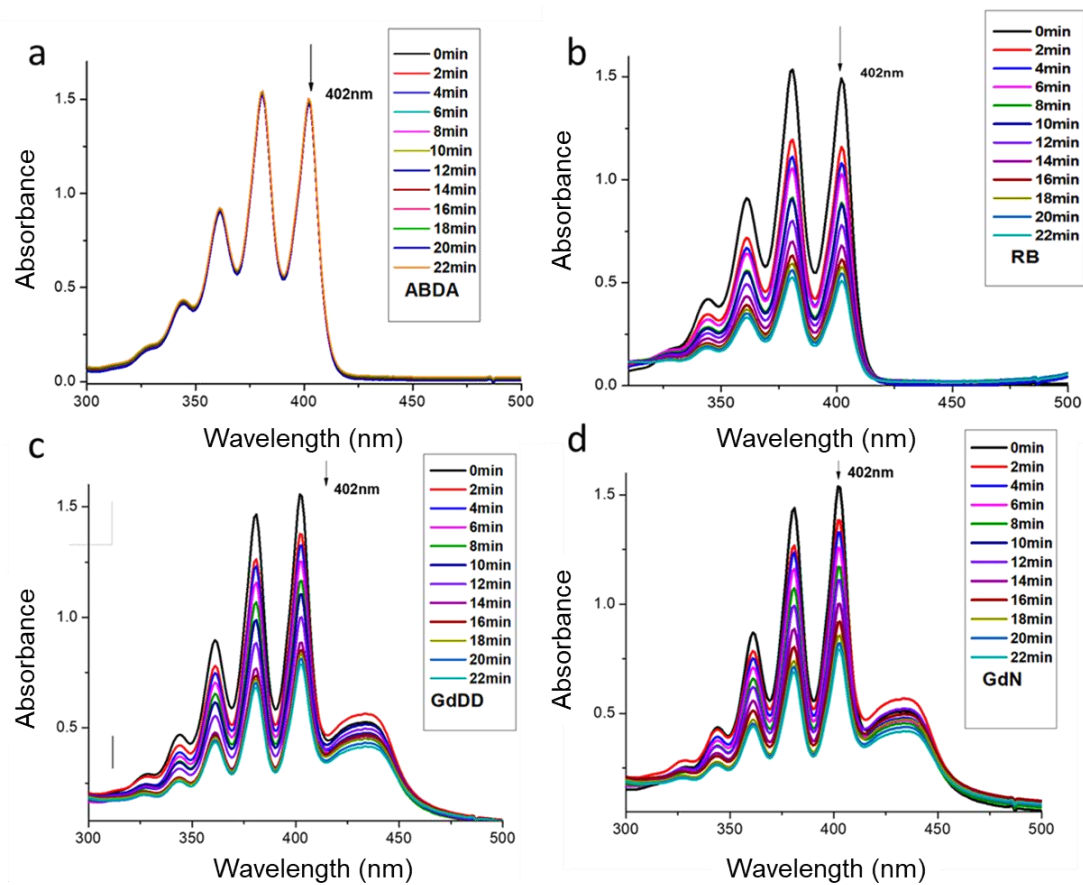
Figure 2.11. Absorption spectra of ABDA mixed with different probes: (a) no probe; (b) Rose Bengal; (c) GdDD; (d) GdN in phosphate-buffered saline (PBS) buffer. The excitation power density was 6 mW cm^{-2}.
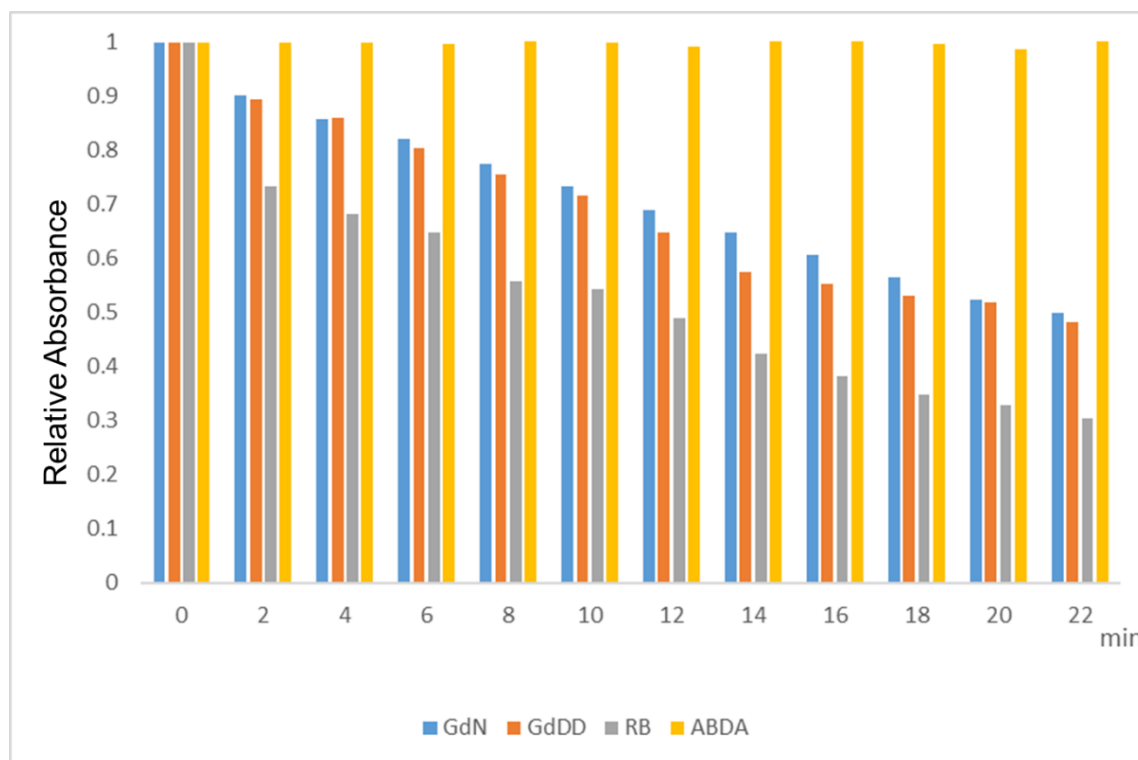
Figure 2.12. Plots of the changes in absorbance of ABDA at 402 nm (mixed with10 µM GdDD, GdN, and standard RB) *versus* the irradiation time (with a power density of 6 mW cm^{-2}).

2.2.8 Low-temperature phosphorescence spectra

The energy gap between the antenna donor state and the lanthanide ion plays a crucial role in energy transfer efficiency, including luminescence intensity and singlet oxygen formation. The lowest triplet state of the lanthanide double-decker complex was determined experimentally from phosphorescence. The 77 K phosphorescence spectra of GdDD and GdN are shown in Figure 2.13. The zero-phonon lines are at a very similar wavelength (~745 nm: 13405 cm^{-1}) and the prominent vibrational progression in the ring carbon-nitrogen stretching mode of 1410 cm^{-1} is at lower energy. The triplet energy level is therefore located at 2610 cm^{-1} above the highest $^2F_{5/2}$ level of Yb^{3+} in YbDD.

The optimum energy gap has been given as between 2000 cm^{-1} to 5000 cm^{-1} to eradicate back energy transfer.[6] The weak features marked 1 and 2 in Figure 2.13 correspond to the singlet fluorescence bands $S_1(0,0)$ and $S_1(0,1)$, as in Figure 2.8 for YbDD at 298 K. The triplet state lifetimes of GdDD and GdN at 77 K were measured as 0.21±0.03 ms and 0.14±0.02 ms, respectively.
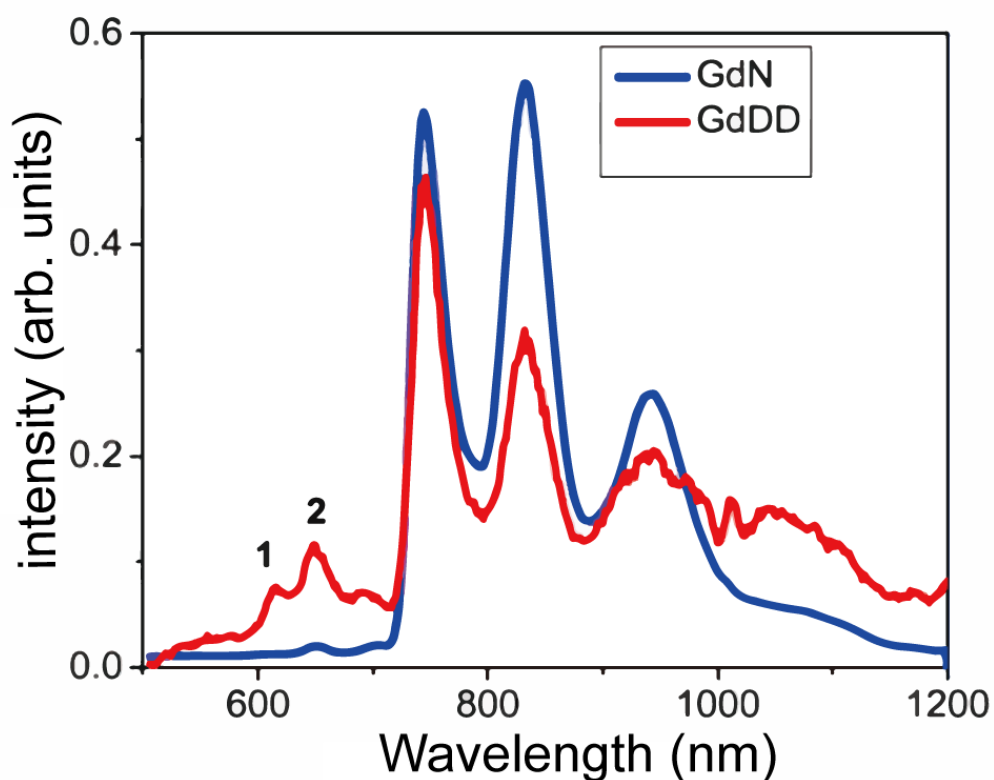
Figure 2.13. The 77 K phosphorescence spectrum of GdDD and GdN in MeOH (Conc.: 10 μM, λ_{ex} = 425 nm).

Table 2.3 Photophysical properties of LnDD (Ln = Yb, Er, Gd, La).

Compounds	Absorption peaks (nm)[a] and molar absorption coefficients (logε, [dm^3 mol^{-1}cm^{-1}])	Emission peaks (nm),[a] and lifetimes[b]	Singlet oxygen quantum yields[c] in CHCl$_3$	Singlet oxygen quantum yields[d] in PBS buffer	Emission peaks at 77 K (nm)[e] and lifetimes[f]
YbDD	408 (5.12), 545 (4.36), 580 (4.11)	647, 699, 923, 949 (23.62 µs), 978 (28.2 µs), 1001, 1018, 1044	/	/	978 (3.45 µs), 1006, 1018
ErDD	408 (5.36), 545 (4.82), 580 (4.48)	647, 701, 1533 (7.37 µs), 1602	/	/	1531, 1545
GdDD	412 (5.35), 545 (4.13), 580 (4.72)	646, 703	0.66	0.46	744 (0.24 ms), 830, 938, 1062
LaDD	406 (5.23), 506 (3.78), 545 (4.18)	647, 701	/	/	/

[/] Not measured. [a] measured in aqueous solutions at 298K. [b] The lifetime was measured at 298 K in toluene or H$_2$O. (Conc: 1 µM, λ_{ex}= 425 nm) [c] determined by emission method. The standard used in this study was tetraphenylporphyrin (H$_2$TPP) in anhydrous CHCl$_3$ ($\Phi_\triangle$ = 55% on the same conditions). [d] determined by absorption method. The standard sample in PBS buffer was RB. [e] measured in MeOH (Conc.:10 µM, λ_{ex}= 425 nm)). [f] measured at 77 K in MeOH (Conc.:10 µM, λ_{ex} = 425 nm).

2.2.9 Transient absorption spectroscopy

Transient absorption spectroscopy (TAS), as two-dimensional spectroscopy, was used to investigate both spectral and temporal properties of the samples.
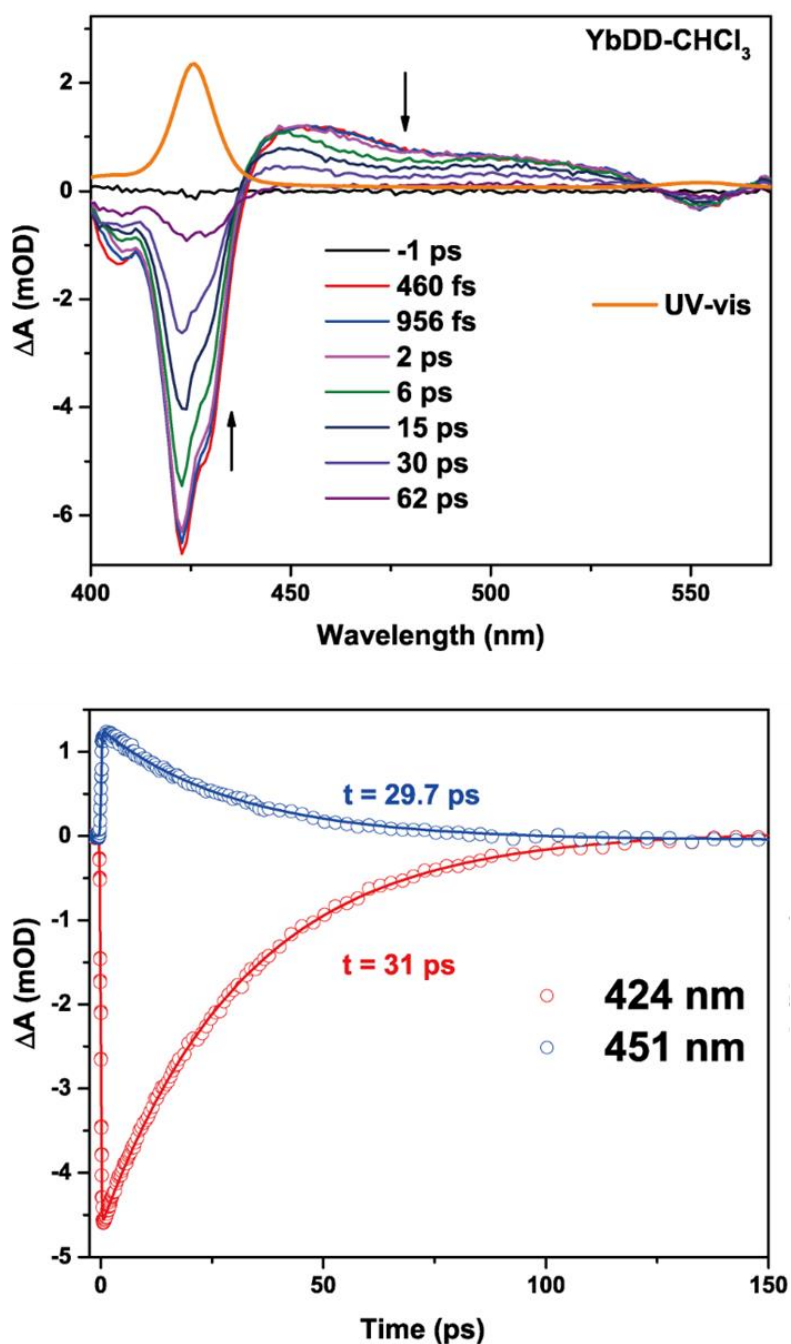
Figure 2.14. (*Top*) fs-TA spectra at different time delays at low pump fluence (15 µJ cm^{-2}), (*bottom*) ground state bleach recovery dynamics at 424 nm, and excited-state

decay at 451 nm of YbDD in chloroform following 395 nm laser excitation.

The femtosecond (fs) TA spectra at different delay times for YbDD in chloroform at low laser fluence are displayed in Figure 2.14. The $S_0 \rightarrow S_2$ Soret (B) absorption band is shown in orange color and its stimulated emission band has a small redshift with respect to the ground-state bleach and gives a negative signal.[59] The triplet-triplet ($T_1 \rightarrow T_n$) absorption bands are observed at longer wavelengths (440-530 nm), with maximum intensity at 451 nm, corresponding to the terminal state energy of 35578 cm^{-1}. The lifetimes of the bleach and the excited state transients for YbDD were determined by monitoring at the wavelengths 424 and 451 nm, respectively (Figure 2.14 bottom). The two results are effectively the same and are in the picosecond scale, denoting a rapid singlet-to-triplet intersystem crossing (ISC).
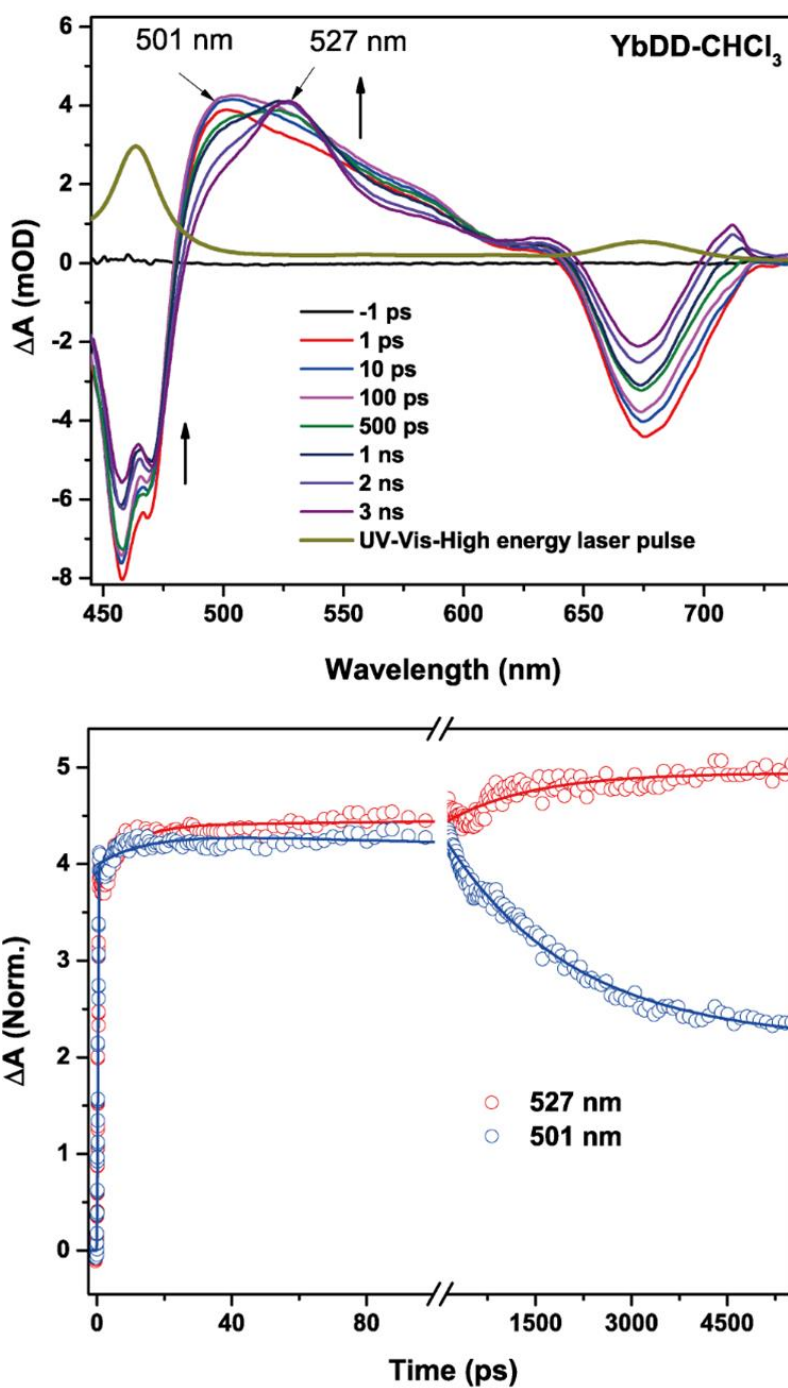
Figure 2.15. (*Top*) Spectral evolution in fs-TA at 395 nm laser excitation having 45 μJ cm^{-2} fluences. (*bottom*) Normalized excited state decay kinetics at 501 and 527 nm.

Femtosecond TA absorption spectra were also obtained by using a higher pump fluence (Figure 2.15). The pulsed laser with high fluence produces a thermal effect of the YbDD,

which causes distortions of the porphyrin structures and results in significant redshifts in the electronic absorption spectra. In contrast to the lower fluence, a redshift of the Soret band ($\Delta\lambda = +36$ nm) and the $T_1 \rightarrow T_n$ absorption bands were observed. It is worth noting that the structural change was detected instantly by ultrafast TA spectroscopy: the peak at 501 nm started to shift to 527 nm after 100 picoseconds, and the whole conformation changing process was completed in nanoseconds (Figure 2.15 bottom). Furthermore, the formation of the triplet state from the singlet excited state is observed from the kinetics at 527 nm. In contrast to the 527 nm, the excited singlet state at 501 nm de-excited exponentially to the ground states.
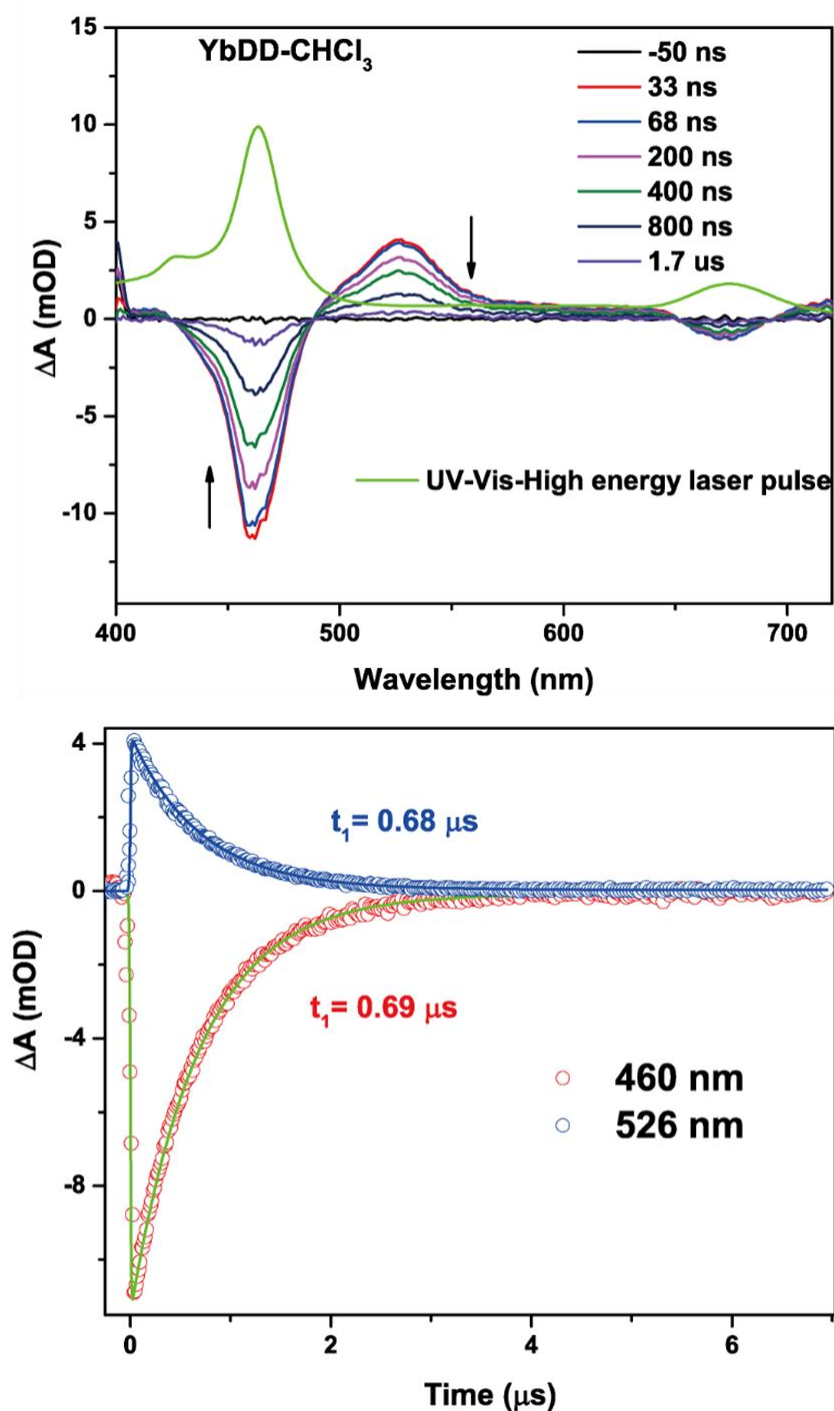
Figure 2.16. (*Top*) ns-TA spectra at different time delays having 45 µJ cm^{-2} pump fluence. (*Bottom*) Ground state bleach recovery dynamics at 460 nm and excited state decay at 526 nm of YbDD in chloroform following 395 nm laser excitation. The UV-vis spectra of YbDD are added in upper panels to guide the ground state bleach.

However, when using nanosecond (ns) TA spectroscopy, the detailed kinetics of the triplet-triplet absorption peak at around 526 nm could not be resolved since the conformation was changing too quickly. The ground state bleach recovery lifetime was extracted from the nanosecond TA spectra (0.69 μs), which is consistent with the decay lifetime by monitoring the deactivation of the triplet state signal at 526 nm (0.69 μs) (Figure 2.16). Isosbestic points were found in all TA spectra, which suggests that only one single photoexcited species was formed in each case.

2.2.10 Stability tests

Stability is one important standard for a good photosensitizer. The first test was to check whether the emission profiles of YbDD have dramatic changes in different pH conditions. pH5 and pH7 PBS solutions were chosen to simulate tumor microenvironments because they are similar in osmolarity and ion concentrations matching with the human body.[55]

Considering the most intense emission peak at 975 nm belong to Yb(III), at the same concentration of PBS buffer, emission intensity dropped 8% when the pH value decreased from 7 to 5. At the same pH value, the emission intensity dropped 22% when PBS buffer concentrated from 1X to 5X.
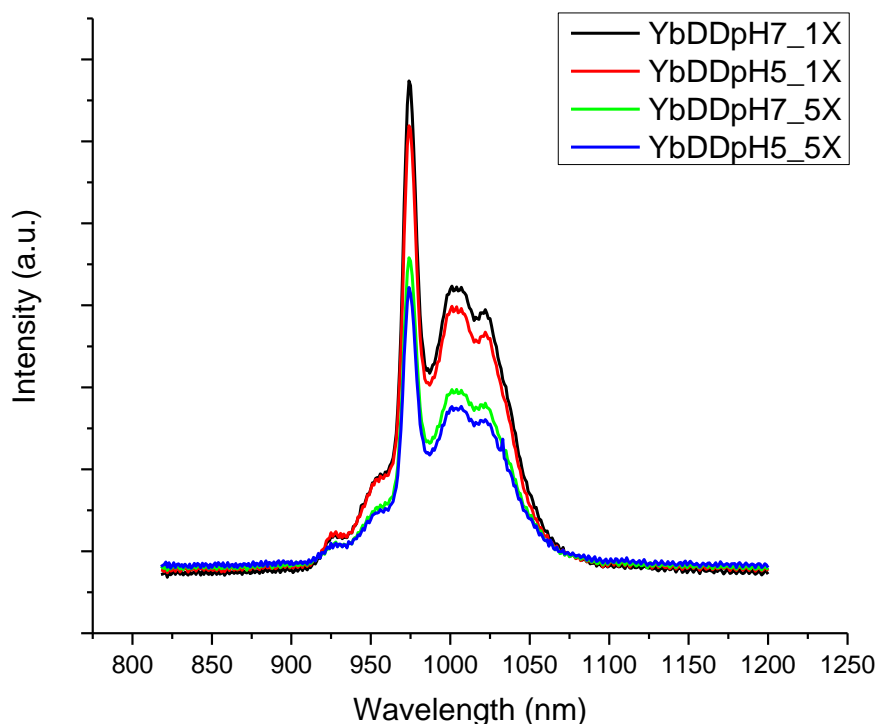
Figure 2.17. Emission spectra of 100 µM **YbDD** in 1X or 5X concentrated PBS buffer at pH=5 or pH=7 at 298 K (λ_{ex} = 425 nm).

2.2.11 Photodynamic therapy studies

To evaluate the photodynamic therapeutic efficiency of GdDD and ErDD, MTT (a colorimetric assay) and PDT assays were carried out in HeLa (cervical cancer cells) and MRC5 (normal lung cells). Both GdDD and ErDD are safe when there is no light irradiation owing to their high dark IC_{50}. IC_{50} is the maximal concentration for the half inhibition, and it is safer for a compound with higher IC_{50} which means a higher concentration is needed to achieve bad effects.

Upon light irradiation, both of them showed a therapeutic effect on the cell lines. The photodynamic therapeutic index (PTI) was introduced here for judging the performance

as a photosensitizer. The PTI is the ratio of Dark IC_{50} over Photo IC_{50}. The higher PTI values mean the larger therapeutic effects under irradiation and the better PDT effects. From the Table 2.4 summarized below, comparisons have been made with the previously reported potential PDT agent, GdN. Unfortunately, exact IC_{50} values are only given for dark cytotoxicity in the reference paper, but photo-cytotoxicity can be roughly obtained from the line charts. Although two complexes have lower dark IC_{50} values than that of GdN, both GdDD and ErDD have similar photo IC_{50} values with GdN. More importantly, GdDD showed a large photodynamic therapeutic index which suggests its high potential as a PDT agent.
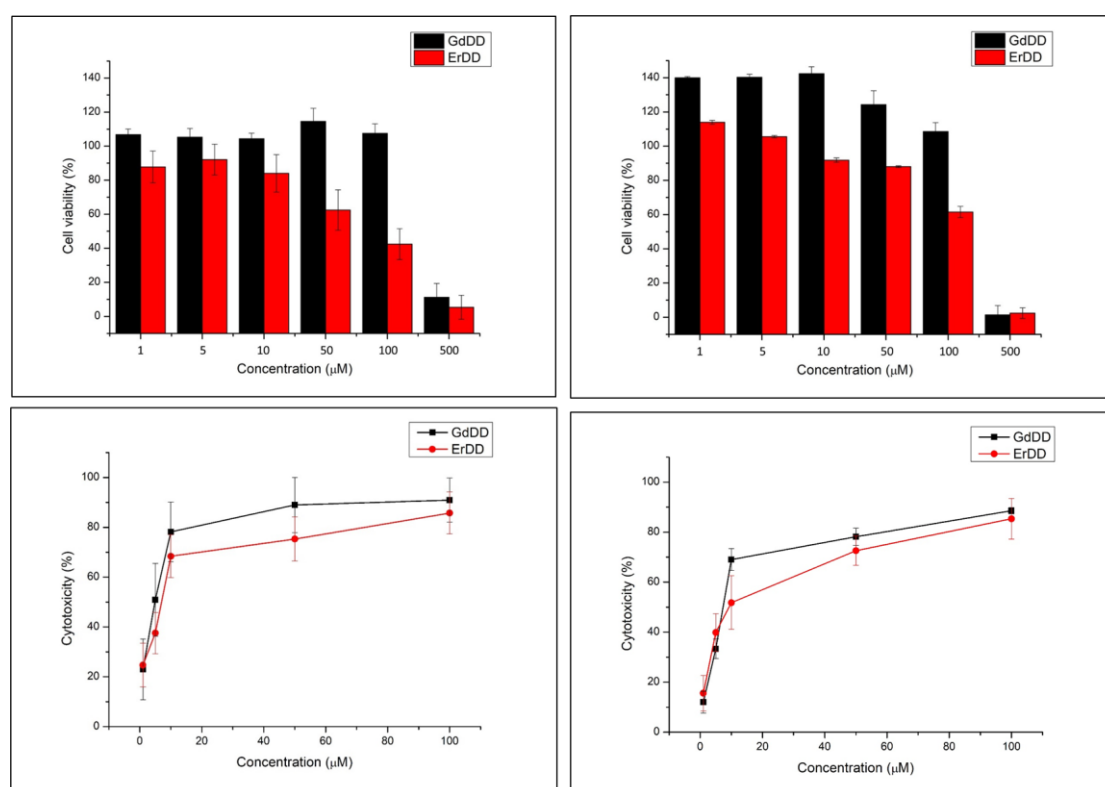
Figure 2.18. (*Top*) Dark toxicity of GdDD nad ErDD in HeLa cells (*left*) and MRC5 cells (*right*); (*bottom*) light cytotoxicity of GdDD and ErDD in MRC5 cells under light dosage of 1 J/cm^2.

Table 2.4. Photo and Dark cytotoxicity of GdDD and ErDD towards cervical cancer cell HeLa, and normal lung cell MRC5 under 1 J/cm^2 light irradiation (λ_{ex} = 430 nm), MTT assays were carried out after incubation at 37 °C for 24 h.

Photo IC$_{50}$ (μM) (Dark IC$_{50}$ (μM)) Photodynamic Therapeutic Index	HeLa	MRC5
GdDD	3.6 (322) 90.4	10.8 (323) 30.0
ErDD	6.7 (188) 28.2	9.2 (246) 26.8
GdN	~3 (780) Very high	>4 (700) Very high

2.3 Conclusion

In this project, rarely reported is a series of water-soluble lanthanide–porphyrin double-decker complexes with structural characterization using NMR, HRMS, STM, and TAS techniques. Bioapplications including NIR imaging and cytotoxic $^1O_2$ generation of the complexes have also been developed. The major improvement for photophysical performance— although considering the low-quantum yield of Yb^{3+} in the NIR region—comes from the enhancement of the brightness of the potential bioimaging probe YbDD. This property, brightness, has not yet been widely recognized as the yardstick for applicability, compared with quantum yield, but it shows higher practical significance for bioimaging purposes.

2.4 Experimental

2.4.1 Synthetic procedures
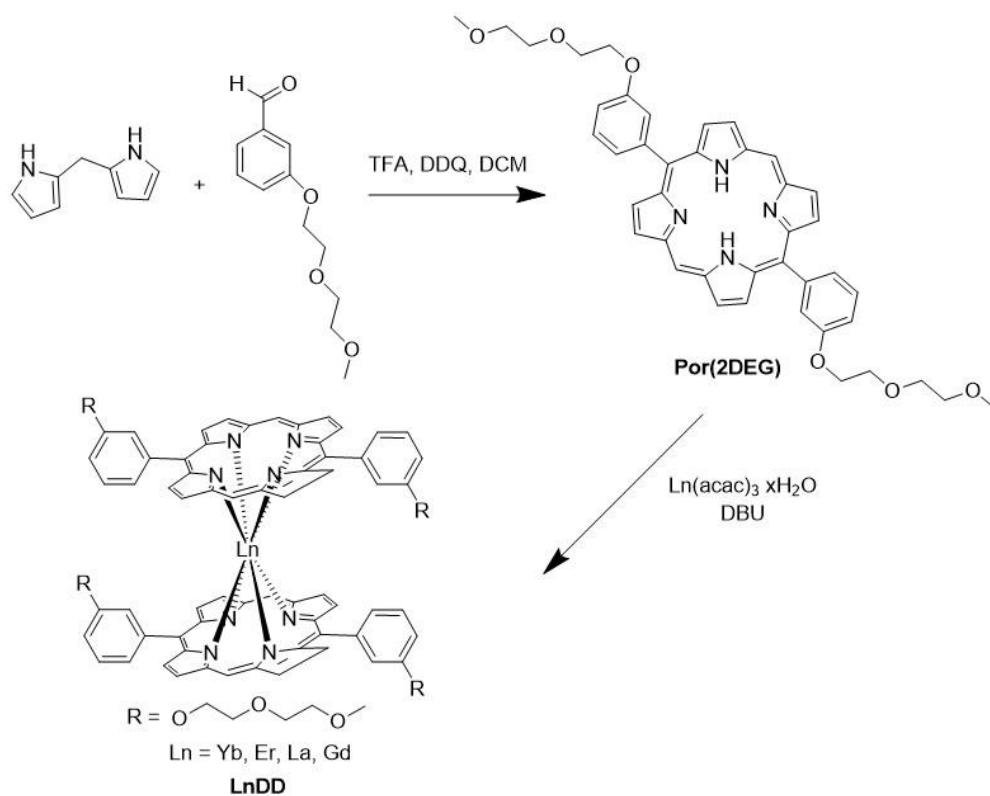
Scheme 1. The synthetic scheme of the double-decker porphyrinate lanthanide complexes.

General synthesis

All anhydrous solvents were prepared properly before use. For details, dichloromethane (DCM), methanol (MeOH), and x-hexanol were dried by carefully refluxing with calcium hydride. Other chemicals and reagents were purchased from certificated suppliers used directly with no purification. All reaction processes were monitored by using thin-layer chromatography (TLC) techniques, also with UV lamps or iodine for visualization. Column chromatography technique was used in isolation of most products, and standard silica gel or alumina oxide was used for column packing. As for high-polar intermediates or products, the reverse-phase HPLC technique was applied for purification. NMR spectra for all compounds were obtained on either a 400 (^{1}H: 400 MHz, ^{13}C: 100 MHz) or a 500 (^{1}H: 500 MHz, ^{13}C: 1250 MHz) spectrometer. Mass-

spectra or high-resolution mass spectra were recorded on a Bruker Autoflex Matrix-Assisted Laser Desorption/Ionization – Time of Flight (MALDI – TOF) mass spectrometer. All NMR spectra and mass spectra were shown in the Appendix.

Preparation of 5,15-bis(3-(2-(2-methoxyethoxy)ethoxy)phenyl)porphyrin (Por-2DEG)
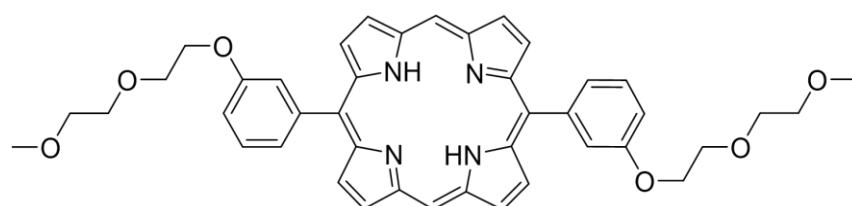
5,4 mmol di(1H-pyrrol-2-yl)methane (788.9 mg) was dissolved in 1 L anhydrous DCM and 1 equivalent of 3-(2-(2-methoxyethoxy)ethoxy)benzaldehyde (1.21 g, 5.4 mmol) was added into the same round bottom flask. The mixture was stirred under nitrogen for 30 min to drive out oxygen or trace water. 3.24 mmol trifluoroacetic acid (0.24 ml) was added dropwisely. After 3-hour stirring at room temperature, 6.28 mmol 2,3-Dichloro-5,6-dicyano-1,4-benzoquinone (DDQ) (1.47 g) was added with another 1 hour stirring. After the completion of the reaction, 2 ml triethylamine (TEA) was added to quench the reaction and the excessive TFA. The solvent was removed by distillation under a reduced vacuum. The crude product was purified on a silica gel column with elutes (DCM:MeOH = 100:1). ^{1}HNMR (CDCl$_3$): -3.16 (s, 2H), 0.387 (s, 9H), 3.37 (s, 6H), 3.60 (d, 4H), 3.77 (d, 4H), 3.96 (d, 4H), 4.37 (d, 4H), 7.30 (d, 2H), 7.60 (d, 2H), 7.87 (d, 4H), 9.10 (d, 2H), 9.37 (d, 2H), 10.30 (s, 2H), MS (MALDI) calcd. for C$_{42}$H$_{42}$N$_4$O$_6$ [M+H]$^+$ 699.3123, found. 699.3173.

Preparation of lanthanide-double-decker complexes (LnDD, Ln = Yb, Er, Gd and La)
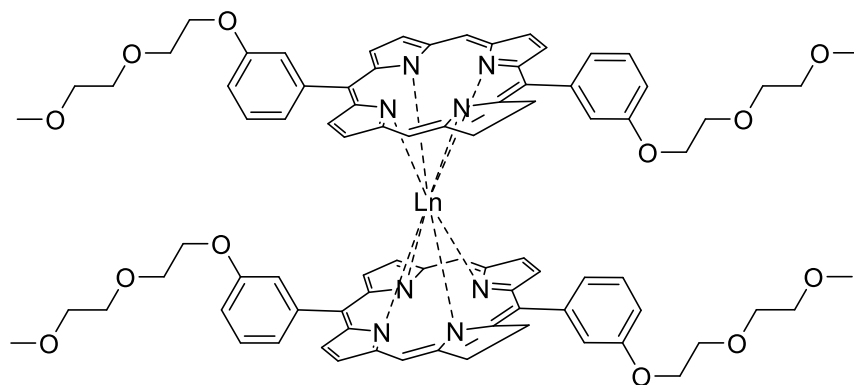
0.12 mmol 5,15-bis(3-(2-(2-methoxyethoxy)ethoxy)phenyl)porphyrin (80.0 mg) was dissolved into 10 ml anhydrous hexanol with the addition of 0.48 mmol Yb(acac)$_3$·xH$_2$O and 0.79 mmol 1,8-Diazabicyclo[5.4.0]undec-7-ene (DBU) (114 μL). Nitrogen was bubbled in the solution for 30 minutes to remove oxygen and the solution was refluxing for 12 hours. When the reaction finished, the solution was diluted with 30 ml hexane. The solvent was removed by distillation under a reduced vacuum. The crude product was purified on a silica gel column with elutes (DCM:MeOH = 20:1). The final product was isolated on a preparative HPLC (C18 column, 10.0 × 250 mm, 5 μm particle size).

YbDD: Yield: 45%; MALDI-TOF MS: calcd. for C$_{84}$H$_{80}$N$_8$O$_{12}$Yb [M]$^+$ 1566.5312, found: 1566.5379.

ErDD: The same procedure were applied as for YbDD. The salts used was Er(acac)$_3$·xH$_2$O but not Yb(acac)$_3$·xH$_2$O. Yield: 45%. MALDI-TOF MS: calcd. for C$_{84}$H$_{80}$N$_8$O$_{12}$Er [M+H]$^+$ 1561.5214, found: 1561.5352.

GdDD: The same procedure as for YbDD. The salts used was Gd(acac)$_3$·xH$_2$O but not Yb(acac)$_3$·xH$_2$O. Yield: 10%. MALDI-TOF MS: calcd. for C$_{84}$H$_{80}$N$_8$O$_{12}$Gd [M+H]$^+$

1551.5229, found: 1551.5362.

LaDD: The same procedure as for YbDD. The salts used was La(acac)$_3 \cdot x$H$_2$O but not Yb(acac)$_3 \cdot x$H$_2$O. Yield: 10%. ^{1}HNMR (CDCl$_3$): 1.879(s, 12H), 2.883(m, 8H), 3.051 (m, 8H d), 3.260(d, 8H), 3.685(s, 8H), 6.730 (m, 4H), 7.060 (m, 4H), 7.160 (M, 8H)), 8.435 (d, 8H), 8.814 (d, 8H), 9.747 (s, 4H). MALDI-TOF MS: calcd. for C$_{84}$H$_{80}$N$_8$O$_{12}$La [M+H]$^+$ 1532.5032, found: 1532.4982.

2.4.2 HPLC characterization of LnDD (Ln = Yb, Er, Gd and La).

Table 2.5. Solvent system for preparative HPLC. Flow rate: 1 mL/min.

Time (min)	Water with 0.05% formic acid (%)	MeOH (%)
0	30	70
5	20	80
15	0	100
20	0	100
30	20	80
35	30	70

2.4.3 Scanning tunneling microscopy

These related experiments were conducted by Dr. Partha Maity, Dr. George T. Harrison, Dr. Aram Amassian, and Prof. Omar F. Mohammed from the King Abdullah University

of Science and Technology (KAUST) on their instrument. The samples were provided by our group. Prof. Wong, Gary Ka-Leung and I provided general guidance. Both institutes discussed the results and composed the relevant part in the manuscript. Highly Orientated Pyrolytic Graphite HOPG (0001) single crystals were cleaned by cleaving in the air using scotch tape. A drop (15 μL) of YbDD (10^{-6} -10^{-5} M) dissolved in chloroform was placed on the surface and allowed to dry at RT in ambient conditions, depositing the film. The sample was dried at 10^{-2} mbar (2 hours) then transferred to the UHV chamber for STM analysis.

STM was performed at room temperature using an Omicron multi-probe (XPS/STM) UHV (10^{-9} mbar) system, which housed a VT-STM. Purchased STM tips (Pt/Ir) (Omicron) were prepared by repeated exposure *in-situ* to electron bombardment (950 V, 2 mA, 2 s) with a tip preparation tool (Omicron). STM tips were judged to be suitable for measurements when the surface of clean HOPG(0001) could be atomically resolved. In-plane x-y distance calibration was performed from measurements of clean HOPG(0001). During measurements, STM tips were conditioned by +5 V sample bias, 1.6 ms, open feed-back loop pulses.

2.4.4 Variable-temperature NMR spectra

Variable-temperature (VT) NMR experiments have been performed to investigate any tautomerism in the structures. According to VT NMR results, NH proton was more shielded (moving from -3.18 to -3.51 ppm) when the temperature decreased from 298 K to 198 K, which could result from less motion and more planarity of the porphyrin rings at low temperature. However, there is no observable change for the β-pyrrolic proton signals (doublet-doublet peaks, 9~10 ppm), which means that tautomerization

of the one free proton is unlikely.

2.4.5 General photophysical measurements

Steady-state absorption spectra of the products were measured in the UV-visible range on an HP Agilent UV-8453 Spectrophotometer. Emission spectra in visible-NIR range were obtained on a Horiba Fluorolog-3 spectrometer equipped with Time-Correlated Single Photon Counting (TCSPC) system for lifetime measurements. This is equipped with a NL-C2 Pulsed Diode Controller NanoLED, which produces picosecond and nanosecond optical pulses at a wide range of wavelengths from the ultraviolet to NIR. Long-pass filters were used properly according to the excitation and emission ranges.

2.4.6 NIR Emission quantum yield

The NIR quantum yields of **YbDD** were measured by comparison with the standard YbTPP(Tp) which was reported with a quantum yield of 3.2% in DCM with the excitation wavelength at 425 nm. The NIR emission quantum yield of YbDD was calculated by the following equation:

$$\Phi_s = \frac{G_s}{G_r}\left(\frac{\eta_s}{\eta_r}\right)^2\Phi_r \qquad\qquad (11)$$

The subscripts *r* and *s* represent the reference (r) and sample (s), respectively; Φ means quantum yield; *G* (gradient) is the slope of the plot: integrated emission intensity *vs* absorbance; η (refractive index) is the same here. All spectra were corrected for the wavelength sensitivity response of the instrument.

2.4.7 Singlet oxygen quantum yield measurements

Emission method in organic solvent (chloroform)

Singlet oxygen was quantified by measuring its phosphorescence intensity at around 1270 nm, and the quantum yield (Φ_Δ) of GdDD was measured by comparing the $^1O_2$ emission intensity of GdN and H_2TPP. Using the equation (11):

$$\Phi_\Delta^S = \Phi_\Delta^R \times \left(\frac{\eta^S}{\eta^R}\right)^2 \frac{I_\Delta^S}{I_\Delta^R} \times \frac{A^S}{A^R} \qquad (12)$$

The subscripts r and s represent the reference (r) and sample (s), respectively; Φ_Δ is the singlet oxygen quantum yield; I_Δ is the emission peak area of singlet oxygen at around 1270 nm; A represents the absorbance values for the analytes at 420 nm; η (refractive index) is the same here.

Absorption method in aqueous solvent (PBS buffer)

ABDA was mixed with a photosensitizer in PBS buffer and exposed to visible light (λ_{irr} = 400–700 nm) irradiation for singlet oxygen detection in aqueous solution by the absorption method. The concentration of the indicator ABDA was 200 μM and that of the photosensitizer was 10 μM which guaranteed that the generated singlet oxygen could be fully reacted and the indicator would not be completely consumed in the period of measurement time. The process of ABDA oxidation was monitored by the decrease of absorbance at 402 nm (one intense absorption peak). The absorbance spectra were recorded at different time points of light irradiation for calculating the rate of the photosensitizing process. Rose Bengal (RB) was used as a reference with a reported singlet oxygen quantum yield 75% in water. The singlet oxygen quantum yield of photosensitizer (Φ_{PS}) was calculated according to the following formula:

$$\Phi_{PS} = \Phi_{RB} \frac{K_{PS}}{K_{RB}} \qquad (13)$$

The subscripts PS and RB represent the target photosensitizer (PS) and the reference Rose Bengal (RB), respectively; K is the reaction rate of ABDA oxidized by the

photosensitizer which can be calculated by the slopes of plots (absorbance vs. time); Φ_{RB} is the singlet oxygen quantum yield.

2.4.8 Methodology of transient absorption spectroscopy

These related experiments were conducted by Dr. Partha Maity, Dr. George T. Harrison, Dr. Aram Amassian, and Prof. Omar F. Mohammed from the King Abdullah University of Science and Technology (KAUST) on their instrument. The samples were provided by our group. Prof. Wong, Gary Ka-Leung and I provided general guidance. Both institutes discussed the results and composed the relevant part in the manuscript.Helios spectrometers (Ultrafast systems, Florida, USA) were used to perform femtosecond transient absorption spectroscopy. The detailed experimental setup of the fs-TA in detail can be found in literature.[60] Briefly, a white-light continuum probe pulse was generated in a 2-mm-thick sapphire plate utilizing a small fraction of the fundamental output of a Ti: sapphire femtosecond regenerative amplifier which was operating at 800 nm with 35 fs pulses and a repetition rate of 1 kHz is operated by the setup. Pump pulses at 395 nm were formed in an optical parametric amplifier (Newport Spectra-Physics). In a 2-mm-thick cuvette cell containing the sample solutions, the pump and probe pulses were overlapped temporally and spatially. The probe light transmitted from the sample was gathered and focused on a broadband UV–Vis detector to observe the change in the absorbance (ΔA). The nanosecond TA spectroscopic measurements were also performed at 395 nm following laser pulse excitation. The ns-TA spectra were recorded using the pump-probe EOS setup (Ultrafast systems, Florida, USA), in which a standard probe beam is split into two: one travels through the sample, and the other one is sent directly to the reference spectrometer, which monitors the fluctuations in the probe beam intensity. The detailed experimental setup of the EOS can be found elsewhere.[61]

2.4.9 Cell culture

All cell culture-related experiments were practically conducted by the collaborative biology labs, while I provided general plans and spectated some experiments. Human cervical carcinoma HeLa cell (HeLa) lines were grown in Dulbecco's Modified Eagle Medium (DMEM). Human normal lung fibroblast (MRC-5) cell lines were grown in Minimum Essential Medium (MEM). Both media was supplemented with 10% fetal bovine serum, 1% penicillin and streptomycin, and 5% CO_2. The cell lines were incubated at 37 °C.

Chapter III "All-in-One" Double Chelator Complexes Achieving Multimodal Theranostics

3.1 Introduction

Researchers and doctors never stop exploring the "all-in-one" systems that can be applied to biomedical fields, and recently there is a mount of reports related to the those systems targeting cancer therapy.[62] The "all-in-one" system is one platform where individual constituents with unique functions are integrated and attain multifunctionality. The key reason why there is a rising demand for "all-in-one" systems is because two objectives can be achieved in such one molecule: to facilitate clearer imaging in diagnosis; and to produce synergistic therapeutic effects. Besides the constituents are usually readily available and have been approved effectively. An "all-in-one" system is always a multimodal theranostic agent in which its building blocks feature imaging capability and positive therapeutic effects.

Different molecular imaging techniques can be incorporated into "all-in-one" systems for the visualization of biological structures and the monitor of a biochemical process. Firstly, magnetic resonance imaging (MRI) is a powerful diagnostic technique that can be used to provide immense 3D contrasts of tissues and organs under skin covering. The administration of MRI contrast agents are necessary to improve diagnostic accuracy,[63] and Gd(III)-based MRI contrast agent together with other paramagnetic metal ions chelates are quite commonly used in ^1H T_1-weighted MRI.[64] Secondly, positron emission tomography (PET) imaging is more sensitive than most imaging techniques because it utilizes scintillators to capture emitted energy and generate signals.[65] In a PET process, a positron-emitting radionuclide is administrated to the

patient, and then those positrons become stable after the nuclear transmutation and the positron annihilation. Gallium-68 (^{68}Ga-isotope) is one common radiotracer for PET imaging with its moderate half-life of 68 minutes.[66] However, it has a major drawback that PET cannot provide anatomical information, so it is usually coupled with other imaging techniques, such as PET/MRI or PET/CT.[67] Thirdly, lanthanide luminescence shows its great potential for biomedical imaging and analyses.[68] emission from lanthanides mostly feature much longer lifetimes (0.5-10 millisecond) than those from common organic luminophores (1-100 nanosecond) so the time-resolved detection is available which improves the signal-to-noise ratio largely. Some lanthanides such as Yb(III) and Er(III) have strong emission in the second near-infrared window for biological tissue (NIR-II, 1000-1700 nm) which is suitable for the deep tissue in vivo imaging.

Porphyrins are widely considered to be used as biomedical agents mainly because of their aromatic macrocyclic structure. Having absorbed light, a porphyrin can hold the excitation energy on its triplet state after some initial energy transfer (internal conversion, fluorescence emission, and intersystem crossing). The relatively long lifetime of triplet states (micro to milli-seconds) allows porphyrins to: (1) transfer the energy to another acceptor; (2) undergo radiative decay in the form of phosphorescence; and (3) interact with surrounding molecular oxygen to generate reactive oxygen species.[69] The first two outcomings provide roots for imaging applications, and the last one endows porphyrins with photodynamic therapy potential. The central chelation of porphyrins with different metals expands their scopes in imaging techniques. For example, ^{67}Ga for single-photon emission computed tomography (SPECT), ^{68}Ga or ^{63}Zn for PET, and Gd(III) for MRI. Besides, by fully or partially changing the porphyrin

meso-substituents, it is easy to either alter the porphyrins' energy states and intrinsic optical properties; or linking porphyrin rings with other building blocks for the introduction of new functions or improving existing abilities.[70]

Although the field of porphyrin theranostics has been studied for many years, there still demonstrates the immense potential and remains one critical question – "Comparing with individual medicines, does it produce beneficial effects more efficiently by combing diagnosis and therapy modalities into one single-molecular system?" To answer this question and to explore better theranostic agents, we herein report a series of porphyrin-cyclen-based complexes. Either a rigid or a flexible linker is used to bridge two macrocycles. The porphyrin moiety is capable of chelating Zn(II), Ga(III), and the bridged DOTA-amide ligand can serve for Gd(III), Yb(III), or Eu(III). Different combinations of metals could provide the corresponding complexes with two different imaging abilities including MRI, PET, and NIR molecular imaging, while the complexes are preserving PDT effects by generating singlet oxygen.
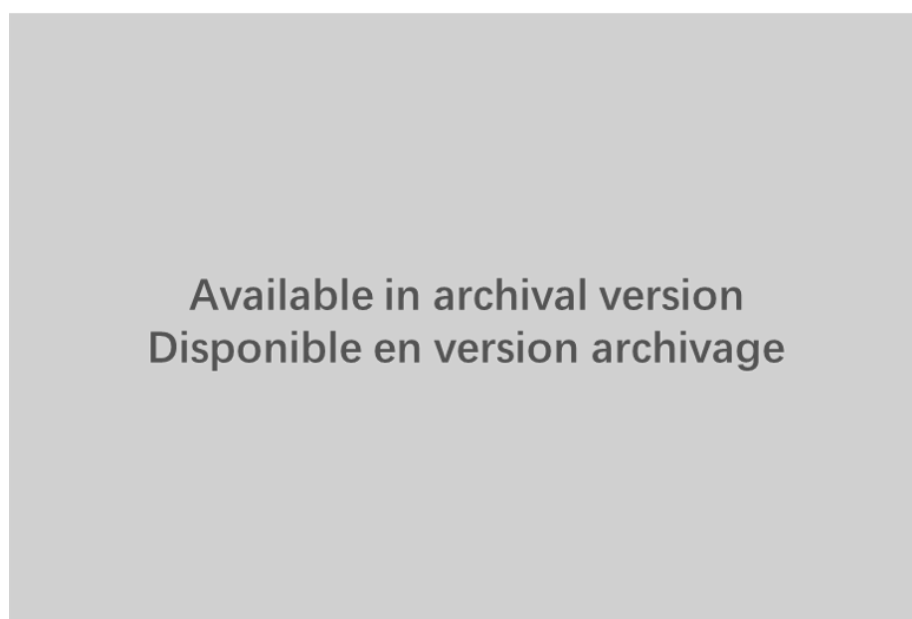
Figure 3.1. Molecular structures of the binuclear complexes studied in this work.

3.2 Results and Discussion

3.2.1 Steady-State absorption spectra

Absorption spectra were recorded as fundamental photophysical properties for this series of porphyrin-cyclen complexes. Absorbance was measured at five different concentrations (1, 2, 3, 4, 5 μM, except for PfLGd 1μM only) in water with 1% DMSO. DMSO was used to dissolve the compounds and to prepare the stock solutions because as an organic polar aprotic solvent, it shows amphiphilicity and can help the dissolution of small hydrophobic drug molecules. It is no or tolerable toxic effects to cell lines when DMSO concentration is smaller than 1% (v/v).[71] Plots were established for absorbance values and concentrations. According to the Beer-Lambert law, the relationship is supposed to follow the linearity at a low range (0.2-0.5). It was found that for my samples, all five curves fit with the linearity greatly with the absorbance up to 1, so they are not highly scattering.

Each porphyrinate complex features one strong Soret band (also called B band) corresponding to an $S_2 \leftarrow S_0$ transition with the maximum locating at around 420 nm. These most intense peaks all have large molar absorption coefficients ε around 10^5. Therefore, excitation light wavelength is chosen to be 420 nm for the ligands' best energy harvesting. There are four more absorption peaks (Q bands) found in the range 500-700 nm in absorption spectra of PLGd, PLYb, PfLGd, and PfLYb corresponding to the $S_1 \leftarrow S_0$ transition with much lower intensities. Only two bands could be found for zinc-coordinated complexes because the NH protons are replaced by zinc and no split happens on the original two Q bands. However, neither Q (0,0) band for zinc porphyrinate complexes nor Q_x (0,0) band for other porphyrinate complexes were

observed because the introduction of one substituent on the meso position resulted in the loss of D_{2h} symmetry.

Table 3.1. Summary of absorption spectra for the porphyrin-cyclen complexes.

Compound	Absorption peaks	Molar absorption coefficient (ε, $M^{-1} \cdot cm^{-1}$)
PLGd	408 nm (S band), 513 nm, 545 nm, 587 nm	166830
PLYb	417 nm (S band), 512 nm, 547 nm, 587 nm	123670
PZnLGd	420 nm (S band), 554 nm	199440
PZnLYb	422 nm (S band), 556 nm	108310
PfLGd	417 nm (S band), 512 nm, 546 nm, 589 nm	131140
PfLYb	419 nm (S band), 512 nm, 548 nm, 587 nm	118948
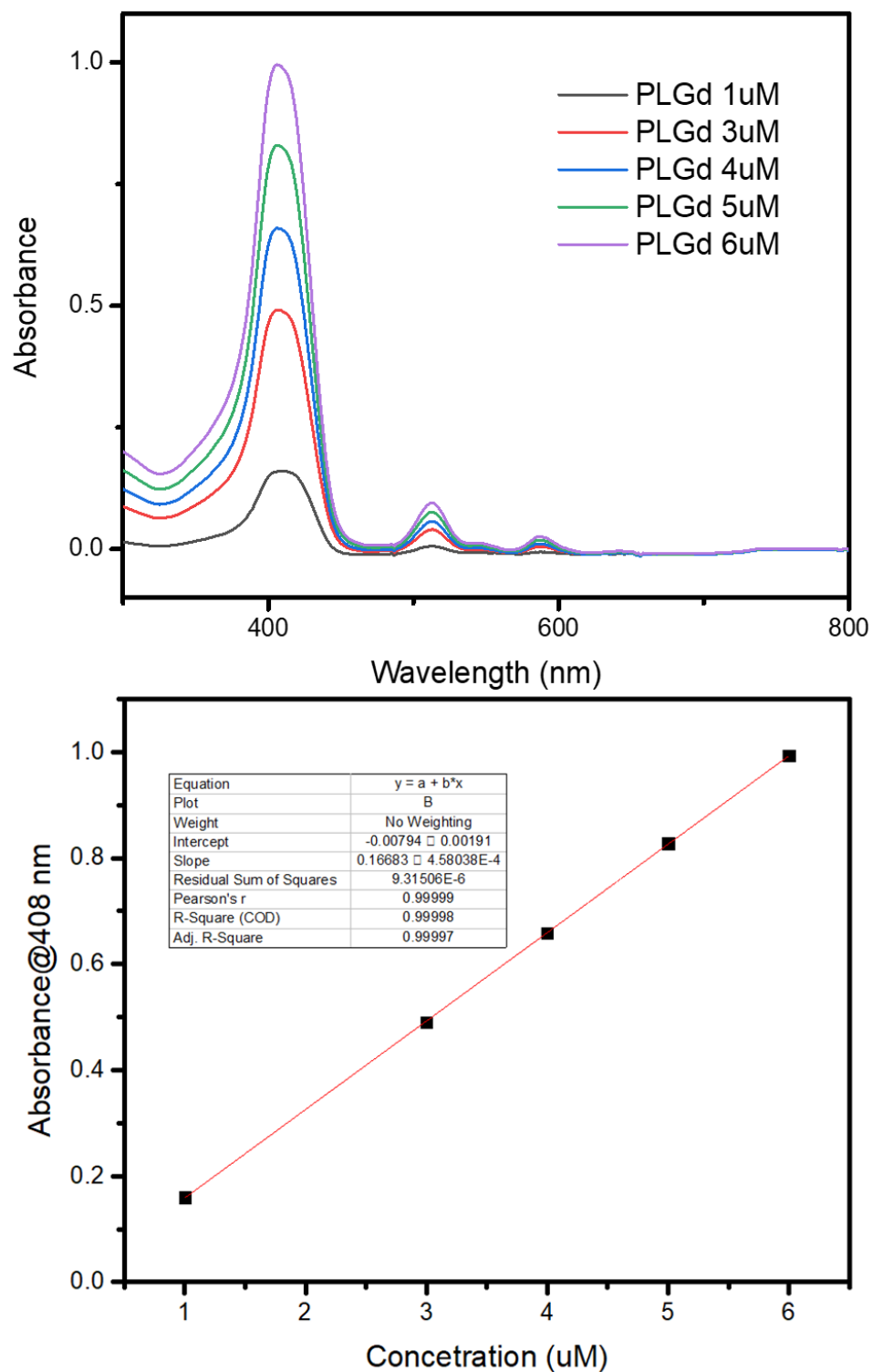
Figure 3.2. (*Top*) Absorption spectra of PLGd at different concentrations in aqueous solutions (1% DMSO). (*Bottom*) linear fitting for the maximal absorbance at 408 nm.
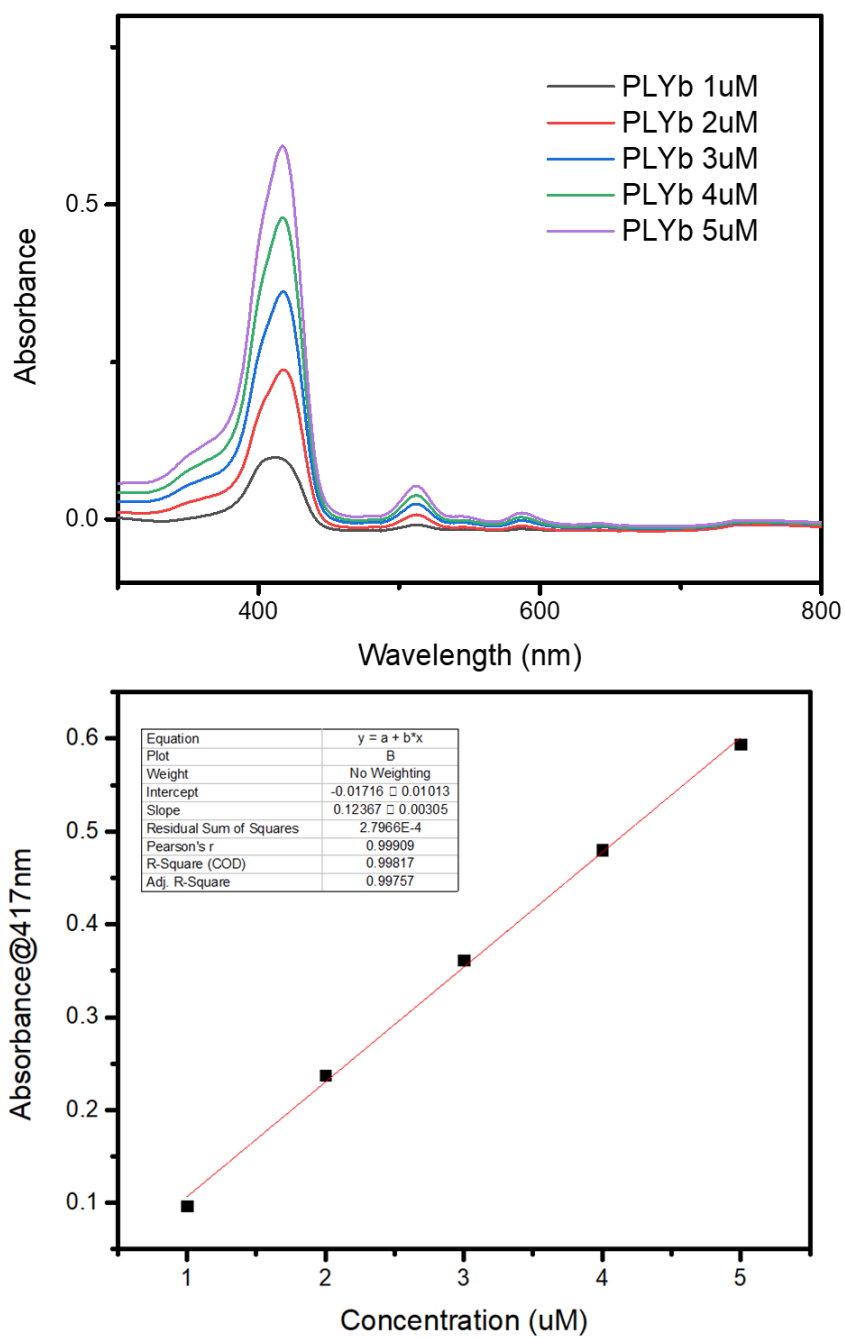
Figure 3.3. (*Top*) Absorption spectra of PLYb at different concentrations in aqueous solutions (1% DMSO). (*Bottom*) linear fitting for the maximal absorbance at 417 nm.
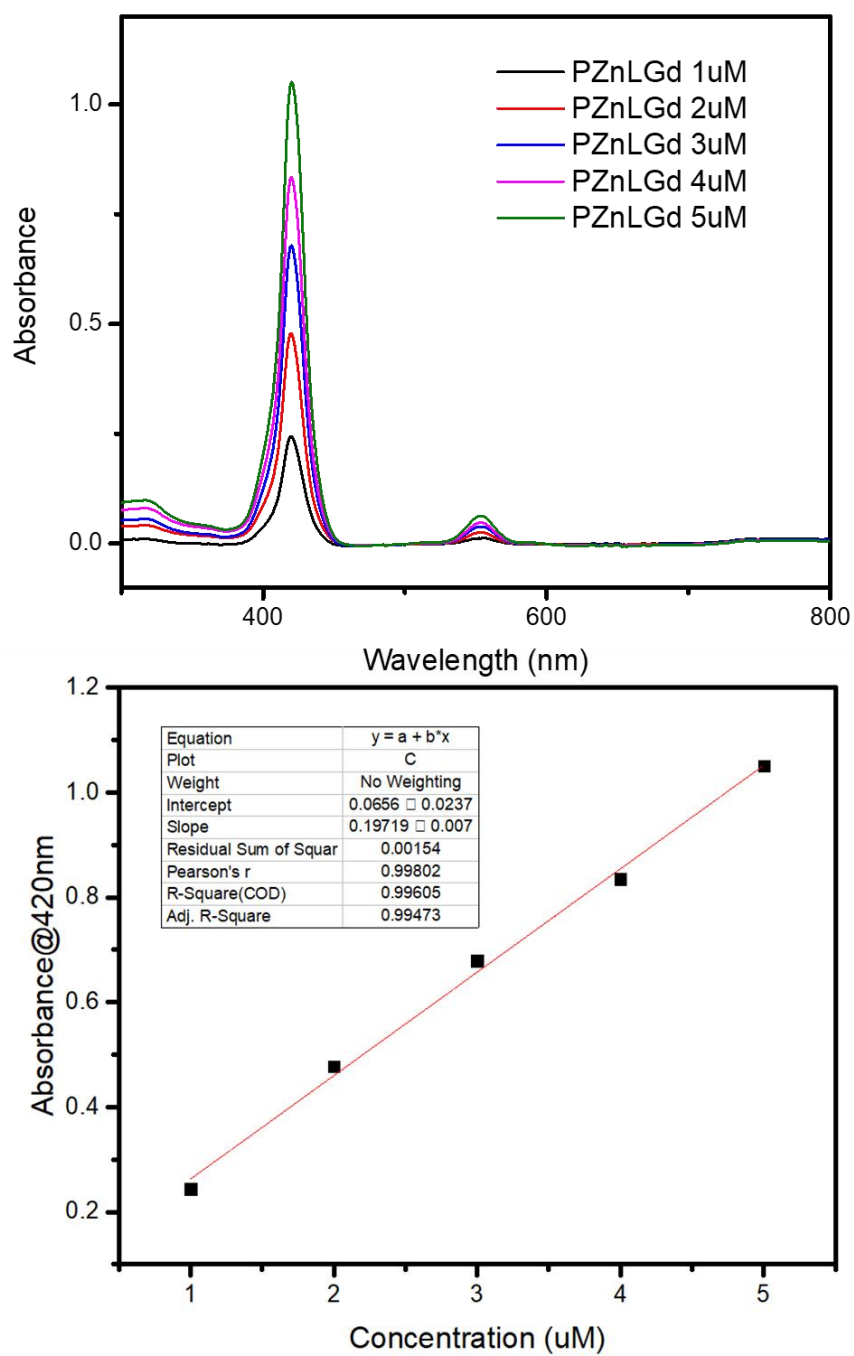
Figure 3.4. (*Top*) Absorption spectra of PZnLGd at different concentrations in aqueous solutions (1% DMSO). (*Bottom*) linear fitting for the maximal absorbance at 420 nm.
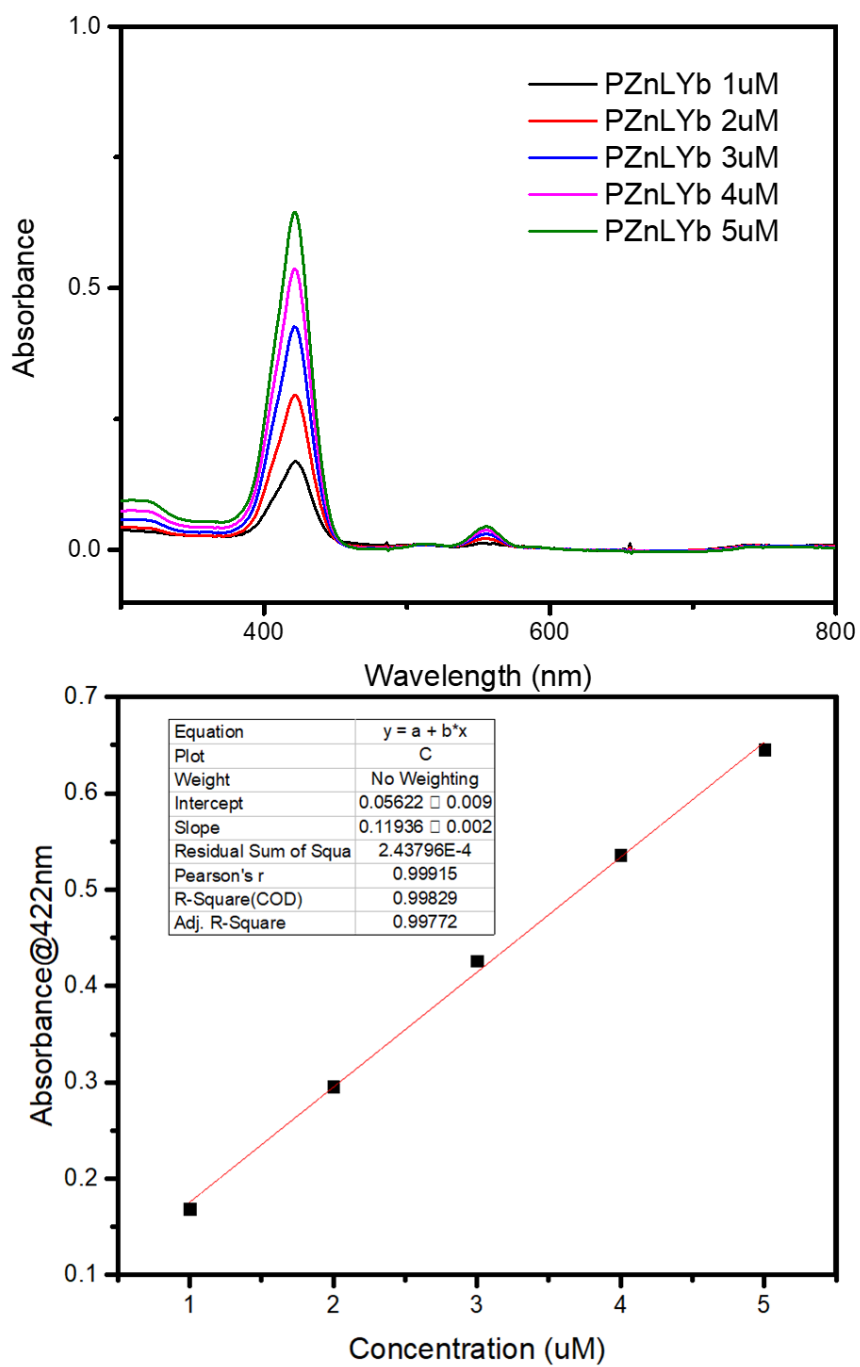
Figure 3.5. (*Top*) Absorption spectra of PZnLYb at different concentrations in aqueous

solutions (1% DMSO). (*Bottom*) linear fitting for the maximal absorbance at 422 nm.
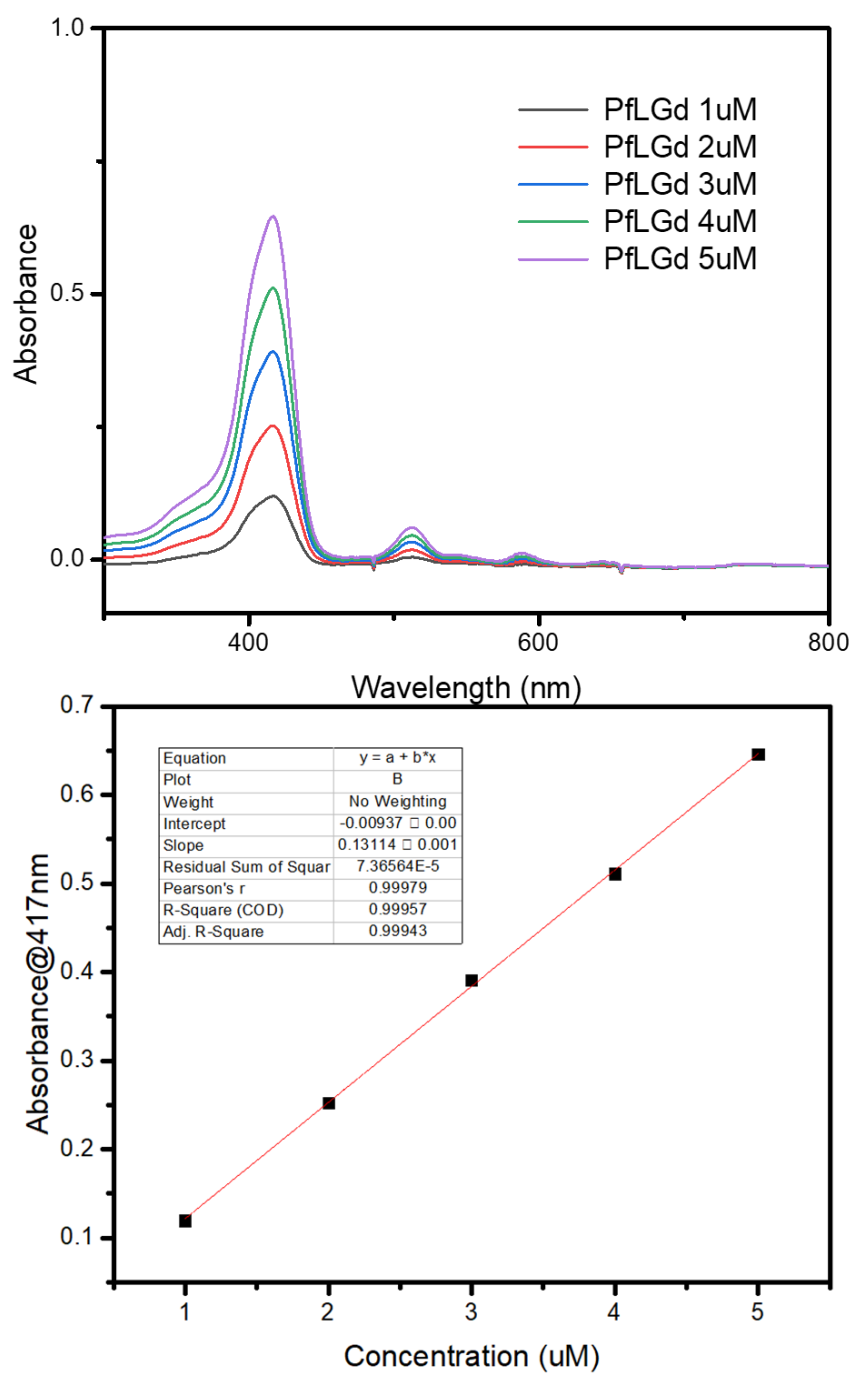
Figure 3.6. (*Top*) Absorption spectra of PfLGd at different concentrations in aqueous

solutions (1% DMSO). (*Bottom*) linear fitting for the maximal absorbance at 417 nm.
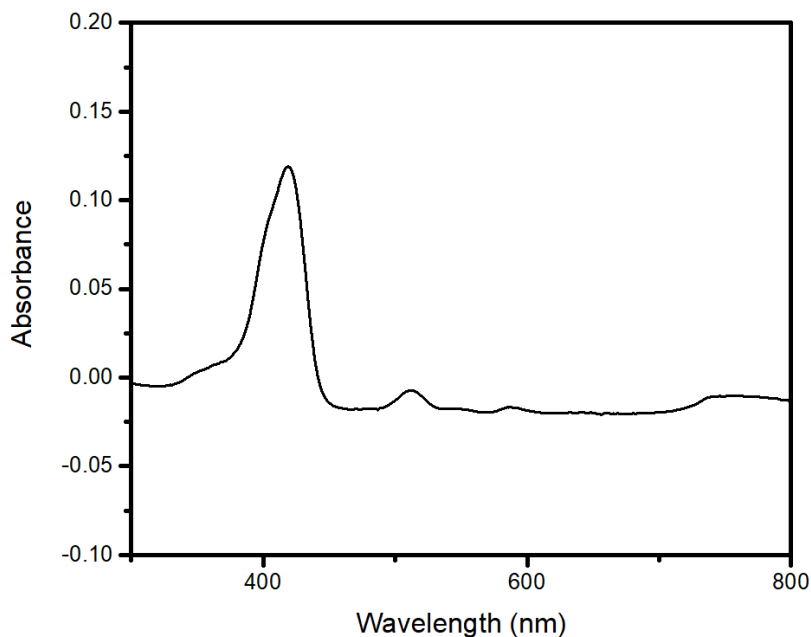
Figure 3.7. Absorption spectra of PfLYb at 1μM in aqueous solutions (1% DMSO).

3.2.2 Emission spectra

Although absorption spectra provide important evidence for the singlet excited state energy level of porphyrin rings in these complexes. Direct determination of excited-state energy transitions can be obtained from the emission spectra. More importantly, lanthanide luminescence can be observed from the emission spectra where characteristic lanthanide emission peaks are liable to be affected by the differences in the surrounding environment and energy transfers. In my cases, Eu(III) and Yb(III) emission could provide evidence in energy transfer pathways, but Gd(III) cannot emit because of its high excited energy states difficult to populate.

The room temperature emission spectra for three ligands (PL, PZnL, and PfL) were measured in both organic and aqueous solutions. The Gd(III) complexes were measured in chloroform. The ligands coordinated with either Gd(III) or Yb(III) were recorded at in water with 1% DMSO. The excitation wavelength was 420 nm where all samples

could be efficiently excited. Noteworthy, the spectra for Gd(III)-based complexes were recorded by a photomultiplier tube (PMT) system capable of measuring emission from 300 nm up to 1600 nm with proper correction. Common UV-visible spectrometers have the longest detection limit to around 800 nm while common NIR spectrometers give reliable results after 900 nm. However, it might be interesting to see porphyrin phosphorescence locating around 800 nm.[72, 73] There have been some studies on the room-temperature phosphorescence from lanthanide porphyrins and their applications in sensing.[74] Unfortunately, no emission was found in that range at room temperature, as expected that fast energy transfer from triplet states and possible quenching happened at room temperature. Low temperature (77 K) and time-resolved phosphorescence spectroscopy should be tried in the future. The spectra for Yb-based complexes were obtained from two different spectrometers either in the visible range or in NIR range because the latter spectrometer was more sensitive to NIR and provided clearer Yb(III) emission spectra.
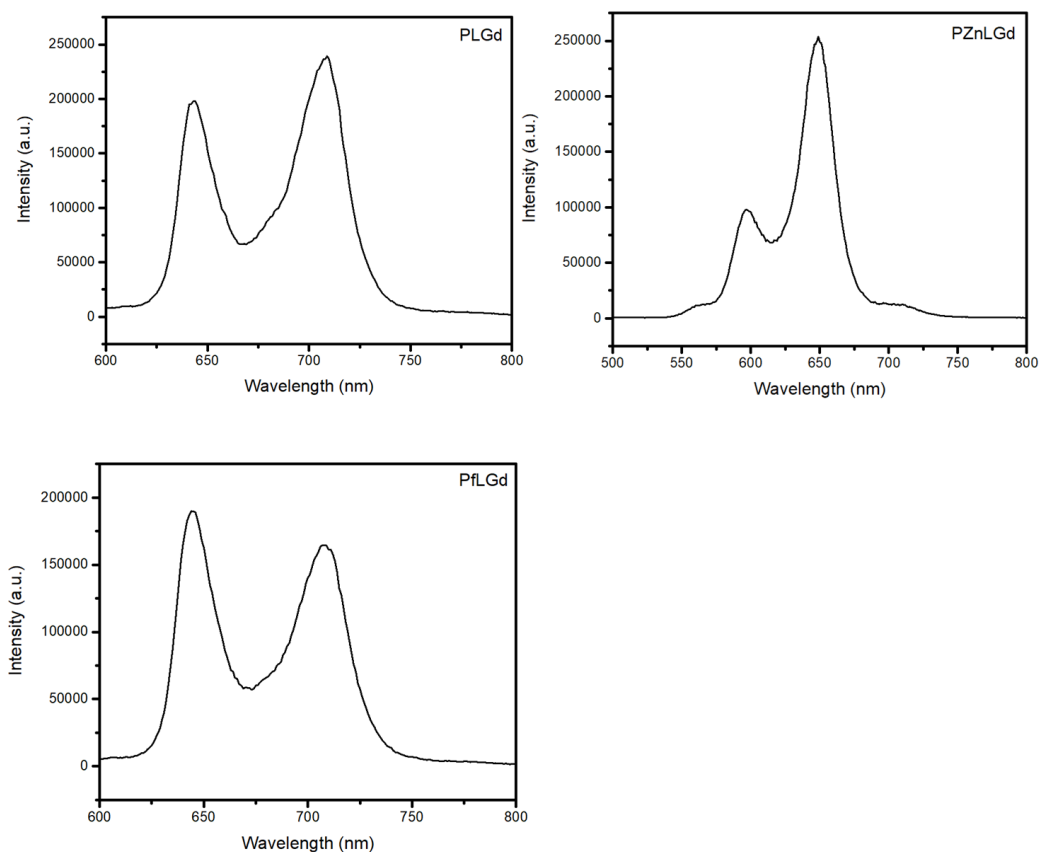
Figure 3.8. Emission spectra of PLGd, PZnLGd, and PfLGd in chloroform at 298 K (λ_{ex} = 420 nm, conc. = 1 μM).

All three complexes revealed strong emission in the visible range. Both PLGd and PfLGd had emission peaks located at 644 nm and 709 nm which corresponded to typical $S_1 \rightarrow S_0$ energy transitions in a free base porphyrin. As for PZnLGd, emission peaks for the same transitions were largely blue-shifted to 597 and 649 nm respectively. It is because that metalloporphyrins usually have a lifted lowest singlet excited state, S_1.
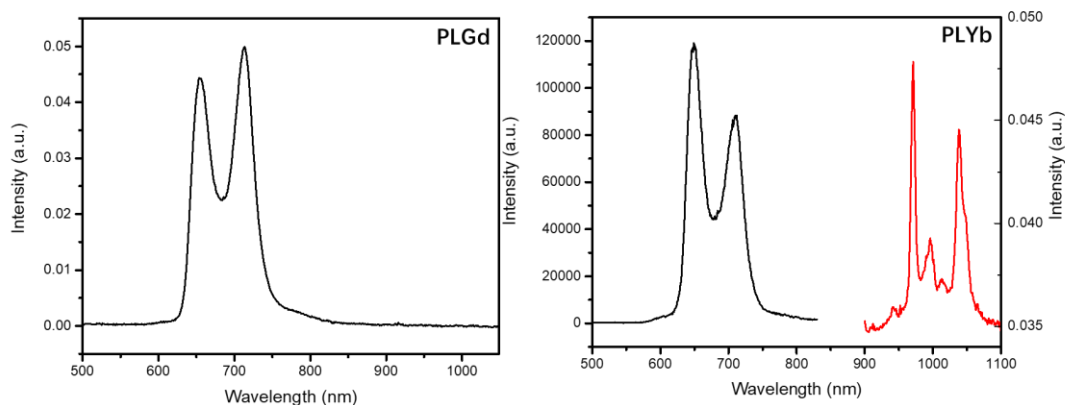
Figure 3.9. Emission spectra ($\lambda_{ex} = 420$ nm) of H_2O solution (1% DMSO) of PLGd and PLYb (conc. = 1 μM) at 298 K. The red part is enlarged in Yb(III) NIR emission range.

Both PLGd and PLYb had fluorescence from porphyrin moiety and the emission peaks were at 654 nm and 713 nm for PLGd (649 nm and 712 nm for PLYb). These two peaks are assigned to the $S_1 \rightarrow S_0$ energy transitions labeled as Q(0,0) for shorter wavelength and Q(0,1) for longer wavelength respectively. One difference is that for PLGd, Q(0,0) line was slightly weaker than Q(0,1) line but the reverse is true in PLYb where Q(0,0) line was stronger. As for NIR emission, two intense peaks were found at 971 nm and 1038 nm corresponding to two ytterbium $^2F_{5/2} \rightarrow {}^2F_{7/2}$ energy transitions. Noted that all three Yb-based samples were measured on the same conditions and at the same time, so it is reliable to compare the Yb emission from each. PLYb gave the strongest NIR emission which means that more efficient ED transitions happened through a rigid liner (PLYb vs. PfLYb) and free porphyrin rings had an optimal energy state for transition (PLYb vs. PZnLYb).
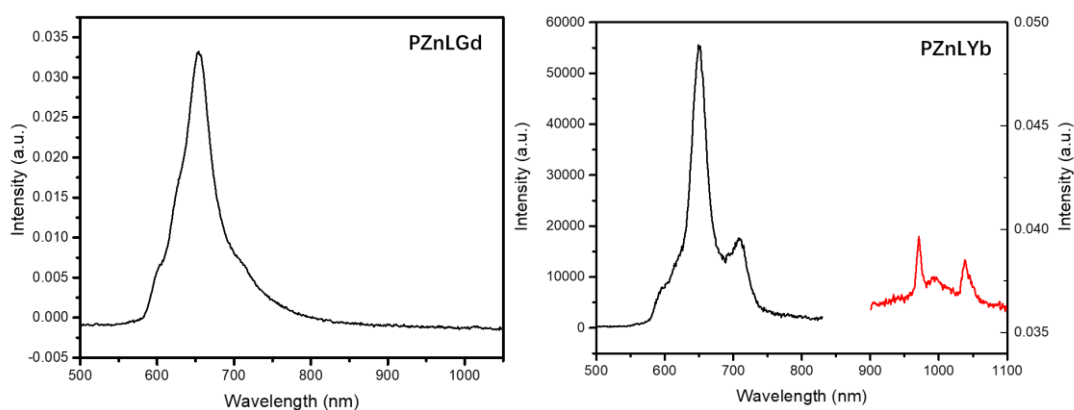
Figure 3.10. Emission spectra ($\lambda_{ex} = 420$ nm) of H_2O solution (1% DMSO) of PZnLGd and PZnLYb (conc. = 1 μM) at 298 K. The red part is enlarged in Yb(III) NIR emission range.

The shape of emission spectra for zinc-coordinated complexes was quite different. The most intense peaks found in both spectra (652 nm for PZnLGd, and 649 nm for PZnLYb) were assigned to Q(0,1) transitions, and they were highly preferred by energy transfer. The weaker peak in the blue area was assigned to Q(0,0) transitions. Both Q(0,0) and Q(0,1) emission peaks were blue-shifted comparing with those in PLLn which indicates that metalloporphyrin has a lifted lowest singlet excited state, S_1. There was one more emission peak found in the longer wavelength for each complex, located at 713 nm for PZnLGd and 709 nm for PZnLYb. It is confusing to see such a peak because it is seldom to have more energy transition pathways from porphyrin excited singlet states to their ground states. It is also noticeable that the position of these additional peaks was quite similar to Q(0,1) transitions of PLGd or PLYb. One possible reason could be the dissociation of the complex in the solution during measurements. The release of zinc left the resulting PLGd or PLYb which was emitting in the testing solutions. However,

the additional peak was not found in the PZnLGd emission spectrum done in chloroform (Figure 3.8).
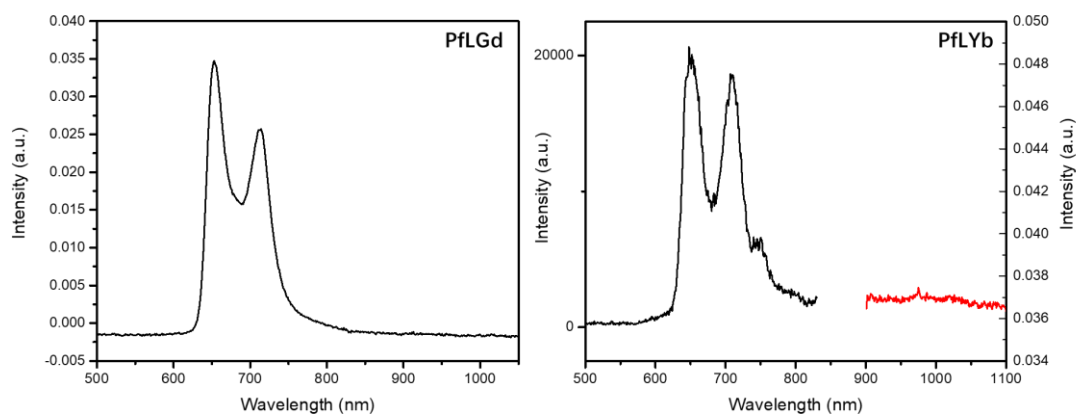
Figure 3.11. Emission spectra (λ_{ex} = 420 nm) of H_2O solution (1% DMSO) of PfLGd and PfLYb (conc. = 1 µM) at 298 K. The red part is enlarged in Yb(III) NIR emission range.

Both PfLGd and PfLYb featured two emission peaks located at 653 nm and 714 nm which are assigned to two $S_1 \rightarrow S_0$ energy transitions labeled as Q(0,0) and Q(0,1). Those are typical free porphyrin fluorescence and also observed in PLGd and PLYb. However, the fluorescence intensity of PLYb was much weaker than PLGd on the same conditions which suggest that more excitation energy underwent transitions from singlet states to triplet states. Although there was expected to have greater energy transfer from porphyrin triplet states to Yb(III) excited states as what was observed in the PLYb case, negligible Yb(III) emission was detected in the NIR range. The reason why no Yb(III) was found could because of the quenching of water molecules since the energy gap between the most populated excited state and ground state of Yb(III) is around 10200

cm^{-1} which is efficiently coupled with the third vibrational overtone of O-H oscillators (~3300-3500 cm^{-1}).[75]
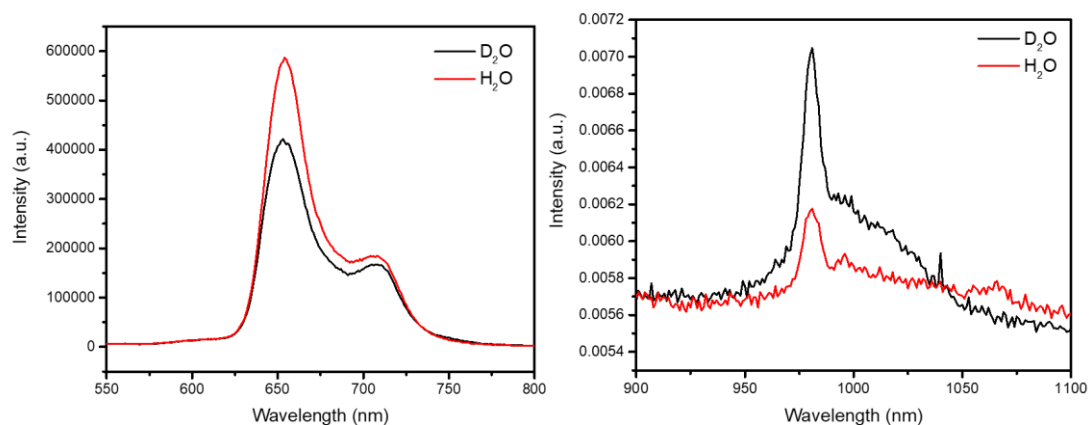
Figure 3.12. Emission spectra (λ_{ex} = 420 nm) of H_2O and D_2O (both 1% DMSO) solutions of PfLYb (conc. = 10 μM) within visible range (*left*) and NIR range (*right*) at 298 K.

To investigate the effect of O-H bonds on the energy transfer and luminescence from PfLYb. Emission spectra were measured in both H_2O and D_2O at the concentration of 20 μM for the sample. As for the fluorescence from porphyrin singlet states, it was seen that the emission at 654 nm was weaker in D_2O than in H_2O which suggested that O-D oscillators might interfere Q(0,0) labeled $S_1 \leftarrow S_0$ energy transition. Yb(III) emission at 981 nm was much stronger in D_2O than in H_2O which was consistent with our hypothesis.
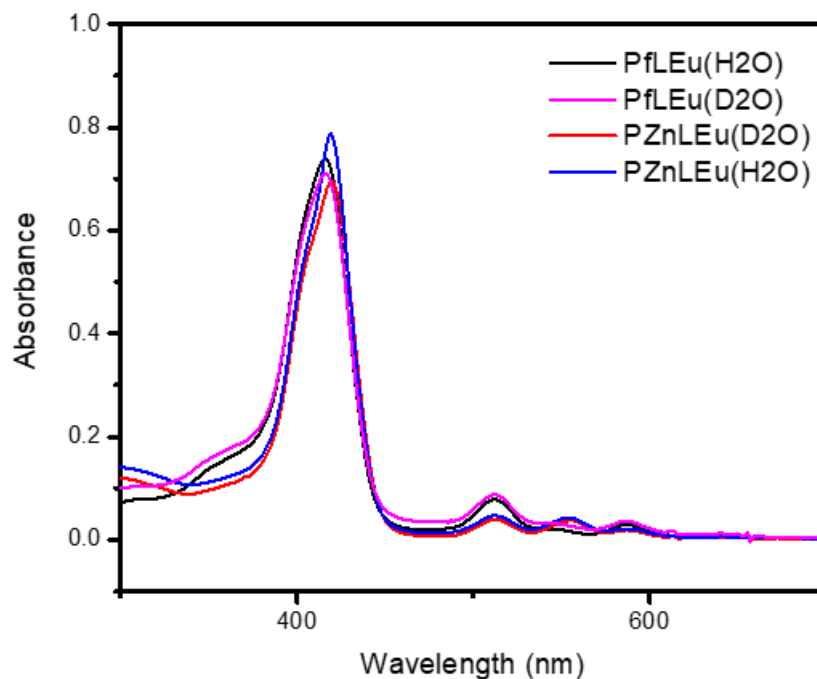
Figure 3.13. Absorption spectra of H_2O and D_2O (both 1% DMSO) solutions of PfLEu and PZnLEu (conc. = 10 μM) at 298 K.

Europium(III) coordinated complexes (PfLEu and PZnLEu) were prepared to determine the q-value for this series of complexes. Q-value describes the number of water molecules bound to the metal center of the lanthanide complex. It is usually determined by measuring the lifetime difference in water and deuterium water because deuterium water is considered to have little quenching on the luminescence. The equation for calculating q-values is:

$$q = A \times (\frac{1}{\tau_{H2O}} - \frac{1}{\tau_{D2O}})$$ *(14)*

A is empirical parameters, and different for different lanthanides.

Both PfLEu and PZnLEu had a strong Soret band at around 420 nm in absorption spectra. Noteworthy, PZnLEu showed one extra absorption peak at 355 nm which was originated from the rigid linker. The linker consists of large unsaturated structures and

91

can sensitize Eu(III) directly.[76] Upon excitation at 420 nm, there was no obvious Eu(III) emission found in the 500-800 nm range but strong porphyrin fluorescence. When exciting PZnLEu with 355 nm light, porphyrin was not effectively excited and weak Eu(III) emission was observed at 612 nm. The lifetimes for PZnLEu at 612 nm were measured to be 1.63 ms in D_2O and 0.56 ms in H_2O respectively. Therefore the q value was calculated to be 1.12 by applying the reported parameters.[75] It proved that approximately one water molecule bound to the metal center of the cyclen part and quenches the luminescence in PZnLLn and possibly PLLn (Ln=Yb, Eu). Although no Eu(III) emission was found from PfLEu and no luminescence lifetime could be measured, it is believed that more water molecules bound to the lanthanide because the number of coordination positions for PfLLn is one fewer than PZnLLn or PLLn (Figure 3.1).

3.2.3 MRI T_1 relaxivity

One imaging function for my "all-in-one" chelators is their potential as MRI contrast agents when coordinating with Gd(III) ions. Although its water exchange rate is not great as DOTA,[77] the (N-methyl)amide substituted cyclen ring is still an ideal ligand for Gd(III). All prepared Gd(III)-based complexes were undergone in vitro relaxivity measurements to investigate what factors contribute to the relaxation rate of water molecules and look for the best theranostic agents among them.

Four samples were measured and GdDOTA was used as a reference sample. According to Figure 3.14 and Table 3.2, PLGd revealed the highest relaxivity value, $r_1 = 7.86$ mM^{-1}s^{-1}, which is much higher than that of GdDOTA (5.44 mM^{-1}s^{-1} at 25°C). It is the same trend at 37°C where PLGd was 5.08 mM^{-1}s^{-1} and GdDOTA was 3.22 mM^{-1}s^{-1} (see

appendix Figure 5.28.). The r_1 values for GdDOTA were similar to the literature value,[78] and it proved that our testing conditions and parameters were qualified. The major reason why PLGd featured such great relaxivity is that both its molecular weight and size are larger than GdDOTA so the molecular motion for PLGd was decelerated and the effective correlation time was longer which resulted in an increased relaxivity. By comparing PLGd and PfLGd, the latter one with much lower r_1, it was found that the linker flexibility dramatically affected the motion of molecules – the flexible linker made the Gd(III) moiety tumble fast and difficult to bound water molecules, even though PfLGd could have been more promising because of more binding positions for water molecules ($q \geq 2$). It is worth noting that even if PfLGd showed great relaxivity, it would be cautious to use it as an MRI GBCA since fewer chelating positions from the ligand could result in lower complex stability and possible toxicity.

PZnLGd with different cations (-OTf, trifluoromethanesulfonate group, and -Cl, chloride) were also measured on the same conditions. Various anions are presenting in the physiological conditions that could affect the motion (and subsequently the relaxivity) of the Gd(III) complexes. Trifluoromethanesulfonate group, although not abundant in biological tissues, was chosen as a coordinating anion to compare with chloride and see if the size of coordinating groups on Zn(II) can affect the overall relaxivity. Two Zn(II)-Gd(III)-complexes exhibited similar T_1 relaxivities (less than 10% difference), suggesting the sizes of Zn(II) coordinating groups only slightly contributed to the relaxivity. However, it should be emphasized that although the size did not affect, the presence of additional coordination on the porphyrin metal core has already severely decreased the relaxivity. Both relaxivities for PZnLGd-OTf and PZnLGd-Cl (4.16 mM^{-1}s^{-1} and 3.77 mM^{-1}s^{-1} respectively) were much lower than PLGd, even GdDOTA. The

same trend was also found at 37 °C (Figure 3.14). Unfortunately, there is no report summarizing the effects of neighboring metal on Gd(III) T_1 relaxivity, and it is always difficult to predict and control the relationship between molecular motion and its relaxivity. It should be noted that although there were some Zn(II)-Porphyrin-Gd(III)-DOTA complexes reported to have increased T1 relaxivity,[79] the reasons behind were found to be the stacking of the neutral metalloporphyrins and the resulting aggregation of their amphiphilic complexes (hydrophobic porphyrin and hydrophilic GdDOTA derivatives). Our PZnLGd did not show the same trend because the rigid and short linker is not suitable for the formation of micelles. Besides, high relaxivities originated from aggregation or locally high concentrations are not intrinsic improvement in GBCAs and not practical in clinical applications.

The relaxation rate of the promising PET/MRI dual-imaging agent, PGaLGd, was also measured at lower concentrations (Appendix Figure 5.29). Surprisingly, unlike the other metalloporphyrinate PZnLGd, PGaLGd revealed the highest T_1 relaxivity among all prepared Gd(III)-complexes (10.37 mM^{-1}s^{-1}). This phenomenon could be attributed to the major difference between PGaLGd and PZnLGd in which they have different metal coordinated on the porphyrin rings. Zn(II) ion has only two positive charges which are perfectly balanced by the porphyrin, whereas Ga(III) requires an additional ligand (acetate in this case). It has been reported that the carboxylate could attract additional water molecules and enhance the 2nd sphere effects where the effective molecular weight will be larger and the 2nd sphere water molecules are easier to be relaxed.[80]
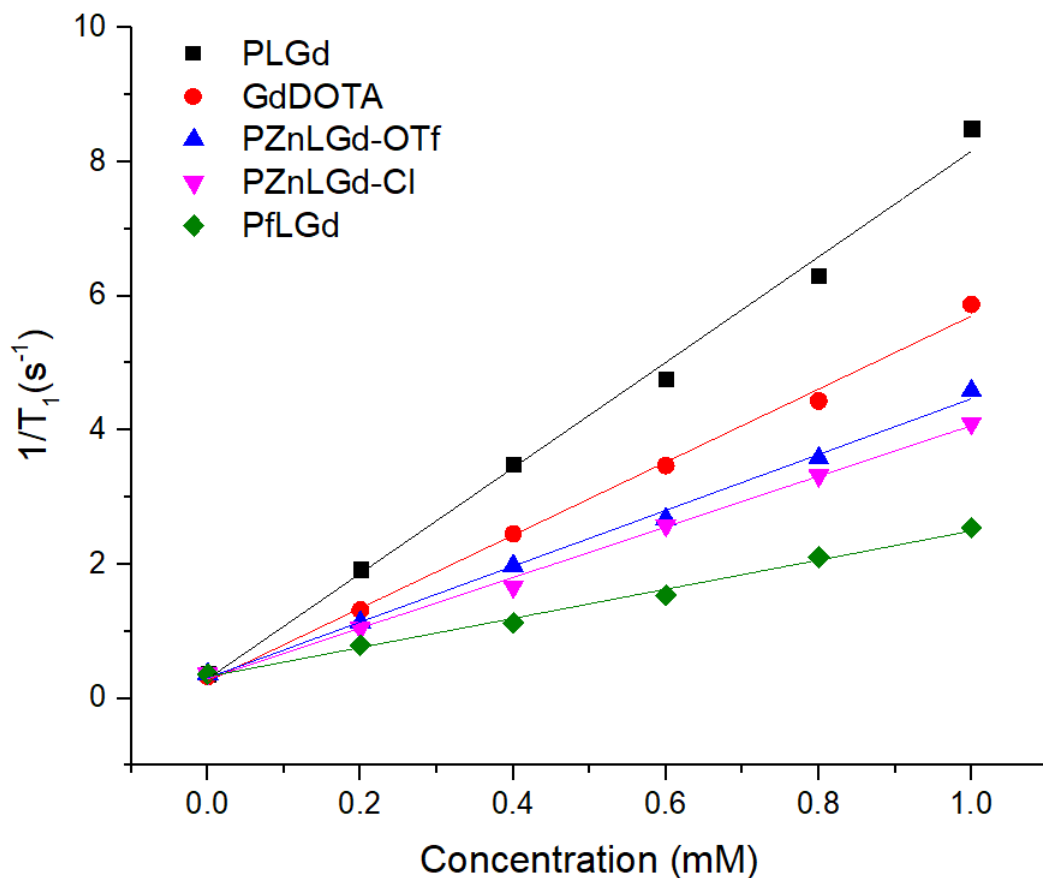
Figure 3.14. Relaxation rates $1/T_1$ vs. sample concentrations for the prepared complexes (3 Tesla, 25 ºC).

Table 3.2. Parameters for all curves in figure 3.14. The slopes equal to the T_1 relaxivity (r_1) values.

	Slope (Relaxivity, r_1, mM^{-1}s^{-1})	Adj. R-Square
PLGd	7.86314	0.9924
Gd-DOTA	5.44181	0.99583
PZnLGd-TfO	4.1599	0.9962
PZnLGd-Cl	3.77227	0.99673
PflGd	2.17157	0.99201
PGaLGd	10.37058	0.95334

3.2.4 Singlet oxygen

The PDT capability of the Gd(III)-complexes was evaluated by measuring the phosphorescence of the generated singlet oxygen. Singlet oxygen is an active species that can rapidly destroy biomolecules and kill cells. Therefore, if a photosensitizer can produce more singlet oxygen during short light irradiation, it means the photosensitizer has better PDT effects. The amount of singlet oxygen formed was determined by its phosphoresce intensity. The samples were prepared in chloroform at the same concentration, except for PGaLGd dissolved by DMSO before dilution. The $^1O_2$ phosphorescence emission peak was located at 1270 nm (Figure 3.15). The integrated areas for the emission peaks are proportional to the amount of singlet oxygen produced. Tetraphenylporphyrin, a classical photosensitizer, was chosen as the standard with its singlet oxygen quantum yield as 0.55 reported in literature.[81] The quantum yields for all samples in this work can be determined by comparing the emission peaks integrated area with the one for H$_2$TPP. Most complexes showed superior singlet oxygen quantum yields over H$_2$TPP (PLGd: 0.87, PZnLGd: 0.86, PfLGd: 0.84). The major reason for the improved PDT effect is because meso-tri(pentafluorophenyl)porphyrin was used instead of phenyl porphyrin, and its triplet-state is higher, resulting in a more efficient sensitization of oxygen.[82] All samples have the same porphyrin structure, so they gave the similar values. However, PGaLGd showed inferior performance ($^1O_2$ quantum yield = 0.47). This could be due to the fact that the coordinated Ga(III) made the complex too polar to well dispersed in chloroform, but it is promising for PGaLGd exhibiting great PDT effect in polar solvents, such as water.
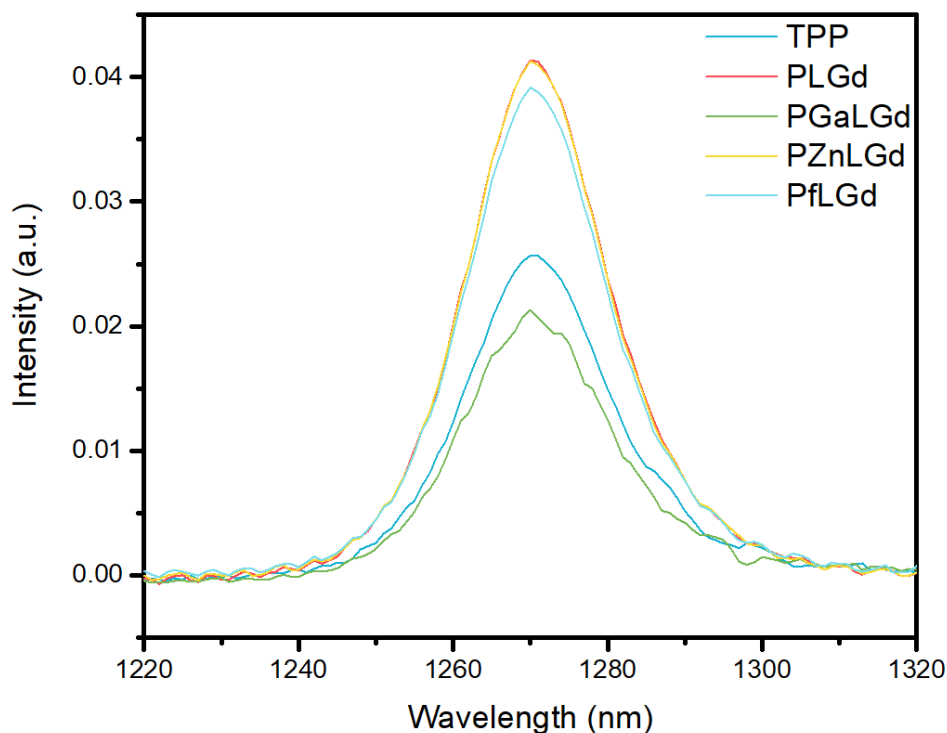
Figure 3.15. Emission spectra of the $^1O_2$ NIR phosphorescence generated by different complexes in chloroform (PGaLGd with extra 1% v/v DMSO) at 298 K (λ_{ex} = 420 nm, conc. = 5 μM) . Tetraphenylporphyrin H$_2$TPP was used as a standard sample.

3.2.5 PET cold labeling

[68]Gallium has been widely used in radiopharmaceutical research because it is relatively cost-effective in production and easy to coordinate with host molecules or vectors. Comparing with other radionuclides, ^{68}Ga can be prepared in an automated generator. Its short half-life time results in shorter examination time and effective does, although it hampers the application in medical dosimetry. Porphyrins are a group of promising chelator and their chelation with Ga(III) can be achieved under microwave heating quickly. Therefore, microwave-assisted cold labeling of Ga(III) on the as-synthesized PLGd was conducted to optimize the reaction conditions for future hot-labeling experiments, and the prepared complexes, PGaLGd, containing abundant gallium ([69]Ga or [71]Ga) were tested for their PDT and MRI abilities. After microwave reaction, the

97

crude products were purified either by solid-phase extraction (SPE) with special cartridges or on a preparative HPLC system. The former one was practicable in hot-labeling preparation and the latter one was to obtain the products with high purity for other tests. The ^{68}Ga hot-labeling and the PET imaging will be performed in a collaborative lab with isotope generators and PET scanning instrumentation.

3.3 Conclusion

A series of porphyrin-cyclen-based lanthanide complexes have been designed and synthesized. Different metal ions could be coordinated to achieve different imaging purposes. It was found that the complexes with a rigid linker connecting two macrocycles possess NIR luminescence, which guaranteed NIR cell imaging experiments could be conducted in the future by using them, in addition to other biological tests. Meanwhile, PLGd and PGaLGd exhibited high T_1 relaxivity, resulting from their increased molecular weights and possible second-sphere effects. Their PDT capability was evaluated by measuring their singlet oxygen quantum yields and most of them outperformed tetraphenylporphyrin, a conventional photosensitizer. Synergistic effects can be achieved by integrating diagnostic and therapeutic moieties, although in this work the ligand (PfLLn) with a flexible linker did not show better performance in imaging. Cold-labeling of Gallium(III) was successful and it is promising to see the PET functions of these compounds on animal models soon.

3.4 Experimental

3.4.1 Synthetic procedures

Scheme 2. The synthetic route for PZnLGd.

Available in archival version
Disponible en version archivage

Scheme 3. The synthetic route for PfLGd.

Synthesis of ██ **(Por)**

██

██

██

██

██

██

████████████████████████████████ Having removed solvents by reduced pressure distillation, the crude products were purified by column chromatography with the mobile phase (DCM: Hexane=1:6). The preparation of porphyrin moiety followed general procedures where the yield was quite low (5~10%) and the formation of side products could be hardly avoided. ^{1}HNMR (400 MHz, Chloroform-d) δ ████████████████████████████████

████████████████████████████████

Synthesis of ███

███████████████
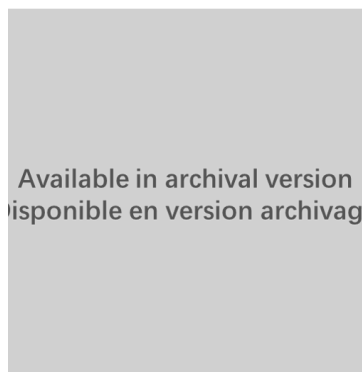
0.63 mmol zinc acetate (0.138 g) and 0.06 mmol Por (61 mg) was added into 100 ml DCM. The solution was stirred at room temperature for 4 hours. The crude product was purified on a silica column by eluting with 100% DCM. ^{1}H NMR (400 MHz, Chloroform-d) δ ██

██

Synthesis of ███████████████████████████████████████

██

██

██

██

██

███████████████████████████ This solution was stirred without external heating for 15 hours on an inert condition. After the completion of the reaction, the solution was extracted with water, and the organic phase was dried with anhydrous Na_2SO_4. The solvent was removed and the crude was isolated by column chromatography on a silica

gel column with methanol/DCM = 1:20 as eluent. The desired product was yellow solids. 1H NMR (400 MHz, Chloroform-d) δ ██████████████████████████████

███████████████████

Synthesis of ████████████████████████

██

██

███████████████████████ The solution was stirred at room temperature for 1 hour. After the completion of the reaction, the solution was extracted with water, and the organic phase was dried with anhydrous Na_2SO_4. The solvent was removed and the crude was isolated by column chromatography on a silica gel column with hexane/ethyl acetate = 2:1 as eluent. The desired product was yellow solids. 1H NMR (400 MHz, Chloroform-d) δ ██

████████████

Synthesis of PZnPy

██

██ Nitrogen gas was

bubbled into the solution for 30 min, followed by the addition of excessive DIPEA The reaction was stirred and heated at 65°C overnight under nitrogen protection. After completing the reaction, column chromatography was used to purify the crude product with DCM: MeOH = 20:1. 1H NMR (400 MHz, Methanol-d4) δ ███████████

██

██ MALDI-TOF

MS ([M]⁺, m/z): Calcd. for ████████████████████████

Synthesis of PZnL

Available in archival version
Disponible en version archivage

██

██

██

████████████████ The solution was stirred at room temperature for 30 min. After the completion of the reaction, the solvent was removed by reduced vacuum distillation. A small amount of DCM was added to dissolve and extracted with water. After collecting and drying the organic phase, PZnOMS was obtained. It was then dissolved in 50 ml acetone followed by the addition of ████████████████████ The reaction was heated at 65°C for 1 hour. After the reaction was completed, the solvent was removed and the crude was purified by column chromatography with the eluate EA:Hexane = 1:4. The purified intermediate was then dissolved in 100 ml acetonitrile (ACN) followed by the

addition of 1.0 mmol K_2CO_3 (139.5 mg) and 0.5 mmol pre-synthesized ███████ ██ (ligand L, 256 mg). The solution was heated at 65 $^\circ$C for two days. When the reaction was completed, the solvent was removed and the crude product was purified on a silica column with DCM:MeOH = 10:1. MALDI-TOF MS analysis ($[M+Na]^+$, m/z): Calcd. For ███████████████████████████████████████

Synthesis of PZnLGd

Available in archival version
Disponible en version archivage

██

██
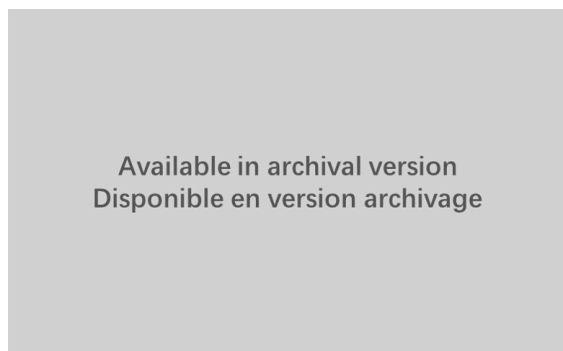
███████████████████████ The mixture was stirred at 80°C for 2 days. The product was purified by preparative liquid chromatography (mobile phase is ACN and Milli-Q water with 0.1%TFA). ESI-HRMS analysis ($[M]^{3+}$, m/z): Calcd. For ██████████████████████████████████

Synthesis of PLGd

Available in archival version
Disponible en version archivage

██
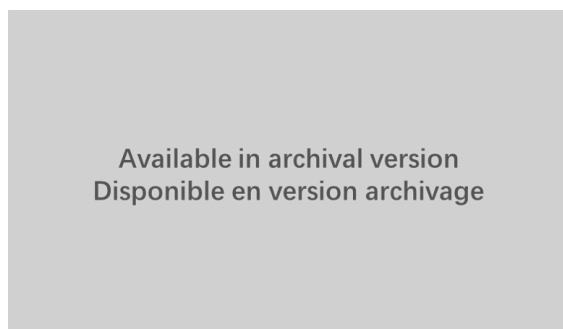
███ was

dissolved into a 10 mL mixed solvents (TFA:DCM = 1:1 v/v). The solutions was stirred

at room temperature for one hour. After removing the solvents, the crude product was

purified by a silica column with eluates MeOH:DCM = 1:20. Final product ESI-HRMS

analysis ($[M]^{3+}$, m/z): calcd. For █████████████████████████

██████████████████

Synthesis of ████████████████████████████████

Available in archival version
Disponible en version archivage

This product was synthesized according to the literature.[83]

^{1}H NMR (400 MHz, Chloroform-d) δ ████████████████████

██

Synthesis of Pf

Available in archival version
Disponible en version archivage

██

████████████████████████████ was dissolved in 50ml DMF, followed by the

dropwise addition of ████████████████████████████████████ After the reaction having completed, the solvent was removed by reduced pressure distillation, and the crude product was purified by column chromatography (DCM: Hexane = 1: 2). Yield: 1.0g, 90.5%. ^{1}H NMR (400 MHz, Chloroform-d) δ ██████████████

██

██████████████████████████████████████

Synthesis of PfL

Available in archival version
Disponible en version archivage

██

████████████████████████████████████ were dissolved in 100 ml ACN under nitrogen protection. The mixture was reacted at 80 °C for 12 hours. After the reaction completed, the solvent was removed by reduced pressure distillation, and the crude material was purified by column chromatography (DCM: MeOH = 10: 1). Yield: 161.9 mg, 56.3%. ESI MS ([M]$^+$, m/z): Calcd. for █████████████████

██████████████████████

Synthesis of PfLGd

███

███

██ The mixture was heated and stirred at 80 °C for 48 hours. After the reaction was completed, the solvent was removed by reduced pressure distillation, and the crude material was purified by Preparative-HPLC (mobile phase). Yield: 90.6 mg, 81.2%. ESI MS ($[M]^+$, m/z): calcd. for ████████████████████████████

████████████████

Synthesis of PGaLGd

███

███

██████████████ The reaction was performed in a specific reacting microwave oven equipped with a refluxing tube. The reacting power was set as ████████████████

██. After the reaction was completed, the reaction was cooled for 10 min and diluted with DI water. The solution was purified by using solid-phase extraction (SPE) columns

██

██ The solvents were removed under

a reduced pressure. Further analysis could be performed by dissolved it in DMSO firstly

and then to a stock solution. ESI MS ([M+COOCH$_3$]$^+$, m/z): calcd. for

██

3.4.2 HPLC characterization of products

Table 3.4. Solvent system for preparative HPLC. Flow rate: 1 mL/min.

Time (min)	Milli-Q water (%)	ACN with 0.1% TFA (%)
0	70	30
30	0	100
35	0	100
37	70	30

3.4.3 Photophysical Properties Measurements

UV–visible absorption spectra in the spectral range 200–1100 nm were recorded on an

HP Agilent UV-8453 spectrophotometer. The emission spectra were measured with a

Horiba Fluorolog-3 spectrophotometer equipped with a 450 W xenon lamp; or with a

Horiba iHR550 imaging spectrometer equipped with Hamamatsu near-infrared

photomultiplier tubes R5509-43 equipped and Hamamatsu C9940 series cooler.

Luminescence decay lifetime measurements were recorded on a Horiba Fluorolog-3

spectrophotometer with a NanoLED as the pulsed excitation source. Long-pass filters

were used properly according to the excitation and emission ranges.

3.4.4 T1 relaxivity measurements

In vitro T_1-weighted MR relaxivity for all complexes was measured on a 60 MHz (1.41 Tesla)-scanner MRI instrument (magritek Spinsolve^{TM} 60). T_1 relaxation rates (1/T_1) with different Gd(III) concentrations were obtained. All samples were dissolved in H_2O with 5% DMSO.

3.4.5 Singlet oxygen quantum yields determination

Emission method in organic solvent (chloroform)

Singlet oxygen phosphorescence was measured at its typical position of 1270 nm by using the Fluorolog-3 TCSPC (HORIBA) luminescence spectrometer. The singlet oxygen quantum yield (Φ_Δ) of the Gd(III) complexes in $CHCl_3$ were determined through the comparison of the $^1O_2$ emission intensity of H_2TPP and a reference material (H_2TPP, Φ_Δ = 0.55 in $CHCl_3$) as illustrated in equation (11) also presented in the previous chapter:

$$\Phi_\Delta^S = \Phi_\Delta^R \times \left(\frac{n^S}{n^R}\right)^2 \frac{I_\Delta^S}{I_\Delta^R} \times \frac{A^S}{A^R} \qquad (12)$$

The subscripts *r* and *s* represent the reference (r) and sample (s), respectively; Φ_Δ is the singlet oxygen quantum yield; I_Δ is the emission peak area of singlet oxygen at around 1270 nm; *A* represents the absorbance values for the analytes at 420 nm; η (refractive index) is the same here.

Absorption method in aqueous solvent (PBS buffer)

ABDA was mixed with a photosensitizer in PBS buffer and exposed to visible light irradiation for singlet oxygen detection in aqueous solution by the absorption method. The concentration of the indicator ABDA was 200 μM and that of the photosensitizer was 10 μM which guaranteed that the generated singlet oxygen could be fully reacted and the indicator would not be completely consumed in the period of measurement time.

The light source is an external xenon lamp (Beijing NBet, HSX-UV300, 200–2500 nm), equipped with a 390 nm long-pass filter and neutral density filter. The output power of irradiation light was 80 mW. The process of ABDA oxidation was monitored by the decrease of absorbance at 402 nm (one intense absorption peak). as monitored by the decrease of absorbance at 402 nm (one intense absorption peak). The absorbance spectra were recorded at different time points of light irradiation for calculating the rate of the photosensitizing process. Rose Bengal (RB) was used as a reference with a reported singlet oxygen quantum yield 75% in water. The singlet oxygen quantum yield of photosensitizer (Φ_{PS}) was calculated according to the following formula, also mentioned in the previous chapter:

$$\Phi_{PS} = \Phi_{RB}\frac{K_{PS}}{K_{RB}} \qquad (13)$$

The subscripts *PS* and *RB* represent the target photosensitizer (PS) and the reference Rose Bengal (RB), respectively; K is the reaction rate of ABDA oxidized by the photosensitizer which can be calculated by the slopes of plots (absorbance vs. time); Φ_{RB} is the singlet oxygen quantum yield.

Chapter IV A Chromophore-Expanding Strategy for Monitoring Bioorthogonal Reaction by Off-On Lanthanide Luminescence

4.1 Introduction

It is monumental when Bertozzi *et al.* introduced the term – Bioorthogonal Chemistry in 2003.[84] They proposed that chemists would be able to perform reactions in complex biological environments rather than in refluxing organic solvents. Researchers pioneering the fields of bioorthogonal chemistry never stop exploring the reactions that can efficiently proceed in the aqueous solutions full of proteins and sugars but not impacting those biological bodies. There have been many impressive applications of bioorthogonal chemistry in recent years, including molecular imaging, protein lipidation, and in vivo diagnosis.[85, 86]

Click reaction is ideal to be applied in bioorthogonal because it is usually considered to be highly specific and requires no harsh conditions.[87] Cu(I) catalysts are widely used in azide-alkyne cycloadditions common for nucleic acid labeling.[88] However, "copper-free" click chemistry is much more attractive to bioorthogonal chemists from the view of biosafety. There are several strategies to process click-type reactions without copper catalysts, including the (ring-)strain-promoted azide-alkyne cycloadditions (SPAAC) firstly reported by Bertozzi.[89] They used cyclooctyne to react with azide where the second-order rate constant was only 0.0012 $M^{-1}s^{-1}$, much lower than those of copper(I)-catalyzed reactions (k_2 = 10-200 $M^{-1}s^{-1}$).[90]

Many cyclooctyne derivatives were studied to facilitate the SPAAC, and dibenzocyclooctyne (DBCO; also called aza-dibenzocyclooctyne, DIBAC) reagents were introduced as representatives. At a physiological temperature and pH range, DBCO does not easily react with amines or hydroxyls which means they are relatively inert to most biomolecules, while they are reacting with azide groups at much higher rates than with thiol groups.[91] This reagent allows copper-free click reactions in living organisms and prefer cycloadditions with azide groups. Not only does the fusion of dibenzo systems improve the reactivity of cycloalkynes,[92] but introducing a nitrogen atom on the strained ring also decreases the molecular hydrophobicity and ease the probe conjugation which facilitates specific reaction with azides.[93] The second-order reaction rates for DBCO groups with azide groups are around 1 $M^{-1}s^{-1}$, which are nearly one thousand times higher than a simple cyclooctyne.[94]

Lanthanide luminescence shows its great potential for biomedical imaging and analyses.[68] Emission from lanthanides mostly feature much longer lifetimes (0.5-10 millisecond) than those from common organic luminophores (1-100 nanosecond) so the time-resolved detection is available which improves the signal-to-noise ratio largely. To utilize lanthanide trivalent ions in molecular imaging, the metal must be incorporated into a suitable ligand which: (1) prevent the contact with solvent water molecules which severely deactivate the lanthanide emission through O-H vibrations.; (2) can harvest excitation energy and transfer it to the lanthanide excited states efficiently since lanthanides' intrinsic f-f transitions are quite weak and need sensitization.[4]

There are only a few reports concerning the application of luminescent lanthanide complexes in bioorthogonal chemistry. In 2016, O'Malley *et al.* prepared terbium(III)

complexes that can conjugate to biomolecules through a click reaction between an alkyne group and an azide group.[95] The successful conjugation would result in a significant Tb(III) emission enhancement. However, the usage of Cu(I) catalyst inevitably causes cytotoxicity from the resulting Cu(I) salts. Another example was reported by Zheng and his co-workers in 2020.[96] A biocompatible Tb(III) complex underwent ligation with cell surface glycans which resulted in a large increase in luminescence. It is because the cycloaddition reaction changed the electronic structures of the linked quencher, and the energy transfer from the antenna to Tb(III) was promoted. Unfortunately, the reported Tb(III) system only showed 5-fold emission enhancement and no off-on property, which limit its sensitivity.

We herein reported a Eu(III)-based complex, Eu-BT, featuring ████████████ ███████████████████████████. It can specifically perform SPAAC reactions with DBCO reagents, where DBCOs are readily available and capable of subsequent conjugation with other biomolecules through their carboxylic groups. Prior to SPAAC reactions, our complex provides no light signal with excitation above 250 nm. After the specific cycloaddition with the cyclooctyne ring, the triazoyl moiety formed, together with the pyridine and two benzene rings, and served as an expanded conjugation system, which efficiently sensitizes the Eu(III) excited states. The emission intensities were proportional to the extent of this bioorthogonal reaction, and the kinetic evaluation of the cycloaddition of Eu-BT and DBCO-acid was performed by nuclear magnetic resonance (NMR) techniques (the second-order reaction constant, $k_2 = 0.39 \pm 0.007$ M^{-1} min^{-1}). The DBCO-acid is commercially available and can conjugate to a wide range of biomolecules from its carboxylic group, for example, it can conjugate to mannosamine, a metabolic precursor on the cell surface.[97] This reaction and the

chromophore-expanding strategy shows broad application and fills the gap of monitoring bioorthogonal chemistry by off-on luminescence.

Figure 4.1. The illustration of the off-on luminescence generation process. The SPACC reaction expands the chromophore and makes it suitable to transfer excitation energy to the Eu(III) center.

4.2 Results and Discussion

4.2.1 Kinetic studies on SPAAC reactions

The evolution of strained alkyne reagents is driven by the demands for improved kinetics, that is, the higher second-order rate constants. Reaction rates are primarily calculated by changes in the amounts of reagents and products. There is a typical method to determine those concentrations by comparing the integrals of intensity peaks for the reagents at the initial stages and different time points. With the known initial concentrations of DBCO acid and the La-BT complex, the concentration of the conjugated product can be determined. A time-resolved NMR experiment was performed by mixing the DBCO acid and La-BT in an NMR tube and monitoring the NMR spectra up to 780 minutes (Figure 4.2). Here La-BT was used instead of Eu-BT in NMR spectroscopy because Eu(III) is a paramagnetic metal having unpaired

electrons and usually causes severe interference on the spectra. La(III) is diamagnetic and La-BT did not have this problem.

At the beginning of the reaction (0 minute), there was an obvious doublet peak located at 8.49 and 8.50 ppm. This doublet peak is attributed to a hydrogen on the pyridine ring near the nitrogen. The proton signal was split due to spin-spin coupling with its neighboring hydrogen. With the reaction processing, the doublet peak shifted downfield and turned to be a series of broad peaks. This could be explained by the fact that the nearby conjugated unsaturated systems de-shielded that proton but caused more couplings. After 600 minutes, there was no obvious signal at 8.5 ppm but a strong one at around 8.7 ppm. Considering the peak integral at t = 0 corresponding to the initial concentration of La-BT, the instantaneous concentrations can be calculated at different time points, as shown in Figure 4.3. The curve exhibits a nonlinear decay which suggests the reaction was not of zero order.

As for a standard second-order reaction, A + B → P, we have

$$\frac{d[A]}{dt} = -k[A][B] \tag{15}$$

Integrating from 0 to t,

$$\frac{1}{[B]_0 - [A]_0} ln \frac{[B][A]_0}{[A][B]_0} = kt \tag{16}$$

where [A], [B], and [P] are the concentrations of La-BT complex, DBCO acid, and the conjugated product respectively. We can obtain the real-time [A] by comparing the NMR peak integrals and [B] = [B]$_0$ – [A].

By plotting time (t) versus $\left(\frac{1}{[B]_0-[A]_0} \ln \frac{[B][A]_0}{[A][B]_0}\right)$, we can obtain the reaction rate constant

k from its slope (Figure 4.4) in the dynamic range (0-270 minutes), where neither

reagent was fully consumed. The reaction rate constant k was determined from the slope

as 3.92×10^{-4} mM^{-1} min^{-1} (0.39 M^{-1}min^{-1}). There are two reasons why our value is much

smaller than those in the literature for SPAAC between azide and DBCO: firstly, the

reaction process was monitored in the NMR machine where the reaction solution was

rarely stirred, which slowed down the reaction rate considerably; secondly, instead of

alkyl azides that were used to determine reaction rates before, we focused on an

azidopyridine where the electrons were stabilized on the conjugated π-bond system and

less reactive.
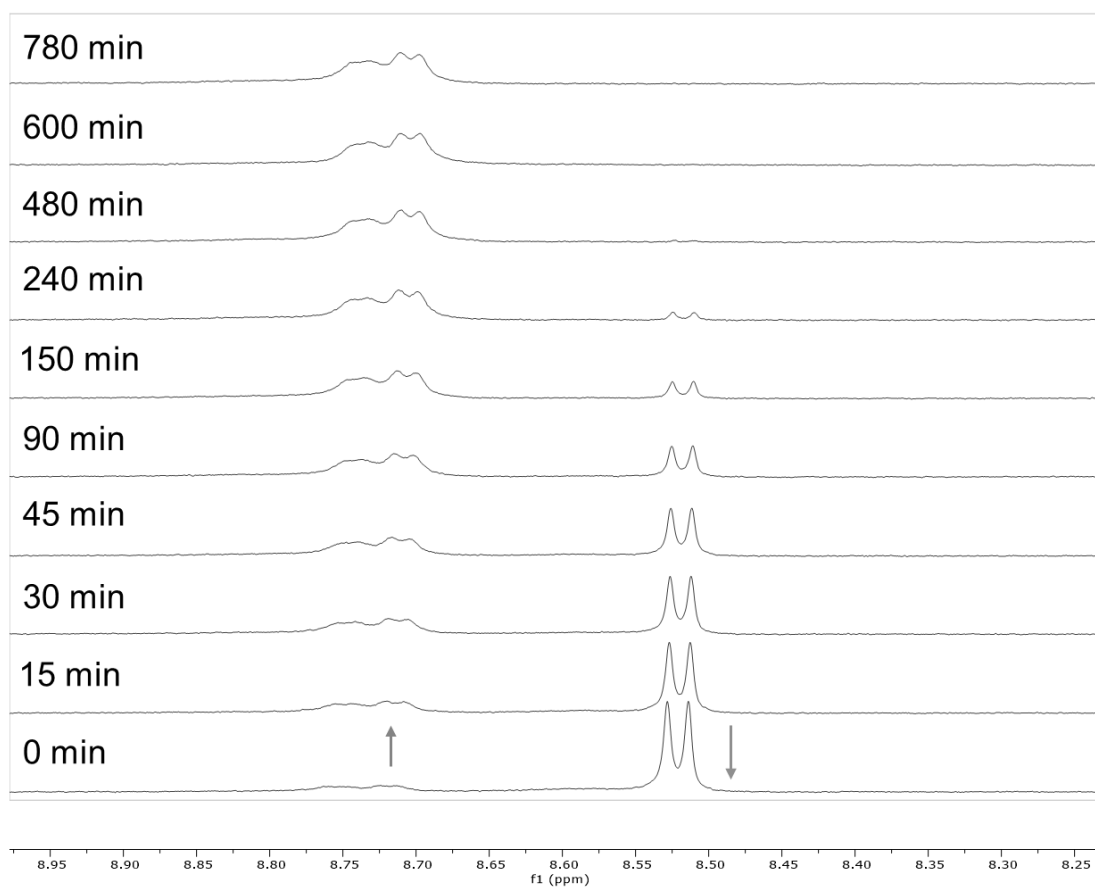
Figure 4.2. Overlapping ^{1}HNMR spectra of La-BT and DBCO-acid mixing solutions (in CD_3OD) at different time points.
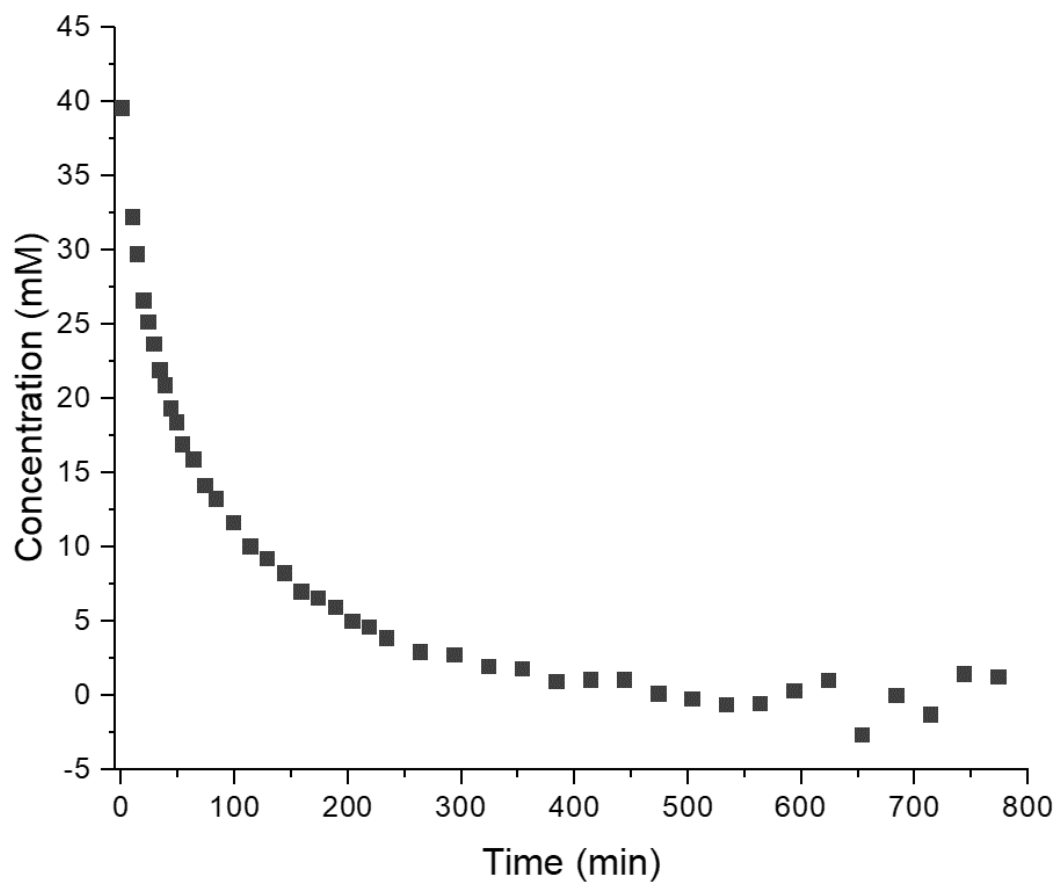
Figure 4.3. The plot of the calculated concentrations of La-BT (by the NMR peak integrals at 8.5 ppm) vs. reaction time.
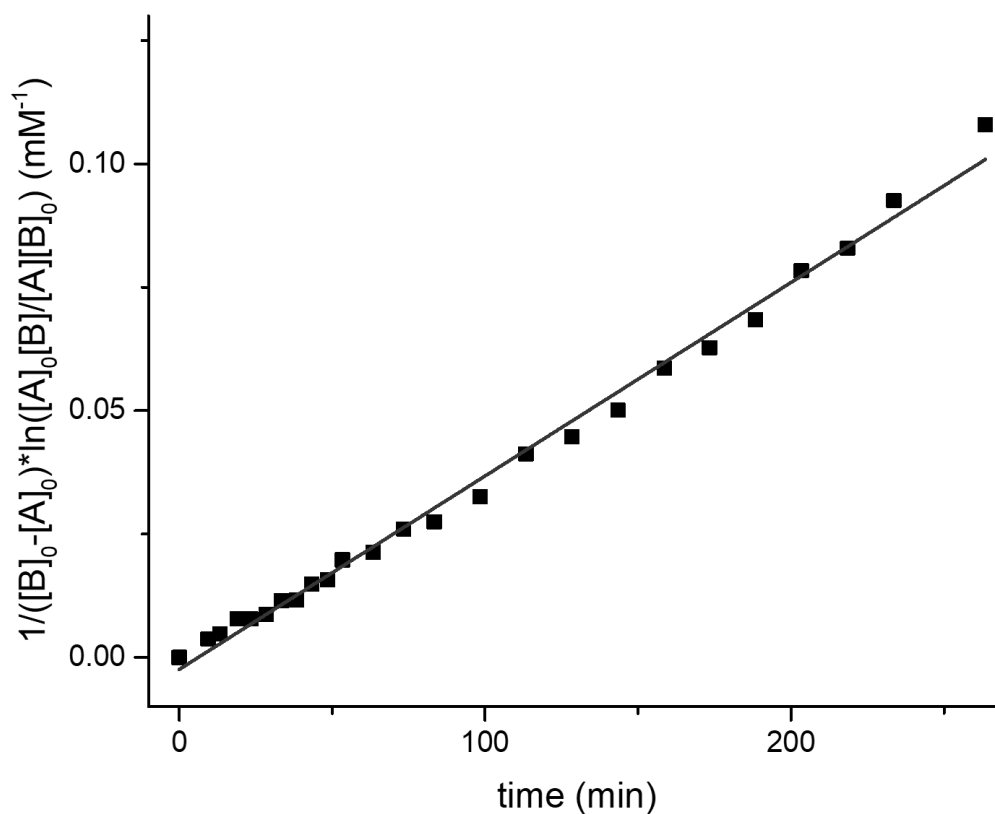
Figure 4.4. Logarithmic plot of the reaction of compound 10 with benzyl azide in CD$_3$OD.

Table 4.1. Parameters for the fitting curve in figure 4.4. with y = ax + b. The slope equals the reaction rate constant.

Intercept	Value	-0.00244
	Standard Error	8.42286E-4
Slope	Value	3.92086E-4
(Reaction rate constant)	Standard Error	6.73067E-6
Statistics	Adj. R-Square	0.99298

4.2.2 Excitation and emission spectra

Lanthanide luminescence is the key factor for the evaluation of the bioorthogonal progress in our case. Figure 4.5 provides the fundamental photophysical results for the Eu-BT-DBCO-conjugated product, where the antenna had been expanded and the Eu(III) was sensitized. The black part is the emission spectrum of Eu-BT-DBCO which features a typical Eu(III) emission pattern under 320 nm excitation light. According to the absorption spectrum of the product (Figure 5.42), there was no absorbance above 320 nm while the maximal absorbance was at 210 nm, not functional for our light source. Emission peaks at 578, 587, 616, 652, and 700 nm are assigned to $^5D_0 \rightarrow {^7F_J}$ ($J = 0, 1, 2, 3, 4$) transitions respectively. The excitation spectrum was obtained by monitoring the 616 nm emission peak, and the emission was found to be sensitized by the light ranging from 230 to 350 nm. There is one noticeable observation: in many europium luminescence spectra, the $^5D_0 \rightarrow {^7F_2}$ transitions have the most intense emission peaks. However, for our case, the $^5D_0 \rightarrow {^7F_4}$ transition dominated while $^5D_0 \rightarrow {^7F_2}$ was much weaker. This phenomenon was also found in other Eu(III)-cyclen complexes.[76, 98] It was claimed by Binnemans[99] that Eu(III)-complexes with D_{4d} symmetry have intense $^5D_0 \rightarrow {^7F_4}$ transitions because of the absence of a center of symmetry but the $^5D_0 \rightarrow {^7F_2}$ transition is forbidden. As for Ln(III)-tetrasubstitutedcyclen chelates, they usually adopt either a monocapped twisted square antiprismatic (TSAP) geometry or a monocapped square antiprismatic (SAP) geometry where SAP geometry has a perfect D_{4d} symmetry. Even though our complex does not feature an undistorted SAP geometry but it is still close to a square antiprism partially and results in an intense $^5D_0 \rightarrow {^7F_4}$ emission peak.
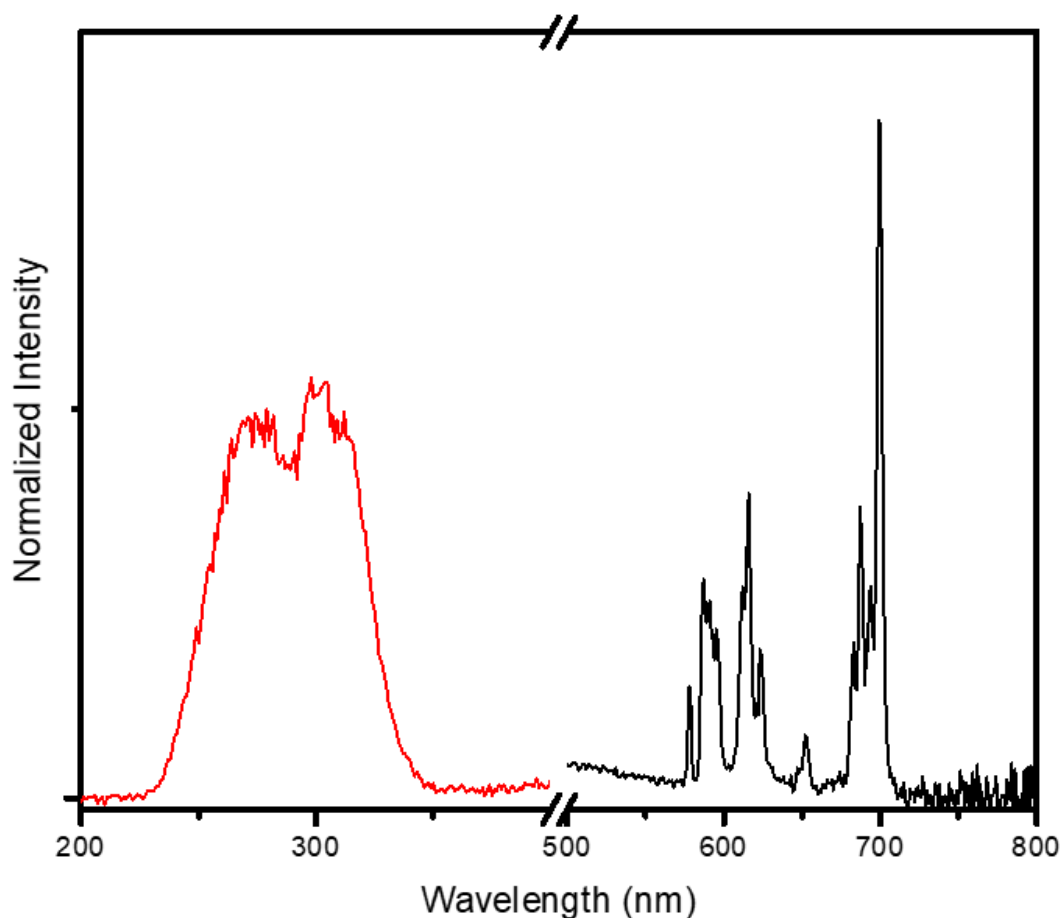
Figure 4.5. Excitation (red, λ_{mon} = 616 nm) and emission (black, λ_{exc} = 320 nm) of Eu-BT-DBCO conjugated in methanol (conc. = 10 μM).

4.2.3 Kinetic analysis of off-on/ luminescence property

One of the advantages of our Eu-BT complex in bioorthogonal chemistry is the off-on luminescent properties. With 320 nm light irradiation, the Eu-BT alone has no light emission before the conjugation, but after the successful SPAAC reaction with DBCO acids, the Eu(III) center will be effectively sensitized and produce long-lived, characteristic visible emission. The emission intensity is enhanced with the progression of the reaction and the formation of conjugated products. Emission spectra were obtained from a reacting solution of Eu-BT and DBCO. Strong Eu(III) emission was

121

observed after 5 minutes of the reaction. After 140 min, Eu-BT had mostly been reacted

and the emission intensity at 616 nm and 700 nm was 3.8 times stronger.
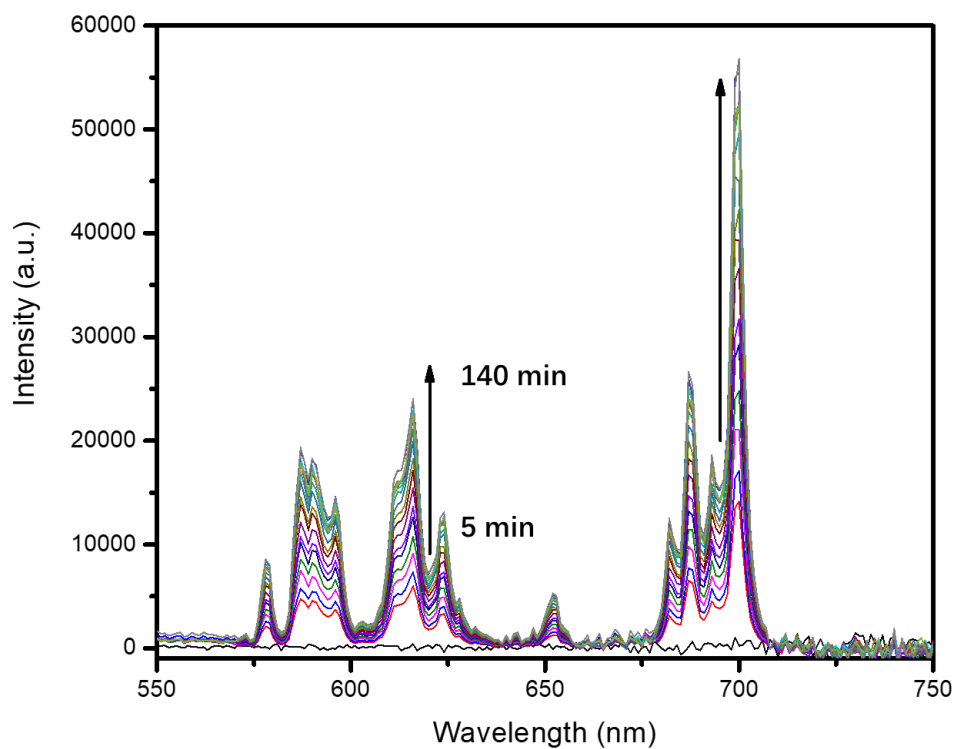
Figure 4.6. Emission spectra of the solution for an ongoing bioorthogonal reaction between Eu-BT and DBCO-acid at different time points. The reaction and the measurement were both performed at room temperature in methanol (excessive Eu-BT before the reaction with the addition of DBCO-acid conc. = 10 μM, λ_{ex} = 320 nm).
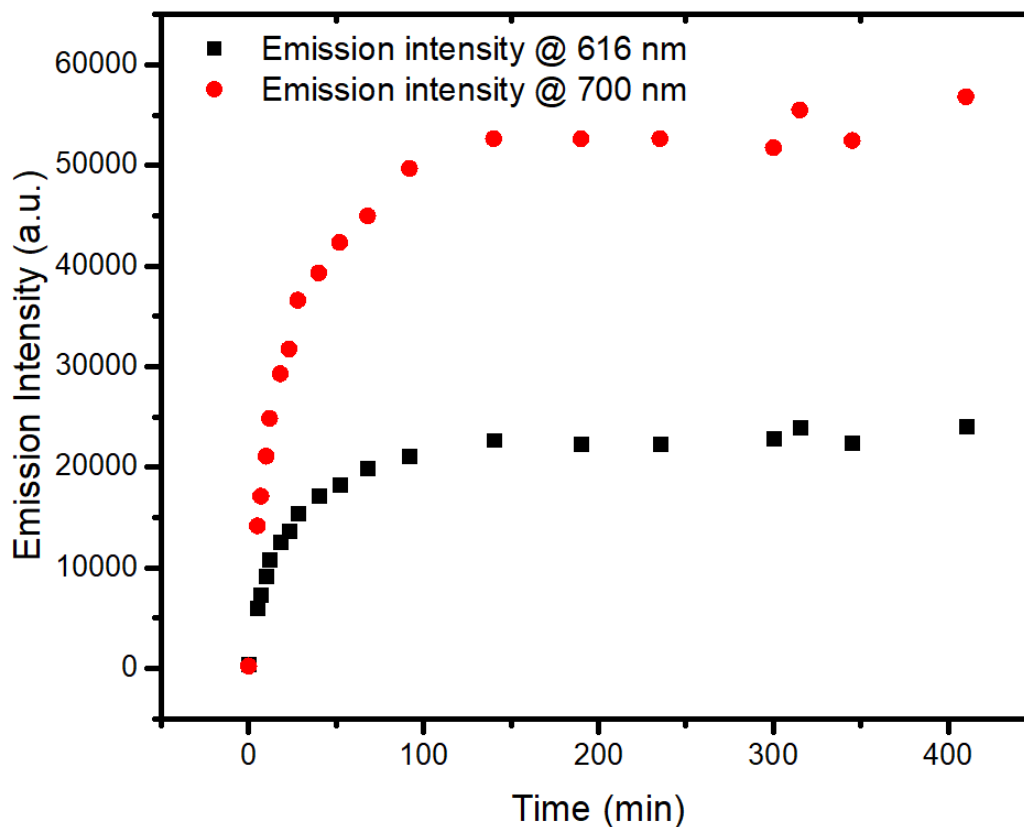
Figure 4.7. The changes in the intensity vs. time of emission peaks at 616 nm and 700 nm. Data are extracted from Figure 4.6.

4.2.4 Monitoring the SPACC reaction by HPLC

Qualification analysis was performed also by HPLC as all results were shown in the Appendix (Figures 5.27-5.30). On the same mobile phase conditions, pure Eu-BT came out from the column at retention time t = 6.25 min and DBCO-acid at 47.82 min. The reacting solution was prepared by adding a limiting amount of Eu-BT into excessive DBCO-acid in methanol at room temperature. After overnight stirring temperature in methanol, the mixture was sent for another HPLC test. Although the peak for DBCO-acid was high at t = 47.81 min, there was no peak for Eu-BT found around t = 6 min. Additional peaks were found at t < 20 min should be assigned for the conjugated products. However, there were two peaks located closely at 18.5 min and 19.1 min.

They could belong to two isomers of the conjugating products (Figure 4.8). Although they showed similar polarity in HPLC, there was no difference in the emission spectra and negligible effect on the NMR spectra.

Available in archival version
Disponible en version archivage

Figure 4.8. Molecular structure of the Eu-BT-DBCO isomers simultaneously formed in the SPAAC reaction.

4.3 Conclusion

Bioorthogonal chemistry is one of the most promising fields in modern chemistry as it could enable controlled chemistry in living cells and organisms, rather than in glassware or under harsh conditions. However, many limitations remains before its wide applications. One is that the bioorthogonal reaction rate is always a concern for efficient reactions. On the other hand, there are only a few reports on the real-time monitoring of bioorthogonal reaction by visible emission and no example capable of off-on luminescence. My work involves Eu(III)-based complexes undergoing a typical SPACC reaction simultaneously with a commercially available reagent DBCO, and the highly-differentiated light signal (sharp and time-resolved emission peaks) were generated and enhanced with the reaction process. Although the rate was measured to

be substandard because of the stabilized azide group, it is inevitable when introducing the expanding-chromophore strategies.

4.4 Experimental

4.4.1 Synthetic procedures

Scheme 4. The synthetic route for LnBT (Ln = La, Eu).
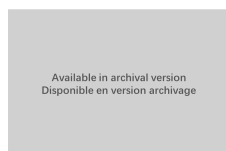
Scheme 5. The synthetic route for DBCO-mannosamine conjugate.

Synthesis of ███████████████████

████████████████████████████████████

████████████████████████████████████
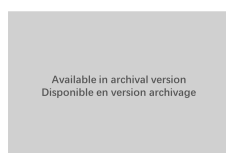
██████████████████ The reaction was monitored by TLC. Upon completion, the solvent was vaporized, and extracted with EtOAc/water. The combined organic layer was washed with brine, then dried with Na_2SO_4, and concentrated under vacuum. The product was used for next step without further purification. Yield, 68 %. ^{1}H NMR

(400 MHz, Chloroform-*d*) δ ███████████████████████████████

███████████████████████████

Synthesis of ████████████████████████████████

██████████████████████████████

Available in archival version
Disponible en version archivage

██

██

██

██████████████████████████████████ The reaction was monitored by

TLC (eluent: Hexane/EA=1:1), and a new product with a higher R_f value can be

observed. Upon completion, the solvent was vaporized under a vacuum. The dried

crude product was redissolved in ACN (5 mL), and was transferred into a suspension

of ███

████████████████████████████████████. The resulting mixture was

stirred at 50 °C overnight. Upon completion, the solvent was vaporized, and extracted

with DCM/water. the combined organic layer was washed with brine, then dried with

Na_2SO_4, and concentrated under vacuum. The crude product was then purified by

preparative HPLC. ESI-MS: calc. for $[M+H]^+$ ████████████████████

█████████████████████████████ ^{1}H NMR (400 MHz,

Chloroform-*d*) δ ███████████████████████████████

███████████████████████████████████ ^{13}C NMR (101 MHz,

Chloroform-*d*) δ ███████████████████████████████████

████████████████

General synthetic procedure for LnBT

Available in archival version
Disponible en version archivage

To deprotect carboxylic groups, the solution of ████████████████████

██

████████████████████████████████ Upon completion, the solvent was

evaporated, and 1 mL MeOH, 1 mL water, and 0.12 mmol $LnCl_3 \cdot nH_2O$ added. The pH

of the solution was adjusted to around 8 by adding 1M NaOH (aq.) and stirred at r.t for

12 h. The product was then purified by preparative-HPLC.

LaBT

Pale-yellow powder. Yield 38.6 %. Analytical HPLC: Retention time: 6.3 min, Purity:

96.4 %. ESI-MS: calc. for ████████████████████████████████

██████████████ ^{1}H NMR (400 MHz, Methanol-*d*4) δ ████████████████

██

EuBT

Pale-yellow powder. Yield 37.8 %. Analytical HPLC: Retention time: 6.3 min, Purity:

96.9 %. ESI-MS: calc. for ████████████████████████████████

Synthesis of ██████████████████████████

███

██

██

██

The crude product was then purifed by preparative HPLC. ESI-MS: calc. for $[M+H]^+$

███████████████████████████████████████ ^{1}H NMR (400 MHz,

Methanol-d_4) δ ██████████████████████████

███

██

^{13}C NMR (101 MHz, Methanol-d_4) δ ████████████████

██

██

███.

4.4.2 Photophysical measurements

UV–visible absorption spectra were recorded on an Agilent Technologies Cary 8454 UV-vis spectrophotometer. The emission spectra were measured with a Horiba steady-state bench-top spectrofluorometer Fluoromax-4 spectrophotometer equipped with a 150 W xenon lamp. Long-pass filters were used properly according to the excitation and emission ranges.

4.4.3 Kinetic studies on NMR spectrometer

The Eu-BT was dissolved in 250 μL CD₃OD at the concentration of 39.6 mmol, followed by the addition of DBCO-acid, which was dissolved in 250 μL CD₃OD at the concentration of 58.5 mmol. The total volume was 500 μL for appropriate NMR spectroscopic measurements. 1HNMR spectra were obtained automatically at different time points, and the total time length was 780 minutes. The automatic measurements were controlled by a TopSpin® NMR data analyzer. The exact consumption of Eu-BT was determined by the changes from the signals of one aromatic proton. By using the initial peak area as the standard, the concentration of Eu-BT at different time points can be obtained and the concentrations of the DBCO-acid and the conjugation products.

4.4.4 HPLC characterization of products.

Table 4.2. Solvent system for preparative HPLC. Flow rate: 0.5 mL/min.

Time (min)	Water with 0.1% TFA (%)	ACN with 0.1% TFA (%)
0	70	20
40	20	80
41	0	100
55	0	100

Appendix

Additional figures for Chapter II Impressive Near-Infrared Brightness and Singlet Oxygen Generation from Strategic Lanthanide–Porphyrin Double-Decker Complexes in Aqueous Solution

HPLC profiles
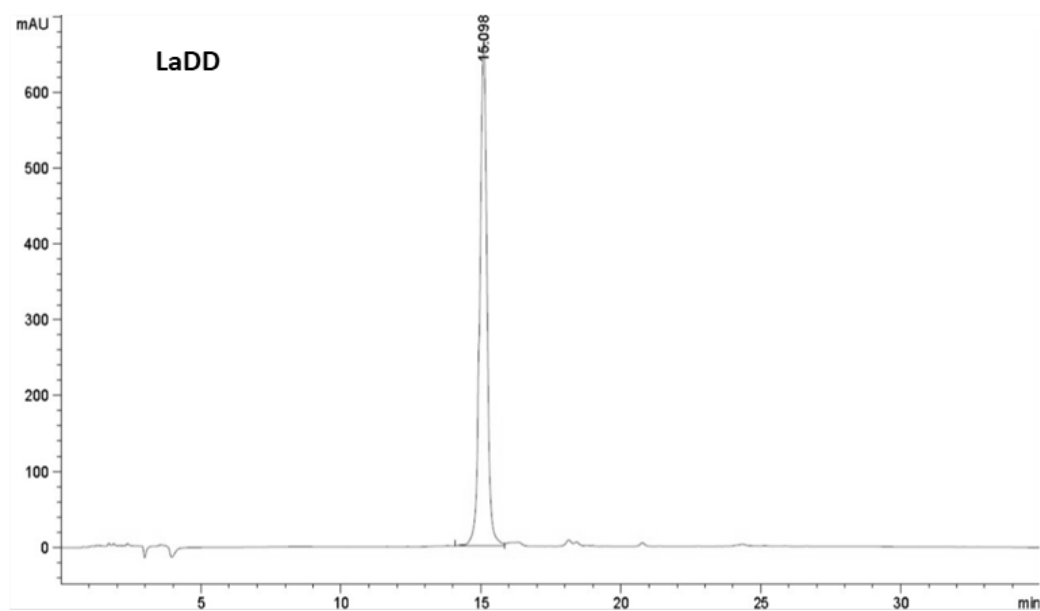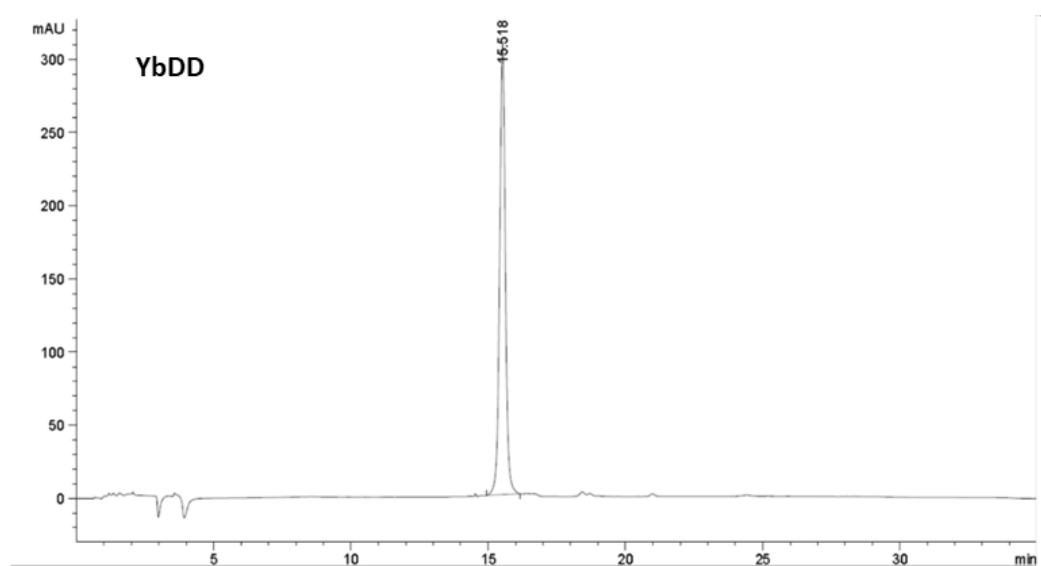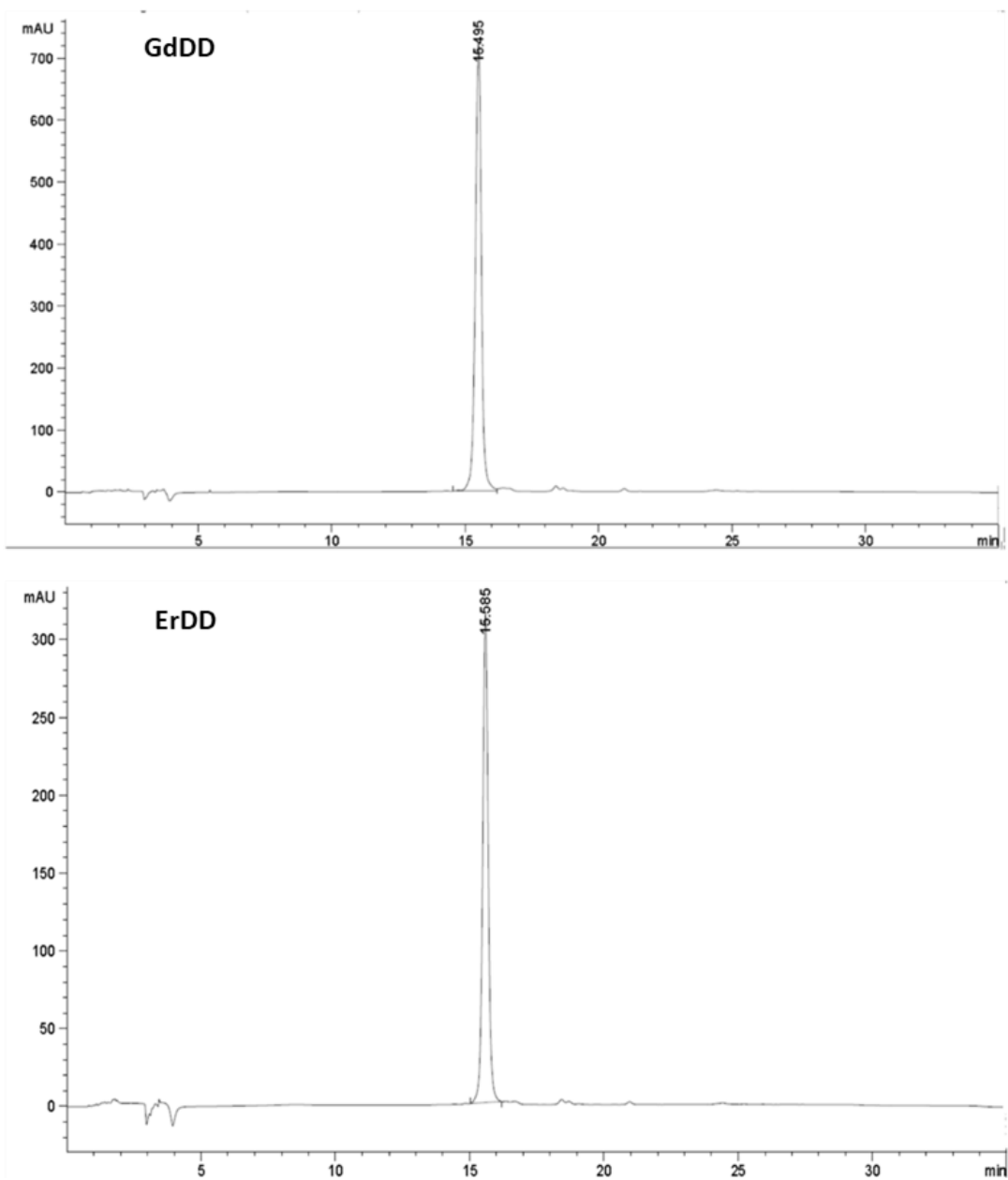
Figure 5.1. HPLC chromatograms of LnDD (Ln = Yb, Er, La and Gd).

NMR spectra
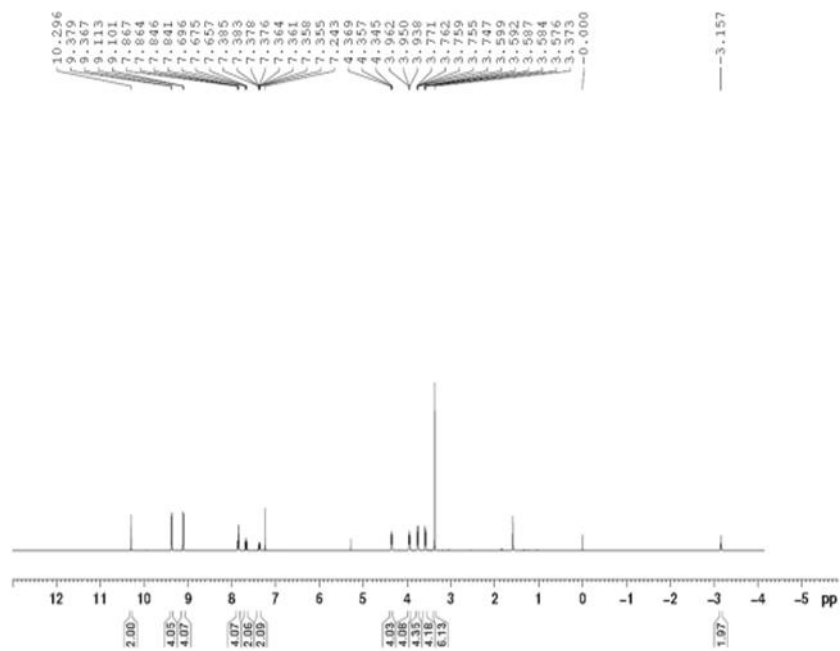
Figure 5.2. The room-temperature 400 MHz 1H-NMR (CDCl$_3$) spectrum of Por-2DEG.
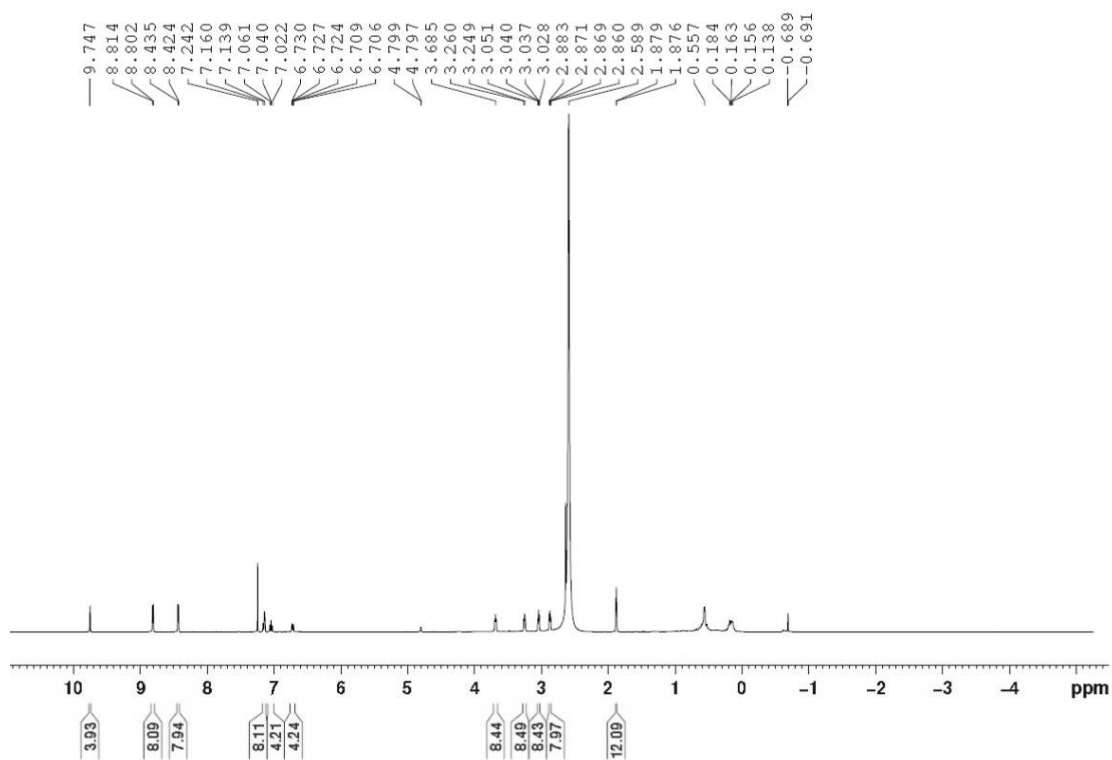
Figure 5.3. The room-temperature 400 MHz 1H-NMR spectrum of LaDD in

CDCl₃:DMSO-*d6* mixing solvents.

10.4093
9.4905
9.4815
9.1651
9.1556
7.8911
7.8746
7.8392
7.7587
7.7382
7.7185
7.3973
7.3777
5.3379
4.3198
3.9947
3.8782
3.8350
3.7106
3.6763
3.5550
3.4787
3.3981
3.3381
3.2625
3.2047
2.1268
1.7276
1.2145
0.8478
-3.3493

12 11 10 9 8 7 6 5 4 3 2 1 0 -1 -2 -3 -4 ppm

10.4198
9.4994
9.4895
9.1642
9.1537
7.8856
7.8177
7.7514
7.7316
7.7122
7.3654
7.3491
7.3210
5.3377
4.2896
3.9577
3.8378
3.8382
3.5425
3.3279
2.1201
1.1779
-3.4313

12 11 10 9 8 7 6 5 4 3 2 1 0 -1 -2 -3 -4 ppm

134

Figure 5.4. The variable-temperature NMR spectra of LaDD in CD₂Cl₂ (temperatures from top: 298K, 273K, 248K, 223K, 198K).

Mass spectra

HONG KONG BAPTIST UNIVERSITY, DEPARTMENT OF CHEMISTRY (MALDI-TOF)

Date of acquisition	2017-02-15 12:04:13
Comment 3	ERROR = -0.5900 PPM
Instrument type	autoflex
Serial instrument number	25001.00216
PIE delay in [ns]	60 nsec
Voltage polarity	POS
Comment 1	TRUE [M+1]+ = 699.317712
Comment 2	FOUND [M+1] = 699.3173
Laser repetition rate in Hz	20 psec
Linear detector voltage	0
Ion source voltage 1	19.040001
Ion source voltage 2	17.030001
Ion source lens voltage	8.100000400000001
Mass calibration Constant 1	723063.6300523349
Mass calibration Constant 2	47.96131470497736
Third calib constant	-0.06446874164625006
Number of shots	130

Acquisition method name   D:\Methods\flexControlMethods\20140609_john\RP_PepMix\RP_PepMix 1-4-2014_from David_LOM.par
Sample name (file name prefix) ZY-Por-PEG-SA\0_A4\1

printed: 02/15/2017 12:04:53 PM

Figure 5.5. MALDI-TOF mass spectrum of Por-2DEG.
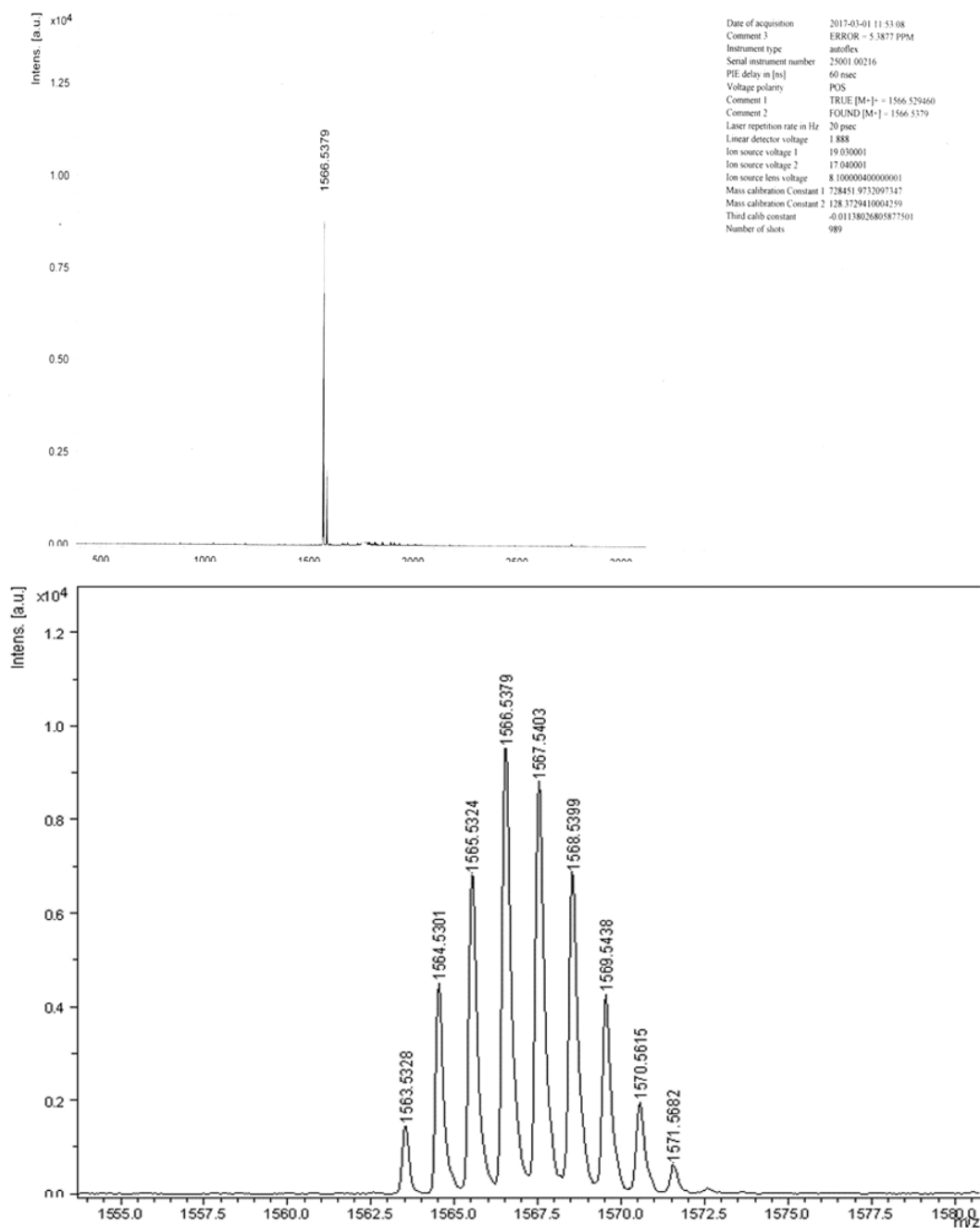
Figure 5.6. MALDI-TOF mass spectrum of YbDD**.**

Figure 5.7. MALDI-TOF mass spectrum of ErDD**.**
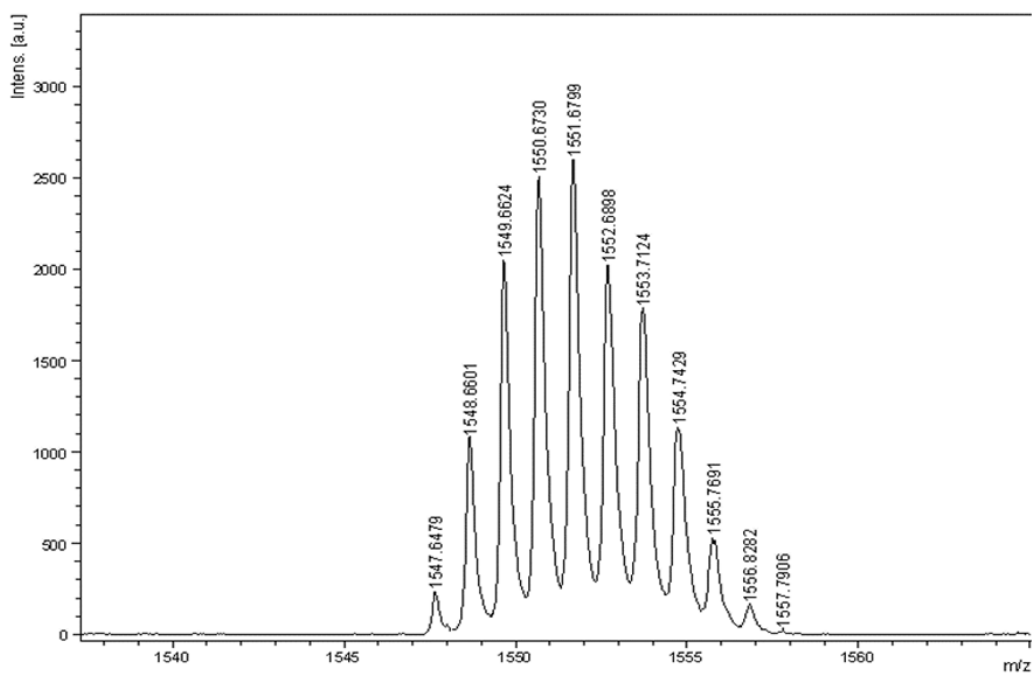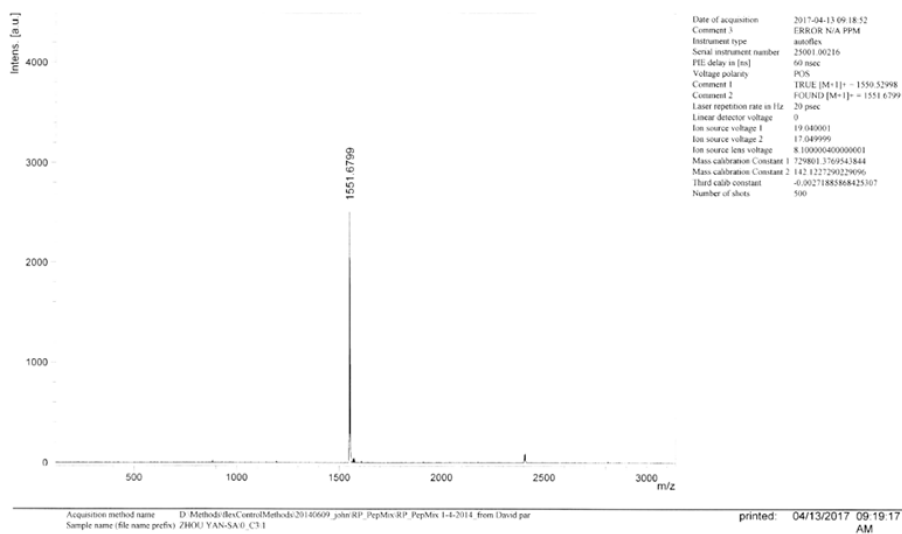
Figure 5.8. MALDI-TOF mass spectrum of GdDD**.**

Figure 5.9. MALDI-TOF mass spectrum of LaDD.

Additional figures for Chapter III "All-in-One" Double Chelator Complexes Achieving Multimodal Theranostics

HPLC profiles
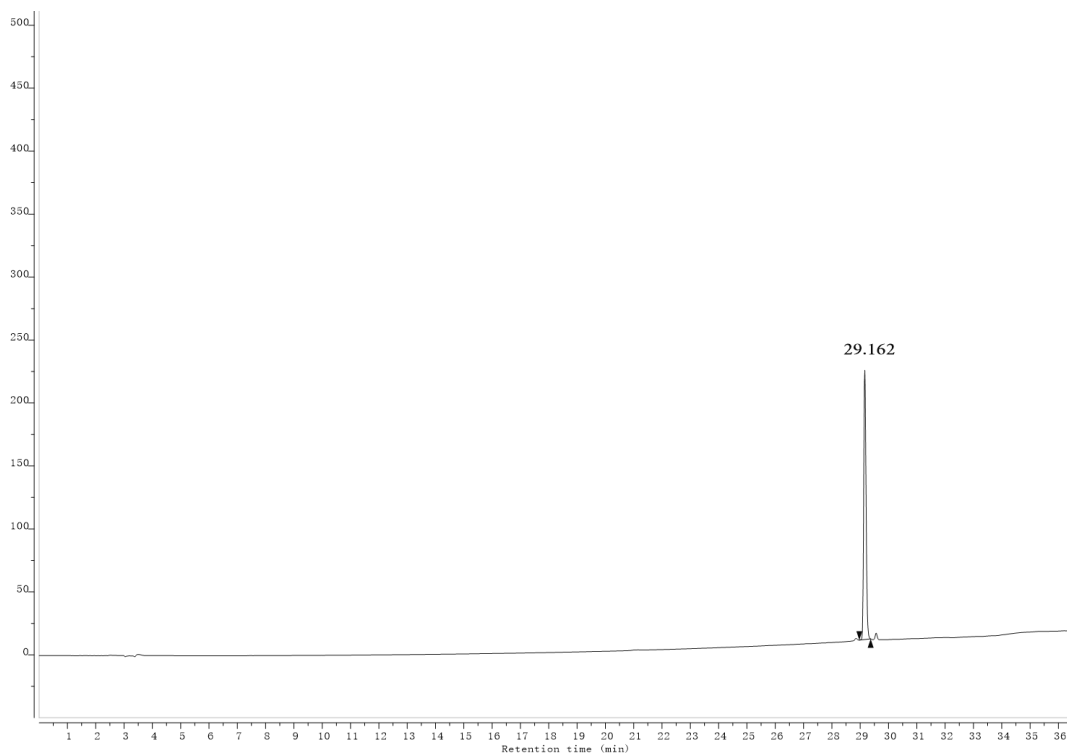
Figure 5.10. HPLC chromatograms of PLGd.
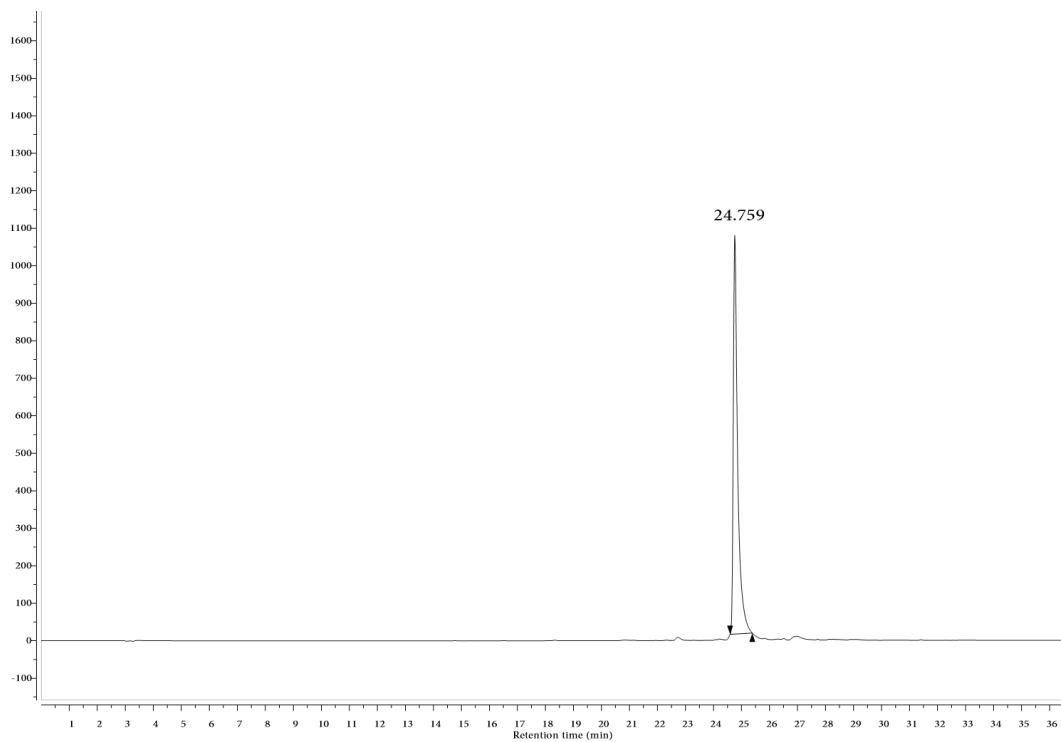
Figure 5.11. HPLC chromatograms of PZnLGd.
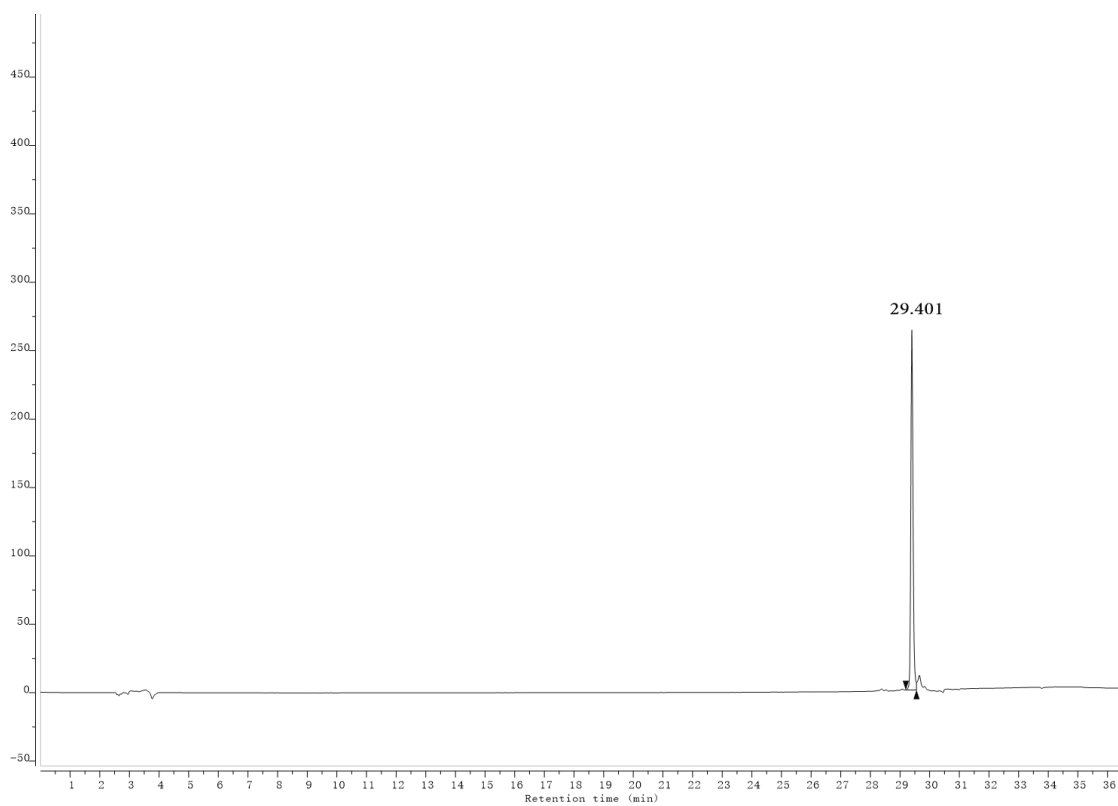
Figure 5.12. HPLC chromatograms of PfLGd.
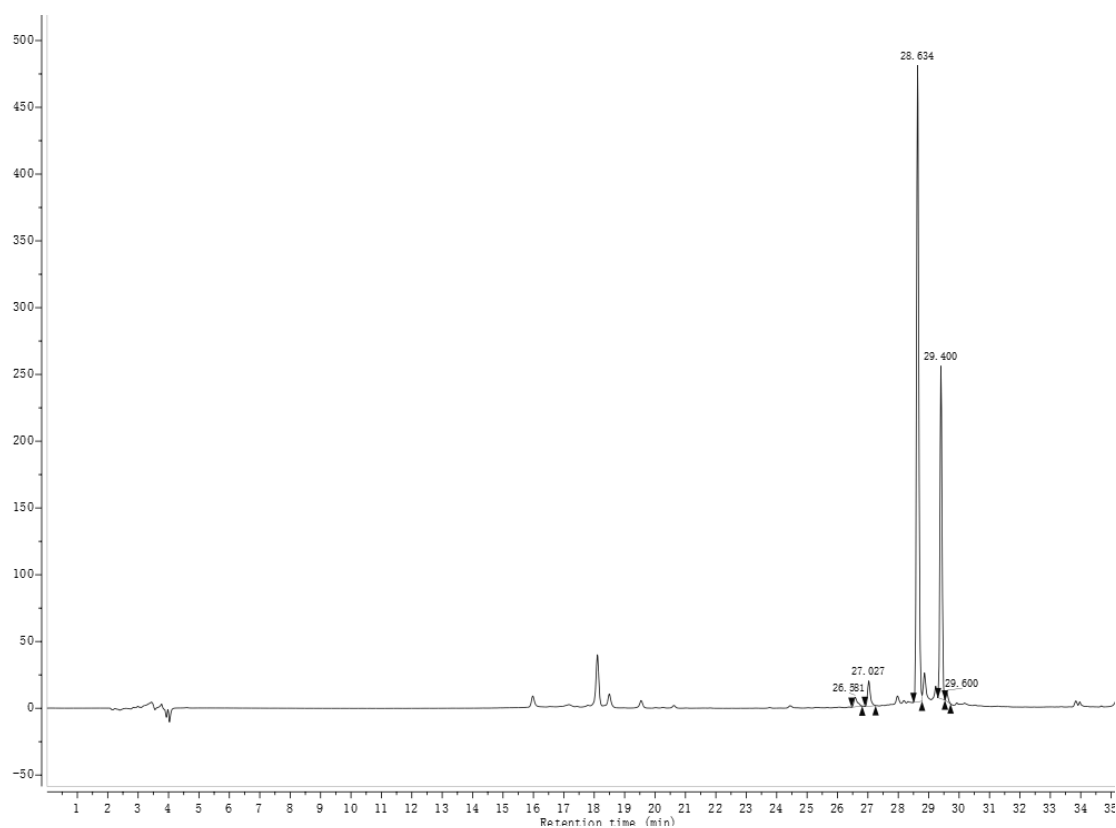
Figure 5.13. HPLC chromatograms of PGaLGd, prepared by microwave reaction and purified by SPE columns. The crude product was found at t = 28.634 min and the starting material PLGd was found at t = 29.40 min.

NMR spectra

Available in archival version
Disponible en version archivage
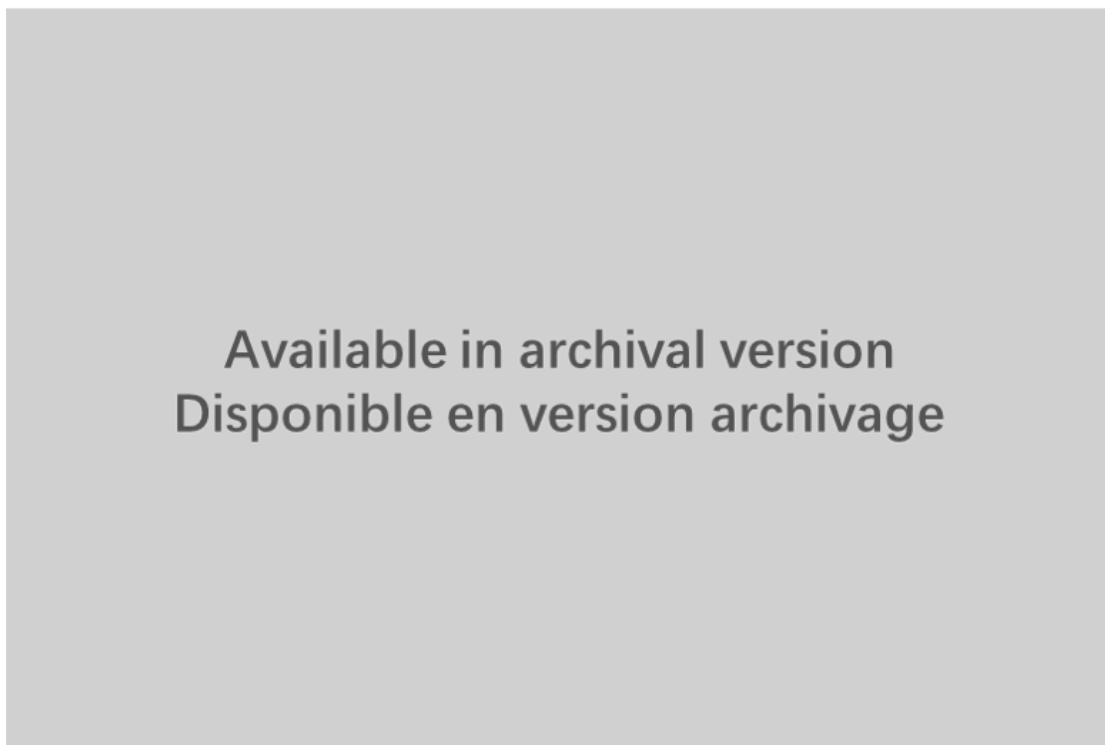
Figure 5.14. The room-temperature 400 MHz 1H-NMR (CDCl$_3$) spectrum of (4-(trimethylsilyl)ethynyl)pyridin-2-methanol.

Available in archival version
Disponible en version archivage

Figure 5.15. The room-temperature 400 MHz 1H-NMR (CDCl$_3$) spectrum of (4-ethynylpyridin-2-yl)methanol.

Available in archival version
Disponible en version archivage

Figure 5.16. The room-temperature 400 MHz 1H-NMR (CDCl₃) spectrum of Por.

Available in archival version
Disponible en version archivage

Figure 5.17. The room-temperature 400 MHz 1H-NMR (CDCl₃) spectrum of PZn.

Figure 5.18. The room-temperature 400 MHz 1H-NMR (CDCl$_3$) spectrum of PznPy.

Figure 5.19. The room-temperature 400 MHz 1H-NMR (CDCl₃) spectrum of 4-(10,15,20-tris(perfluorophenyl)porphyrin-5-yl)phenol.

Figure 5.20. The room-temperature 400 MHz 1H-NMR (CDCl$_3$) spectrum of Pf.

Mass spectra

Available in archival version
Disponible en version archivage
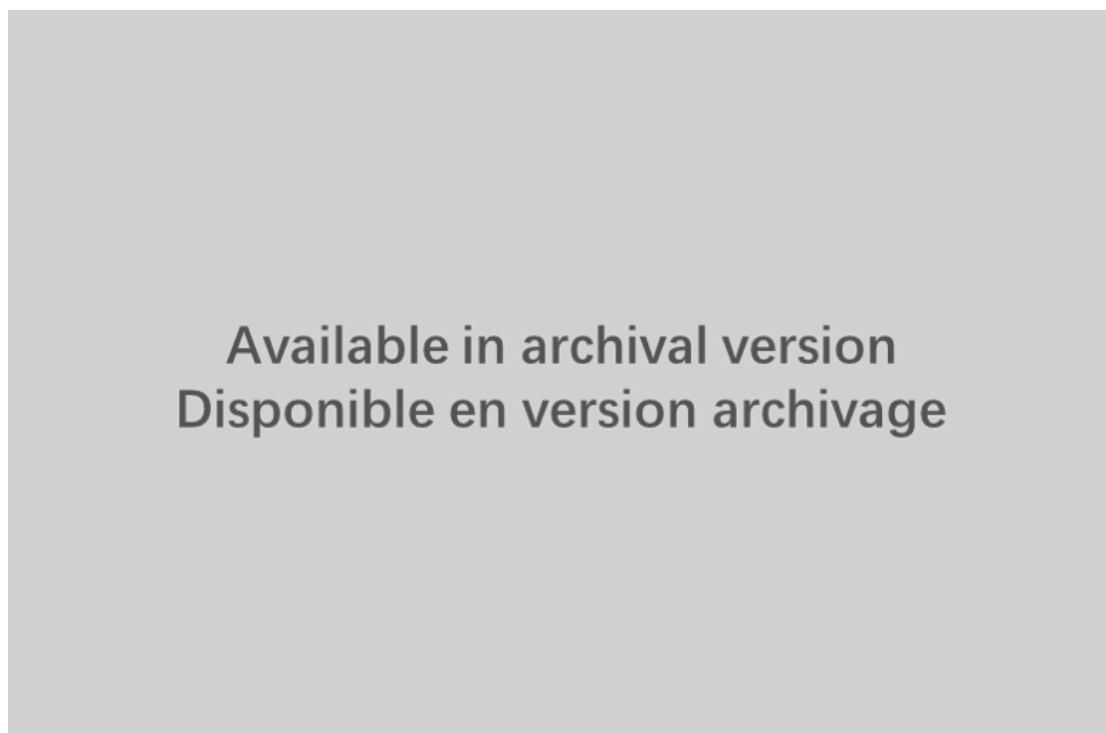
Figure 5.21. MALDI-TOF MS spectrum of PZnLPy.

Available in archival version
Disponible en version archivage

Figure 5.22. MALDI-TOF MS spectrum of PZnL.

Figure 5.23. ESI-MS spectrum of PZnLGd.

Figure 5.24. ESI-MS spectrum of PLGd.

Figure 5.25. ESI-MS spectrum of PfL.

Figure 5.26. ESI-MS spectrum of PfLGd.

Figure 5.27. ESI-MS spectrum of PGaLGd, prepared by microwave reaction and purified by SPE columns.

T1 relaxivity measurements

PLGd

$$y = 5.0829x - 0.1741$$
$$R^2 = 0.9992$$

PZnLGd

$$y = 3.1803x + 0.1158$$
$$R^2 = 0.992$$
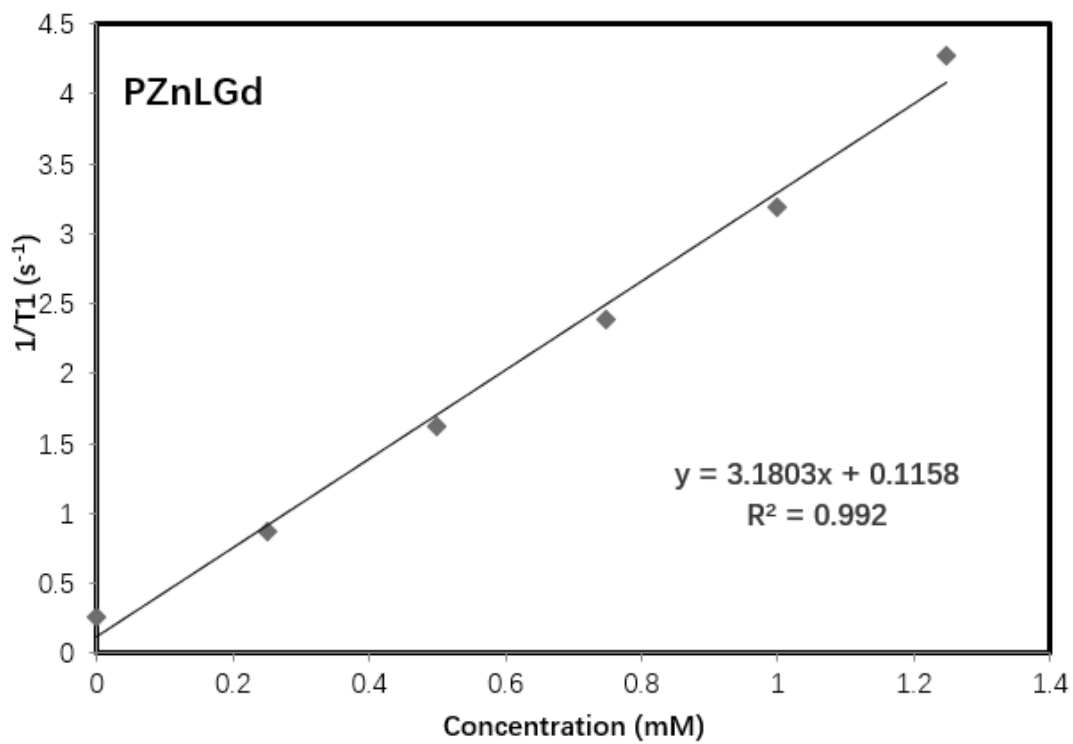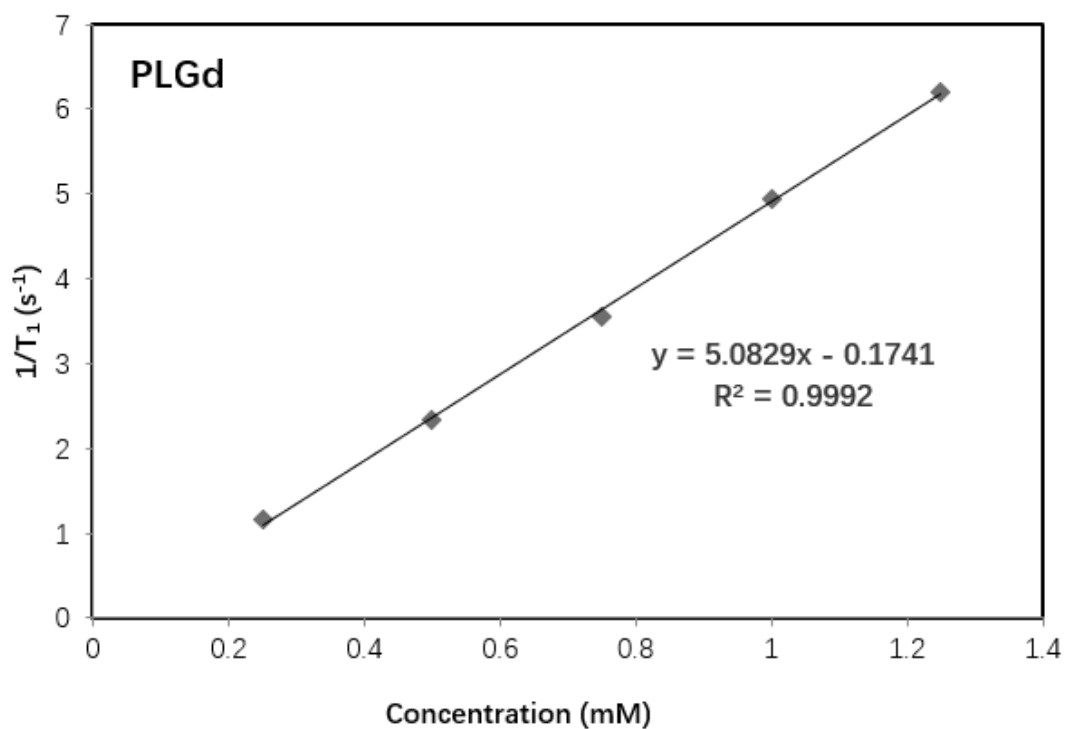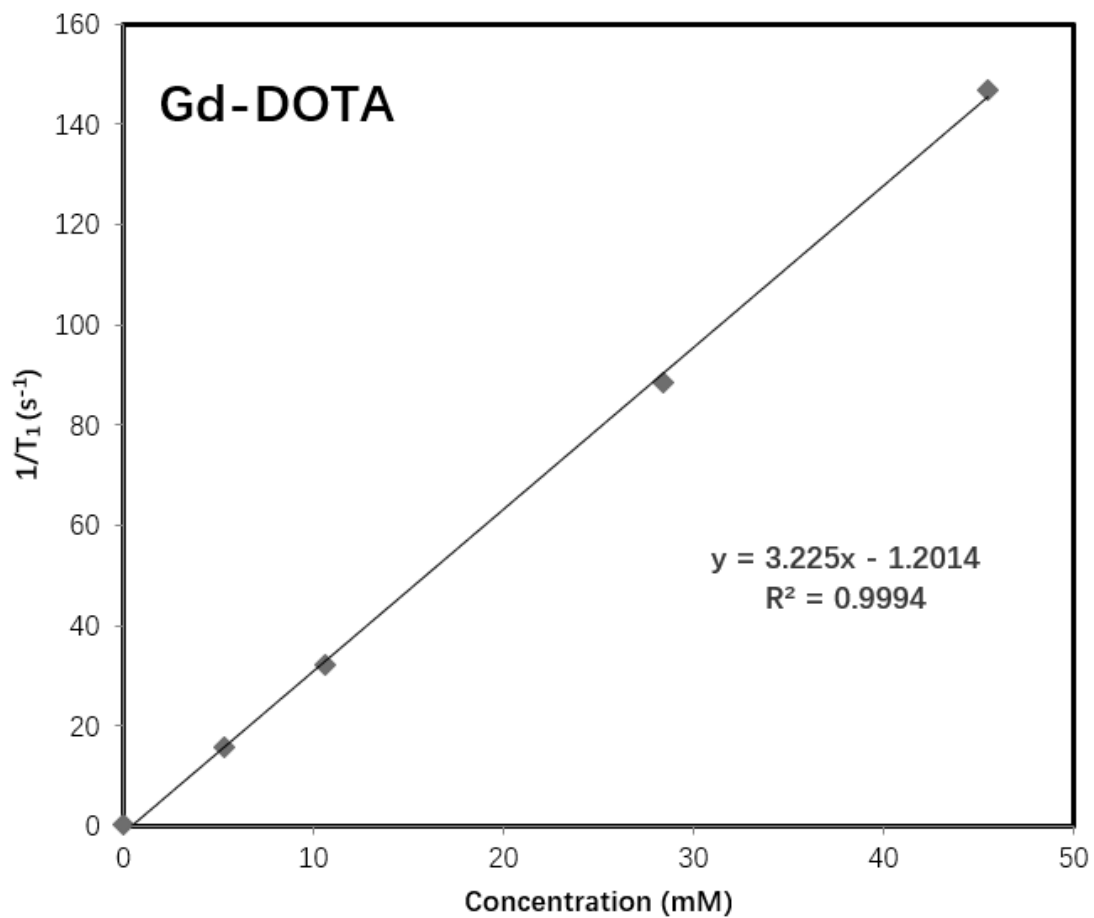
Figure 5.28. Relaxation rates $1/T_1$ vs. sample concentrations (3 T, 37 °C) for the prepared Gd(III)-complexes PLGd, PZnLGd, and GdDOTA.
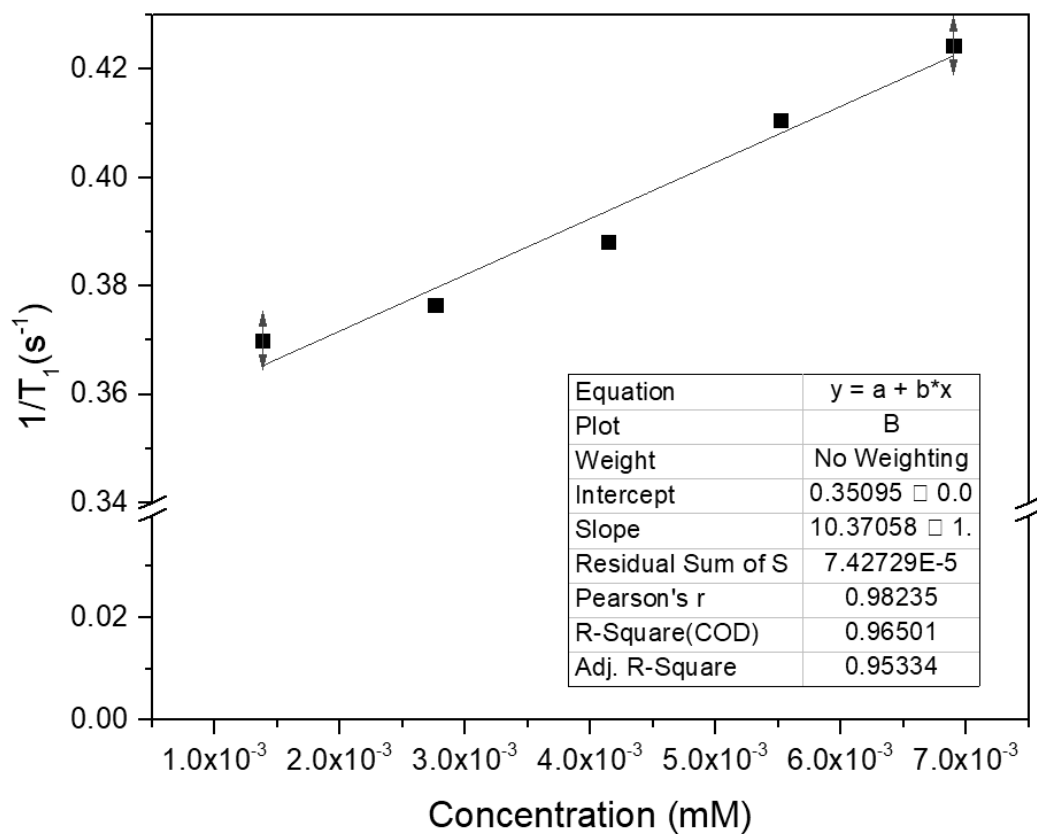
Figure 5.29. Relaxation rates $1/T_1$ vs. sample concentrations (3 T, 25 $^{\circ}$C) for PGaLGd.

Additional figures for Chapter IV A Chromophore-Expanding Strategy for Monitoring Bioorthogonal Reaction by Off-On Lanthanide Luminescence

HPLC profile
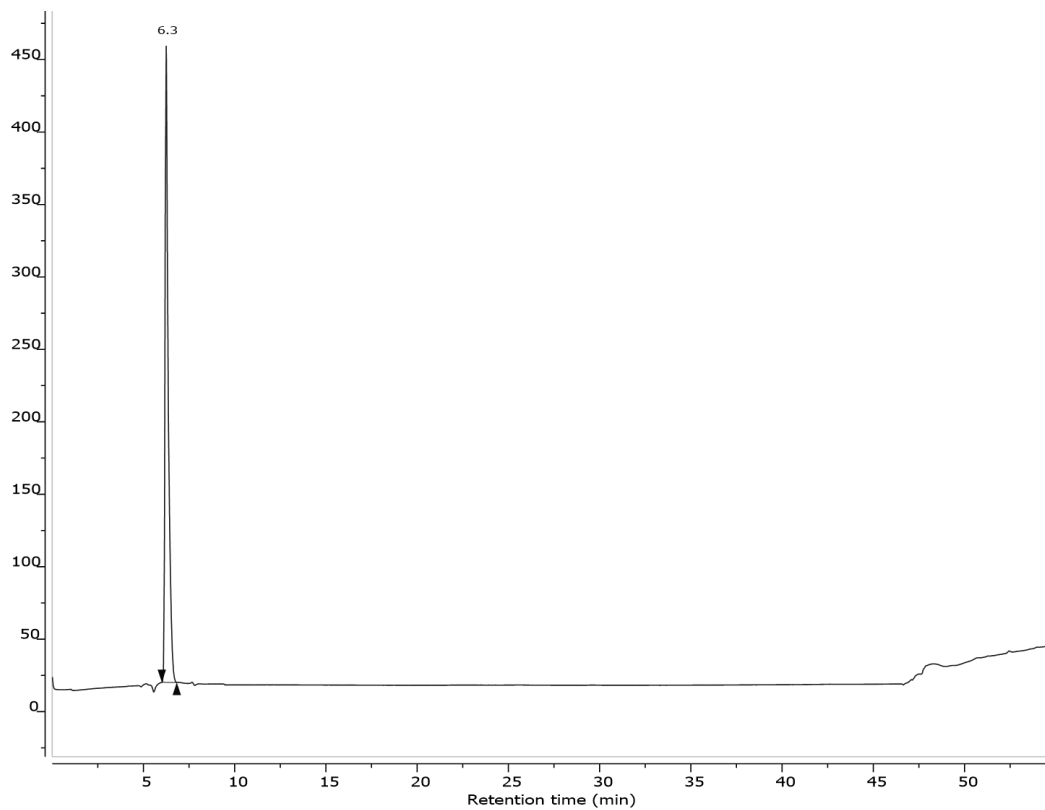
Figure 5.30. HPLC chromatograms of La-BT.
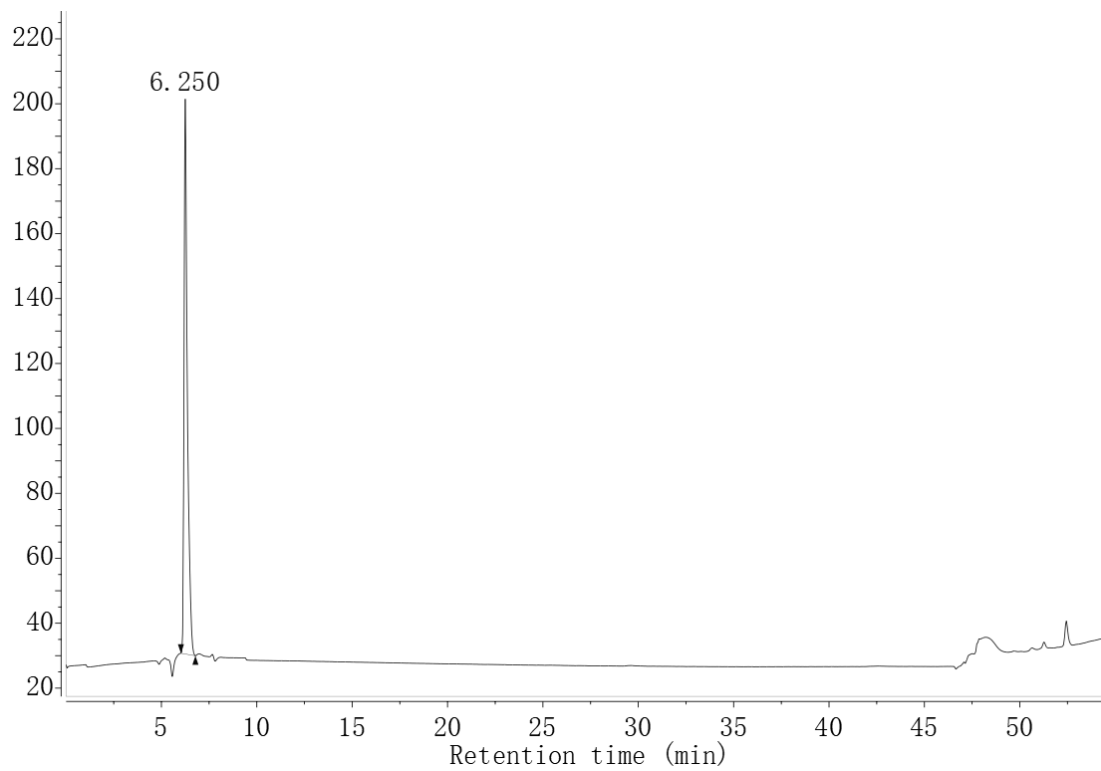
Figure 5.31. HPLC chromatograms of Eu-BT.
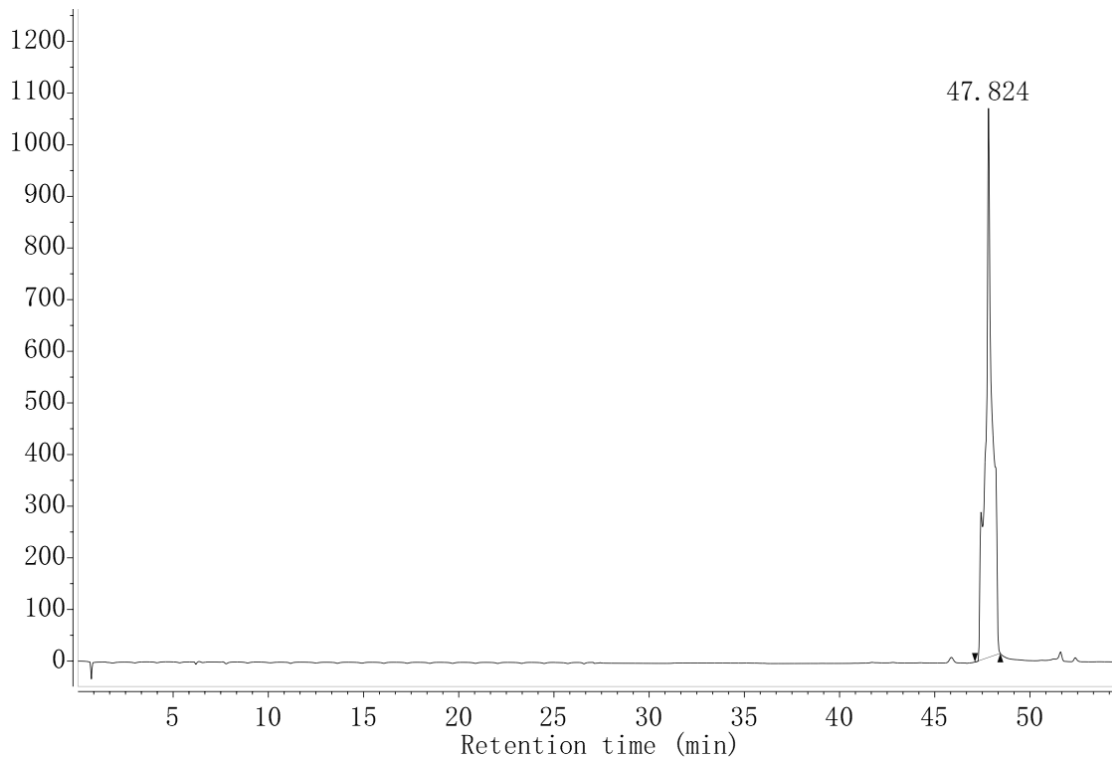
Figure 5.32. HPLC chromatograms of DBCO-acid.
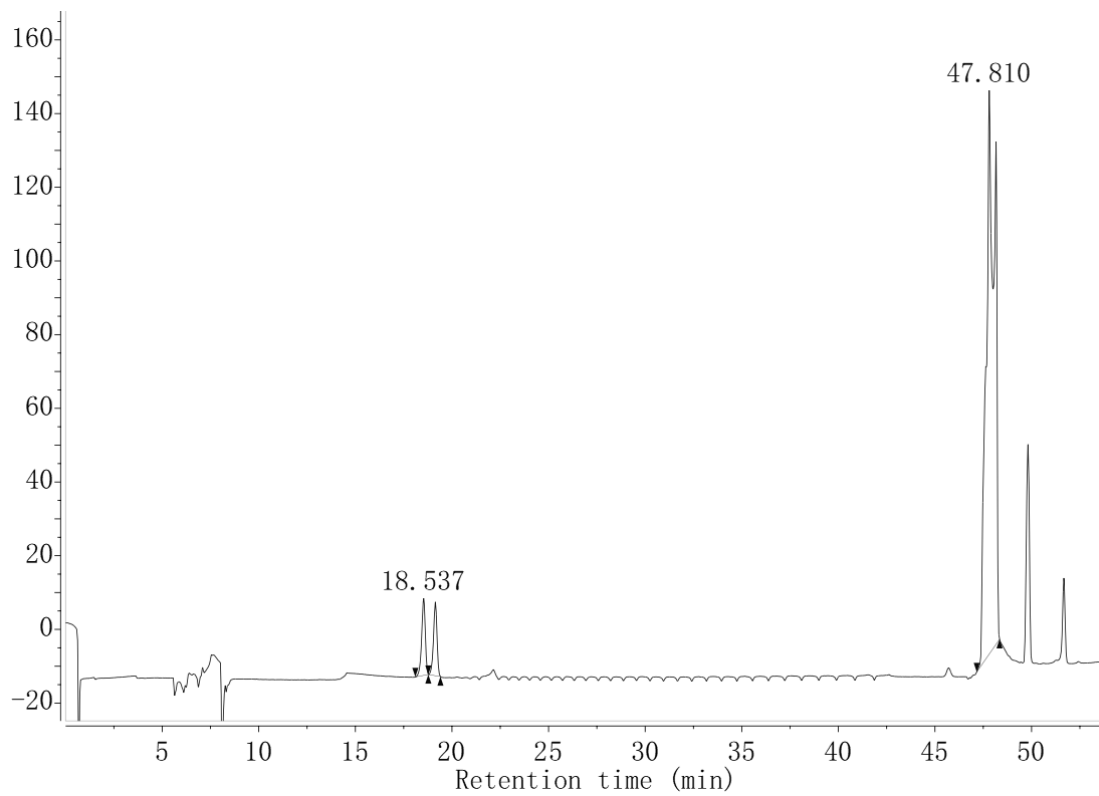
Figure 5.33. HPLC chromatograms of bioothogonal reaction solution.

NMR spectra

Available in archival version
Disponible en version archivage

Figure 5.34. The room-temperature 400 MHz- ^{13}C NMR (CDCl$_3$) spectrum of (4-azidopyridin-2-yl)methanol.

Available in archival version
Disponible en version archivage
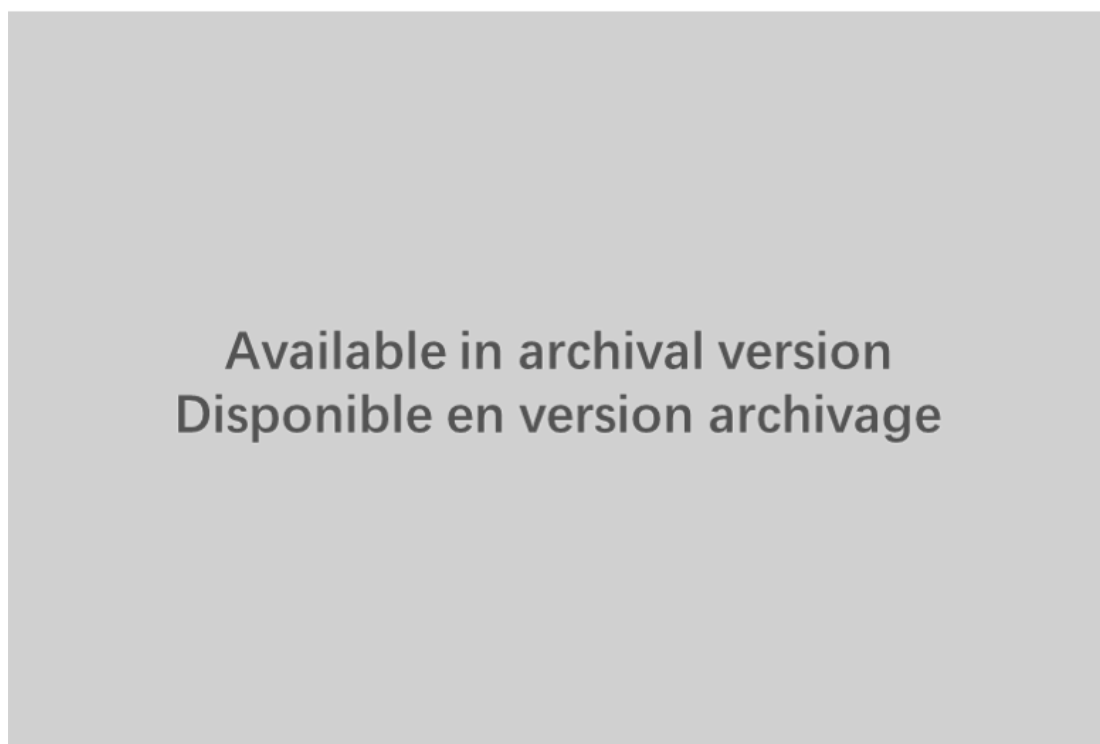
Figure 5.35. The room-temperature 400 MHz-^{1}HNMR (CDCl$_3$) spectrum of tri-*tert*-butyl 2,2',2"-(10-((4-azidopyridin-2-yl)methyl)-1,4,7,10-tetraazacyclododecane-1,4,7-triyl)triacetate.

Available in archival version
Disponible en version archivage

Figure 5.36. The room-temperature 400 MHz-^{13}CNMR (CDCl$_3$) spectrum of tri-*tert*-butyl 2,2',2"-(10-((4-azidopyridin-2-yl)methyl)-1,4,7,10-tetraazacyclododecane-1,4,7-triyl)triacetate.

Available in archival version
Disponible en version archivage

Figure 5.37. The room-temperature 400 MHz-^{1}HNMR (CDCl$_3$) spectrum of La-BT.

Available in archival version
Disponible en version archivage

Figure 5.38. The room-temperature 400 MHz-^{1}HNMR (CDCl$_3$) spectrum of DBCO-mannosamine conjugate.

Available in archival version
Disponible en version archivage

Figure 5.39. The room-temperature 400 MHz-^{13}CNMR (CDCl$_3$) spectrum of DBCO-mannosamine conjugate.

Mass spectra

Figure 5.40. ESI-MS spectrum of tri-*tert*-butyl 2,2',2"-(10-((4-azidopyridin-2-yl)methyl)-1,4,7,10-tetraazacyclododecane-1,4,7-triyl)triacetate (compound 2).

Available in archival version
Disponible en version archivage

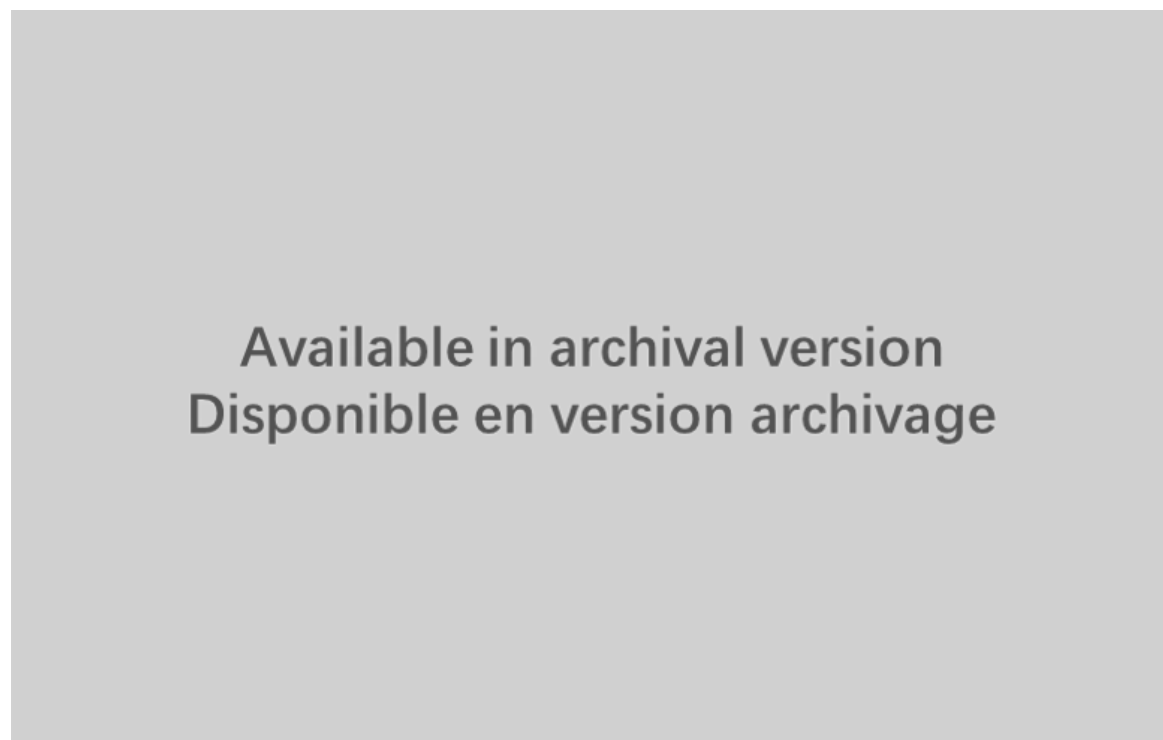**Figure 5.41.** ESI-MS spectrum of La-BT.

Available in archival version
Disponible en version archivage

Figure 5.42. ESI-MS spectrum of Eu-BT.
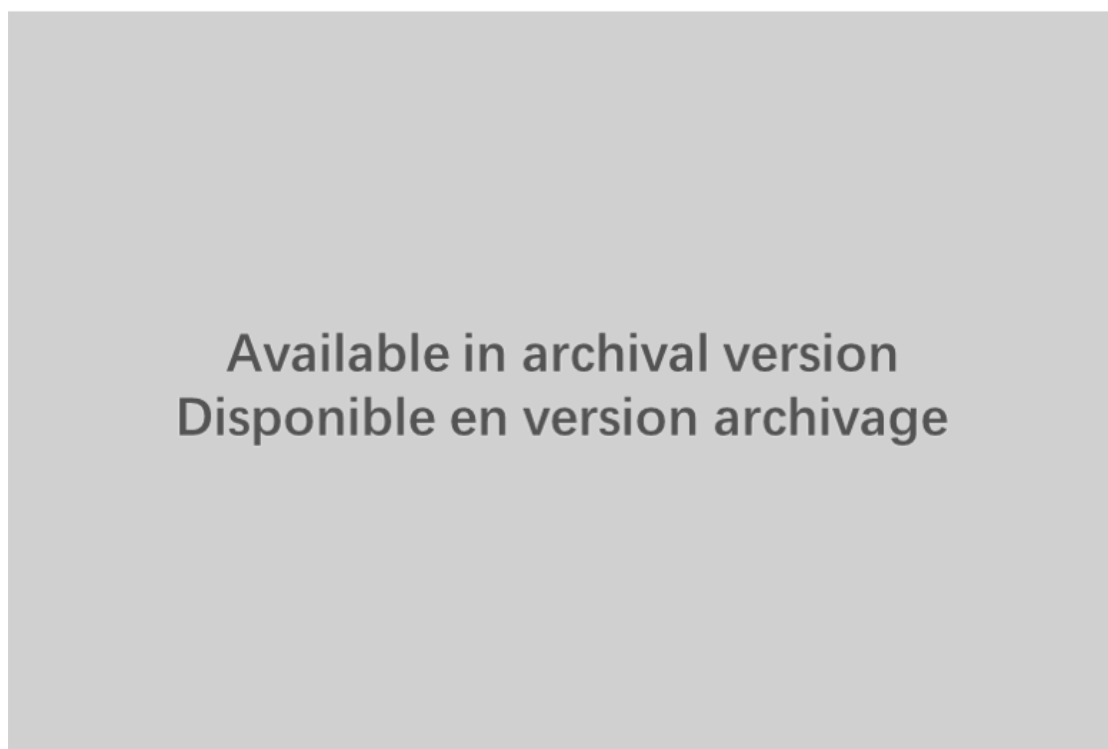
**Figure 5.43.** ESI-MS spectrum of DBCO-acid.
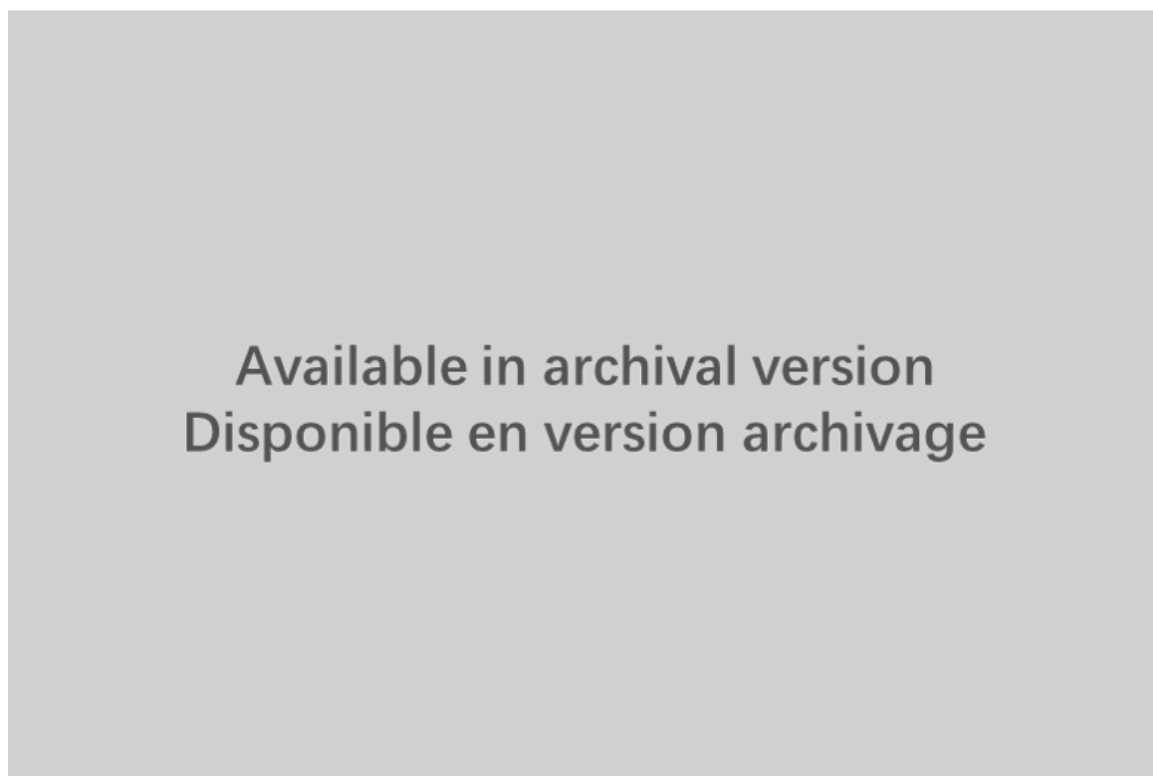
Figure 5.44. ESI-MS of DBCO-mannosamine conjugate.
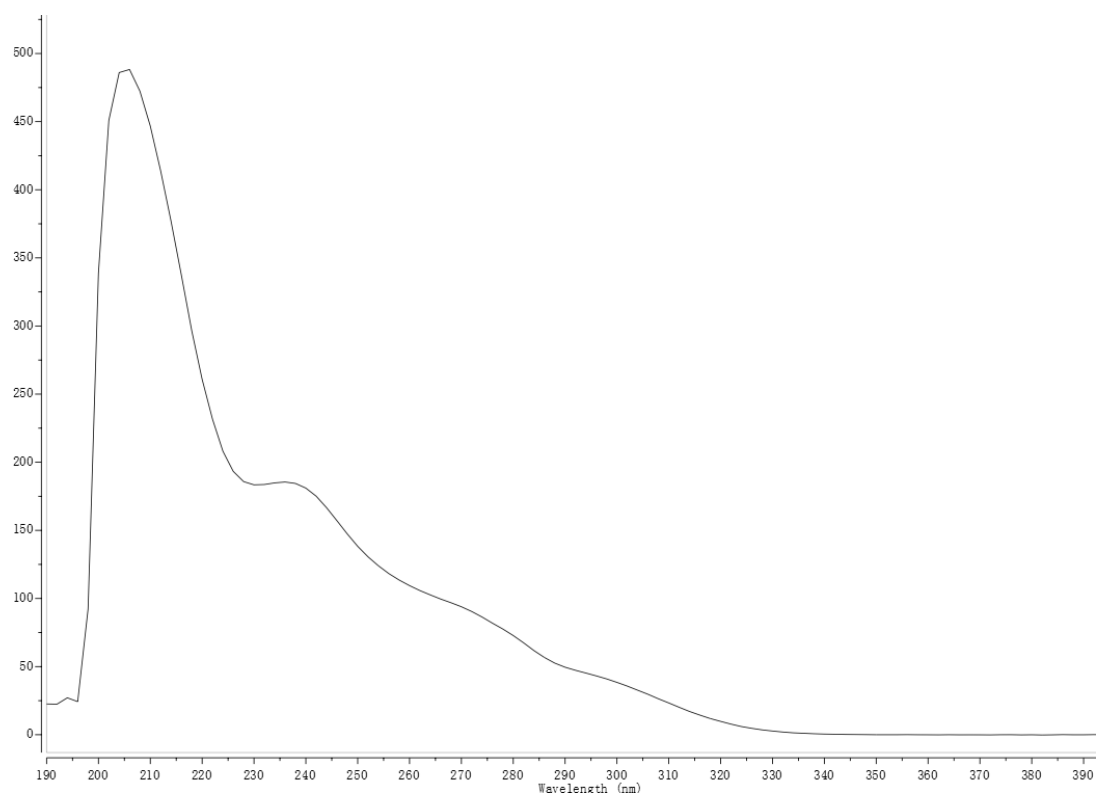
Figure 5.45. Absorption spectra of Eu-BT-DBCO conjugate products, obtained from a

HPLC coupled UV detector measuring the corresponding fragment.

List of References

1.   U.S. Geological Survey, 2020, Mineral commodity summaries 2020: U.S. Geological Survey, 200 p., https://doi.org/10.3133/ mcs2020.

2.   Anil Das (7 January 2011). "2011 spells desperate search for rare earth minerals". *International Business Times*.

3.   Donnot, M.; Guigues, J.; Lulzac, Y.; Magnien, A.; Parfenoff, A.; and Picot, P.,   Un nouveau type de gisement d'europium : la monazite grise á europium en nodules dans les schistes paléozoïques de Bretagne.   *Mineralium Deposita (in French)*, **1973**, *8*, 7–18.

4.   Bünzli, J. C.; Piguet, C.; Taking advantage of luminescent lanthanide ions. *Chem Soc Rev* **2005,** *34* (12), 1048-77.

5.   Karpo, A. B.;   Pushkarev, V. E.;   Krasovskii, V. I.; Tomilova, L. G. Z-scan study of nonlinear absorption in novel lanthanide bis-phthalocyanines. *Chem. Phy. Lett.* **2012,** *554*, 155-158.

6.   Ala-Kleme T.; Bünzli J.-C. G.; Bazin H.; Eliseeva S.V.; Faulkner S.; Hanninen P.; Harma H.; Hemmila I.; Hyppanen I.; Kankare J.; Kulmala S.; Kuusisto A.; Laitala V.; Mathis G.; Nann T.; Schaferling M.; Soukka T.; Spangler C.; Stenman U.-H.; Suom J.,D.; Sykes D.; Tanke H.J.; Tanner P.A.; Wang H.-Q.; Werts M.H.V., *Lanthanide Luminescence: Photophysical, Analytical and Biological Aspects*. Hänninen P.; Härmä H., Ed.; Springer: Springer-Verlag Berlin Heidelberg, **2011**; Vol. 7.

7.   Peijzel, P. S.;   Meijerink, A.;   Wegh, R. T.;   Reid, M. F.; Burdick, G. W., A complete $4f^n$ energy level diagram for all trivalent lanthanide ions. *J. Solid State Chem.* **2005,** *178* (2), 448-453.

8.   Dorenbos, P., The $4f^n$-$4f^{n-1}5d$ transitions of the trivalent lanthanides in halogenides

and chalcogenides. *J. Lumi.* **2000,** *91*, 91-106.

9. Gorller-Walrand C.; Binnemans K., Spectral intensities of f-f transitions. In *Handbook on the Physics and Chemistry of Rare Earths* Elsevier B. V.: Amsterdam, **1998**; Vol. 25, pp 101-264.

10. Tanner, P. A., Some misconceptions concerning the electronic spectra of tri-positive europium and cerium. *Chem. Soc. Rev.* **2013,** *42* (12), 5090-101.

11. IUPAC. Compendium of Chemical Terminology, 2nd ed. (the "Gold Book"). Compiled by A. D. McNaught and A. Wilkinson. Blackwell Scientific Publications, Oxford (1997). Online version (2019-) created by S. J. Chalk. ISBN 0-9678550-9-8. https://doi.org/10.1351/goldbook.

12. Roberto A.; Raffaele M.; Nicklas P., Pharmaceuticals in STP effluents and their solar photodegradation in aquatic environment. *Chemosphere* **2003,** *50*, 1319–1330.

13. Wong, K.-L.; Bünzli, J.-C. G.; Tanner, P. A., Quantum yield and brightness. *J. Lumi.* **2020,** *224*.

14. IUPAC. Compendium of Chemical Terminology, 2nd ed. (the "Gold Book"). Compiled by A. D. McNaught and A. Wilkinson. Blackwell Scientific Publications, Oxford (1997). Online version (2019-) created by S. J. Chalk. ISBN 0-9678550-9-8. https://doi.org/10.1351/goldbook.

15. Cranfill, P. J.; Sell, B. R.; Baird, M. A.; Allen, J. R.; Lavagnino, Z.; de Gruiter, H. M.; Kremers, G. J.; Davidson, M. W.; Ustione, A.; Piston, D. W., Quantitative assessment of fluorescent proteins. *Nat. Methods* **2016,** *13* (7), 557-62.

16. Strieth-Kalthoff, F.; James, M. J.; Teders, M.; Pitzer, L.; Glorius, F., Energy transfer catalysis mediated by visible light: principles, applications, directions. *Chem. Soc. Rev.* **2018,** *47* (19), 7190-7202.

17. Karin Pettersson K.; Krychenco A.; Rönnow E.; Ljungdahl T.; Mårtensson J.;

Albinsson B., Singlet Energy Transfer in Porphyrin-Based Donor-Bridge-Acceptor Systems: Interaction between Bridge Length and Bridge Energy. *J. Phys. Chem.* **2006,** *110*, 310-318.

18. Sekar, R. B.; Periasamy, A., Fluorescence resonance energy transfer (FRET) microscopy imaging of live cell protein localizations. *J. Cell Biol.* **2003,** *160* (5), 629-33.

19. N.J.Turro, *Molecular Photochemistry*, W. A. Benjamin, New York, **1967**.

20. Lazarides, T.; Sykes, D.; Faulkner, S.; Barbieri, A.; Ward, M. D., On the mechanism of d-f energy transfer in RuII/LnIII and OsII/LnIII dyads: Dexter-type energy transfer over a distance of 20 A. *Chemistry* **2008,** *14* (30), 9389-99.

21. Förster, T., *Delocalized excitation and excitation transfer. .* Academic Press Inc.: New York, **1965**; Vol. 3.

22. Centers for Disease Control and Prevention. Skin Cancer Prevention Progress Report. Atlanta, GA: Centers for Disease Control and Prevention, US Department of Health and Human Services; **2017.**

23. Ke, X. S.; Yang, B. Y.; Cheng, X.; Chan, S. L.; Zhang, J. L., Ytterbium(III) porpholactones: β-lactonization of porphyrin ligands enhances sensitization efficiency of lanthanide near-infrared luminescence. *Chemistry* **2014,** *20* (15), 4324-33.

24. Wong, W.-K.; Hou, A.; Guo, J.; He, H.; Zhang, L.; Wong, W.-Y.; Li, K.-F.; Cheah, K.-W.; Xue, F.; Mak, T. C. W., Synthesis, structure and near-infrared luminescence of neutral 3dâ€"4f bi-metallic monoporphyrinate complexes. *J. Chem. Soc., Dalton Trans.* **2001,** (20), 3092-3098.

25. Leung, W.; Zhang, Q.; Yi, X., Recent developments in the coordination and organometallic chemistry of Kläui oxygen tripodal ligands. *Coord. Chem. Rev.* **2007,** *251* (17-20), 2266-2279.

26. Zhu, X. J.; Wang, P.; Leung, H. W.; Wong, W. K.; Wong, W. Y.; Kwong, D. W., Synthesis, characterization, and DNA-binding and -photocleavage properties of water-soluble lanthanide porphyrinate complexes. *Chem. Eur. J.* **2011,** *17* (25), 7041-7052.

27. Hu, J. Y.;Ning, Y.; Meng, Y. S.; Zhang, J.; Wu, Z. Y.; Gao, S.; Zhang, J. L., Highly near-IR emissive ytterbium(iii) complexes with unprecedented quantum yields. *Chem. Sci.* **2017,** *8* (4), 2702-2709.

28. Semenishyn, N.; Rusakova, N.; Mazepa A. V.; Korovin, Y., Synthesis of Ditopic Porphyrins and Lanthanide Complexes on their Basis: Luminescent Features. *Macroheterocycles* **2009,** *2* (1), 57-59.

29. Rusakova, N.; Semenishyn, N.; Korovin, Y., Heteronuclear lanthanide-containing complexes on the base of modified porphyrins and their luminescent properties. *J. Porphyr. Phthalocyanines* **2010,** *14* (02), 166-169.

30. Semenishyn, N.; Rusakova, N., Study of Structure−Properties Relationship for Lanthanide Tetrapyrrolic Macrocycles Modified with Aminopolycarboxylate Substituents. *Macroheterocycles* **2016,** *9* (2), 163-168.

31. Buchler, J. W.; De Cien, A.; Fischer, J.; Kihn-Botulinski, M.; Paulus, H.; Weiss, R., Cerium(IV) Bis(octaethylporphyrinate) and Dicerium(III) Tris(octaethylporphyrinate): Parents of a New Family of Lanthanoid Double-Decker and Triple-Decker Molecules. *J. Am. Chem. Soc.* **1986,** *108*, 3652-3659.

32. Jiang, J.; Machida, K.; Adachi, G., Synthesis of Water-Soluble Lanthanide Porphyrin Sandwich Complexes: Bis(tetrapyridylporphyrinato) Cerium(IV), [Ce(tptp)2], and Bis(tetramethylpyridylporphyrinato Cerium(IV), [Ce(tmpyp)2]. *Bull. Chem. Soc. Jpn.* **1992,** *65* (7), 1990-1992.

33. Chabach, D.; Tahiri, M.; De Cian, A.; Fischer, J.; Weiss, R.; Bibout, M. E. M., Tervalent-Metal Porphyrin-Phthalocyanine Heteroleptic Sandwich-Type Complexes.

Synthesis, Structure, and Spectroscopic Characterization of Their Neutral, Singly-Oxidized, and Singly-Reduced States. *J. Am. Chem. Soc.* **1995,** *117*, 8548-8556.

34. Chabach, D.; Tahiri, M.; De Cian, A.; Fischer, J.; Weiss, R.; Bibout, M. E. M., Mixed-Metal Triple-Decker Sandwich Complexes with the Porphyrin/Phthalocyanine/Porphyrin Ligand System. *Angew. Chem. Int. Ed.* **1996,** *35* (8), 898-899.

35. Jiang, J.; Liu, W.; Cheng, K; Poon, K.; Ng, K. P., Heteroleptic Rare Earth Double-Decker Complexes with Porphyrinato and 2,3-Naphthalocyaninato Ligands − Preparation, Spectroscopic Characterization, and Electrochemical Studies. *Eur. J. Inor.. Chem.* **2000,** *2001* (2), 413-417.

36. Birnbaum, D. W.; Birnbaum, E. R., Lanthanide ions activate α-amylase. *Biochemistry* **1973,** *12* (18), 3489–3491.

37. Spencer, A.; Wilson, S.; Harpur, E.; Gadolinium chloride toxicity in the mouse. *Hum. Exp. Toxicol.* **1998,** *17* (11), 633-637.

38. Thompson, M. K.; Botta, M.; Nicolle, G.; Helm, L.; Aime, S.; Merbach, A. E.; Raymond, K. N., A Highly Stable Gadolinium Complex with a Fast, Associative Mechanism of Water Exchange. *J. Am. Chem. Soc.* **2003,** *125* (47), 14274–14275.

39. Cacheris, W. P.; Quay S. C.; Rocklage, S. M., The relationship between thermodynamics and the toxicity of gadolinium complexes. *Magn. Reson. Imaging* **1990,** *8* (4), 467-481.

40. Clough, T. J.; Jiang, L.; Wong, K. L.; Long, N. J., Ligand design strategies to increase stability of gadolinium-based magnetic resonance imaging contrast agents. *Nat. Commun.* **2019,** *10* (1), 1420.

41. Zhao, J.; Zhong, D.; Zhou, S., NIR-I-to-NIR-II fluorescent nanomaterials for biomedical imaging and cancer therapy. *J. Mater. Chem. B* **2018,** *6* (3), 349-365.

42. Ethirajan, M.; Chen, Y.; Joshi, P.; Pandey, R. K., The role of porphyrin chemistry in tumor imaging and photodynamic therapy. *Chem. Soc. Rev.* **2011,** *40* (1), 340-62.

43. Zhang, J.; Jiang, C.; Figueiro Longo, J. P.; Azevedo, R. B.; Zhang, H.; Muehlmann, L. A., An updated overview on the development of new photosensitizers for anticancer photodynamic therapy. *Acta Pharm. Sin. B.* **2018,** *8* (2), 137-146.

44. Macdonald, I. J.; Dougherty, T. J., Basic principles of photodynamic therapy. *J. Porphyr. Phthalocyanines* **2001,** *5*, 105–129.

45. Strecker, E. A.; Palmer, H. P.; Braceland, F. J., HEMATOPORPHYRIN AS A THERAPEUTIC AGENT IN THE PSYCHOSES. *Am. J. Psychiatry* **1934,** *90* (6), 1157-1173.

46. Issa, M. C. A.; Manela-Azulay, M., Photodynamic therapy: a review of the literature and image documentation. *An. Bras. Dermatol.* **2010,** *85* (4), 501-511.

47. Otsuki, J., STM studies on porphyrins. *Coord. Chem. Rev.* **2010,** *254* (19-20), 2311-2341.

48. Beeby, A.; Dickins, R. S.; FitzGerald, S.; Govenlock, L. J.; Parker, D.; Williams, J. A. G.; Maupin, C. L.; Riehl, J. P.; Siligardi, G., Porphyrin sensitization of circularly polarised near-IR lanthanide luminescence: enhanced emission with nucleic acid binding. *Chem. Comm.* **2000,** (13), 1183-1184.

49. Wong, W.; Zhu, X.; Wong, W., Synthesis, structure, reactivity and photoluminescence of lanthanide(III) monoporphyrinate complexes. *Coord. Chem. Rev.* **2007,** *251* (17-20), 2386-2399.

50. Birin, K. P.; Gorbunova, Y. G.; Tsivadze, A. Y., Selective one-step synthesis of triple-decker (porphyrinato)(phthalocyaninato) early lanthanides: the balance of concurrent processes. *Dalton Trans.* **2011,** *40* (43), 11539-49.

51. Zhang, T.; Zhu, X.; Cheng, C. C.; Kwok, W. M.; Tam, H. L.; Hao, J.; Kwong, D.

W.; Wong, W. K.; Wong, K. L., Water-soluble mitochondria-specific ytterbium complex with impressive NIR emission. *J. Am. Chem. Soc.* **2011,** *133* (50), 20120-2.

52. Otsuki, J.; Kawaguchi, S.; Yamakawa, T.; Asakawa, M.; Miyake, K., Arrays of Double-Decker Porphyrins on Highly Oriented Pyrolytic Graphite. *Langmuir* **2006,** *22* (13), 5708–5715.

53. Tanner, P. A.;Zhou, L.; Duan, C.; Wong, K. L., Misconceptions in electronic energy transfer: bridging the gap between chemistry and physics. *Chem. Soc. Rev.* **2018,** *47* (14), 5234-5265.

54. Shavaleev, N. M.; Eliseeva, S. V.; Scopelliti, R.; Bünzli, J. C., Influence of symmetry on the luminescence and radiative lifetime of nine-coordinate europium complexes. *Inorg. Chem.* **2015,** *54* (18), 9166-73.

55. Zhang, T.; Lan, R.; Chan, C. F.; Law, G. L.; Wong, W. K.; Wong, K. L., In vivo selective cancer-tracking gadolinium eradicator as new-generation photodynamic therapy agent. *Proc. Natl. Acad. Sci. U S A* **2014,** *111* (51), E5492-7.

56. Tanielian, C.; Wolff, C.; Esch, M., Singlet Oxygen Production in Water: Aggregation and Charge-Transfer Effects. *J. Phys. Chem.* **1996,** *100* (16), 6555–6560.

57. Ke, X.; Wang. D.; Chen, C.; Yang, A.; Han, Y.; Ren, L.; Li, D.; Wang H., Co-enhancement of fluorescence and singlet oxygen generation by silica-coated gold nanorods core-shell nanoparticle. *Nanoscale Res. Lett.* **2014,** *9*, 666.

58. Song, R.; Feng, Y.; Wang, D.; Xu, Z.; Li, Z.; Shao, X., Phytoalexin Phenalenone Derivatives Inactivate Mosquito Larvae and Root-knot Nematode as Type-II Photosensitizer. *Sci. Rep.* **2017,** *7*, 42058.

59. Berera, R.; van Grondelle, R.; Kennis, J. T., Ultrafast transient absorption spectroscopy: principles and application to photosynthetic systems. *Photosynth. Res.* **2009,** *101* (2-3), 105-18.

60. Bose, R.; Ahmed, G. H.; Alarousu, E.; Parida, M. R.; Abdelhady, A. L.; Bakr, O. M.; Mohammed, O. F., Direct Femtosecond Observation of Charge Carrier Recombination in Ternary Semiconductor Nanocrystals: The Effect of Composition and Shelling. *J. Phys. Chem. C* **2015,** *119* (6), 3439-3446.

61. El-Ballouli, A. O.; Alarousu, E.; Bernardi, M.; Aly, S. M.; Lagrow, A. P.; Bakr, O. M.; Mohammed, O. F., Quantum confinement-tunable ultrafast charge transfer at the PbS quantum dot and phenyl-C(6)(1)-butyric acid methyl ester interface. *J. Am. Chem. Soc.* **2014,** *136* (19), 6952-9.

62. Wang, Q.; Dai, Y.; Xu, J.; Cai, J.; Niu, X.; Zhang, L.; Chen, R.; Shen, Q.; Huang, W.; Fan, Q., All-in-One Phototheranostics: Single Laser Triggers NIR-II Fluorescence/Photoacoustic Imaging Guided Photothermal/Photodynamic/Chemo Combination Therapy. *Adv. Funct. Mater.* **2019,** *29* (31).

63. Merbach, A.; Helm, L.; Tóth, É., *The Chemistry of Contrast Agents in Medical Magnetic Resonance Imaging*. 2 ed.; John Wiley & Sons, Ltd: **2013**.

64. Li, H.; Meade, T. J., Molecular Magnetic Resonance Imaging with Gd(III)-Based Contrast Agents: Challenges and Key Advances. *J. Am. Chem. Soc.* **2019,** *141* (43), 17025-17041.

65. Townsend, D. W., Physical principles and technology of clinical PET imaging. *Ann. Acad. Med. Singap.* **2004,** *33* (2), 133-145.

66. Martiniova, L.; De Palatis L.; Etchebehere, E.; Ravizzini, G., Gallium-68 in Medical Imaging. *Curr. Radiopharm.* **2016,** *9* (3), 187-207.

67. Brady, Z.; Taylor, M. L.; Haynes, M.; Whitaker, M.; Mullen, A.; Clews, L.; Partridge, M.; Hicks, R. J.; Trapp, J. V., The clinical application of PET/CT: a contemporary review. *Australas. Phys. Eng. Sci. Med.* **2008,** *31* (2), 90-109.

68. Bünzli, J.-C. G., Lanthanide Luminescence for Biomedical Analyses and Imaging.

Chem. Rev. **2010,** *110* (5), 2729–2755.

69. Rajora, M. A.; Lou, J. W. H.; Zheng, G., Advancing porphyrin's biomedical utility via supramolecular chemistry. *Chem. Soc. Rev.* **2017,** *46* (21), 6433-6469.

70. Pasternack, F.; Huber, P. R.; Boyd, P.; Engasser, G.; Francesconi, L.; Gibbs, E.; Fasella, P.; Venturo, G. C.; Hinds, L., Aggregation of meso-substituted water-soluble porphyrins. *J. Am. Chem. Soc.* **1972,** *94* (13), 4511–4517.

71. Galvao, J.; Davis, B.; Tilley, M.; Normando, E.; Duchen, M. R.; Cordeiro, M. F., Unexpected low-dose toxicity of the universal solvent DMSO. *FASEB. J.* **2014,** *28* (3), 1317-30.

72. Gouterman, M.; Khalil, G.-E., Porphyrin free base phosphorescence. *J. Mol. Spectrosc.* **1974,** *53* (1), 88-100.

73. Harriman, A., Luminescence of porphyrins and metalloporphyrins. Part 1.—Zinc(II), nickel(II) and manganese(II) porphyrins. *J. Chem. Soc., Faraday Trans.2* **1980,** *76* (0).

74. Ermolina, E. G.; Kuznetsova, R. T.; Solodova, T. A.; Tel'minov, Evegenii, N. T.; Kopylova, T. N.; Mayer, G. V.; Semenishyn, N. N.; Rusakova, N. V.; Korovin, Y. V., Photophysics and oxygen sensing properties of tetraphenylporphyrin lanthanide complexes. *Dyes Pigm.* **2013,** *97* (1), 209-214.

75. Beeby, A.; Clarkson, I. M.; Dickins, R. S.; Faulkner, S.; Parker, D.; Royle, L.; de Sousa, A. S.; Williams, J. A. G.; Woods M., Non-radiative deactivation of the excited states of europium, terbium and ytterbium complexes by proximate energy-matched OH, NH and CH oscillators: an improved luminescence method for establishing solution hydration states. *J. Chem. Soc. Perkin Trans. 2* **1999**, 493-504.

76. Li, H.; Xie, C.; Lan, R.; Zha, S.; Chan, C. F.; Wong, W. Y.; Ho, K. L.; Chan, B. D.; Luo, Y.; Zhang, J. X.; Law, G. L.; Tai, W. C. S.; Bunzli, J. G.; Wong, K. L., A Smart

Europium-Ruthenium Complex as Anticancer Prodrug: Controllable Drug Release and Real-Time Monitoring under Different Light Excitations. *J. Med. Chem.* **2017,** *60* (21), 8923-8932.

77. Powell, D. H.; Dhubhghaill, O. M. N.; Pubanz, D.; Helm, L.; Lebedev, Y. S.; Schlaepfer, W.; Merbach, A. E., Structural and Dynamic Parameters Obtained from ^{17}O NMR, EPR, and NMRD Studies of Monomeric and Dimeric Gd^{3+} Complexes of Interest in Magnetic Resonance Imaging: An Integrated and Theoretically Self-Consistent Approach. *J. Am. Chem. Soc.* **1996,** *118* (39), 9333–9346.

78. Shen, Y.; Goerner, F. L.; Snyder, C.; Morelli, J. N.; Hao, D.; Hu, D.; Li, X.; Runge, V. M., T1 relaxivities of gadolinium-based magnetic resonance contrast agents in human whole blood at 1.5, 3, and 7 T. *Invest. Radiol.* **2015,** *50* (5), 330-8.

79. Ke, X.-S.; Tang, J.; Yang, Z.-S.; Zhang, J.-L., β-conjugation of gadolinium(III) DOTA complexes to zinc(II) porpholactol as potential multimodal imaging contrast agents. *J. Porphyr. and Phthalocyanines* **2014,** *18* (10&11), 950-959.

80. De Leon-Rodriguez, L. M.; Martins, A. F.; Pinho, M. C.; Rofsky, N. M.; Sherry, A. D., Basic MR relaxation mechanisms and contrast agent design. *J. Magn. Reson. Imaging* **2015,** *42* (3), 545-65.

81. Schmidt, R.; Afshari, E., Comment on "Effect of solvent on the phosphorescence rate constant of singlet molecular oxygen (1.DELTA.g)". *J. Phys. Chem.* **1990,** *94* (10), 4377–4378.

82. Samaroo, D.; Vinodu, M.; Chen, X.; Drain, C. M., meso-Tetra(pentafluorophenyl)porphyrin as an efficient platform for combinatorial synthesis and the selection of new photodynamic therapeutics using a cancer cell line. *J. Comb. Chem.* **2007,** *9* (6), 998-1011.

83. Lim, G. N.; Obondi, O. C.; D'Souza, F., A High-Energy Charge-Separated State of

1.70 eV from a High-Potential Donor–Acceptor Dyad: A Catalyst for Energy-Demanding Photochemical Reactions. *Angew. Chem. Int. Ed.* **2016,** *55* (38), 11517-11521.

84. Hang, H. C.; Yu, C.; Kato, D. L.; Bertozzi, C. R., A metabolic labeling approach toward proteomic analysis of mucin-type O-linked glycosylation. *Proc. Natl. Acad. Sci. U S A* **2003,** *100* (25), 14846-14851.

85. Hang, H. C.; Wilson, J. P.; Charron, G., Bioorthogonal Chemical Reporters for Analyzing Protein Lipidation and Lipid Trafficking. *Acc. Chem. Res.* **2011,** *44* (9), 699–708.

86. Devaraj, N. K.; Thurber, G. M.; Keliher, E. J.; Marinelli, B.; Weissleder, R., Reactive polymer enables efficient in vivo bioorthogonal chemistry. *Proc. Natl. Acad. Sci. U S A* **2012,** *109* (13), 4762-7.

87. Kolb, H. C.; Finn, M. G.; Sharpless K. B., Click Chemistry: Diverse Chemical Function from a Few Good Reactions. *Angew. Chem. Int. Ed.* **2001,** *40* (11), 2004-2021.

88. El-Sagheer, A. H.; Brown, T., Click chemistry with DNA. *Chem. Soc. Rev.* **2010,** *39* (4), 1388-405.

89. Agard, N. J.; Prescher, J. N.; Bertozzi, C. R., A Strain-Promoted [3+2] Azide-Alkyne Cycloaddition for Covalent Modification of Biomolecules in Living Systems. *J. Am. Chem. Soc.* **2004,** *126* (46), 15046–15047.

90. Wang, K.; Sachdeva, A.; Cox, D. J.; Wilf, N. M.; Lang, K.; Wallace, S.; Mehl, R. A.; Chin, J. W., Optimized orthogonal translation of unnatural amino acids enables spontaneous protein double-labelling and FRET. *Nat. Chem.* **2014,** *6* (5), 393-403.

91. Zhang, C.; Dai, P.; Vinogradov, A. A.; Gates, Z. P.; Pentelute, B. L., Site-Selective Cysteine-Cyclooctyne Conjugation. *Angew. Chem. Int. Ed. Engl.* **2018,** *57* (22), 6459-6463.

92. Ning, X.; Guo, J.; Wolfert, M. A.; Boons, G. J., Visualizing metabolically labeled glycoconjugates of living cells by copper-free and fast huisgen cycloadditions. *Angew. Chem. Int. Ed. Engl.* **2008,** *47* (12), 2253-5.

93. Sletten, E. M.; Bertozzi, C. R., A Hydrophilic Azacyclooctyne for Cu-Free Click Chemistry. *Org. Lett.* **2008,** *10* (14), 3097–3099.

94. Ramil, C. P.; Lin, Q., Bioorthogonal chemistry: strategies and recent developments. *Chem. Commun. (Camb.)* **2013,** *49* (94), 11007-22.

95. O'Malley, W. I.; Abdelkader, E. H.; Aulsebrook, M. L.; Rubbiani, R.; Loh, C. T.; Grace, M. R.; Spiccia, L.; Gasser, G.; Otting, G.; Tuck, K. L.; Graham, B., Luminescent Alkyne-Bearing Terbium(III) Complexes and Their Application to Bioorthogonal Protein Labeling. *Inorg. Chem.* **2016,** *55* (4), 1674-82.

96. Zheng, J.; Zhan, Q.; Jiang, L.; Xing, D.; Zhang, T.; Wong, K.-L., A bioorthogonal time-resolved luminogenic probe for metabolic labelling and imaging of glycans. *Inorg. Chem. Front.* **2020,** *7* (21), 4062-4069.

97. Sampathkumar, S. G.; Li, A. V.; Yarema, K. J., Synthesis of non-natural ManNAc analogs for the expression of thiols on cell-surface sialic acids. *Nat. Protoc.* **2006,** *1* (5), 2377-85.

98. Kiraev, S. R.; Mathieu, E.; Siemens, F.; Kovacs, D.; Demeyere, E.; Borbas, K. E., Lanthanide(III) Complexes of Cyclen Triacetates and Triamides Bearing Tertiary Amide-Linked Antennae. *Molecules* **2020,** *25* (22).

99. Binnemans, K., Interpretation of europium(III) spectra. *Coord. Chem. Rev.* **2015,** *295*, 1-45.

CURRICULUM VITAE

Academic qualifications of the thesis author, Mr. XIE Chen:

- Received the degree of Bachelor of Science (Honours) from Hong Kong Baptist University, November 2015.

- Received the degree of Master of Philosophy from Hong Kong Baptist University, November 2017.

<div align="right">August 2021</div>

Résumé étendu en français

Complexes à base de lanthanides en tant que systèmes intégrés multifonctionnels en théranostique photodynamique

XIE Chen

RÉSUMÉ

Cette thèse présente mes travaux de conception, de préparation et de caractérisation de plusieurs types de nouveaux complexes de lanthanides pour des applications dans le domaine de la théranostique photodynamique. Tous les produits rapportés fonctionnent comme des systèmes intégrés sur lesquels diverses fonctions peuvent être réalisées simultanément. Bien que les termes "complexes de lanthanides" et "théranostique photodynamique" soient des domaines de recherche relativement larges. Les intérêts spécifiques se concentrent sur l'utilisation des lanthanides et de leurs ligands dans d'éventuelles imageries cliniques et thérapies photodynamiques (PDT). Les lanthanides dont il sera question ici sont principalement Eu(III), Gd(III) et Yb(III), en raison de leurs propriétés spectroscopiques uniques. Les méthodes de diagnostic à utiliser sont l'imagerie moléculaire par lumière visible/proche infrarouge et l'imagerie par résonance magnétique. Les effets médicaux possibles sont justifiés par la génération d'oxygène singulet, une espèce active dans la PDT.

Projet 1: Luminosité impressionnante dans le proche infrarouge et production d'oxygène singulet à partir de complexes stratégiques à double étage de lanthanide et de porphyrine en solution aqueuse.

1.1 Introduction

Quatre complexes à double étage de lanthanides à base de porphyrine solubles dans l'eau (LnDD, où Ln = La, Er, Gd et Yb) ont été présentés, et certains présentent des propriétés photophysiques remarquables dans le proche infrarouge en solution aqueuse. Après l'installation stratégique de deux chaînes de diéthylène glycol (DEG) hydrophiles et courtes sur la porphyrine Por(2DEG) pour la complexation en sandwich des lanthanides, l'YbDD a présenté un rendement quantique et une durée de vie de la luminescence dans le proche infrarouge dans l'eau qui dépassent ceux de l'YbN rapportés précédemment1. L'efficacité de la génération d'oxygène singulet en termes de rendement quantique (Φ_{1O2}) du GdDD a été mesurée comme étant légèrement supérieure à celle du GdN.[1] Ce travail fournit des résultats uniques pour les données photophysiques du LnDD en milieu aqueux et, plus important encore, une nouvelle dimension pour la conception et le développement futurs de bisporphyrinates de lanthanide à double étage hydrosolubles basés sur la théranostique moléculaire. Une élucidation structurelle dans cette étude a été menée par différentes techniques, comme décrit ci-dessous.
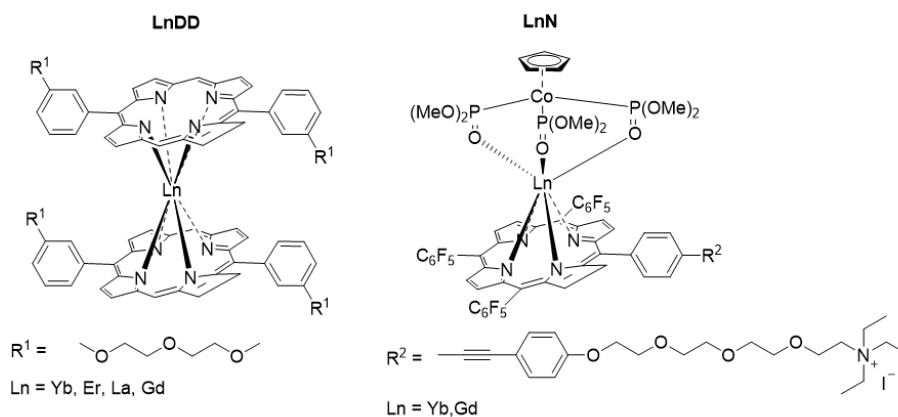
Figure 1. Structures moléculaires du LnDD dans ce travail et du LnN comme échantillons de référence pour comparaison.[1]

1.2 Résultats et discussion

1.2.1 Caractérisation structurelle par résonance magnétique nucléaire

En raison des propriétés paramagnétiques résultant des électrons sur les orbitales f des complexes de Gd(III) et d'Yb(III), le LaDD a été synthétisé comme analogue pour l'analyse par résonance magnétique nucléaire (RMN) 1H. Après l'ajout d'hydrate d'hydrazine, un spectre RMN bien résolu de LaDD a pu être obtenu (figure 2), car l'hydrate d'hydrazine a servi d'agent réducteur et a favorisé la formation de complexes diamagnétiques monoanioniques. Les protons du ligand unique Por(2DEG) peuvent être classés en deux catégories : périphériques et internes. Les protons aromatiques périphériques sont généralement situés autour de 6,5-10,0 ppm, tandis que les protons aliphatiques de la chaîne latérale du DEG se situent normalement dans la gamme de 1,5-4,0 ppm. Le pic de l'hydrate d'hydrazine mélangé au DMSO-d$_6$ (DMSO : diméthylsulfoxyde) est observé à 2,6 ppm. L'effet du courant de cycle déplace fortement les deux protons internes de la porphyrine vers le haut du champ à -3,2 ppm. La disparition des pics N-H internes et le déplacement des protons peuvent alors servir

d'indication de la métallisation avec l'ion lanthanide. Aucun signal n'est observé dans la gamme négative (équivalente aux protons N-H internes) dans le spectre de LaDD, tandis que tous les pics sont soumis à un décalage vers le haut du champ en raison de l'anisotropie de l'ion métallique f ainsi que de l'impact des décalages induits par les lanthanides. Il est à noter que les trimères supramoléculaires théoriquement les plus possibles ou même les structures d'agrégats multiples peuvent également donner lieu à des spectres RMN similaires, mais les images MS et STM à haute résolution corroborent sans ambiguïté la structure à double étage du LaDD (et donc de la série des LnDD).
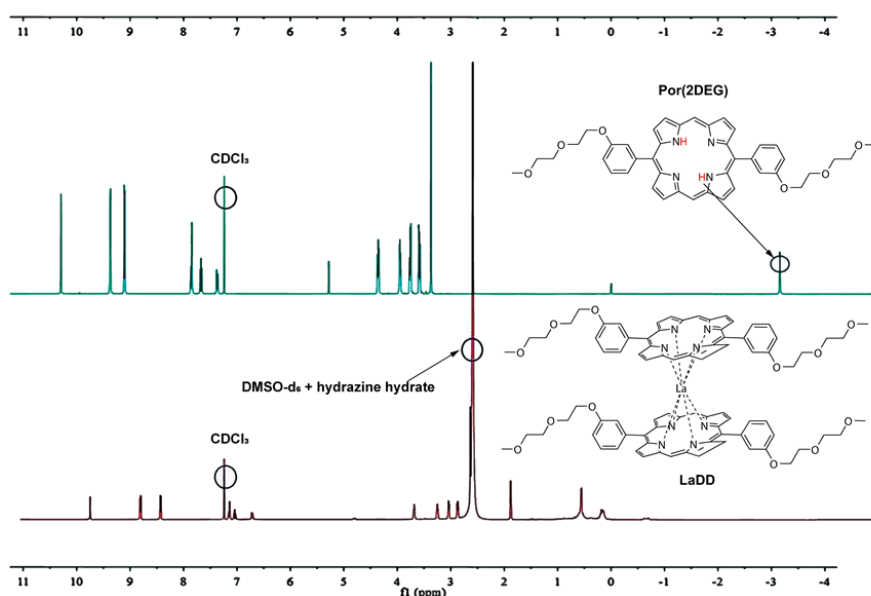
Figure 2. Spectre RMN-1H à température ambiante de (a) le ligand Por(2DEG) dans CDCl$_3$ et (b) LaDD dans CDCl3 : DMSO-d$_6$ 1:1 mélangé avec 1% d'hydrate d'hydrazine.

1.2.2 Caractérisation structurelle par microscopie à effet tunnel à balayage

La microscopie à effet tunnel à balayage est une technique avancée qui peut être utilisée pour sonder les assemblages moléculaires sur la base de molécules individuelles, comme mentionné dans la section d'introduction. L'étude de l'assemblage et de la structure des porphyrines à l'interface vide-liquide sur des surfaces est relativement

avancée. En particulier, plusieurs études ont été entreprises sur la molécule structurée à deux étages.[2] L'YbDD a été déposé sur une surface HOPG (0001) propre en plaçant une goutte de solution diluée et en l'évaporant à température ambiante. Les molécules ont formé des motifs auto-assemblés sans autre traitement, par adsorption et diffusion en surface. Image topographique STM La figure 2.3 montre une image à fort grossissement d'une région d'une surface coulée en gouttes avec des caractéristiques supplémentaires décorant les bords des marches. Comme le montre le zoom, celles-ci forment une rangée périodique d'une séparation de ~4 nm et d'une hauteur apparente de ~ 1 nm (profil de ligne de la figure 3). Cette hauteur enregistrée à l'état rempli à -1,5 V est fortement influencée par les effets électroniques de l'apex de la pointe et des jonctions moléculaire-surface.
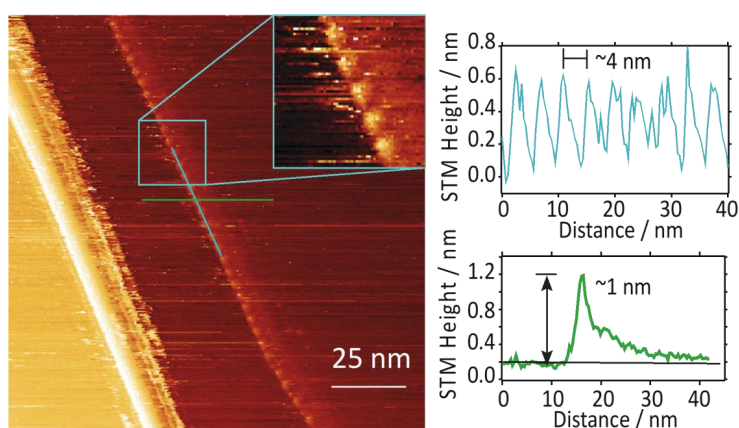
Figure 3. Caractérisation de la structure. Imagerie STM pour la coulée de gouttes d'YbDD sur HOPG : (gauche) 5 µL de toluène avec 1 mmol d'échantillon d'YbDD, 140 × 140 nm^2, polarisation de l'échantillon de -1,5 V, 50 pA, (encart) boîte bleue : une image à fort grossissement, lignes cyan et vertes : indiquant les profils de ligne de hauteur. (en haut à droite) Profil de ligne à partir de la figure de gauche le long de la rangée de caractéristiques ; (en bas à droite) profil de ligne à travers le bord de la marche HOPG, la hauteur de la caractéristique ~1 nm (terrasse inférieure) est indiquée.

1.2.3 Emission spectra

Comme le montre la figure 4, le spectre d'émission de l'YbDD comprend plusieurs parties : l'émission visible-NIR du ligand porphyrine et l'émission NIR de l'Yb^{3+} ($2F_{5/2}$ → $2F_{7/2}$), affichée avec une hauteur de pic égale dans cette figure. Les pics à 647 nm et 699 nm représentent la fluorescence de la porphyrine provenant du singulet de la bande Q nominalement étiqueté S1. L'émission du singulet S2 (bande B) est également observée à une intensité beaucoup plus faible et à des longueurs d'onde plus courtes. Les bandes d'émission chaude 1, 2 et 3 de la figure 4 peuvent correspondre aux transitions des trois états excités de $^2F_{5/2}$. On observe que le transfert d'énergie des ligands de la porphyrine vers l'ion Yb3+ est efficace puisque l'ion métallique n'est pas excité par le rayonnement de 425 nm en l'absence d'antenne. Cependant, la présence à la fois de la fluorescence des ligands et de l'émission des lanthanides à température ambiante suggère que le taux de transfert d'énergie de la porphyrine à Yb3+ est similaire au régime nanoseconde. Le rendement quantique d'émission plus faible de l'YbDD dans l'eau que dans le toluène est attribuable à l'extinction par les vibrations O-H à haute fréquence. Les ions lanthanides trivalents appartiennent à la catégorie des acides de Lewis durs avec un nombre de coordination allant jusqu'à 8-12, de sorte que la sous-saturation de la sphère de coordination interne des lanthanides par les ligands offre des espaces libres pour la coordination des molécules de solvant. Le système YbN a été confirmé comme ayant un Yb^{3+} insaturé à sept coordinations : quatre N provenant du cycle porphyrine et trois O provenant des atomes d'oxygène coiffés par l'anion Kläui $[(5-C_5H_5) Co\{(MeO)_2P=O\}_3]-$. Pour protéger l'ion Yb^{3+} dans un environnement aqueux et supprimer l'extinction de la luminescence, la stratégie de complexation à deux étages dans l'YbDD répond à l'exigence d'un nombre de coordination de huit.
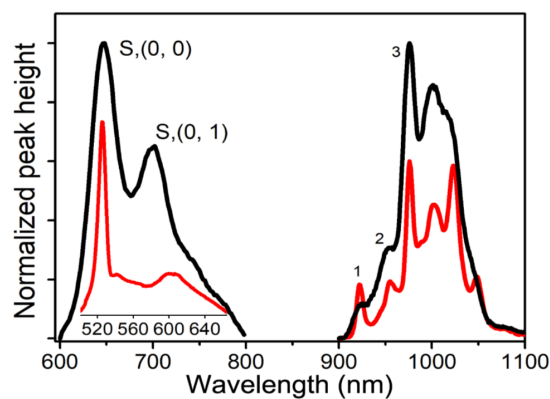
Figure 4. Comparaison des bandes d'émission de YbN (noir) et YbDD (rouge) à 298 K en solution aqueuse (λ_{ex} = 425 nm).

1.2.4 Brightness and lifetime

La luminosité est le produit du rendement quantique et du coefficient d'atténuation molaire,[3] et elle démontre l'énergie radiante émise par unité de surface d'intervalle de fréquence par angle solide. Pour les besoins de la bioimagerie, où un faible dosage est préférable en raison des effets indésirables, la luminosité est un indicateur d'applicabilité supérieur au rendement quantique, car avec une luminosité plus élevée, les composés fluorescents à faible abondance sont détectés plus facilement. La luminosité de l'YbDD dépasse celle de l'YbN par un facteur de 1,37 (tableau 1). Pour expliquer ce résultat : L'YbDD possédant deux groupes ligands d'antenne devrait dépasser l'YbN n'en possédant qu'un seul. Les durées de vie d'émission pour les transitions $^2F_{5/2} \rightarrow \, ^2F_{7/2}$ ont été déterminées à la fois dans l'eau et le toluène pour l'YbDD et dans le toluène pour l'YbN. La durée de vie de l'YbDD est de 23,6 µs dans l'eau (figure 5) et de 28,2 µs dans le toluène, qui sont toutes deux supérieures à la valeur de l'YbN (tableau 1). L'YbDD présente une durée de vie $^2F_{5/2} \rightarrow \, ^2F_{7/2}$ plus longue qui résulte principalement de sa symétrie plus élevée que celle de l'YbN. Avec une structure plus symétrique, il y a moins de transitions f-f possibles, et la durée de vie pour une

transition spécifique sera plus longue.[4] Cette tendance est cohérente avec les rendements quantiques d'émission NIR mesurés dans l'eau et le toluène. Il convient de noter que la plupart des colorants NIR à base de porphyrine pour les applications biologiques ont une faible émission dans la fenêtre biologique NIR-II en raison de l'absence de coordination métallique, tandis que leurs pics d'absorption maximaux sont généralement situés entre 650 et 800 nm, ces deux raisons limitant leurs perspectives d'application.

Tableau 1 2.2. Durée de vie de la luminescence (τ), rendement quantique (Φ) et brillance (BR) de YbDD et YbN dans le toluène ou l'eau.

	τ (µs)[a]		Φ (%)[b]		BR[c]
Solvent	Toluene	H_2O	Toluene	H_2O	H_2O
YbDD	28.19	23.62	3.5	2.8	2540
YbN	23.02	/	2.8	2.7	1850

[a]Déterminé à partir de la courbe de décroissance de l'émission surveillée à λem = 978 nm ($^2F_{5/2} \rightarrow {}^2F_{7/2}$) avec λex = 425 nm (Conc. : 1 µM). [b]Les rendements quantiques relatifs de l'émission de Yb^{3+} (λex = 425 nm) des deux complexes Yb^{3+} dans le toluène et H_2O ont été obtenus par comparaison avec l'étalon YbTPP(Tp). [c]Calculé à partir de BR = coefficient d'atténuation molaire × rendement quantique ; les coefficients d'atténuation molaire ont été obtenus à partir des spectres d'absorption dans l'eau à 425 nm en appliquant la loi de Beer-Lambert.
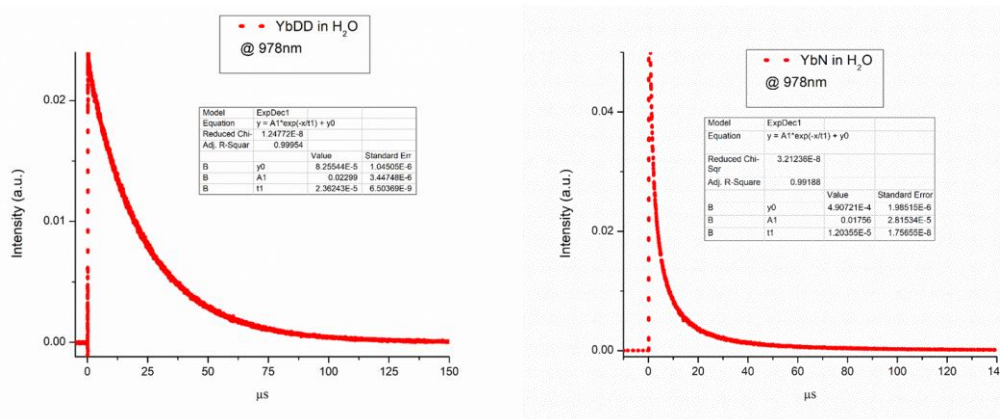

Figure 5. Courbe de décroissance de l'émission de Yb^{3+} sous forme de complexe YbDD (en haut) ou YbN (en bas) et avec ajustement de la fonction monoexponentielle.

1.2.5 Génération d'oxygène singulet

À titre de validation intersystème, le rendement quantique en oxygène singulet du GdDD a également été examiné dans le chloroforme par comparaison avec le spectre

du composé de référence H₂TPP ($\Phi\Delta$ = 55 % dans CHCl₃). Un agent anticancéreux de nouvelle génération, le GdN, qui ne comprend qu'un seul cycle porphyrine et dont le rendement quantique de l'oxygène singulet est élevé, a été choisi pour servir de comparaison.[5] Les spectres de phosphorescence $^1O_2$ dans le proche infrarouge du GdDD, du GdN et de la référence sont présentés dans la figure 6. D'après ces spectres, les rendements quantiques de l'oxygène singulet du GdDD et du GdN ont été mesurés à 66 % et 51 %, respectivement. Le GdDD a donc montré une génération supérieure d'oxygène singulet dans les milieux organiques et aqueux.
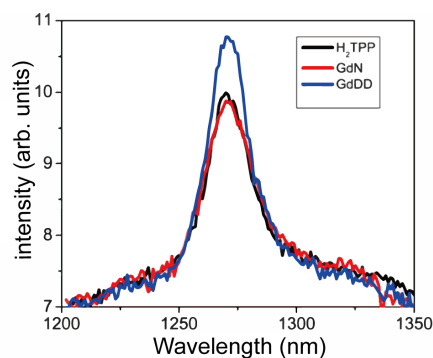
Figure 6. Spectre de phosphorescence du $^1O_2$ dans le proche infrarouge sensibilisé par le GdDD, le GdN et la tétraphénylporphyrine standard H₂TPP.

1.3 Conclusion

Dans ce projet, il est rarement fait état d'une série de complexes double-decker lanthanide-porphyrine solubles dans l'eau avec une caractérisation structurelle utilisant les techniques RMN, HRMS, STM et TAS. Des bio-applications incluant l'imagerie NIR et la génération de 1O2 cytotoxique des complexes ont également été développées. L'amélioration majeure des performances photophysiques - bien que tenant compte du faible rendement quantique de Yb^{3+} dans la région NIR - provient de l'augmentation de la luminosité de la sonde potentielle de bioimagerie YbDD. Cette propriété, la luminosité, n'a pas encore été largement reconnue comme le critère d'applicabilité, par

rapport au rendement quantique, mais elle présente une plus grande importance pratique

pour la bioimagerie.

Projet 2: Complexes double chélateur "tout-en-un" permettant une théranostique multimodale

2.1 Introduction

Bien que le domaine du théranostic à base de porphyrines ait été étudié depuis de nombreuses années, un immense potentiel est encore démontré et une question cruciale demeure : "Comparé aux médicaments individuels, produit-il des effets bénéfiques plus efficacement en combinant les modalités de diagnostic et de thérapie dans un seul système moléculaire ? Pour répondre à cette question et explorer de meilleurs agents théranostiques, nous présentons ici une série de complexes à base de porphyrine-cyclène. Un lieur rigide ou flexible est utilisé pour relier deux macrocycles. La partie porphyrine est capable de chélater Zn(II), Ga(III), et le ligand DOTA-amide ponté peut servir pour Gd(III), Yb(III), ou Eu(III). Différentes combinaisons de métaux pourraient conférer aux complexes correspondants deux capacités d'imagerie différentes, notamment l'IRM, la TEP et l'imagerie moléculaire dans le proche infrarouge, tandis que les complexes préservent les effets de la TPD en générant de l'oxygène singulet.

Available in archival version
Disponible en version archivage

Figure 7. Structures moléculaires des complexes binucléaires étudiés dans ce travail.

2.2 Résultats et discussion

2.2.1 Spectres d'émission

Les spectres d'émission à température ambiante pour trois ligands (PL, PZnL et PfL) ont été mesurés dans des solutions organiques et aqueuses. Les complexes de Gd(III) ont été mesurés dans le chloroforme. Les ligands coordonnés avec Gd(III) ou Yb(III) ont été enregistrés dans de l'eau avec 1% de DMSO. La longueur d'onde d'excitation était de 420 nm où tous les échantillons ont pu être excités efficacement. Il convient de noter que les spectres des complexes à base de Gd(III) ont été enregistrés par un système de tube photomultiplicateur (PMT) capable de mesurer l'émission de 300 nm à 1600 nm avec une correction appropriée. Les spectromètres UV-visible courants ont la limite de détection la plus longue jusqu'à environ 800 nm, tandis que les spectromètres NIR courants donnent des résultats fiables après 900 nm. Cependant, il pourrait être intéressant de voir la phosphorescence des porphyrines se situer autour de 800 nm.[6, 7]
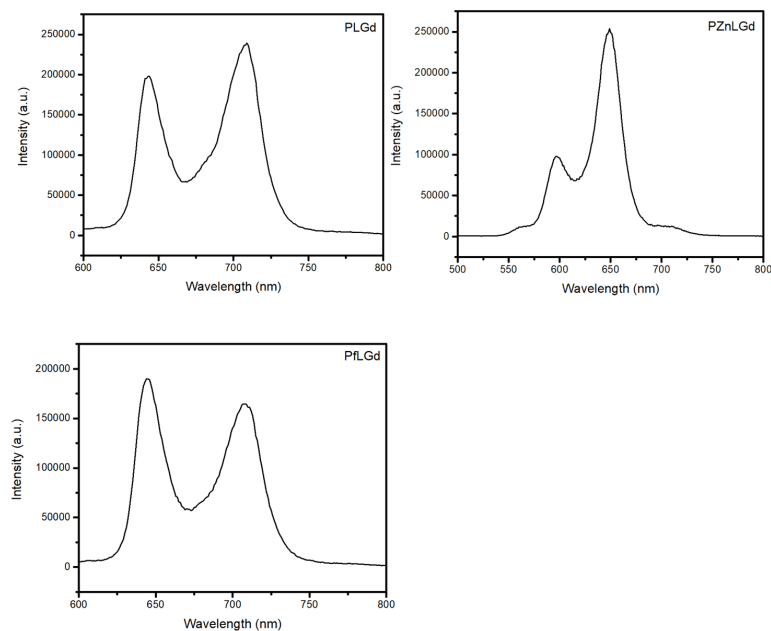

Figure 8. Spectres d'émission de PLGd, PZnLGd et PfLGd dans le chloroforme à 298 K (λ_{ex} = 420 nm, conc. = 1 μM).

Les trois complexes ont révélé une forte émission dans le domaine visible. Le PLGd et le PfLGd présentaient tous deux des pics d'émission situés à 644 nm et 709 nm qui correspondaient aux transitions énergétiques typiques S1→S0 dans une porphyrine à base libre. Quant au PZnLGd, les pics d'émission pour les mêmes transitions étaient largement décalés vers le bleu, respectivement à 597 et 649 nm. C'est parce que les métalloporphyrines ont généralement un état excité singulet le plus bas soulevé, S1.

Figure 9. Spectres d'émission ($\lambda_{ex} = 420$ nm) d'une solution H_2O (1% DMSO) de PLGd et PLYb (conc. = 1 µM) à 298 K. La partie rouge est agrandie dans la gamme d'émission NIR de l'Yb(III).

Le PLGd et le PLYb présentaient tous deux une fluorescence provenant de la partie porphyrine et les pics d'émission étaient à 654 nm et 713 nm pour le PLGd (649 nm et 712 nm pour le PLYb). Ces deux pics sont attribués aux transitions énergétiques S1→ S0 étiquetées respectivement Q(0,0) pour une longueur d'onde plus courte et Q(0,1) pour une longueur d'onde plus longue. Une différence est que pour PLGd, la ligne Q(0,0) était légèrement plus faible que la ligne Q(0,1) mais l'inverse est vrai pour PLYb où la ligne Q(0,0) était plus forte. Quant à l'émission dans le proche infrarouge, deux pics intenses ont été trouvés à 971 nm et 1038 nm correspondant à deux transitions

énergétiques $^2F_{5/2} \rightarrow {}^2F_{7/2}$ de l'ytterbium. Notez que les trois échantillons à base d'Yb ont été mesurés dans les mêmes conditions et au même moment, il est donc fiable de comparer l'émission d'Yb de chacun. Le PLYb a donné la plus forte émission NIR, ce qui signifie que des transitions ED plus efficaces se sont produites à travers un revêtement rigide (PLYb vs. PfLYb) et que les anneaux de porphyrine libre avaient un état énergétique optimal pour la transition (PLYb vs. PZnLYb).
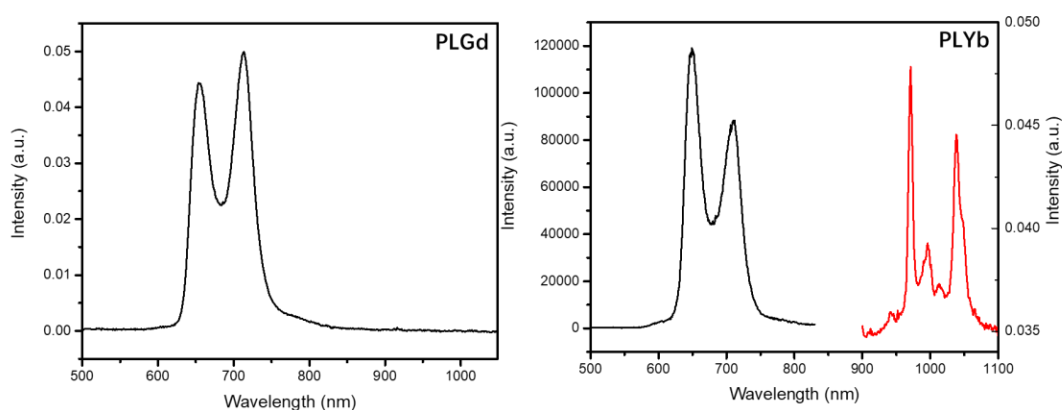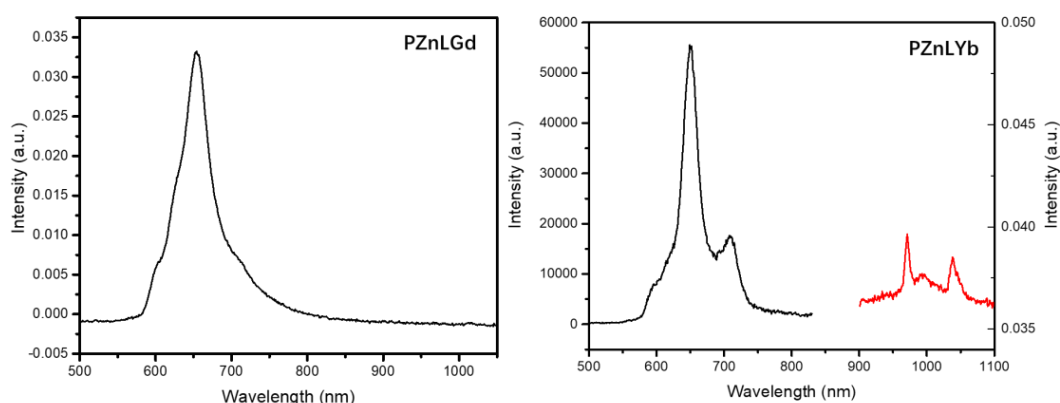

Figure 10. Spectres d'émission (λ_{ex} = 420 nm) d'une solution H_2O (1% DMSO) de PZnLGd et PZnLYb (conc. = 1 μM) à 298 K. La partie rouge est agrandie dans la gamme d'émission NIR de l'Yb(III).

La forme des spectres d'émission des complexes coordonnés au zinc était très différente. Les pics les plus intenses trouvés dans les deux spectres (652 nm pour PZnLGd, et 649 nm pour PZnLYb) ont été attribués aux transitions Q(0,1), et ils ont été hautement préférés par le transfert d'énergie. Le pic plus faible dans la zone bleue a été attribué aux transitions Q(0,0). Les pics d'émission Q(0,0) et Q(0,1) étaient décalés vers le bleu par rapport à ceux de PLLn, ce qui indique que la métalloporphyrine possède un état excité singulet le plus bas, S1. Il y avait un autre pic d'émission trouvé dans la plus grande longueur d'onde pour chaque complexe, situé à 713 nm pour PZnLGd et 709 nm

pour PZnLYb. Il est déroutant de voir un tel pic car il est rare d'avoir plus de voies de

transition d'énergie des états singlets excités des porphyrines vers leurs états

fondamentaux. Il est également à noter que la position de ces pics supplémentaires était

assez similaire aux transitions Q(0,1) de PLGd ou PLYb. Une raison possible pourrait

être la dissociation du complexe dans la solution pendant les mesures. La libération du

zinc a laissé le PLGd ou PLYb résultant qui émettait dans les solutions de test.

Cependant, le pic supplémentaire n'a pas été trouvé dans le spectre d'émission du

PZnLGd réalisé dans le chloroforme (Figure 8).
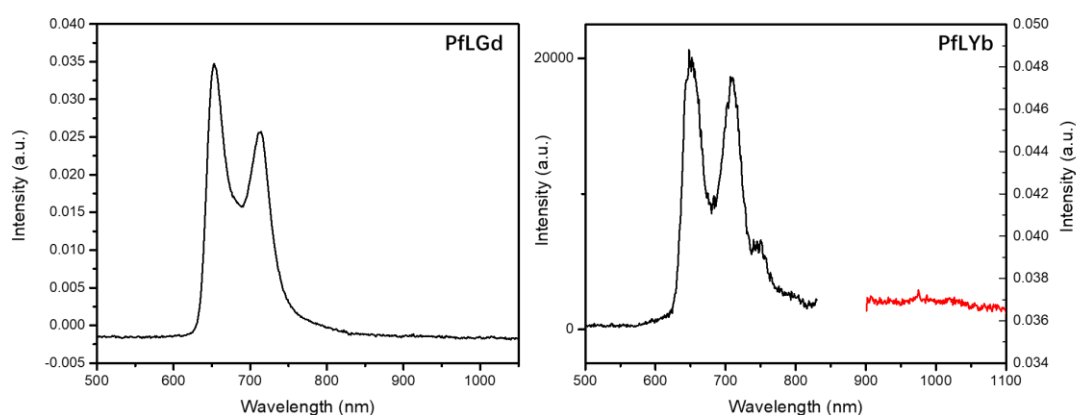
Figure 11. Spectres d'émission (λ_{ex} = 420 nm) d'une solution H_2O (1% DMSO) de

PfLGd et PfLYb (conc. = 1 μM) à 298 K. La partie rouge est agrandie dans la gamme

d'émission NIR de l'Yb(III).

PfLGd et PfLYb présentent deux pics d'émission situés à 653 nm et 714 nm qui sont

attribués à deux transitions énergétiques S1→S0 étiquetées Q(0,0) et Q(0,1). Ces pics

sont typiques de la fluorescence des porphyrines libres et sont également observés dans

le PLGd et le PLYb. Cependant, l'intensité de fluorescence du PLYb était beaucoup plus

faible que celle du PLGd dans les mêmes conditions, ce qui suggère qu'une plus grande

quantité d'énergie d'excitation a subi des transitions des états singlets aux états triplets.

Bien que l'on s'attende à un transfert d'énergie plus important des états triplets de la porphyrine vers les états excités de l'Yb(III) comme cela a été observé dans le cas du PLYb, une émission négligeable d'Yb(III) a été détectée dans le domaine du NIR. La raison pour laquelle aucune émission d'Yb(III) n'a été trouvée pourrait être due à l'extinction des molécules d'eau puisque l'écart énergétique entre l'état excité le plus peuplé et l'état fondamental de l'Yb(III) est d'environ 10200 cm^{-1}, ce qui est efficacement couplé avec le troisième harmonique vibrationnel des oscillateurs O-H ($\sim$3300-3500 cm^{-1}).[8]
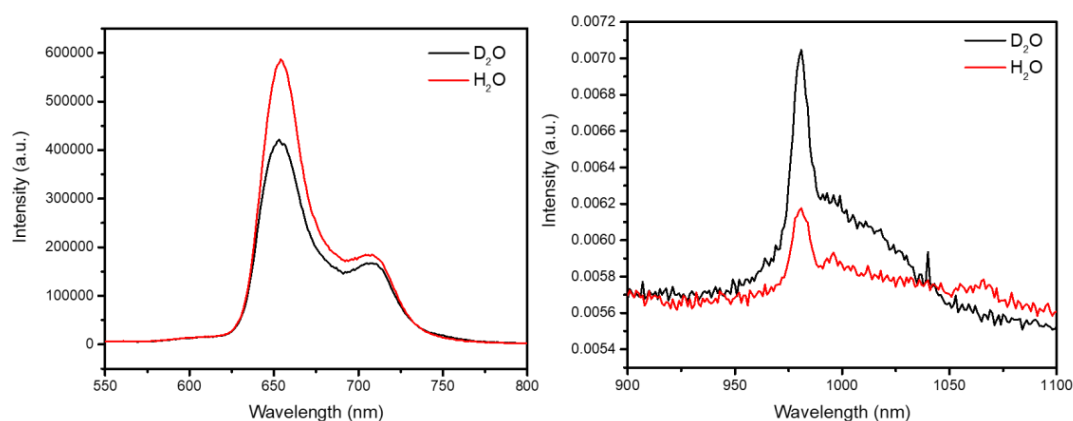
Figure 12. Spectres d'émission (λ_{ex} = 420 nm) de solutions H_2O et D_2O (toutes deux à 1 % de DMSO) de PfLYb (conc. = 10 μM) dans le domaine visible (à gauche) et le domaine proche infrarouge (à droite) à 298 K.

2.2.2 MRI T_1 relaxivity

Une fonction d'imagerie pour mes chélateurs "tout-en-un" est leur potentiel en tant qu'agents de contraste pour l'IRM lorsqu'ils se coordonnent avec des ions Gd(III). Bien que le taux d'échange d'eau ne soit pas aussi important que celui du DOTA9, le cycle cyclénique substitué par un (N-méthyl)amide est toujours un ligand idéal pour le Gd(III). Tous les complexes préparés à base de Gd(III) ont été soumis à des mesures de relaxivité

in vitro afin d'étudier les facteurs qui contribuent au taux de relaxation des molécules d'eau et de rechercher les meilleurs agents théranostiques parmi eux.

Quatre échantillons ont été mesurés et le GdDOTA a été utilisé comme échantillon de référence. Selon la figure 13 et le tableau 2, le PLGd a révélé la valeur de relaxivité la plus élevée, r_1 = 7,86 mM^{-1}s^{-1}, qui est beaucoup plus élevée que celle du GdDOTA (5,44 mM^{-1}s^{-1} à 25ºC). La tendance est la même à 37ºC où le PLGd était de 5,08 mM^{-1}s^{-1} et le GdDOTA de 3,22 mM^{-1}s^{-1}. Les valeurs de r_1 pour le GdDOTA étaient similaires à celles de la littérature,[9] ce qui prouve que nos conditions et paramètres d'essais étaient qualifiés. La principale raison pour laquelle le PLGd présente une si grande relaxivité est que son poids moléculaire et sa taille sont plus importants que ceux du GdDOTA. Le mouvement moléculaire du PLGd est donc ralenti et le temps de corrélation effectif est plus long, ce qui entraîne une relaxivité accrue. En comparant PLGd et PfLGd, ce dernier ayant un r_1 beaucoup plus faible, il a été constaté que la flexibilité du lieur affectait considérablement le mouvement des molécules - le lieur flexible a fait que la fraction Gd(III) culbute rapidement et qu'il est difficile de lier les molécules d'eau, même si PfLGd aurait pu être plus prometteur en raison de plus de positions de liaison pour les molécules d'eau (q $\geqslant$ 2). Il convient de noter que même si le PfLGd a montré une grande relaxivité, il serait prudent de l'utiliser comme GBCA pour l'IRM car moins de positions de chélation du ligand pourrait entraîner une moindre stabilité du complexe et une possible toxicité.

PZnLGd avec différents cations (-OTf, groupe trifluorométhanesulfonate, et -Cl, chlorure) ont également été mesurés dans les mêmes conditions. Divers anions sont présents dans les conditions physiologiques qui pourraient affecter le mouvement (et

ensuite la relaxivité) des complexes Gd(III). Le groupe trifluorométhanesulfonate, bien que peu abondant dans les tissus biologiques, a été choisi comme anion coordinateur pour le comparer au chlorure et voir si la taille ou les groupes coordinateurs sur Zn(II) peuvent affecter la relaxivité globale. Deux complexes Zn(II)-Gd(III) ont présenté des relaxivités T1 similaires (différence inférieure à 10 %), ce qui suggère que la taille des groupes de coordination de Zn(II) ne contribue que légèrement à la relaxivité. Cependant, il faut souligner que, bien que la taille n'ait pas affecté, la présence d'une coordination supplémentaire sur le noyau métallique de la porphyrine a déjà sévèrement diminué la relaxivité. Les deux relaxivités pour PZnLGd-OTf et PZnLGd-Cl (4,16 mM^{-1}s^{-1} et 3,77 mM^{-1}s^{-1} respectivement) étaient beaucoup plus faibles que celles de PLGd, voire de GdDOTA. La même tendance a été observée à 37 $^{\circ}$C (figure 13). Malheureusement, il n'existe aucun rapport résumant les effets du métal voisin sur la relaxivité du Gd(III) T$_1$, et il est toujours difficile de prédire et de contrôler la relation entre le mouvement moléculaire et sa relaxivité. Il faut noter que, bien que certains complexes Zn(II)-Porphyrine-Gd(III)-DOTA aient été rapportés comme ayant une relaxivité T$_1$ accrue,[9] les raisons en sont l'empilement des métalloporphyrines neutres et l'agrégation résultante de leurs complexes amphiphiles (porphyrine hydrophobe et dérivés GdDOTA hydrophiles). Mon PZnLGd n'a pas montré la même tendance car le lieur rigide et court ne convient pas à la formation de micelles. En outre, les relaxivités élevées provenant de l'agrégation ou de concentrations localement élevées ne constituent pas une amélioration intrinsèque des GBCA et ne sont pas pratiques dans les applications cliniques.

Le taux de relaxation de l'agent prometteur de double imagerie PET/MRI, PGaLGd, a également été mesuré à des concentrations plus faibles. Étonnamment, contrairement à

l'autre métalloporphyrinate PZnLGd, PGaLGd a révélé la plus grande relaxivité T_1 parmi tous les complexes de Gd(III) préparés (10,37 mM^{-1}s^{-1}). Ce phénomène pourrait être attribué à la différence majeure entre PGaLGd et PZnLGd dans laquelle ils ont différents métaux coordonnés sur les anneaux de porphyrine. L'ion Zn(II) présente seulement deux charges positives qui sont parfaitement équilibrées par la porphyrine, alors que Ga(III) nécessite un ligand supplémentaire (acétate dans ce cas). Il a été rapporté que le carboxylate pourrait attirer des molécules d'eau supplémentaires et renforcer les effets de 2ème sphère où le poids moléculaire effectif sera plus grand et les molécules d'eau de 2ème sphère seront plus faciles à relaxer.[10]
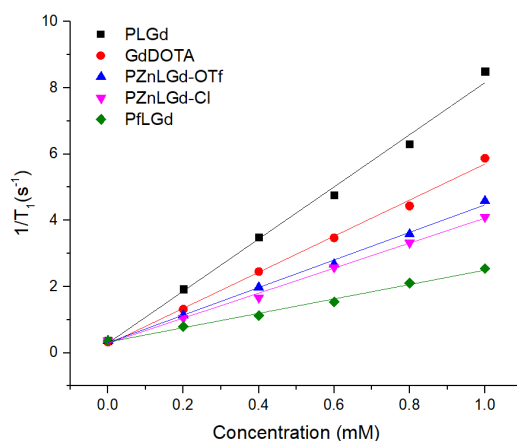
Figure 13. Taux de relaxation $1/T_1$ en fonction des concentrations de l'échantillon pour les complexes préparés (3 Tesla, 25 °C).

Tableau 2. Paramètres pour toutes les courbes de la figure 13. Les pentes sont égales aux valeurs de la relaxivité T1 (r_1).

	Slope (Relaxivity, r_1, mM^{-1}s^{-1})	Adj. R-Square
PLGd	7.86314	0.9924
Gd-DOTA	5.44181	0.99583
PZnLGd-tfo	4.1599	0.9962

PZnLGd-cl	3.77227	0.99673
PflGd	2.17157	0.99201
PGaLGd	10.37058	0.95334

2.2.3 Singlet oxygen

La capacité de PDT des complexes de Gd(III) a été évaluée en mesurant la phosphorescence de l'oxygène singulet généré. L'oxygène singulet est une espèce active qui peut rapidement détruire les biomolécules et tuer les cellules. Par conséquent, si un photosensibilisateur peut produire plus d'oxygène singulet lors d'une courte irradiation lumineuse, cela signifie que le photosensibilisateur présente de meilleurs effets PDT. La quantité d'oxygène singulet formée a été déterminée par son intensité de phosphorescence. Les échantillons ont été préparés dans le chloroforme à la même concentration, à l'exception du PGaLGd dissous par le DMSO avant la dilution. Le pic d'émission de phosphorescence du 1O2 était situé à 1270 nm (Figure 14). Les surfaces intégrées des pics d'émission sont proportionnelles à la quantité d'oxygène singulet produite. La tétraphénylporphyrine, un photosensibilisateur classique, a été choisie comme standard avec un rendement quantique de l'oxygène singulet de 0,55 rapporté dans la littérature.[11] Les rendements quantiques de tous les échantillons de ce travail peuvent être déterminés en comparant la surface intégrée des pics d'émission avec celle du H2TPP. La plupart des complexes ont montré des rendements quantiques d'oxygène singulet supérieurs à ceux du H_2TPP (PLGd : 0,87, PZnLGd : 0,86, PfLGd : 0,84). La raison principale de l'amélioration de l'effet PDT est que la méso-tri(pentafluorophényl)porphyrine a été utilisée au lieu de la phénylporphyrine, et que son état triple est plus élevé, ce qui entraîne une sensibilisation plus efficace de

l'oxygène.[12] Tous les échantillons possèdent la même structure de porphyrine, ils ont donc donné des valeurs similaires. Cependant, PGaLGd a montré des performances inférieures (rendement quantique de $^1O_2$ = 0,47). Cela pourrait être dû au fait que le Ga(III) coordonné rend le complexe trop polaire pour être bien dispersé dans le chloroforme, mais c'est prometteur pour le PGaLGd qui présente un grand effet PDT dans les solvants polaires, comme l'eau.
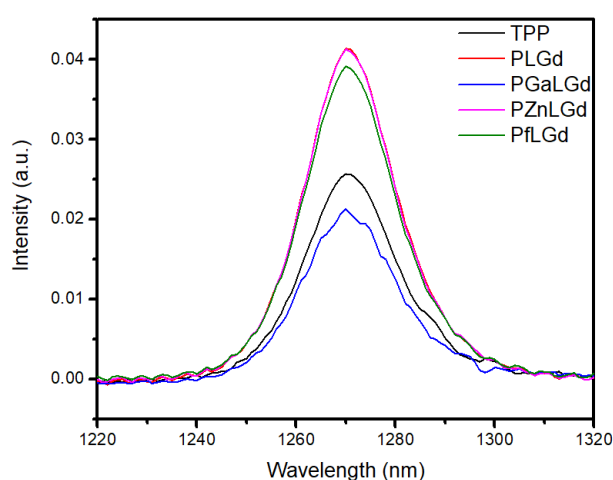

Figure 14. Spectres d'émission de la phosphorescence NIR $^1O_2$ générée par différents complexes dans le chloroforme (PGaLGd avec extra 1% v/v DMSO) à 298 K (λ_{ex} = 420 nm, conc. = 5 μM) . La tétraphénylporphyrine H$_2$TPP a été utilisée comme échantillon standard.

2.3 Conclusion

Une série de complexes de lanthanides à base de porphyrine et de cyclène a été conçue et synthétisée. Différents ions métalliques peuvent être coordonnés pour atteindre différents objectifs d'imagerie. Il a été constaté que les complexes avec un lieur rigide reliant deux macrocycles possèdent une luminescence NIR, de sorte que des expériences d'imagerie cellulaire NIR pourraient être menées à l'avenir en les utilisant,

en plus d'autres tests biologiques. Parallèlement, PLGd et PGaLGd ont présenté une relaxivité T1 supérieure, résultant de l'augmentation de leur poids moléculaire et d'éventuels effets de seconde sphère. Leur capacité de PDT a été évaluée en mesurant leurs rendements quantiques en oxygène singulet et la plupart d'entre eux étaient plus performants que la tétraphénylporphyrine, un photosensibilisateur classique. Des effets synergiques peuvent être obtenus en intégrant des fragments diagnostiques et thérapeutiques, bien que dans ce travail le ligand ayant un lieur flexible (PfLLn) n'ait pas montré de meilleures performances en imagerie. Le marquage à froid du Gallium(III) a été un succès et il est prometteur de voir bientôt les fonctions TEP de ces composés sur des modèles animaux.

Projet 3: Une stratégie d'expansion des chromophores pour le suivi des réactions bioorthogonales par luminescence des lanthanides off-onn

3.1 Introduction

On rapporte un complexe à base d'Eu(III), Eu-BT, ███████████████ ████████████████████████. Il peut spécifiquement procéder à des réactions de cycloadditions azide-alkyne (SPAAC) promues par le cycle et la souche avec des réactifs dibenzocyclooctyne (DBCO), où les DBCO sont facilement disponibles et capables d'une conjugaison ultérieure avec d'autres biomolécules grâce à leurs groupes carboxyliques. Avant les réactions SPAAC, notre complexe ne fournit aucun signal lumineux avec une excitation supérieure à 250 nm. Après la cycloaddition spécifique avec le cycle cyclooctyne, la partie triazoyle formée, ainsi que les cycles pyridine et deux benzènes, servent de système de conjugaison étendu, qui sensibilise efficacement les états excités de l'Eu(III). Les intensités d'émission étaient proportionnelles à l'ampleur de cette réaction bioorthogonale, et l'évaluation cinétique de la cycloaddition de l'Eu-BT et de l'acide DBCO a été réalisée par des techniques de résonance magnétique nucléaire (RMN) (la constante de réaction de second ordre, $k_2 = 0,39 \pm 0,007$ M^{-1} min^{-1}). L'acide DBCO est disponible dans le commerce et peut se conjuguer à une large gamme de biomolécules à partir de son groupe carboxylique, par exemple, il peut se conjuguer à la mannosamine, un précurseur métabolique à la surface des cellules.[13] Cette réaction et la stratégie d'expansion du chromophore montrent une large application et comblent le vide de la surveillance de la chimie bioorthogonale par luminescence off-on.

Figure 15. L'illustration du processus de génération de la luminescence off-on. La réaction SPACC dilate le chromophore et le rend apte à transférer l'énergie d'excitation au centre Eu(III).

3.2 Résultats et discussion

3.2.1 Études cinétiques sur les réactions SPAAC

L'évolution des réactifs alcynes sous contrainte est motivée par la demande d'une meilleure cinétique, c'est-à-dire de constantes de vitesse du second ordre plus élevées. Les vitesses de réaction sont principalement calculées par les changements de réactifs et de produits. Il existe une méthode typique pour déterminer ces concentrations en comparant les intégrales des pics des réactifs aux étapes initiales et à différents moments. Avec les concentrations initiales connues de l'acide DBCO et du complexe La-BT, la concentration du produit conjugué peut être déterminée. Une expérience de RMN résolue dans le temps a été réalisée en mélangeant l'acide DBCO et le La-BT dans un tube RMN et en surveillant les spectres RMN jusqu'à 780 minutes (Figure 16). Ici, le La-BT a été utilisé à la place du Eu-BT dans la spectroscopie RMN car l'Eu(III) est un métal paramagnétique ayant des électrons non appariés et provoque généralement de graves interférences sur les spectres. La(III) est diamagnétique et La-BT n'a pas eu ce problème.

Au début de la réaction (0 minute), il y avait un pic doublet évident situé à 8,49 et 8,50 ppm. Ce pic doublet est attribué à un proton sur le cycle pyridine proche de l'azote. Le signal du proton a été divisé en raison du couplage spin-spin avec son hydrogène voisin. Avec le traitement de la réaction, le pic doublet s'est déplacé vers le bas et s'est transformé en une série de pics larges. Cela pourrait s'expliquer par le fait que les systèmes insaturés conjugués voisins n'ont pas protégé ce proton mais ont causé plus de couplages. Après 600 minutes, il n'y avait pas de signal évident à 8,5 ppm mais un signal fort à environ 8,7 ppm. En considérant l'intégrale du pic à t = 0 correspondant à la concentration initiale de La-BT, les concentrations instantanées peuvent être calculées à différents moments, comme le montre la figure 17. La courbe présente une décroissance non linéaire qui suggère que la réaction n'était pas d'ordre zéro.

Comme pour une réaction standard du second ordre, A + B → P, nous avons

$$\frac{d[A]}{dt} = -k[A][B] \qquad (15)$$

En intégrant de 0 à t,

$$\frac{1}{[B]_0 - [A]_0} ln \frac{[B][A]_0}{[A][B]_0} = kt \qquad (16)$$

où [A], [B] et [P] sont les concentrations du complexe La-BT, de l'acide DBCO et du produit conjugué respectivement. Nous pouvons obtenir le temps réel [A] en comparant les intégrales des pics de RMN et $[B] = [B]_0 - [A]$.

En traçant le temps (t) en fonction de $(\frac{1}{[B]_0 - [A]_0} ln \frac{[B][A]_0}{[A][B]_0})$, nous pouvons obtenir la constante de vitesse de réaction k à partir de sa pente (figure 18) dans la plage dynamique (0-270 minutes), où aucun des réactifs n'a été entièrement consommé. La

constante de vitesse de réaction k a été déterminée à partir de la pente comme étant 3,92×10-4 mM-1 min-1 (0,39 M-1min-1). Il y a deux raisons pour lesquelles notre valeur est beaucoup plus petite que celles de la littérature pour la SPAAC entre l'azide et le DBCO : premièrement, le processus de réaction a été suivi dans la machine RMN où la solution de réaction était rarement agitée, ce qui a considérablement ralenti la vitesse de réaction ; deuxièmement, au lieu de l'azide d'alkyle qui était utilisé pour déterminer les vitesses de réaction auparavant, nous nous sommes concentrés sur une azidopyridine où l'électron était stabilisé sur le système de liaison π conjugué et moins réactif.
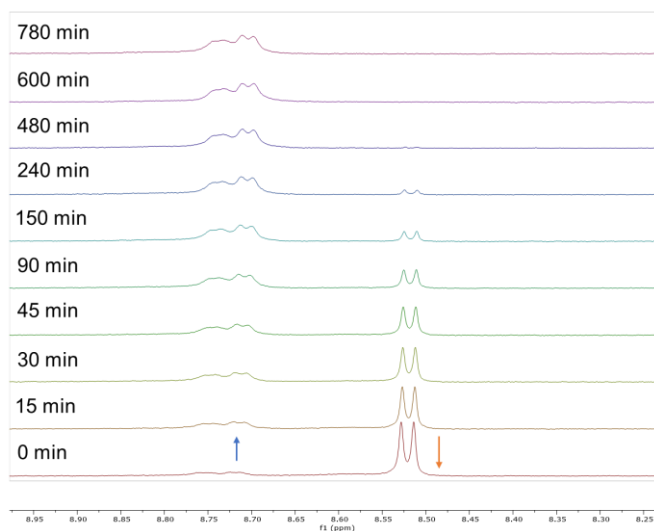

Figure 16. Spectres de RMN-1H superposés des solutions de mélange La-BT et DBCO-acide (dans CD$_3$OD) à différents moments.
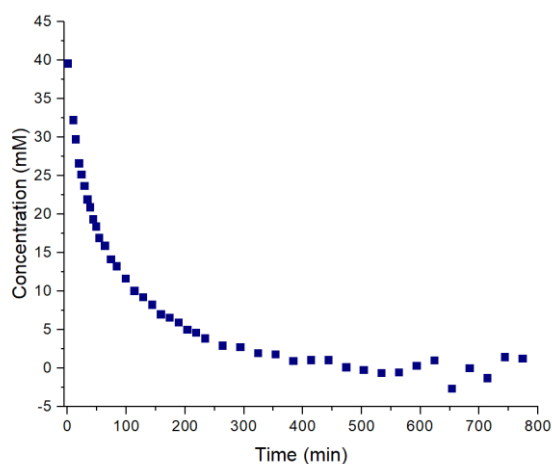
Figure 17. Tracé des concentrations calculées de La-BT (par les intégrales des pics RMN à 8,5 ppm) en fonction du temps de réaction.
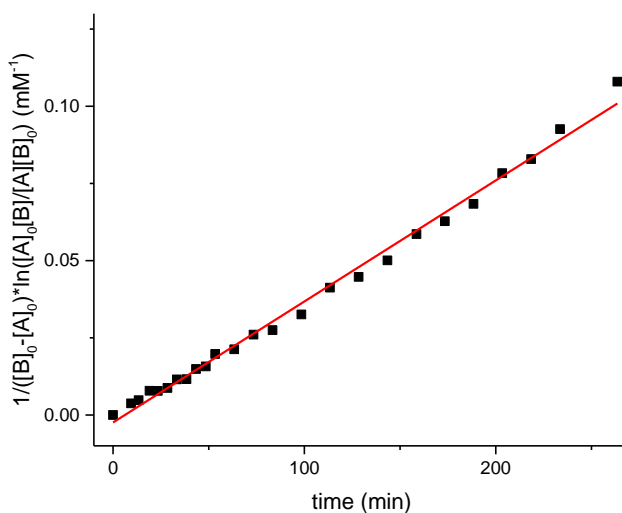

Figure 18. Tracé logarithmique de la réaction du composé 10 avec l'azide de benzyle dans le CD$_3$OD.

3.2.2 Analyse cinétique de la propriété d'extinction/de luminescence

L'un des avantages de notre complexe Eu-BT dans la chimie bioorthogonale est la propriété de luminescence off-on. Avec une irradiation lumineuse de 320 nm, le seul Eu-BT n'a pas d'émission lumineuse avant la conjugaison, mais après la réaction SPAAC réussie avec les acides DBCO, le centre Eu(III) sera efficacement sensibilisé et

produira une émission visible caractéristique et de longue durée. L'intensité de l'émission augmente avec la progression de la réaction et la formation de plus de produits conjugués. Des spectres d'émission ont été obtenus à partir d'une solution réactive d'Eu-BT et de DBCO. Une forte émission d'Eu(III) a été observée après 5 minutes de réaction, et après 140 minutes, l'Eu-BT avait principalement réagi et l'intensité d'émission à 616 nm et 700 nm était 3,8 fois plus forte.
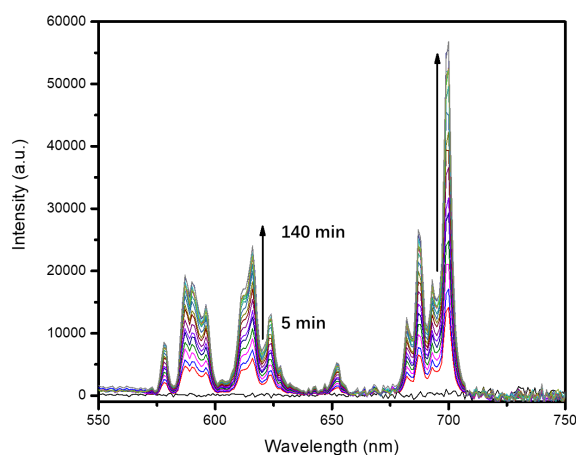

Figure 19. Spectres d'émission de la solution d'une réaction bioorthogonale en cours entre Eu-BT et DBCO-acide à différents moments. La réaction et la mesure ont toutes deux été réalisées à température ambiante dans du méthanol (conc. = 10 µM, λ_{ex} = 320 nm).
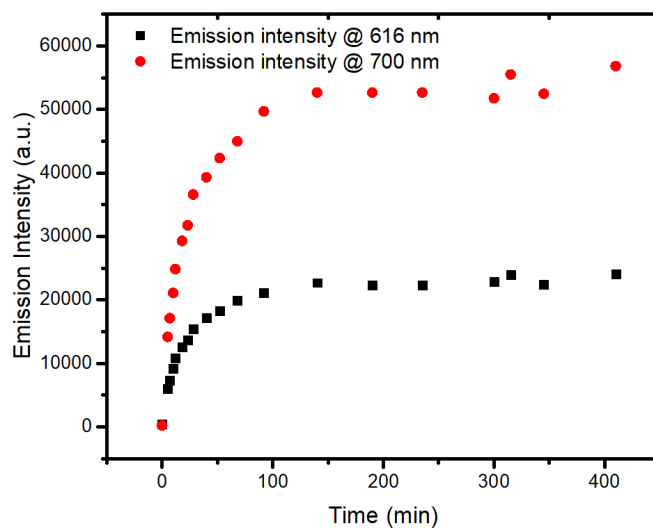
Figure 20. Évolution de l'intensité en fonction du temps des pics d'émission à 616 nm et 700 nm. Les données sont extraites de la figure 19.

3.3 Conclusion

La chimie bioorthogonale est l'un des domaines les plus prometteurs de la chimie moderne, car elle pourrait permettre une chimie contrôlée dans des cellules et des organismes vivants, plutôt que dans des verreries ou dans des conditions difficiles. Cependant, de nombreuses limites subsistent avant son application à grande échelle. L'une d'elles est que la vitesse de réaction bioorthogonale est toujours un problème pour des réactions efficaces. D'autre part, il n'existe que quelques rapports sur le suivi en temps réel des réactions bioorthogonales par émission visible et aucun exemple de luminescence en continu. Mon travail implique des complexes à base d'Eu(III) subissant une réaction SPACC typique simultanément avec un réactif disponible dans le commerce, le DBCO, et le signal lumineux hautement différencié (pics d'émission nets et résolus dans le temps) a été généré et renforcé avec le processus de réaction. Bien que la vitesse ait été mesurée comme étant inférieure à la norme en raison du groupe azide stabilisé, elle est inévitable lors de l'introduction des stratégies de chromophore d'expansion.

Reference

[1] Zhang, T.; Zhu, X.; Cheng, C. C.; Kwok, W. M.; Tam, H. L.; Hao, J.; Kwong, D. W.; Wong, W. K.; Wong, K. L., Water-soluble mitochondria-specific ytterbium complex with impressive NIR emission. *J. Am. Chem. Soc.* **2011,** *133* (50), 20120-2.

[2] Otsuki, J.; Kawaguchi, S.; Yamakawa, T.; Asakawa, M.; Miyake, K., Arrays of Double-Decker Porphyrins on Highly Oriented Pyrolytic Graphite. *Langmuir* **2006,** *22* (13), 5708–5715.

[3] Tanner, P. A.;Zhou, L.; Duan, C.; Wong, K. L., Misconceptions in electronic energy transfer: bridging the gap between chemistry and physics. *Chem. Soc. Rev.* **2018,** *47* (14), 5234-5265.

[4] Shavaleev, N. M.; Eliseeva, S. V.; Scopelliti, R.; Bünzli, J. C., Influence of symmetry on the luminescence and radiative lifetime of nine-coordinate europium complexes. *Inorg. Chem.* **2015,** *54* (18), 9166-73.

[5] Zhang, T.; Lan, R.; Chan, C. F.; Law, G. L.; Wong, W. K.; Wong, K. L., In vivo selective cancer-tracking gadolinium eradicator as new-generation photodynamic therapy agent. *Proc. Natl. Acad. Sci. U S A* **2014,** *111* (51), E5492-7.

[6] Gouterman, M.; Khalil, G.-E., Porphyrin free base phosphorescence. *J. Mol. Spectrosc.* **1974,** *53* (1), 88-100.

[7] Harriman, A., Luminescence of porphyrins and metalloporphyrins. Part 1.—Zinc(II), nickel(II) and manganese(II) porphyrins. *J. Chem. Soc., Faraday Trans.2* **1980,** *76* (0).

[8] Beeby, A.; Clarkson, I. M.; Dickins, R. S.; Faulkner, S.; Parker, D.; Royle, L.; de Sousa, A. S.; Williams, J. A. G.; Woods M., Non-radiative deactivation of the excited states of europium, terbium and ytterbium complexes by proximate energy-matched OH, NH and CH oscillators: an improved luminescence method for establishing solution hydration states. *J. Chem. Soc. Perkin Trans. 2* **1999**, 493-504.

[9] Shen, Y.; Goerner, F. L.; Snyder, C.; Morelli, J. N.; Hao, D.; Hu, D.; Li, X.; Runge, V. M., T1 relaxivities of gadolinium-based magnetic resonance contrast agents in human whole blood at 1.5, 3, and 7 T. *Invest. Radiol.* **2015,** *50* (5), 330-8.

[10] De Leon-Rodriguez, L. M.; Martins, A. F.; Pinho, M. C.; Rofsky, N. M.; Sherry, A. D., Basic MR relaxation mechanisms and contrast agent design. *J. Magn. Reson. Imaging* **2015,** *42* (3), 545-65.

[11] Schmidt, R.; Afshari, E., Comment on "Effect of solvent on the phosphorescence rate constant of singlet molecular oxygen (1.DELTA.g)". *J. Phys. Chem.* **1990,** *94* (10), 4377–4378.

[12] Samaroo, D.; Vinodu, M.; Chen, X.; Drain, C. M., meso-Tetra(pentafluorophenyl)porphyrin as an efficient platform for combinatorial synthesis and the selection of new photodynamic therapeutics using a cancer cell line. *J. Comb. Chem.* **2007,** *9* (6), 998-1011.

[13] Sampathkumar, S. G.; Li, A. V.; Yarema, K. J., Synthesis of non-natural ManNAc analogs for the expression of thiols on cell-surface sialic acids. *Nat. Protoc.* **2006,** *1* (5), 2377-85.